

UCSF

UC San Francisco Electronic Theses and Dissertations

Title

Methods of Assessing Lesion Depth and Severity with Near-IR Light

Permalink

<https://escholarship.org/uc/item/19t3k4dz>

Author

Simon, Jacob C

Publication Date

2021

Peer reviewed|Thesis/dissertation

Methods of Assessing Lesion Depth and Severity with Near-IR Light

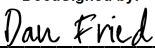
by
Jacob C Simon


DISSERTATION
Submitted in partial satisfaction of the requirements for degree of
DOCTOR OF PHILOSOPHY


in
Oral and Craniofacial Sciences

in the
GRADUATE DIVISION
of the
UNIVERSITY OF CALIFORNIA, SAN FRANCISCO

Approved:

DocuSigned by:

74D904363F2C429... Dan Fried
Chair

DocuSigned by:

DocuSigned by:36... Cynthia Darling


2AD3C69B6058424... Art Miller

Committee Members

Copyright 2020
By
Jacob Carmody Simon

DEDICATION

This dissertation is dedicated to the family and friends who helped me through this long journey.

ACKNOWLEDGEMENTS

I would like to express my sincere appreciation for my mentors Dr. Daniel Fried and Dr. Cynthia Darling for their support and dedication to my personal and educational development over the past eight years. This personal and professional accomplishment would not have been possible without the opportunity to work in the Fried Lab as a staff research associate, the essential guidance in applying to dental and graduate programs, and the development of my scientific knowledge base and research skills during my times as your student.

To Arthur Miller, I express my gratitude of allowing me to rotate in your lab, being a member of my qualification exam, and being a member of my dissertation committee.

Additionally, I would like to extended a warm thank you to all the members of the Fried Lab for your support, sharing of materials and lab space, and friendship throughout our education.

This work was supported by the NIH/NIDCR grants F30-DE026052, RO1-D14698, and RO1-DE019631

CONTRIBUTIONS

Chapter II

Used with permission from Lasers in Surgery and Medicine:

JC Simon, KH Chan, CL Darling, D Fried. (2014). Multispectral near-IR reflectance imaging of simulated early occlusal lesions: Variation of lesion contrast with lesion depth and severity. Lasers in Surgery and Medicine 45 (3), 203-215.

Chapter III

Used with permission from Journal of Biomedical Optics:

C Ng, EC Almaz, JC Simon, D Fried, CL Darling. (2019). Near-infrared imaging of demineralization on the occlusal surfaces of teeth without the interference of stains. Journal of Biomedical Optics 42 (3), 036002.

Chapter IV

Used with permission from Lasers in Dentistry XXIV 10473, 1047305:

JC Simon, DA Curtis, CL Darling, D Fried. (201). Multispectral near-infrared reflectance and transillumination imaging of occlusal carious lesions: variations in lesion contrast with lesion depth. Lasers in Dentistry XXIV.

Chapter V

Used with permission from Lasers in Dentistry XXII 8929, 89290R:

JC Simon, CL Darling, D Fried. (2016). A system for simultaneous near-infrared

reflectance and transillumination imaging of occlusal carious lesions. *Lasers in Dentistry* XXII.

Chapter VI

Used with permission from *Lasers in Dentistry* XXIII 10044, 1004407:

JC Simon, CL Darling, D Fried. (2017) Assessment of cavitation in artificial approximal dental lesions with near-IR imaging. *Lasers in Dentistry* XXIII.

Chapter VII

Used with permission from *Journal of Biomedical Optics*:

H Tom, JC Simon, KH Chan, CL Darling, D Fried. (2014). Near-infrared imaging of demineralization under sealants. *Journal of Biomedical Optics* 19 (7), 077003.

Chapter VIII

Used with permission from *Dental Materials*:

JC Simon, SA Lucas, RC Lee, CL Darling, M Staninec, R Vaderhobli, R Pelzner, D Fried. (2016). Near-infrared imaging of secondary caries lesions around composite restorations at wavelengths from 1300-1700-nm. *Dental materials* 32 (4), 915-923

Chapter IX

Used with permission from *Lasers in Surgery and Medicine*:

JC Simon, SA Lucas, M Staninec, H Tom, KH Chan, CL Darling, M Cozin, RC Lee, D

Fried. (2016). Near-IR transillumination and reflectance imaging at 1,300 nm and 1,500-1,700 nm for in vivo caries detection. *Lasers in Surgery and Medicine* 48 (9), 828-836.

Chapter X

Used with permission *Lasers in Surgery and Medicine*:

JC Simon, H Kang, M Staninec, AT Jang, KH Chan, CL Darling, RC Lee, D Fried.

(2017). Near-IR and CP-OCT imaging of suspected occlusal caries lesions. *Lasers in Surgery and Medicine* 49 (3), 215-224.

ABSTRACT**Methods for assessing lesion depth and severity using Near-IR Light****Jacob C. Simon**

Dental caries (tooth decay) is one of the most prevalent chronic diseases worldwide and is the leading cause of tooth loss in the United States [1-3]. Tooth decay is the demineralization (loss of mineral) of enamel and dentin resulting from chemical reactions between the hard tissue and acids produced by oral bacteria in biofilms [4, 5]. A caries lesion is the effect the disease has on the tooth, which develops over a time period ranging weeks to years, and results in the formation of cavities, quite literally holes in teeth [8-10]. Early detection of primary and secondary dental decay, accompanied by appropriate nonsurgical treatment of the disease process, is the ideal method for practicing preventative dentistry. Clinicians' lack the instrumentation to detect dental decay in its earliest stages with either radiographic imaging or visual tactile examination when the lesion process is reversible. This dissertation investigates the use of near-IR (NIR) light from 1300-1700-nm in wavelength for imaging the development of dental caries lesions. By developing and employing non-ionizing optical imaging technologies for the diagnosis of lesion depth and severity, we can avoid unnecessary surgical intervention (placement of restorations) and allow harmless routine monitoring of dental caries without radiation exposure. Additionally, these technologies are ideal for the production of portable hand-held instruments that can be used to detect decay without x-rays and can increase dental outreach globally.

Table of Contents

CHAPTER I: Introduction.....	1
CHAPTER II: Multispectral near-infrared reflectance imaging of simulated early occlusal lesions: Variation of lesion contrast with lesion depth and severity	15
CHAPTER III: Near-infrared Imaging of Demineralization on the Occlusal Surfaces of Teeth Without the Interference of Stains.....	51
Chapter IV: Multispectral near-infrared reflectance and transillumination imaging of occlusal carious lesions: Variations in lesion contrast with lesion depth	79
Chapter V: A System for Simultaneous Near-Infrared Reflectance and Transillumination Imaging of Occlusal Carious Lesions.....	94
Chapter VI: Assessment of Cavitation in Artificial Approximal Dental Lesions with Near-IR Imaging.....	106
Chapter VII: Near-Infrared Imaging of Demineralization Under Sealants.....	121

Chapter VIII: Near-infrared Imaging of Secondary Caries Lesions around Composite Restorations at Wavelengths from 1300-1700-nm.....	145
Chapter IX: Near-IR Transillumination and Reflectance Imaging at 1300-nm and 1500-1700-nm for <i>In Vivo</i> Caries Detection.....	169
Chapter X: Near-IR and CP-OCT Imaging of Suspected Occlusal Caries Lesions.....	194
Chapter XI: Conclusions.....	219
References.....	226

List of Figures

CHAPTER I: Introduction

Figure 1.4.1	11
Figure 1.4.2	12
Figure 1.4.3	13
Figure 1.4.4	14

CHAPTER II: Multispectral near-infrared reflectance imaging of simulated early occlusal lesions: Variation of lesion contrast with lesion depth and severity

Figure 2.6.1	41
Figure 2.6.2	42
Figure 2.6.3	43
Figure 2.6.4	44
Figure 2.6.5	45
Figure 2.6.6	46
Figure 2.6.7	47
Figure 2.6.8	48
Figure 2.6.9	49
Figure 2.6.10	50

CHAPTER III: Near-infrared Imaging of Demineralization on the Occlusal Surfaces of Teeth without the Interference of Stains

Figure 3.6.1	71
Figure 3.6.2	72
Figure 3.6.3	73
Figure 3.6.4	74
Figure 3.6.5	75
Figure 3.6.6	76
Figure 3.6.7	77
Figure 3.6.8	78

CHAPTER IV: Multispectral Near-Infrared Reflectance and Transillumination Imaging of Occlusal Carious Lesions: Variations in Lesion Contrast with Lesion Depth

Figure 4.5.1	91
Figure 4.5.2	92
Figure 4.5.3	93

CHAPTER V: A System for Simultaneous Near-Infrared Reflectance and Transillumination Imaging of Occlusal Carious Lesions

Figure 5.5.1	102
--------------------	-----

Figure 5.5.2	103
Figure 5.5.3	104
Figure 5.5.4	105

Chapter VI: Assessment of Cavitation in Artificial Approximal Dental Lesions

with Near-IR Imaging

Figure 6.5.1	118
Figure 6.5.2	119
Figure 6.5.3	120

Chapter VII: Near-Infrared Imaging of Demineralization Under Sealants

Figure 7.6.1	137
Figure 7.6.2	138
Figure 7.6.3	139
Figure 7.6.4	140
Figure 7.6.5	141
Figure 7.6.6	142
Figure 7.6.7	143
Figure 7.6.8	144

Chapter VIII: Near-Infrared of Secondary Caries Lesions around Composite Restorations at Wavelengths from 1300-1700-nm

Figure 8.7.1	167
--------------------	-----

Figure 8.7.2	168
--------------------	-----

Chapter IX: Near-IR Transillumination and Reflectance Imaging at 1300-nm

And 1500-1700-nm for In Vivo Caries Detection

Figure 9.6.1	191
Figure 9.6.2	192
Figure 9.6.3	193

Chapter X: Near-IR and CP-OCT Imaging of Suspected

Occlusal Caries Lesions

Figure 10.6.1	215
Figure 10.6.2	216
Figure 10.6.3	217
Figure 10.6.4	218

List of Tables

CHAPTER II: Multispectral near-infrared reflectance imaging of simulated early occlusal lesions: Variation of lesion contrast with lesion depth and severity

Table 2.6.1	38
Table 2.6.2	39
Table 2.6.3	40

CHAPTER IV: Multispectral Near-Infrared Reflectance and Transillumination Imaging of Occlusal Carious Lesions: Variations in Lesion Contrast with Lesion Depth

Table 4.5.1	90
-------------------	----

CHAPTER VI: Assessment of Cavitation in Artificial Approximal Dental Lesions with Near-IR Imaging

Table 6.5.1	117
-------------------	-----

CHAPTER VII: Assessment of Cavitation in Artificial Approximal Dental Lesions with Near-IR Imaging

Table 8.7.1	166
-------------------	-----

**CHAPTER IX: Near-IR Transillumination and Reflectance Imaging at 1300-nm
and 1500-1700-nm for *In Vivo* Caries Detection**

Table 9.6.1	189
Table 9.6.2	190

**Chapter X: Near-IR and CP-OCT Imaging of Suspected
Occlusal Caries Lesions**

Table 10.6.1	214
--------------------	-----

CHAPTER I

Introduction: Methods for Assessing Lesion Depth and Severity with Near-IR Light

1.1 Dissertation Overview

Dental caries (tooth decay) is one of the most prevalent chronic diseases worldwide and is the leading cause of tooth loss in the United States [1-3]. Tooth decay is the demineralization (loss of mineral) of enamel and dentin resulting from chemical reactions between the hard tissue and acids produced by oral bacteria in biofilms [4, 5]. A caries lesion is the effect the disease has on the tooth, which develops over a time period ranging weeks to years, and results in the formation of cavities, quite literally holes in teeth [8-10]. Early detection of primary and secondary dental decay, accompanied by appropriate nonsurgical treatment of the disease process, is the ideal method for practicing preventative dentistry. Clinicians' lack the instrumentation to detect dental decay in its earliest stages with either radiographic imaging or visual tactile examination when the lesion process is reversible. This dissertation investigates the use of near-IR (NIR) light from 1300-1700-nm in wavelength for imaging the development of dental caries lesions. By developing and employing non-ionizing optical imaging technologies for the diagnosis of lesion depth and severity, we can avoid unnecessary surgical intervention (placement of restorations) and allow harmless routine monitoring of dental caries without radiation exposure. Additionally, these technologies are ideal for the production of portable hand-held instruments that can be used to detect decay without x-rays and can increase dental outreach globally.

1.2 Significance

The nature of dental caries has changed markedly over the past century in the United States due to the incorporation of fluoride to the public drinking water and use of fluoride

dentifrices, rinses and topical varnishes at home and in dental offices [11-14]. The nature of the caries problem has changed dramatically with the majority of newly discovered carious lesions being highly localized to the occlusal pits and fissures of the posterior dentition and the proximal contact sites between teeth where they are more difficult to detect. New diagnostic tools are needed for the detection and characterization of carious lesions in their early stages and throughout development [15-18]. The carious process is potentially preventable and curable [19, 20]. If carious lesions are detected early enough, it is likely that they can be arrested or reversed through changes in oral hygiene, fluoride therapy, anti-bacterial therapy, dietary changes, or by lower intensity laser irradiation [15, 21]. Therefore, one cannot overstate the importance of detecting dental decay in the early stages of development at which point non-invasive preventive measures can be taken to halt further decay. Of equal importance is determining the depth and severity of dental decay in order to accurately track lesion progression and determine whether the decay is active and expanding over time, or whether the decay had been arrested and determine if intervention is needed.

We do not understand the risk of low-level exposure to ionizing radiation used from dental radiographs [22-24]. Even greatly reduced levels of radiation exposure may still pose a significant health risk, especially for children and pregnant women, and NIR imaging technology is a safe method with the potential to replace radiographs for the routine screening of caries [25]. Without weighing the health risk of ionizing radiation, the major diagnostic limitation of radiographs is that they are unable to detect early occlusal carious lesions because of the overlapping features of the crowns. It is unlikely that improvements

in radiographic sensitivity will enable detection of early enamel lesions because of this problem.

Clinical studies performed by our group suggest that NIR imaging has the potential for replacing digital radiographs from screening for carious lesions on the proximal and occlusal surfaces where almost all lesions are found [26-28]. Accurately assessing early decay and measuring its depth and severity in order to quantitatively track caries progression or determine if intervention is necessary remains a challenge in modern dentistry. Based on reports from the National Health and Nutrition Survey (NHANES) [29, 30] and recent epidemiological studies utilizing the NIH funded Dental Practice-Based Research Network (DPBRN) [31, 32], approximately one third of all patients have at least one questionable occlusal lesion (QOC) location on a posterior tooth. QOC's are diagnosed based on surface roughness, surface opacities or staining but lack cavitation or radiolucencies, and when QOC's were monitored in patients over a 20-month time period, DPBRN clinicians determined that 90% did not require restorative intervention [33, 34]. The overall accuracy for determining whether a lesion has penetrated the underlying dentin is reported to be very poor with only just a ~50% success rate [35, 36]. NIR imaging holds great potential to overcome this challenge and become a universal caries screening method used in the dental clinic because this method can be employed routinely to image teeth on all tooth surfaces and is highly sensitive to very early changes in the optical properties of enamel that occur upon demineralization.

Currently, despite the ability to image directly through enamel without inference from stains [37, 38], individual NIR imaging modalities cannot be used to reliably estimate deeper

dental decay and determine if the decay has reached the underlying dentin because the outer regions of the lesion block further measurement [39, 40]. The goal of this project is to develop methods to improve the accuracy of depth and severity assessment of occlusal and interproximal decay based on NIR reflectance and transillumination images, by determining the best imaging wavelengths and wavelength combinations for each imaging geometry at various stages in lesion development.

1.3 Dissertation Aims

The overall objective of this dissertation is to advance the capability of near-IR (NIR) imaging to assess the depth and severity of carious lesions (dental decay). Clinicians need new diagnostic tools that can be used routinely to detect carious lesions early and throughout their development. If carious lesions are detected early enough, then they can be arrested/remineralized by non-surgical means with fluoride therapy, anti-bacterial therapy, or by low intensity laser irradiation. Tracking caries progression over an extended period of time can measure whether the lesion is active and expanding, or whether the lesion has been arrested, and determine if intervention is needed. Light scattering in sound enamel and dentin is the principal factor limiting optical transmission through the tooth in the visible range from 400-700-nm. Light scattering in enamel decreases as the wavelength increases ($1/\lambda^3$), where λ represents the wavelength, due to the size of the principal light scatters [41, 42]. The central hypothesis motivating this proposal is that the near-infrared region from 1300- 1700-nm holds the greatest potential for new optical imaging technologies due to markedly increased optical transmission and multispectral

differences in water absorption. Upon demineralization, light scattering increases by orders of magnitude which provides high contrast of carious lesions [40].

AIM 1: To test the hypothesis that multispectral NIR reflectance and transillumination measurements of occlusal carious lesions can be combined for improved assessment of lesion depth and severity. Clinicians need new optical devices to improve the diagnosis of questionable occlusal carious lesions and determine if decay has penetrated to the underlying dentin. Assessing lesion depth from NIR images holds great potential due to the high transparency of enamel and stain to NIR light at $\lambda=1300-1700\text{-nm}$, which allows direct visualization and quantified measurements of enamel demineralization. Unfortunately, NIR reflectance measurements alone are limited in utility for approximating occlusal lesion depth beyond $>200\text{-}\mu\text{m}$ due to light attenuation from the lesion body [43]. Previous experiments comparing reflectance and transillumination techniques at $\lambda=1300\text{-nm}$ found that the lesion contrast and area significantly increased with lesion depth for transillumination but not reflectance measurements [7, 44]. However, the lesion contrast at other NIR wavelengths coincident with higher water absorption were shown to increase more rapidly with increasing depth [45]. I propose multispectral NIR reflectance and transillumination experiments to measure the change in occlusal lesion contrast and area with lesion depth based on histological measurements from transverse microradiography (TMR) and polarized light microscopy (PLM). Using this data, I will determine the best wavelengths for combining multispectral-multimodal NIR measurements and develop image processing algorithms for assessing lesion depth. A combined NIR reflectance and transillumination clinical imaging probe will be designed, fabricated and tested ex vivo.

Previous studies published by our group aimed to combine NIR reflectance and transillumination measurements at $\lambda=1300\text{-nm}$ in order to estimate the depth of occlusal lesions [7]. Data from these studies demonstrated that the ratio between transillumination and reflectance lesion contrast measurements (Fig. 1), as well as the total lesion area (Fig. 2), positively correlated with different lesion depths even though neither method differentiated between enamel (E) and early dentin (D1) lesions with statistical significance. These experiments also revealed that the lesion contrast measured in reflectance at $\lambda=1300\text{-nm}$ did not change significantly with lesion depth (Fig. 2) and was low ranging from 0.17-0.21 percent, and therefore the contrast ratio was no better than the transillumination measurement alone. In a recent study, I performed multispectral NIR reflectance measurements on early artificial occlusal lesions with variable depth ranging from 50-200- μm , and again imaging at $\lambda=1300\text{-nm}$ demonstrated a static ~ 0.21 percent contrast for all lesion depths [45]. These multispectral experiments revealed that even though lesion contrast for reflectance seems nearly constant at $\lambda=1300\text{-nm}$, the lesion contrast increases with increasing lesion depth for other NIR wavelengths. These early occlusal lesions manifested the greatest change in lesion contrast with lesion depth at $\lambda=1460\text{-nm}$, where water absorption is at a maximum in the NIR, and the degree of dependence appears to follow the absorption curve of water throughout the NIR (Fig. 3). Therefore, a more robust experimental approach that quantitatively models multispectral NIR lesion contrast's variance with lesion depth and determines the optimal imaging wavelengths for estimating lesion depth is needed. I hypothesize that combining multispectral NIR reflectance measurements coincident with increased and varying water absorption ($\lambda=1450\text{-}1700\text{-nm}$), with NIR

transillumination measurements captured at wavelengths with minimum absorption ($\lambda=1300\text{-nm}$), will provide increased correlation of the lesion contrast and lesion area with lesion depth.

AIM 2: To test the hypothesis that multispectral NIR reflectance measurements can be used to detect interproximal carious lesions imaged from the occlusal surface. There are marked differences in lesion appearance among multispectral NIR reflectance images that arise from wavelength dependent variations in the absorption coefficient of water from 1300-1700-nm, as well as different endogenous water contents among dental tissues. We previously determined that NIR reflectance images captured at wavelengths coincident with strong water absorption produced maximum lesion contrast for early surface decay. Surprisingly, *in vivo* clinical data from a recent NIR reflectance imaging study using more strongly absorbing $\lambda=1500\text{-}1700\text{-nm}$ light, demonstrated that interproximal lesions located at the contact points can be visualized from the occlusal surface through several millimeters of sound enamel with high contrast [46]. I propose multispectral NIR reflectance and optical coherence tomography (OCT) measurements to determine the optimal NIR wavelengths for detecting interproximal lesions beneath the maximum thickness of sound enamel when imaged from the occlusal surface. NIR measurements will be compared with histological measurements from TMR and PLM. I also seek to determine if multispectral NIR reflectance and OCT measurements can assess the severity of interproximal decay by indicating if the lesion is cavitated.

Detecting interproximal carious lesions by viewing them in NIR reflectance from the occlusal surface is a straightforward approach that capitalizes on a marked reduction in

NIR light scattering with increasing wavelength ($1/\lambda^3$), allowing NIR light to penetrate deep through a layer of sound enamel and detect underlying decay. Previous studies have focused on the use of optical coherence tomography (OCT) at $\lambda=1300\text{-nm}$, where the total attenuation coefficient of enamel is a minimum, $\sim\mu_t= 3.1\pm 0.17\text{-cm}^{-1}$, compared to $\sim\mu_t= 3.8\pm 0.17\text{-cm}^{-1}$ at $\lambda=1500\text{-}1700\text{-nm}$ [42]. The maximum imaging depths for OCT and NIR reflectance are fundamentally limited by light attenuation resulting from the combination of light scattering and absorption, and it is logical that greater imaging depths would be realized by imaging at $\lambda=1300\text{-nm}$ [47]. To our surprise, we discovered from *in vivo* clinical data (Fig. 4) collected during a recent NIH funded NIR imaging study, that interproximal lesions can be visualized directly from the occlusal surface through a layer of sound enamel at $\lambda=1500\text{-}1700\text{-nm}$ [46].

Figure 4B is an *in vivo* NIR reflectance image from that study captured at $\lambda=1500\text{-}1700\text{-nm}$, in which interproximal decay is clearly observed as the area of bright (white) signal indicated by the yellow arrow. Histology from this sample (Fig. 4D) shows the lesion is located well below the occlusal surface. Based on this insight, a detailed analysis of multispectral NIR reflectance and OCT measurements of interproximal lesions is required in order to determine the optimal wavelengths for detecting interproximal carious lesions deep beneath a layer of sound enamel with maximum contrast. Previous OCT studies suggest that choosing the optimal wavelengths in order to realize the maximum imaging depth is more complex than simply a function of total attenuation, and that the balance between light absorption and scattering contributions can allow wavelengths with greater total attenuation to image deeper into

tissue [48, 49]. Imaging at wavelengths where light absorption is increased relative to light scattering can result in higher contrast and spatially resolved images due to a reduction in the fraction of multiply scattered photons detected by the instrument. The fraction of multiply scattered photons detected increases with increasing imaging depths and introduces background noise into the OCT and reflectance images. We need to understand how this complex, wavelength dependent, balance between light scattering and absorption determines the maximum image depths and image contrast in dental enamel.

The ability to determine if interproximal carious lesions have become cavitated is also of importance and needs investigation. Because there is currently no experimental data regarding imaging of this type of decay using a reflectance imaging geometry, we aim to determine if there are multispectral differences in NIR reflectance images between cavitated and noncavitated lesions affecting interproximal tooth surfaces.

1.4 Figures

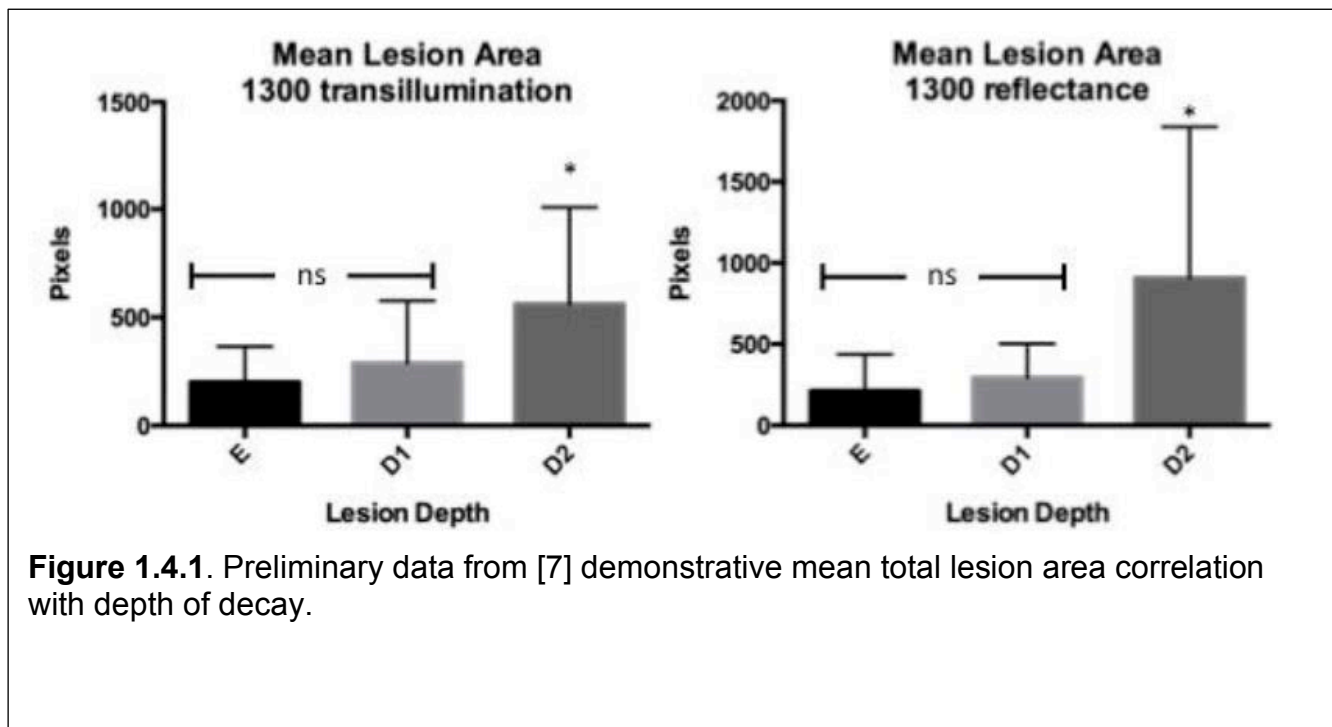
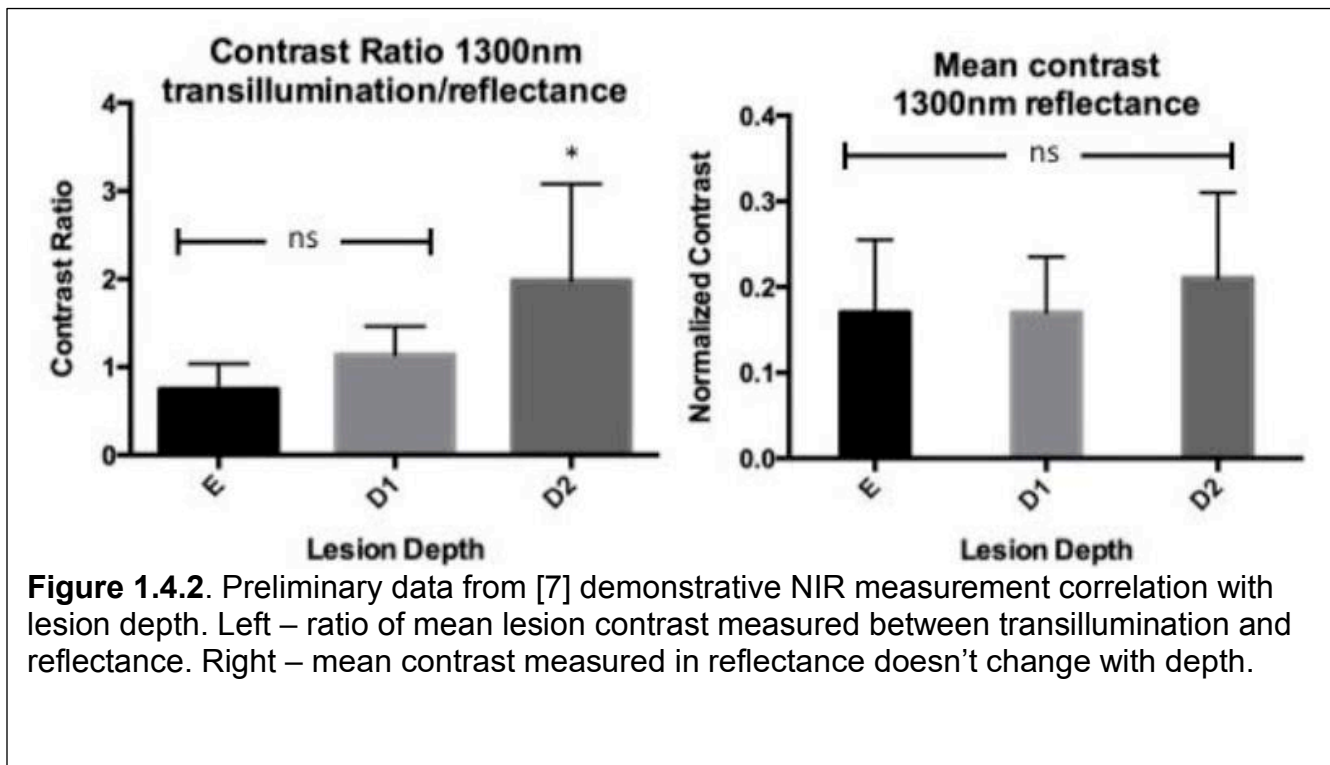
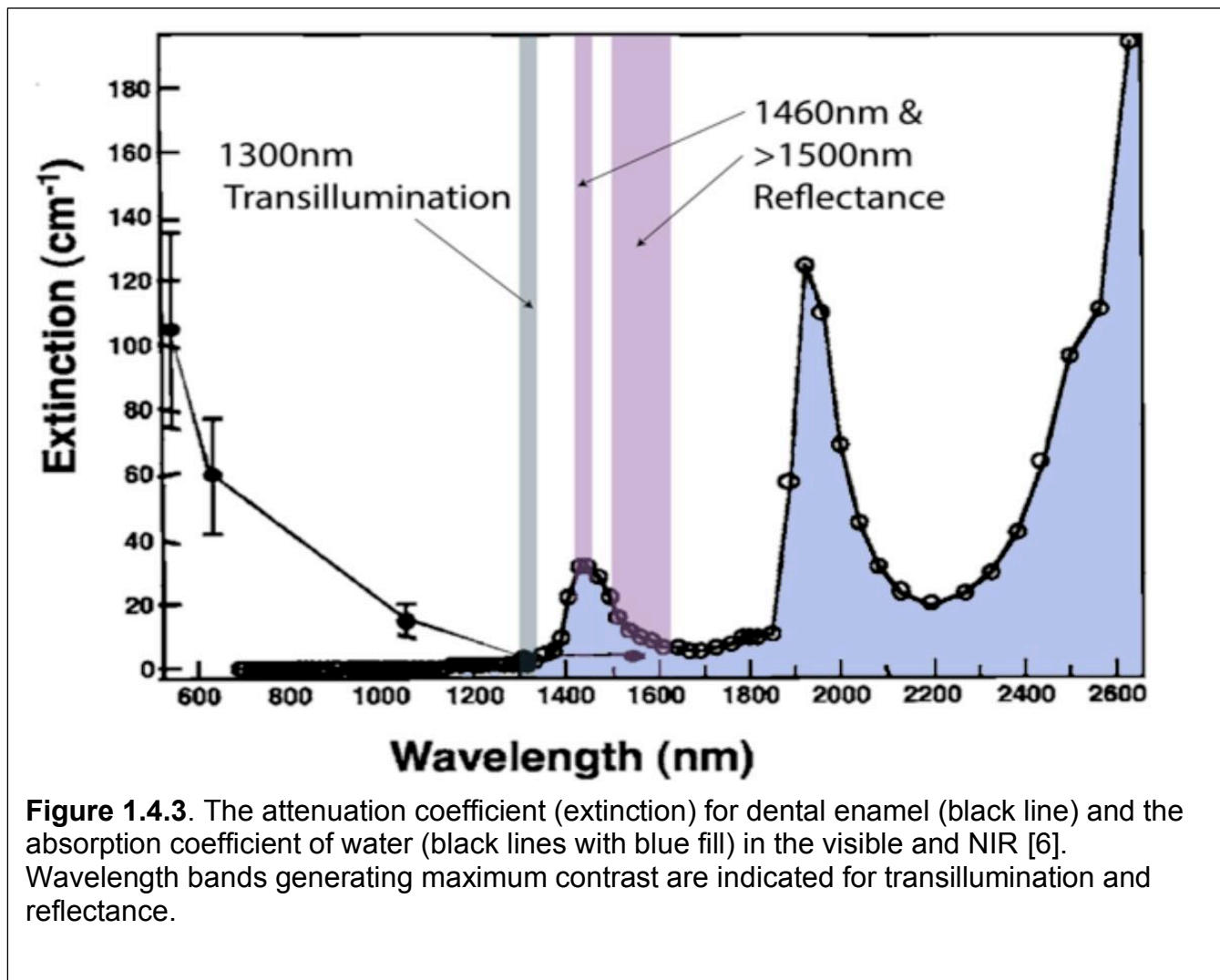


Figure 1.4.1. Preliminary data from [7] demonstrative mean total lesion area correlation with depth of decay.





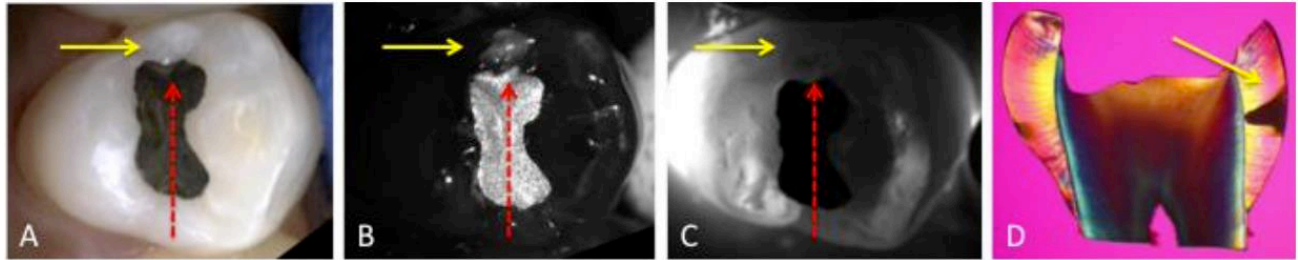


Figure 1.4.4. *In vivo* visible and NIR images of interproximal decay viewed from the occlusal surface. (A) Visible light image. (B) NIR reflectance image at $\lambda=1500\text{-}1700\text{-nm}$. (C) NIR transillumination image at $\lambda=1300\text{-nm}$. (D) Polarized light histology image. Yellow arrow indicates lesion location. Red dashed line indicates PLM section.

CHAPTER II

Multispectral near-infrared reflectance imaging of simulated early occlusal lesions:

Variation of lesion contrast with lesion depth and severity

2.1 Summary

Early demineralization appears with high contrast at near-IR wavelengths due to a ten to twenty-fold difference in the magnitude of light scattering between sound and demineralized enamel. Water absorption in the near-IR has a significant effect on the lesion contrast and the highest contrast has been measured in the spectral regions with higher water absorption. The purpose of this study was to determine how the lesion contrast changes with lesion severity and depth for different spectral regions in the near-IR and compare that range of contrast with visible reflectance and fluorescence.

Artificial lesions appear more uniform on tooth surfaces exposed to an acid challenge at visible wavelengths than they do in the near-IR. Measurements of the lesion depth and severity using CP-OCT shows that the lesion severity varies markedly across the sample windows and that lesion contrast in the visible does not accurately reflect the large variation in the lesion severity. Reflectance measurements at certain near-IR wavelengths more accurately reflect variation in the depth and severity of lesions.

The results of the study suggest that near-IR reflectance measurements at longer wavelengths coincident with higher water absorption are better suited for imaging early caries lesions.

2.2. Introduction

Light scattering in sound dental enamel varies markedly from the UV to the near-IR and exhibits the highest transparency near $\lambda=1310\text{-nm}$ [41, 42]. At this wavelength, the attenuation coefficient is only 2 to 3 cm^{-1} , which is a factor of 20 to 30 times lower than in the visible region [42]. At longer wavelengths, water absorption increases significantly

and reduces the penetration of the near-IR light. Even though the light scattering for sound enamel is at a minimum in the near-IR, the light scattering coefficient of enamel increases by 2-3 orders of magnitude upon demineralization due to the formation of pores. The pores are of similar size scale to the wavelength of the light and act as Mie scatters [43].

Several studies have demonstrated that caries lesions can be imaged with high contrast in the near-IR [44, 50-52]. Recent studies on both natural occlusal lesions [40] and artificial lesions on occlusal surfaces [52] indicate that the contrast is highest for those wavelengths coincident with high water absorption, such as $\lambda=1450\text{-nm}$. Since dentin has a higher water content than enamel it is likely that water absorption in the underlying dentin reduces the intensity of light reflected from sound areas and this increases the contrast of lesion areas. Early enamel with white spot lesions can be discriminated from sound enamel by visual observation or by visible-light diffuse reflectance imaging [53, 54]. Recent studies have shown that very high lesion contrast can be attained for very shallow lesions by using shorter wavelength blue light [55]. Blue light is scattered to a greater degree in sound enamel than longer wavelengths in the visible and near-IR [41, 56, 57]. Monte Carlo simulations in the same paper suggest that the optimal spectral region for the highest lesion contrast depends on the lesion depth and severity, and that shorter wavelengths are likely to yield higher contrast for shallow lesions while longer wavelengths should yield higher contrast for deeper lesions. [55]

In a recent study comparing the contrast of artificial lesions on tooth occlusal surfaces [52] at several wavelengths, we observed that the uniformity of the lesion contrast varied

markedly with the wavelength. In the visible wavelengths, the lesions appeared highly uniform, while in the near-IR the lesion contrast varied considerably. Images taken of those samples with optical coherence tomography and histological examination using polarized microscopy showed that the lesions were highly variable and were not uniform in either depth or severity. This was more consistent with the large variation in the lesion contrast observed at near-IR wavelengths. More extensive studies over a greater range of lesion severity are required to determine the optimum performance ranges for each of the imaging methods. A greater sensitivity of lesion contrast to variation in the lesion severity should make it easier to monitor changes in the lesion severity over time.

In order to reliably produce lesions on the occlusal surfaces, those surfaces have to be cleaned, and all stains need to be removed. The removal of the outside layer of fluoride rich enamel is often necessary to facilitate lesion development. The surface roughness may modify the specular and diffuse scattering from the surface, and this surface scattering can profoundly influence both the reflectivity and fluorescence. There is some concern that the method of sample preparation may increase the surface roughness and the surface scattering. Therefore, two methods of surface preparation were investigated: air abrasion and mechanical polishing (prophy). The surface wetness also profoundly influences the lesion contrast. Clinicians routinely blow air to dry the tooth surface when inspecting tooth surface lesions. Since water absorption varies markedly in the near-IR, surface water is likely to have even greater influence on the lesion contrast than in the visible wavelengths. For that reason, tooth surfaces were imaged both wet and dry.

Optical coherence tomography (OCT) is a well-established imaging method that can be used to acquire depth resolved images of demineralization in teeth. Different approaches have been proposed over the past decade to quantify the severity of demineralization from conventional and cross-polarized OCT images [58-60]. Strong specular reflection from the tooth surface is greatly reduced in the cross-polarization OCT image allowing direct integration of the reflectivity from the lesion areas near the tooth surface [59, 61-64]. This also greatly facilitated automated analysis, which is required to handle the great wealth of data contained in OCT images [65, 66]. Three dimensional tomographic OCT scans can be converted into two dimensional images of the calculated lesion depth and the reflectivity integrated of the calculated lesion depth (ΔR , dB \times μm) that are well suited for representing the severity of demineralization [52, 67]. The unit ΔR is analogous to the unit ΔZ , the integrated mineral loss with depth, which is measured with microradiography and is considered the gold standard for lesion severity. Previous studies have shown that ΔR correlates with ΔZ [61]. Therefore, lesion severity in the context of this paper will be defined as the integrated reflectivity over the depth of the lesion, ΔR . This approach is quite valuable for monitoring lesion severity both *in vivo* and *in vitro* and for comparing the inhibition of demineralization by various anti-caries agents. Two-dimensional projections of the OCT images in the calculated depth and ΔR formats are also advantageous for comparison with other 2D optical imaging methods such as reflectance imaging and fluorescence imaging. The intensity in these images represents either the reflectivity integrated over the depth or the loss of intensity over depth. One goal of this study is to directly compare these OCT image formats pixel by pixel with reflectance and

fluorescence images to determine how the image contrast changes with both lesion severity and lesion depth in the different spectral bands

The purpose of this study was to determine how the lesion contrast changes with lesion severity and depth for different spectral regions in the near-IR and compare that range of contrast with visible reflectance and fluorescence. This was achieved by comparing the acquired fluorescence and reflectance images with two-dimensional images of the lesion depth and integrated reflectivity measured using cross-polarization optical coherence tomography.

2.3. Materials and Methods

2.3.1 Artificial Lesion Sample Preparation

Forty-four extracted posterior teeth were collected from patients in the San Francisco Bay area with approval from the UCSF Committee on Human Research. The teeth were sterilized using gamma radiation and stored in 0.1% thymol solution to maintain tissue hydration and prevent bacterial growth. Samples were initially separated into four groups based on the surface preparation technique and the duration of exposure to demineralization solution. The occlusal surface of each tooth in groups 1, 3 & 4 were prepared by an air abrasion technique employing a constant flow of 25-50- μm AL_3O_2 glass beads for twenty seconds to remove debris and surface staining from the pits and fissures. The occlusal surfaces of teeth in group 2 were prepared using the conventional prophylaxis method, consisting of a two-stroke application using a slow speed hand piece at maximum speed (Butler Eez-Touch prophylaxis angle and Whip Mix Preppies non-fluorinated

pumice), followed by a 15-minute treatment in an ultrasonic cleaner (Branson 3510) to remove any residual pumice. All samples were mounted in black orthodontic acrylic blocks (Great Lakes Orthodontics, Tonawanda, NY).

A 4×4-mm window, or box, was etched on the occlusal surface of each tooth using a CO₂ laser (Impact 2500, GSI Iumonics Rugby, UK). The laser was operated at a wavelength of 9.3- μm , pulse duration of 15- μs , and a pulse repetition rate of 5-Hz. During the ablation procedure, the incident fluence was 170-J/cm² with a spot size of 150- μm , and a water spray was used to regulate the enamel temperature. The 4×4-mm window demarcates the area exposed to demineralization and the 50–100- μm deep etch marks serve as fiducial marks for serial sectioning and polarized light microscopy. The increased resistance to acid dissolution of the laser irradiated perimeter of the window is effective in isolating the sound and demineralized regions and is sufficiently narrow to not interfere with image contrast calculations.

Tooth surfaces outside the window were protected from demineralization solution by application of red acid-resistant varnish (Revlon, New York, NY). Two coats of varnish were applied, and then removed after artificial lesion generation using acetone.

Artificial lesions were produced with the surface softened dissolution model used in prior studies [50, 52]. Samples in groups 1, 2, 3, and 4 were submerged in individual vials containing a 50 ml aliquot of Ca/PO₄/acetate; 2.0-mmol/L Calcium, 2.0-mmol/L phosphate, and 0.075 mol/L acetate: maintained at a pH 4.5 and incubated at a temperature of 37°C for 12 (2 groups), 24 & 48 hours respectively. This procedure sought to produce groups 1 (n=12), 3 (n=10) and 4 (n=10) with increasing lesion severity and

group 2 (n=12) with similar severity to group 1 (dependent of the effective difference between the air abrasion and prophylaxis preparation methods).

Even after extensive surface preparation to remove variability in lesion generation, there was great variability in the lesion severity from group to group. Therefore, we decided it was advantageous to separate the samples based on their actual depth and severity measured nondestructively with CP-OCT. Groups 1, 2, 3, and 4 are ranked by increasing lesion severity in terms of both mean depth and mean integrated reflectivity. The mean values for each adjusted group with the calculated standard deviation are shown in the chart in Fig. 2.1 and Table 2.1.

2.3.2 Polarized Near-Infrared Reflectance Measurements

Strong specular reflectance from tooth surfaces poses a challenge in reflectance imaging due to the high refractive index of enamel. However, the visibility of scattering structures on highly reflective surfaces such as teeth can be enhanced by use of crossed polarizers to remove the glare from the surface [68, 69]. For the acquisition of near-IR reflectance images, a tungsten halogen light source with various band pass (BP) and long pass (LP) filters was used with a high sensitivity InGaAs SWIR camera (SU320KTSX-1.7RT/RS170) from Sensors Unlimited (Princeton, NJ) containing a focal plane array format of 320×256 pixels and a 25- μm pixel pitch. Incident light was polarized using a linear polarizer and a second linear polarizer was placed on the camera oriented orthogonal to the first. Optical long pass and band pass filters were employed to segregate the near-IR spectrum into wavelength regions of interest, often exploiting the absorption of water, in search for the wavelength range yielding the greatest contrast for surface lesions. Long pass filters with

short wavelength cut off's located at 1100, 1200, 1300, 1400 and 1500-nm, in addition to band pass filters centered at 1300, 1377, 1460 and 1550-nm (Spectrogon, FWHM= 80-nm), were attached to the camera lens. Images were processed with a background, dark reference, then normalized over the spatial distribution of a white reference.

2.3.3 Polarized Visible Reflectance Measurements

The contrast between sound and demineralized enamel can be further enhanced by depolarization of the scattered light in the area of demineralized enamel [70, 71]. Visible Reflectance images were acquired using an Ocean Optics fiber-coupled tungsten-halogen lamp (Model HL-2000-FHSA) with a DFK 31AF03 FireWire camera outfitted with a MiniInfinite lens. The light source was equipped with a linear polarizer, and the camera was equipped with a second linear polarizer oriented orthogonal relative to the initial polarizer (crossed polarizers) in order to remove specular reflection from the tooth surface.

2.3.4 Laser Induced Fluorescence (QLF) Measurements

Fluorescence or quantitative light fluorescence (QLF) images were captured for direct comparison with polarized near-IR and polarized visible-light reflectance methods. A "Blu-Ray", 405-nm wavelength, GaN diode laser operating at 150 mW (Photonics Products, UK) was used as an excitation source. The 405-nm wavelength is consistent with the best-reported diagnostic performance in clinical QLF systems [72]. A 500-nm long-pass filter (#C47-616, Edmund Scientific, Barrington, NJ) was used to filter the emitted fluorescence, and images were acquired with a DFK 31AF03 FireWire camera (Imaging

Source, Charlotte, NC) with 1024 × 768 pixels outfitted with a MiniInfinimite lens (Infinity Photo-optical, Boulder, CO) (Figure 2.1). Data was collected in a 'dark room' to avoid ambient room light from entering the camera lens using IC Capture 2.2 software (Imaging Source). Conventional QLF measurements are reported as a contrast ratio of the fluorescence radiance intensity of the apparent lesion area compared to any equivalent sound enamel area.

2.3.5 Image Analysis

A somewhat novel approach was employed to calculate the lesion contrast from the images. The intensity of a 3×3-mm square region centered in the 4×4-mm lesion area was compared with most of the sound area remaining on the occlusal surface outside the box as shown in Fig. 1. This approach seeks to minimize the effects of tooth topography. Images were analyzed using the image analysis package, IgorPro (Wavemetrics, Lake Oswego, OR). Near-IR and visible-light reflectance contrast ratios were produced using the equation $(I_L - I_S)/I_L$, because the increased scattering from demineralized tissue produces a greater intensity signal. QLF reflectance contrast measurements have the opposite contrast and were produced using the equation $(I_S - I_L)/I_S$, because the decreased fluorescence emission from demineralized tissue produces a weaker intensity signal. For each sample, lesion intensity measurements were collected as the mean intensity of a 3×3-mm square region centered within the laser demarcated area. Sound tissue intensities were measured using a polygon method. The polygon method employs a freehand Region of Interest (ROI) tool in order to draw a polygon figure around the entire occlusal surface but excluding the lesion area. Figure 1 illustrates the region

selection for both sound and lesion area on a 48-hour sample. Mean intensities for each region were acquired using the ROI function of Igor Pro. The reported contrast values can range from 0 to 1 where a 0 value represents no contrast, a 1 value represents maximum contrast, and negative values represents inverse contrast. The reported lesion contrast ranges from 0 to 1.0 when the lesion intensity is greater than the measured sound intensity. A negative contrast can occur when the measured sound intensity exceeds the lesion intensity and the reported values do not have a confined range. Contrast values were compared using repeated measures one-way analysis of variance (ANOVA) followed by Tukey-Kramer post-hoc multiple comparison tests using InStat statistical software (GraphPad, San Diego, CA).

2.3.6 Tooth Surface Wetness

The amount of water that adheres to the surface of a tooth during imaging can have a profound effect on the lesion contrast observed. Some of the wavelength regions imaged deliberately overlap distinct near-IR water absorption bands. All samples were imaged in both a dry state, where samples were sprayed with air for a 5-second duration before imaging, and a wet state where they were imaged immediately after removal from the water/ thymol storage solution without air drying.

2.3.7 Polarization Sensitive Optical Coherence Tomography (PS-OCT)

Several studies have demonstrated that the reflectivity in the cross polarization (CP) image integrated over the lesion area, ΔR (dB(decibels) $\times \mu\text{m}$), correlates with ΔZ , the integrated mineral loss (Vol.% mineral $\times \mu\text{m}$) determined using transverse microradiography[59, 61-63]. An all-fiber optical coherence domain reflectometry (OCDR) system from Optiphase (Van Nuys, CA) employing high-speed piezoelectric fiber-stretchers, polarization maintaining (PM) optical fibers, and two balanced InGaAs receivers was used for *in vitro* data collection. This two-channel (\perp & \parallel) system was integrated with a broadband superluminescent diode (SLD) (Denselight, Jessup, MD) operating at a center wavelength of 1317-nm and spectral bandwidth full-width half-maximum (FWHM) of 84-nm. A high-speed XY-scanning system (ESP 300 controller and 850G-HS stages, National Instruments, Austin, TX) was used to scan the sample area. The high power (15-mW) polarized SLD source was aligned using a polarization controller to deliver full power into the slow axis (\perp) of the source arm of the interferometer. The light in the PM fiber was split into the reference and sample arms of the interferometer by a 50/50 PM-fiber coupler. The sample arm was coupled into an AR-coated fiber-collimator to produce a 6-mm diameter collimated beam and focused onto the sample surface using a 20-mm focal length AR-coated planoconvex lens. Configuring the PS-OCT system in this manner produced data sets with a lateral resolution of approximately 20- μm and axial resolution of 10- μm in air with a signal to noise ratio greater than 40–50-dB. The resolution in enamel is even greater because of the higher refractive index ($n=1.63$). The instrument was controlled by a program written with LabVIEW software (National Instruments,

Austin, TX). Individual A-scans were compiled into B-scan cross sectional slices that are aggregated into 3D files.

2.3.8 Automated PS-OCT Image Analysis for Lesion Depth and Integrated Reflectivity

Optical Coherence Tomographic scans were assessed to evaluate lesion quality on a basis of lesion depth and the integrated reflectivity over the lesion depth, using a program written with LabVIEW. The program derived two-dimensional projections of the lesion depth and integrated reflectivity on a per-point basis for use in the assessment of lesion contrast image accuracy and utility [67].

Raw OCT data was linearized and an outlying region of each b-scan was measured as the background noise value and operated to yield the mean background intensity and standard deviation [67]. Four times the background standard deviation plus the mean background intensity was used as a thresholding value to ensure with 99.994% certainty that the accepted signal exceeded the noise [65, 66]. A Gaussian blur was applied through a convolution matrix for the elimination of speckle noise, retention of signal peaks and choosing of integration boundaries. The data set was thresholded a second time, before any depth or integrated reflectivity calculations were performed, to discriminate peaks from sound tissue and that of demineralized enamel. It was empirically determined through analysis of sound samples that demineralized enamel can be identified as having a greater than or equal to 90% contrast for signal amplitude relative to background signal [65, 66]. Peaks for which this threshold is not met are considered to be sound.

For the determination of lesion depths and integration boundaries, an edge-detection approach was used which identified the enamel surface and the deep lesion boundary by application of an edge locator. The OCT data was rescaled to range from 0 to the maximum value by subtraction of the minimum noise level. The depth of the lesion is calculated by locating the upper and lower lesion boundaries of the lesion signal by identifying the first pixels that fail to meet the requirement of being greater than or equal to Ae^{-2} , where A is the peak maximum. The spatial dimensions per-pixel were obtained experimentally by system calibration and applied properly in order to convert pixel depths to micrometer depths. In a prior study, reported OCT lesion depths were verified by histological examination of sectioned samples and measurement using polarized light microscopy [67].

Integrated reflectivity calculations were achieved by standard integration of the signal peak, within the boundaries identified by the previous method. The values reported are in $\text{micron} \times \text{volts} / 3.2 \times 10^{-5}$.

The reported mean depth and mean integrated reflectivity values represent the mean values over the entire 3×3-mm windows.

2.3.9 Thematic Mapping and Accuracy Analysis

Assessing the accuracy of near-IR and visual reflectance images, on a point-by-point basis, was carried out using a LabView program based on thematic mapping solutions presented by Congalton and Green [73]. Near-IR and visible reflectance images were converted into contrast images scaling from 0 to 1.0 based on the sound intensity of each

sample and then transformed into depth and integrated reflectivity maps using linear regression. The manufactured images were then compared with a 2D OCT depth and integrated reflectivity projections as reference, by automatically matching and overlaying the same 3×3-mm regions evaluated in the mean contrast measurements. Pixel values from the near-IR maps were compared to the reference and categorized based on their accuracy as a true representation of the local depth or integrated reflectivity. True assessments classified values within 25% (based on the standard deviation of the regression fit) of the reference value, and greater or lesser values classified the lesion as: over or under-estimates, respectively. The point-by-point classification was used to produce an overall accuracy map indicating where the contrast values correctly or incorrectly represent the actual lesion severity.

2.4. Results

2.4.1 Influence of Surface Preparation on Lesion Contrast

There was some concern that the method chosen for mechanical removal of stain and the fluoride rich outer layer of the enamel in the sample window could significantly alter the surface roughness and the lesion contrast. Two groups (n=12) with sample surfaces treated by air abrasion and prophyl techniques were compared with 12-hr lesions both wet and dry. The calculated mean lesion depth and mean integrated reflectivity in the sample windows calculated from OCT along with the lesion contrast values measured using reflectance and fluorescence are tabulated in Table 2.1. A statistical comparison using a simple t-test between each method indicates that the values are all statistically similar,

and we can conclude that air abrasion does not significantly roughen the surface and alter the contrast.

2.4.2 Lesion Severity Classification based on OCT

Lesion generation is highly variable in the occlusal surfaces, even after extensive cleaning of those surfaces with air abrasion. Therefore, we decided to measure the lesion depth and integrated reflectivity using OCT for the 12 (2 groups), 24, and 48 hour sample sets after lesion generation and separate the samples into four groups based on increasing mean integrated reflectivity (lesion severity) from 1 to 4. The distribution of the adjusted groups is shown in Fig. 2.2 and Table 2.2. The mean integrated reflectivity was chosen to represent the lesion severity because it has been shown to correlate with ΔZ , the integrated mineral loss which is used as the standard measure of lesion severity [59, 61-63].

2.4.3 Contrast Measurements of Dry Sample Groups

Figure 2.3 contains multispectral images of one sample taken from group 4 (the most severe lesions), acquired using fluorescence, visible, and near-IR reflectance with various long-pass (LP) and band-pass (BP) filters. Teeth were removed from a water/thymol solution and were air-dried for 5 seconds. A major factor in the lesion contrast is the intensity of the sound tooth region surrounding the laser-demarcated area. The sound areas appear with the lowest intensity in spectral regions coincident with higher water absorption, namely H, K & L of Fig. 2.3.

The contrast values for the multispectral measurements are tabulated in Table 3 for each imaging method with both wet and dry surfaces. Contrast values are consistently higher for near-IR reflectance in the spectral regions coincident with higher water absorption, the LP1400, BP1460, and LP1500 groups. Reflectance with the LP1500 filter yields the highest contrast for less severe lesions, groups 1 & 2, and reflectance with the BP1460 filter yields the highest contrast for the more severe lesion groups, 3 & 4.

Near-IR reflectance with the LP1400, BP1460 and LP1500 filters produced the greatest range of lesion contrast values, and the contrast increased linearly with increasing lesion depth and severity. Figure 5 contains plots of the contrast values for BP1300, LP1500, BP1460 and visible reflectance along with QLF versus the mean depth measured with OCT. Best fit lines are also shown for each of the five groups. The respective slopes and correlation coefficients are tabulated in Table 4 for both wet and dry samples. The BP1460 filter was chosen for point-by-point lesion mapping analysis based on the large linear increase with lesion depth and severity.

2.4.4 Contrast Measurements of Wet Sample Groups

It is well known that the presence of saliva and water on the tooth surface can profoundly reduce the contrast of early demineralization. Clinicians routinely air dry suspected lesion areas to increase contrast. Understanding how the apparent lesion contrast evolves with varying degrees of surface wetness will likely be important for near-IR reflectance imaging.

Table 2.3 lists the reflection contrast measurements for groups 1–4 acquired with a wet occlusal surface. Samples were removed from a water/thymol solution and were not air-dried. There was a marked reduction in contrast compared to the dry measurements recorded on the same group for most of the methods. The greatest changes in lesion contrast occurred for near-IR reflectance with the LP1400, BP1460, and LP1500 filters coincident with water absorption bands. Lesion areas that manifested very high contrast values when observed while dry actually became darker than the surrounding sounds areas due to water filling the pores and absorbing the incident light, namely the contrast went from positive to negative. At wavelengths where water absorption was lower (visible and BP1300), the reduction in contrast was smaller. Although, it appears that there is a linear increase in contrast for the wet samples in the visible, the slope of the line is small and not significantly different from zero.

Figure 2.4 shows QLF and reflectance images (visible, BP1460 and BP1300 filters) for a 48-hour sample (group 4 lesion). The reduction in lesion contrast is most remarkable for QLF and near-IR reflectance with the BP1460 filter, the lesion almost completely vanishes when wetted.

Figure 2.6 contains the corresponding plots of the contrast values for BP1300, LP1500, BP1460 and visible reflectance along with QLF versus the mean depth measured with OCT for wet surfaces. The integrated reflectivity shows similar trends. Visible and QLF behave similarly when dry and wet with a reduction in the initial contrast of early lesions and a reduced slope with increasing lesion severity for wet samples. BP1460 exhibits a

positive slope when the tooth surface is wet, but it is not significantly different from zero. BP1300 exhibits similar behavior when both dry and wet.

2.4.5 Accuracy of BP1460 and Visible Images with PS-OCT

Point-by-point near-IR (BP1460) and visible reflectance images of the 3×3-mm lesion area (ROI) were compared with PS-OCT 2D depth and integrated reflectivity maps representing the lesion severity. The lesion depth and integrated reflectivity for each pixel in the visible and near-IR images were calculated using the linear fits shown in Fig. 5 for the dry samples. These values were compared on a pixel-by-pixel basis with the depths measured using PS- OCT, and the difference in values (error) is represented by confusion maps.

Point-by-point near-IR (BP1460) and visible images of 3×3-mm lesion areas (ROI) were compared with PS-OCT 2D depth and integrated reflectivity maps representing the lesion severity. The lesion depth and integrated reflectivity for each pixel in the visible and near-IR images were calculated using the linear fits shown in Fig. 2.5 for dry samples. By automatically overlaying the identical regions using a pattern-matching algorithm, a pixel-by-pixel value comparison of the reflectance imaging method and reference PS-OCT measurements produced a difference in values (error) data set represented by confusion maps.

Figure 2.7 shows the respective depth-based images of the 3×3-mm region of interest (ROI) for a group 4 lesion along with the corresponding confusion maps. Figure 8 is an analogous set of images to those shown in Fig. 2.7, but representative of the integrated

reflectivity measure of severity and corresponding accuracy for a less severe, group 1 lesion. Confusion maps classified pixels as true representations of the lesion severity if the value was within 25% (based on the standard deviation of the regression fit) of the reference, and as overestimates or underestimates outside that range. Figures 2.9 & 2.10 represent the distribution of pixel-by-pixel accuracy assessments, based on depth and integrated reflectivity respectively, for BP1460 and visible reflectance methods on a group basis.

The lesion depth and integrated reflectivity values were more often overestimated for visible reflectance, while more often underestimated with near-IR reflectance. More pixels were accurately classified for less severe lesions (groups 1–3) with near-IR reflectance than with visible reflectance. The two methods become similar in accuracy for the most severe lesions (group 4). The near-IR reflectivity is better able to show variation of the lesion severity.

2.5 Discussion

Previous studies have shown that near-IR reflectance measurements yield very high contrast of early caries lesions, particularly at those near-IR wavelengths coincident with high water absorption. However, the lesion contrast is expected to be highly dependent on the lesion severity and studies suggest that the wavelengths which yield the highest contrast of lesions with a particular depth and severity may not yield the highest contrast for other shallower lesions or for other lesion types with different mineral profiles. Moreover, an imaging method that shows a concomitant increase in lesion contrast with increasing lesion severity is more useful since the lesion severity can more easily be

estimated from the images. In this study we measured the lesion contrast for four lesion groups of varying severity with mean depths ranging from 4 to 84- μm in different spectral regions. Several filters were used to measure the reflectance in different near-IR spectral ranges and in the visible. We also measured the contrast of fluorescence (QLF) for comparison. There are studies that suggest higher contrast can be obtained by using blue light instead of including all the visible wavelengths [55]. The emphasis of this study was on the near-IR, therefore, we did not explore different spectral regions in the visible range in this study. In addition, visible light absorption by stains is a major problem for tooth occlusal surfaces. In a recent study of natural lesions in the occlusal surfaces of extracted teeth [40], the image contrast was actually negative as opposed to being positive in visible reflectance measurements indicating that absorption due to stains contributed more than increased scattering due to demineralization to the reflectivity in the visible. Therefore, visible reflectance is of questionable utility in areas that are subject to heavy staining, namely the areas where most lesions are likely to develop. In fact, visible light reflectance was proposed almost three decades ago for use in monitoring early demineralization on tooth surfaces but has proven to be unsuccessful due to the problems indicated above [54].

Near-IR reflectance at wavelengths coincident with higher water absorption produced the greatest range of lesion contrast values and the contrast increased linearly with increasing lesion depth and severity (Fig. 2.5). A greater sensitivity of lesion contrast to variation in the lesion severity should make it easier to gauge the severity of lesions in occlusal surfaces. The higher accuracy of near-IR reflectance for early lesions, is likely

due to higher sensitivity to equivalent changes in lesion depth and severity and are therefore, better suited for monitoring changes in lesion severity over time.

In this paper, we also demonstrate the utility of cross-polarization OCT images converted to the calculated depth and ΔR formats for providing a map of the lesion severity. Reflectance images of a specific region of interest on the tooth surface were compared pixel by pixel with the lesion depth and the reflectivity integrated over the lesion depth to show how accurately the lesion contrast in that image represents the actual variation in lesion severity. This analysis also assesses the ability of near-IR and visible reflectance methods to provide reliable information about the local severity of a lesion in terms of depth and integrated reflectivity, and how that accuracy evolves with a developing (growing) lesion. Evaluating imaging methods in this manner may identify the parameters where optical contrast has great accuracy in diagnosis, and a threshold where contrast information has effectively reached a plateau.

We also explored the influence of the surface wetness on the lesion contrast. The surface wetness causes a profound reduction in the lesion contrast for both fluorescence and reflectance measurements. Wavelengths coincident with water absorption are more profoundly affected. Therefore, it is necessary to air dry tooth surfaces before performing reflectance measurements. One would think that it would not be feasible clinically to use near-IR reflectance at those wavelengths due to the high sensitivity to water. However, we have successfully acquired high contrast *in vivo* images of early lesions in tooth occlusal surfaces at 1480-nm and 1610-nm in preliminary clinical imaging studies using broadband superluminescent light sources. This was achieved without using a longer

period of air drying than is required for visible images. Monitoring the changes in lesion contrast with air drying has been shown to be useful for assessing lesion activity. Lesions with a well-defined surface zone are considered less active, and the surface zone acts as a barrier to water diffusion, and the rate of water loss is lower, since wavelengths coincident with water absorption bands manifest greater changes in contrast with water loss. Therefore, those wavelengths are likely better suited for monitoring the rate of dehydration or water loss.

We also established in this study that air abrasion can be used to clean tooth occlusal surfaces without significant changes in the lesion contrast. This is important because it is very difficult to produce lesions on tooth occlusal surfaces due to stains, debris and the fluoride rich outer layer of enamel.

In conclusion, this study shows that reflectance measurements at longer near-IR wavelengths, coincident with higher water absorption have significant advantages over other methods for imaging caries lesions. These advantages include minimal interference from stains and discoloration, very high lesion contrast over a wide range of lesion severity, and a linear increase in the lesion contrast with increasing lesion severity.

2.6 Tables and Figures

Table 2.6.1. Mean lesion contrast *100 (s.d) for 12-hr samples prepared with air abrasion and prophy for all filters wet and dry. The mean (s.d) lesion depth and integrated reflectivity (ΔR) for 12-hr samples prepared using air abrasion and prophy.

Filter (LP & BP)	Air Abrasion Dry Mean Contrast	Prophy Dry Mean Contrast	Air Abrasion Wet Mean Contrast	Prophy Wet Mean Contrast
LP1100	26(7.6)	23(5.3)	23(6.1)	20(5.2)
LP1200	21(11)	22(5.3)	18(8.0)	18(4.7)
LP1300	20(11)	24(10)	16(9.9)	14(9.9)
LP1400	23(13)	27(17)	5.1(18)	-8.4(14)
LP1500	26(14)	27(14)	12(15)	-0.45(11)
BP1300	24(9.1)	21(4.1)	25(7.8)	21(4.1)
BP1377	25(9.5)	21(4.2)	20(12)	16(6.8)
BP1460	18(15)	22(15)	-29 (33)	-31(19)
BP1550	9.1(12)	8.5(6.9)	-0.95(8.9)	-3.5(3.6)
Visible	25 (3.5)	13(4.6)	13(13)	10(4.7)
QLF	-5.1 (7.3)	-10(8.8)	-18(13)	-14(8.7)
	Air Abrasion Depth (μm)	Prophy Depth (μm)	Air Abrasion ΔR (IU)	Prophy Mean ΔR (IU)
Value	22(27)	11(11)	39(52)	42(83)

* IU= Linear intensity units (detector volts/ 32 μV)

Table 2.6.2. The mean (s.d) depths and integrated reflectivity (ΔR) for adjusted groups 1,2,3 & 4.

Group	Depth (μm)	ΔR (IU)
1	3.9(2.8)	6.5(4.1)
2	21.5(10.8)	35.7(16.2)
3	63.4(10.5)	139(28.1)
4	84.2(22.8)	226(32.9)

* IU= Linear intensity units (detector volts/ 32 μV)

Table 2.6.3. Mean lesion contrast *100 (s.d) for wet and dry samples of varying severity increase from groups 1-4. Groups with the same letter are statistically similar P>0.05.

DRY Filter	Group 1	Stat. group	Group 2	Stat. group	Group 3	Stat. group	Group 4	Stat. group
a)LP1100	22(5.0)	a-h, j	27(3.6)	a-h, j	23(7.9)	a-c, f-g, i, k	32(7.4)	a-c, g, i-k
b)LP1200	19(8.0)	a-h, j	22(3.3)	a-h, j	25(8.5)	a-c, f-g, i-k	35(8.7)	a-c, g, i-j
c)LP1300	18(8.0)	a-h, j	23(8.6)	a-h, j	29(7.9)	a-g, i-k	40(8.0)	a-c, g, i-j
d)LP1400	20(13)	a-h, j	28(11)	a-h, j	35(12)	c-e, h, j	52(12)	d-e, h
e)LP1500	22(9.1)	a-h, j	28(15)	a-h, j	38(14)	c-e, h, j	54(13)	d-e, h
f)BP1300	20(5.5)	a-h, j	24(4.4)	a-h, j	20(7.2)	a-c, g, i, k	20(4.8)	g, k
g)BP1377	20(6.2)	a-h, j	22(4.2)	a-h, j	23(6.0)	a-c f, i, k	30(8.8)	a-c, h-j
h)BP1460	15(9.6)	a-j	23(17)	a-h, j	42(9.8)	d-e, j	56(14)	d-e
i)BP1550	6.7(5.4)	h	9.5(9.1)	-	18(8.8)	a-c, f, g, j	35(13)	a-c, g, j
j)Visible	16(6.4)	a-h	22(9.9)	a-h	36(6.5)	b-e, h	40(9.0)	a-c, g
k)QLF	-8.4(6.1)	-	-5.6(12)	-	18(10)	a-c, e-f, i	24(16)	a, f-g
WET Filter	Group 1	Stat. group	Group 2	Stat. group	Group 3	Stat. group	Group 4	Stat. group
a)LP1100	21(6.3)	a-c, f-g, j	21(4.6)	a-c, f-g, j	13(7.3)	a-c, f-g, j	13(7.6)	a-c, e-g, j
b)LP1200	17(7.6)	a-c, e-g, j	18(5.0)	a-c, e-g, j	11(8.3)	a-c, f-g, j	12(8.4)	a-c, e-g, j
c)LP1300	13(8.7)	a-c, e-g, i-j	12(14)	a-c, e-g, j	6.0(11)	a-g, j	7.6(8.9)	a-g, i-k
d)LP1400	-2.0(17)	d-e, i-k	-3.3(14)	d-e, i-k	-3.7(8.1)	c-e, h-i, k	-2.8(16)	c-e, g-i, k
e)LP1500	4.3(14)	b-e, g, i-k	4.3(11)	b-e, g, i-j	-4.3(13)	c-e, g-i, k	7.1(15)	a-e, i, k
f)BP1300	21(5.3)	a-c, g, j	25(6.9)	a-c, f-g, j	18(7.6)	a-c, g, j	16(6.6)	a-c, g, j
g)BP1377	15(10)	a-c, e-g, j	17(10)	a-c, e-f, j	12(9.1)	a-c, e-f, j	9.9 (11)	e-g, j-k
h)BP1460	-31(27)	k	-37(27)	-	-12(17)	d-e, i, k	-13(17)	d, i, k
i)BP1550	0.9(4.7)	c-e, j-k	-5(5.1)	d-e, k	-6.8(3.8)	d-e, h, k	-2.9(8.2)	c-e, h, k
j)Visible	10(5.5)	a-g, i	11(13)	a-g	16(5.3)	a-c, f-g	17(4.9)	a-c, f-g
k)QLF	-16(9.6)	d, h-i	-14(11)	d, i	-4.3(9.8)	d-e, h-i	-1.8(13)	c-e, g-i

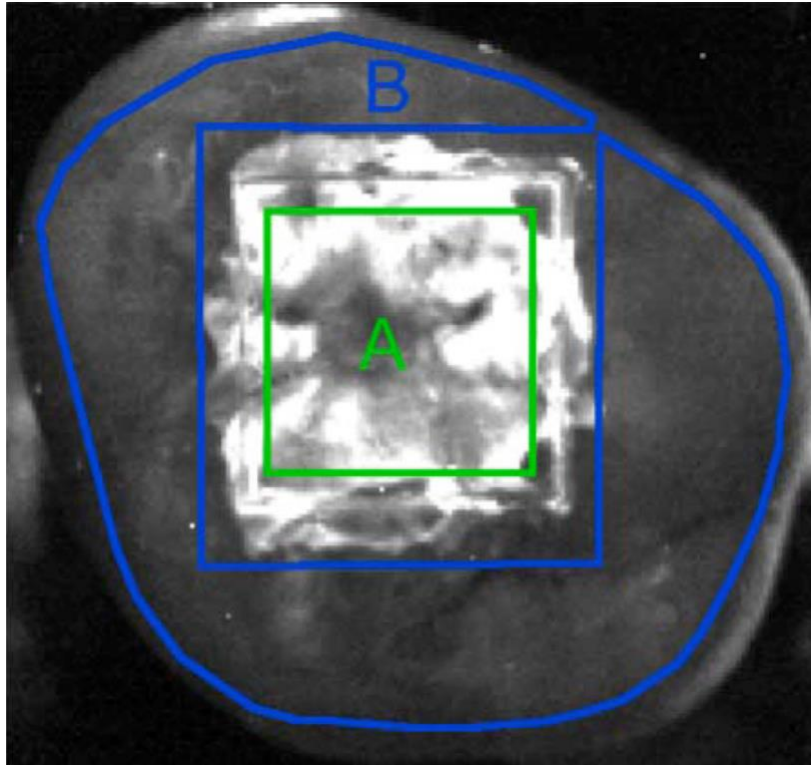


Figure 2.6.1. Near-IR reflectance (BP1460 filter) image of a sample from group 4 (most severe). The 3x3-mm area centered in the 4x4-mm window exposed to demineralization is demarcated in green and labeled 'A'. The polygon region outline in blue and labeled 'B' represents the sound reference area.

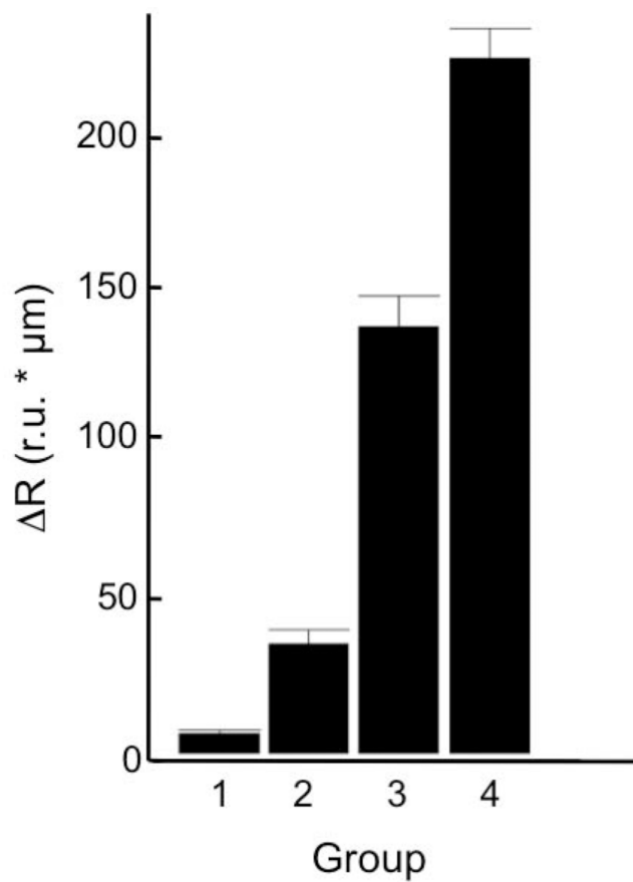


Figure 2.6.2. The mean integrated reflectivity \pm the standard deviation (s.d.) for adjusted groups 1-4.

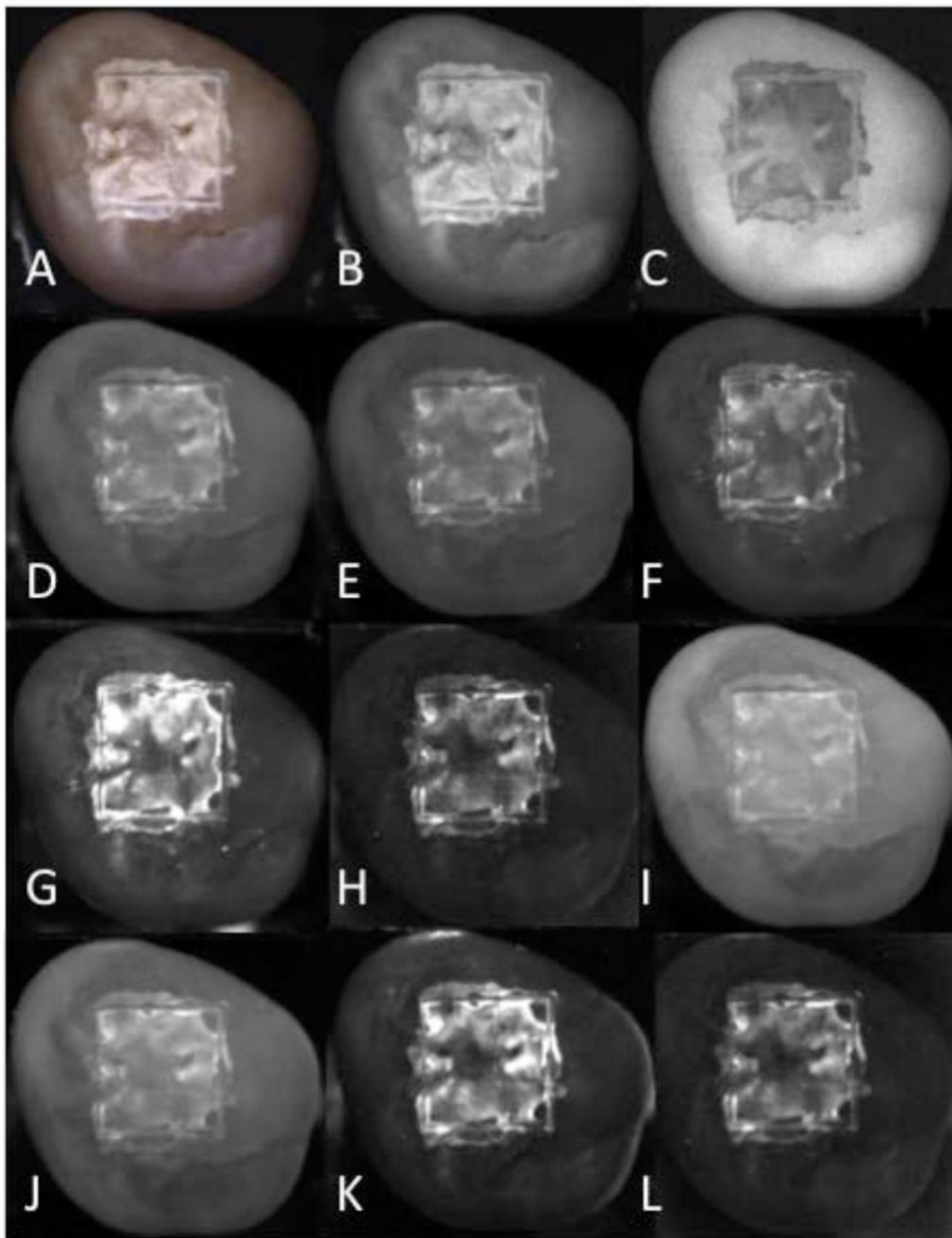


Figure 2.6.3. Set of lesion images for one sample from group 4 (most severe). (A) visible reflectance color image, (B) visible image grayscale, (C) fluorescence (405/500-nm), (D) LP1100, (E) LP1200, (F) LP1300, (G) LP1400, (H) LP1500, (I) BP1300, (J) BP1377, (K) BP1460, (L) BP1550.

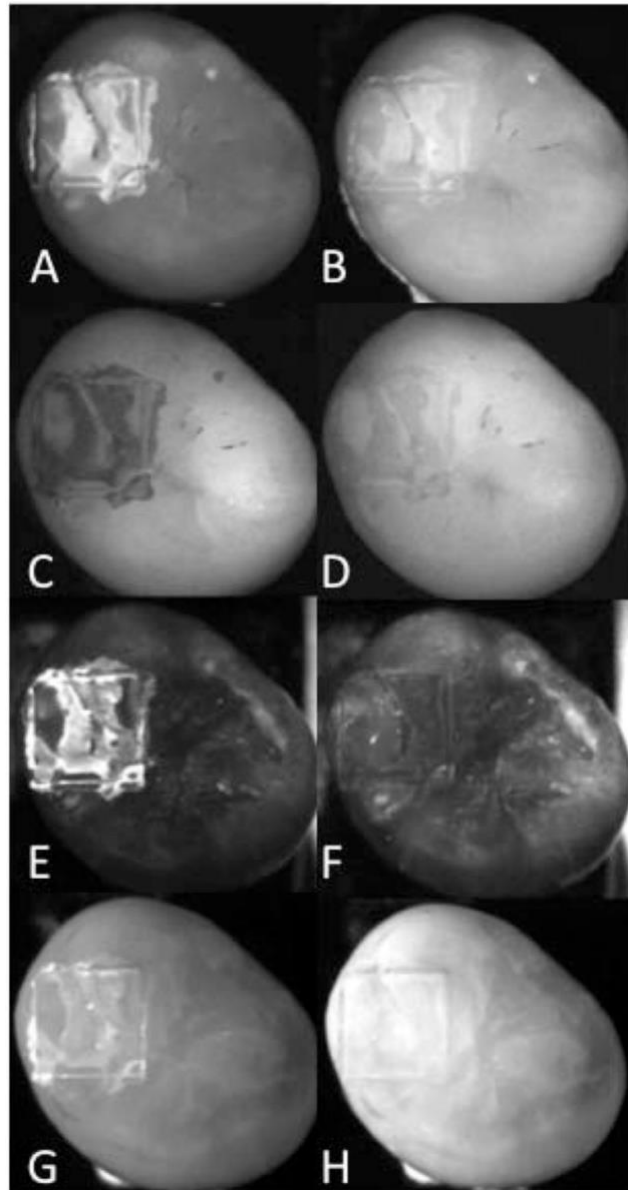


Figure 2.6.4. Comparison of dry (left) and wet (right) images of group 4 lesions. (A-B) Visible, (C-D) fluorescence (405/500), (E-F) BP1460 and (G-H) BP1300.

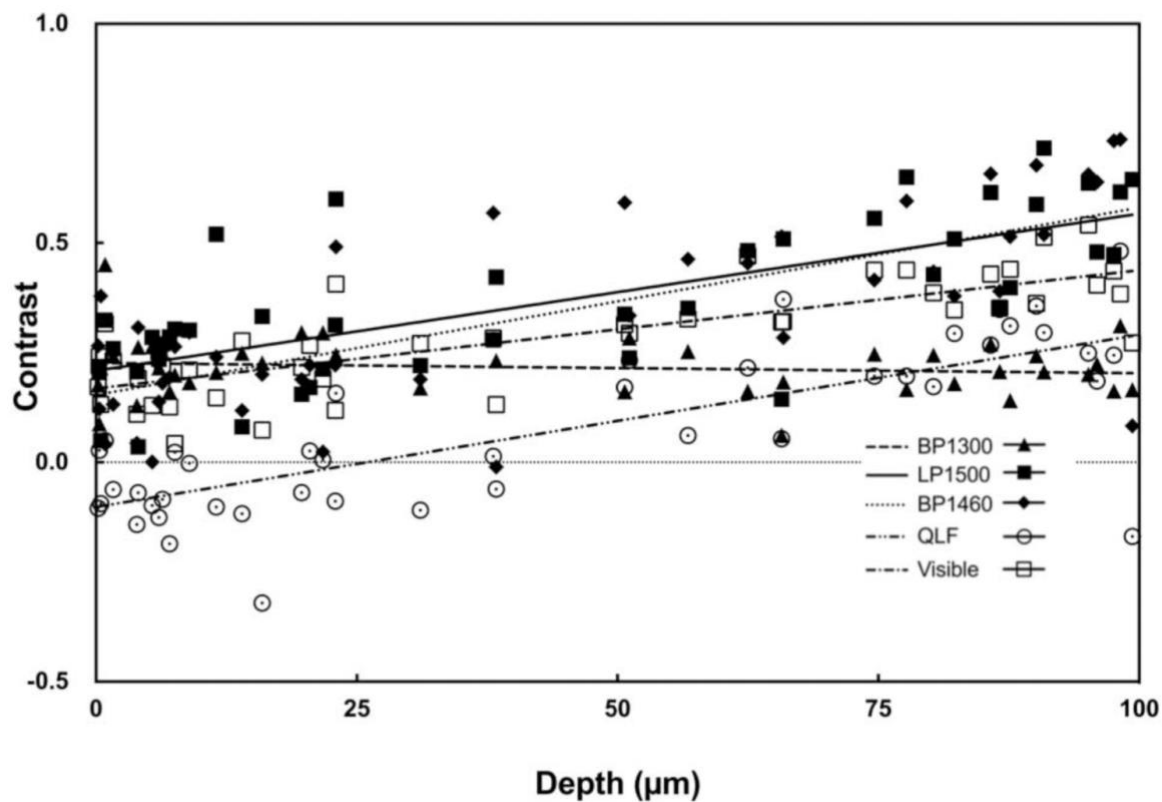


Figure 2.6.5. Plot of the measured lesion contrast for dry samples vs. the mean lesion depth determined using OCT. Data for visible reflectance, QLF, and near-IR reflectance with BP1300, BP1460 and LP1500 are shown along with the best fit linear regression lines.

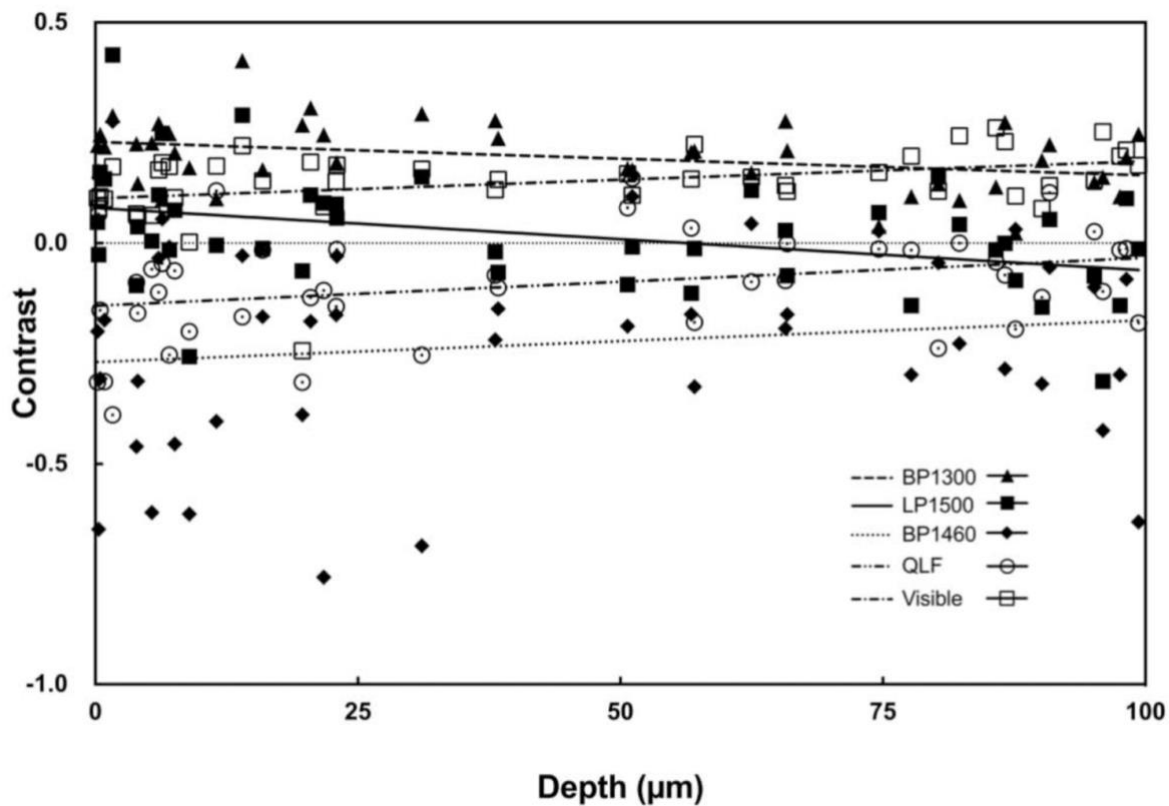


Figure 2.6.6. Plot of the measured lesion contrast for wet samples vs. the mean lesion depth determined using OCT. Data for visible reflectance, QLF, and near-IR reflectance with BP1300, BP1460 and LP1500 are shown along with the best fit linear regression lines.

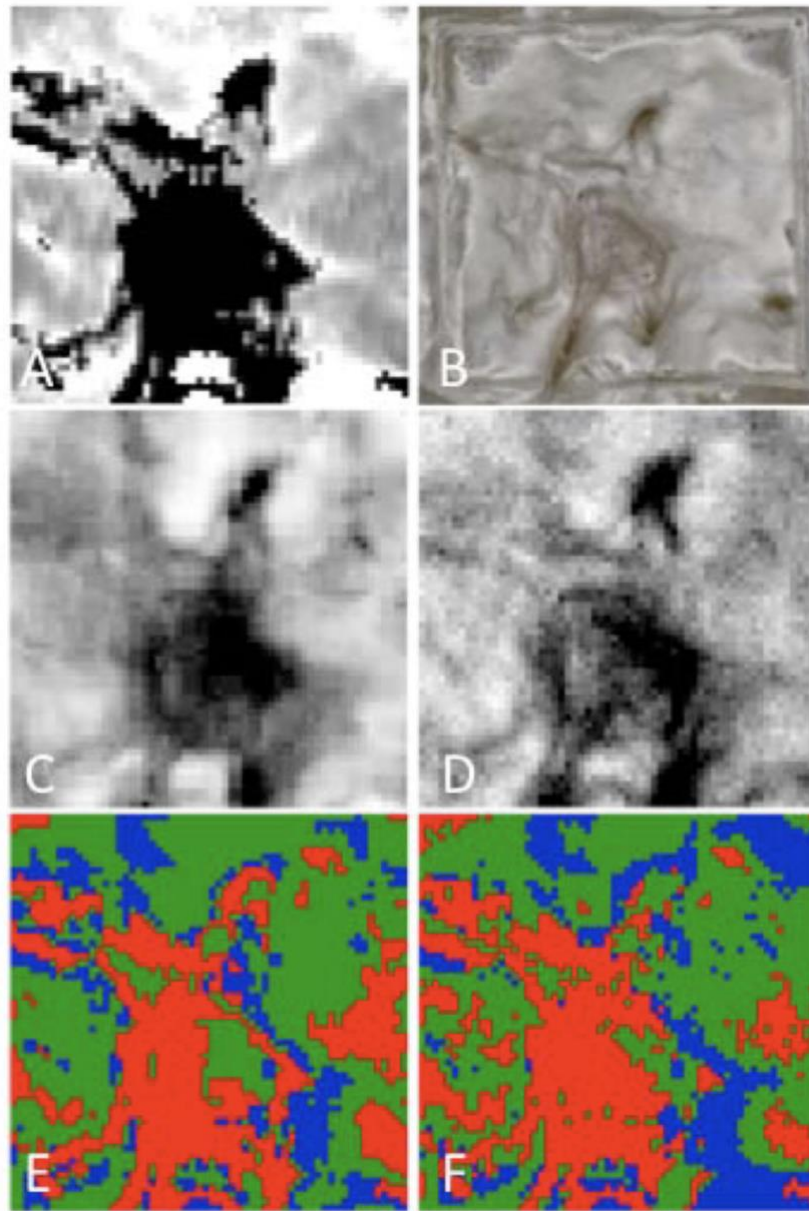


Figure 2.6.7. Maps of the calculated lesion depth for a group 4 sample. (A) Lesion depth from OCT, (B) Visible depth composition image from digital microscope, (C) Lesion depth from near-IR (BP1460), and (D) Lesion depth from visible. Confusion maps of lesion depth comparing OCT lesion depths vs. near-IR (BP1460) (E) and visible (F). Green is true, blue is underestimate and red is overestimate.

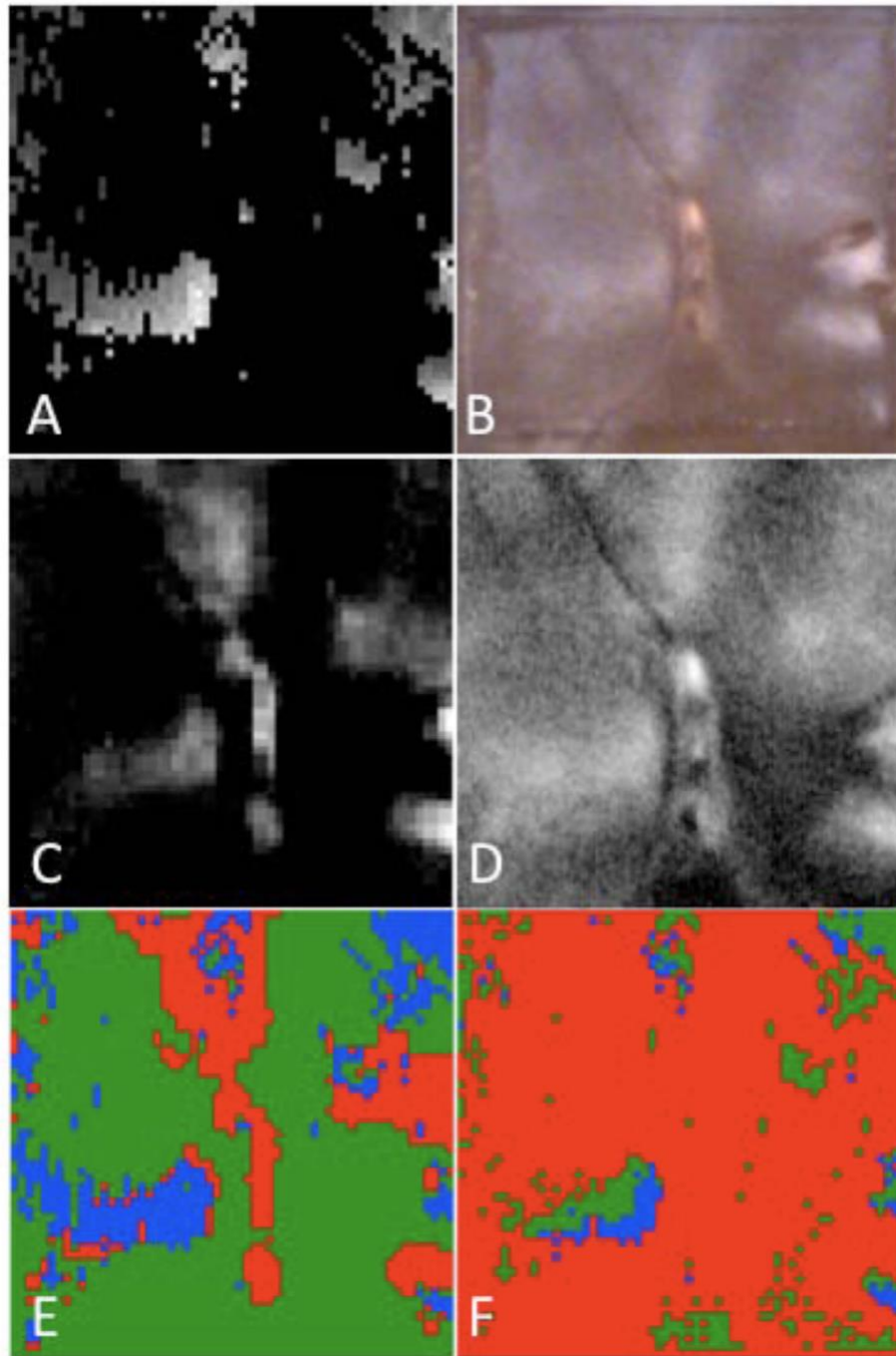


Figure 2.6.8. Maps of the integrated reflectivity with lesion depth (ΔR) from a group 1 sample. (A) Lesion depth from OCT, (B) Visible reflectance image, (C) Lesion integrated reflectively with lesion depth from near-IR (BP1460), and (D) from visible. Confusion maps of lesion depth comparing OCT depths vs. near-IR (BP1460) (E) and visible (F). Green is true, blue is underestimate and red is over estimate.

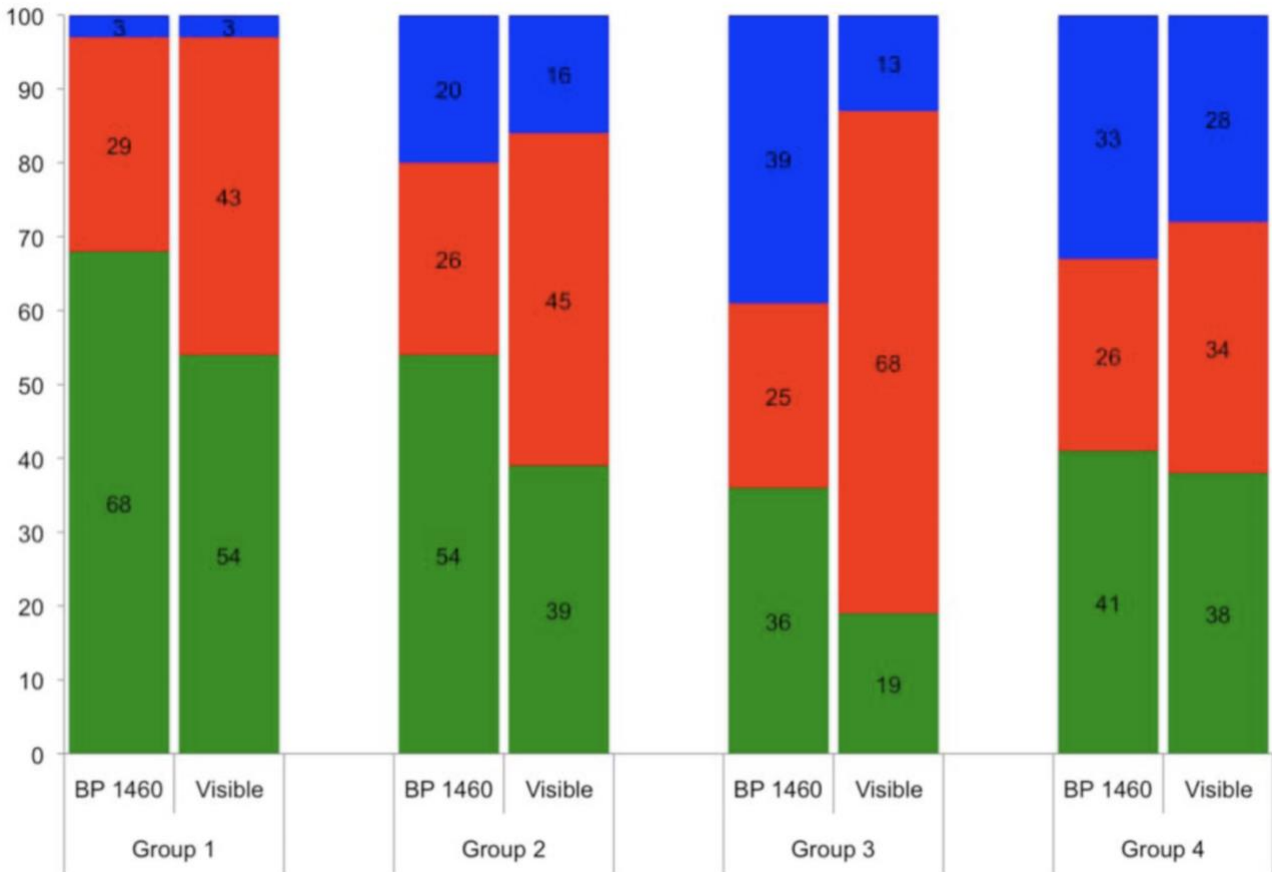


Figure 2.6.9. Stacked bar graph showing accuracy of lesion depth assessment for each lesion group for visible and near-IR (BP1460) reflectance based on point by point comparison with the lesion depth determined using OCT. Green is true, blue is underestimate and red is overestimate.

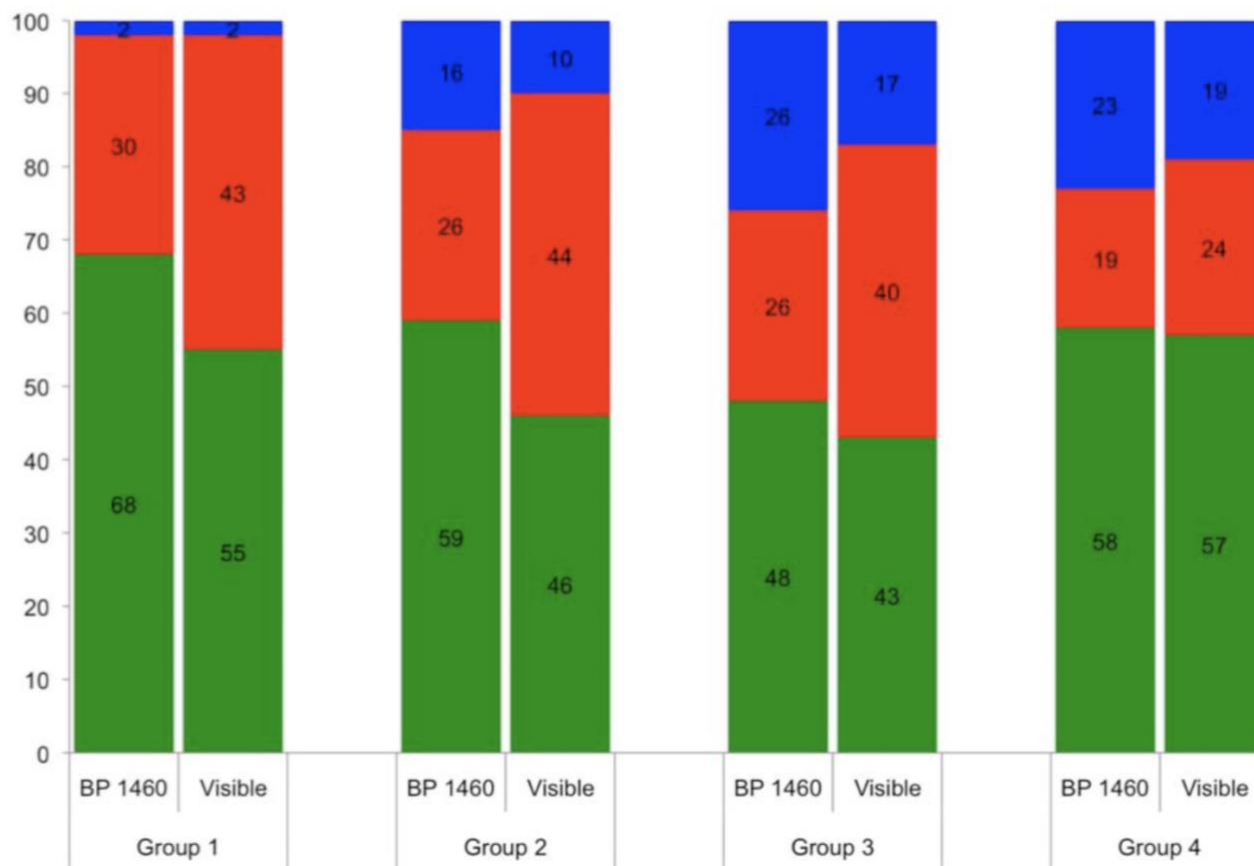


Figure 2.6.10. Stacked bar graph showing accuracy of lesion severity assessment for each lesion group for visible and near-IR (BP1460) reflectance based on point by point comparison with the integrated reflectivity with lesion depth (ΔR) determined using OCT. Green is true, blue is underestimate red is overestimate.

CHAPTER III

Near-Infrared Imaging of Demineralization on the Occlusal Surfaces of Teeth Without the Interference of Stains

3.1 Summary

Most new caries lesions are found in the pits and fissures of the occlusal surface. Radiographs have extremely low sensitivity for early occlusal decay, and by the time the lesion is severe enough to appear on a radiograph, it typically has penetrated well into the dentin and surgical intervention is required. The occlusal surfaces are often heavily stained, and visual and tactile detection have poor sensitivity and specificity. Previous near-infrared imaging studies at wavelengths beyond $\lambda=1300\text{-nm}$ have demonstrated that stains are not visible and demineralization on the occlusal surfaces can be viewed without interference from stains. The objective of our study is to determine how the contrast between sound and lesion areas on occlusal surfaces varies with wavelength from the visible to $\lambda=2350\text{-nm}$ and determine to what degree stains interfere with that contrast. The lesion contrast for reflectance is measured in 55 extracted teeth with suspected occlusal lesions from $\lambda=400\text{-}2350\text{-nm}$ employing silicon and indium gallium arsenide imaging arrays. In addition, the lesion contrast is measured on 25 extracted teeth with suspected occlusal lesions from $\lambda=400\text{-}1600\text{-nm}$ in reflectance and from 830 to $\lambda=1400\text{-nm}$ in transillumination before and after stains are removed using a ultrasonic scaler. The highest lesion contrast in reflectance is measured at wavelengths $\lambda>1700\text{-nm}$. Stains interfere significantly at wavelengths $\lambda<1150\text{-nm}$ (400 to 1150) for both reflectance and transillumination measurements. Our study suggests that the optimum wavelengths for imaging decay in the occlusal surfaces are $\lambda>1700\text{-nm}$ for reflectance (1700 to 2350-nm) and near $\lambda=1300\text{-nm}$ (1250 to 1350-nm) for transillumination.

3.2 Introduction

More than 15 years ago, it was discovered that enamel is highly transparent in the near-infrared (NIR) beyond 1300-nm (Fig. 3.1) [42, 74]. Therefore, the NIR is well-suited for imaging lesions on both proximal and occlusal surfaces. Innovative imaging configurations such as occlusal transillumination and cross-polarization reflectance imaging can be used to image lesions on both occlusal and proximal surfaces [28, 75]. The scattering coefficient of enamel is 20 to 30 times higher in the visible versus the NIR at 1300-nm providing high contrast of demineralization in the NIR [41, 42]. NIR imaging allows greater diagnostic capabilities than the current standard of bitewing radiographs for both inter-proximal and occlusal carious lesions [28, 44, 71, 74-78]. Hyperspectral NIR imaging studies have also been carried out to identify caries lesions [51, 79, 80]. Since those seminal studies, multiple commercial NIR clinical imaging devices have been introduced: CariVu (Dexis, Hatfield, Pennsylvania), which uses NIR occlusal transillumination with 780-nm light [81, 82], and the Vistacam IX (PROXI) from Durr Dental (Bietigheim-Bissingen, Germany), which uses NIR reflectance at 850-nm [83]. For caries detection schemes operating in the visible range such as fiber-optic transillumination [84-89] and the optical caries monitor [54], along with fluorescence-based methods, stains interfere and may produce false positives [90-103]. Both *in vitro* and *in vivo* studies show that stains completely mask demineralization in the pits and fissures [40]. The highly conjugated molecules such as melanin and porphyrins produced by bacteria and those found in food dyes accumulate in dental plaque [104]. They are responsible for the pigmentation in the visible range and do not absorb light beyond 1200-nm [37, 38, 105].

The lesion contrast for reflectance is defined as $(I_L - I_S)/I_L$, where the intensity of the reflected or backscattered light from the lesion is I_L and that from the surrounding sound enamel is I_S . The lesion contrast for reflectance is highest at NIR wavelengths coincident with higher water absorption and low light scattering. The lesion contrast was significantly higher ($P < 0.05$) for NIR reflectance imaging at 1450-nm and 1600-nm than it was for NIR reflectance imaging at 1300-nm, visible reflectance imaging, and quantitative light fluorescence (QLF) [52]. The markedly higher contrast at 1450-nm and 1600-nm wavelengths, coincident with higher water absorption, suggests that these wavelengths are better suited than 1300-nm for imaging early/shallow demineralization on tooth surfaces, and they manifest greater intensity and contrast variation with lesion depth and severity [39]. Imaging at shorter NIR wavelengths near 830-nm was investigated more than a decade ago [76]. The 830-nm system was capable of higher performance than visible systems, but the contrast was significantly lower than that attainable at 1300-nm and simulated lesions could not be imaged through the full enamel thickness due to greater light scattering [76]. In addition, it appears that stains are still visible at the shorter NIR imaging systems, where commercial systems are now operating [81, 82].

Studies indicate that light scattering in dental enamel decreases with increasing wavelength, and increased water absorption decreases the backscattered light (reflectance) from sound tooth structure [40, 41, 45]. Therefore, higher contrast between sound and demineralized enamel is expected at longer NIR wavelengths beyond 1700-nm and preliminary reflectance measurements support this hypothesis. Hyperspectral images of Zakian et al. [51] showed the tooth continuing to get darker and darker with increasing wavelength. The magnitude of absorption by water at 1940-nm (120 cm^{-1}) is

4 times higher than at 1450-nm (29-cm^{-1})[6] (see Fig. 3.1). Higher contrast translates to higher diagnostic performance and earlier detection of demineralization. The spectral response of indium gallium arsenide (InGaAs) can be extended well beyond 1700-nm to reach the strong water absorption band at 1940-nm by removing the underlying indium phosphide substrate on which the InGaAs is deposited. In this study, an extended range InGaAs camera sensitive from 1000-nm to 2350-nm was used. Even though light scattering in enamel is at a minimum in the NIR, light scattering in sound dentin is high. At wavelengths highly absorbed by water, i.e., 145-nm and 1940-nm, deeply penetrating light is absorbed by the water in the surrounding/underlying sound enamel and dentin, thus increasing lesion contrast.

The purpose of this study is to determine the influence of tooth staining found in the pits and fissures of occlusal tooth surfaces on the image contrast of reflectance and transillumination measurements at NIR wavelengths and determine if higher lesion contrast is attainable at wavelengths $>1700\text{-nm}$. We hypothesize that reduced interference from stains, lower light scattering from sound enamel, and increased absorption by water at longer wavelengths will yield higher contrast of caries lesions on tooth occlusal surfaces. Higher lesion contrast translates to higher diagnostic performance and earlier detection.

3.3 Material and Methods

3.3.1 Sample Preparation

Eighty human teeth with suspected noncavitated occlusal surface caries, International Caries Detection and Assessment System scores of 1 to 3, were collected (Committee on Human Research approved) and sterilized with gamma radiation. All teeth were brushed with a dentifrice to remove any loose debris and biofilm, and they were mounted in black orthodontic acrylic blocks. All teeth that were included in the study had stains that were visually apparent on the occlusal surface after brushing. Samples were stored in a moist environment of 0.1% thymol to maintain tissue hydration and prevent bacterial growth [81]. The samples were split into two groups and the first set of samples (n= 55) was used to assess the wavelength dependence on the lesion contrast in reflectance from 400-nm to 2350-nm. QLF measurements were also carried out for comparison. An extended range NIR InGaAs imaging array was used in this study, which was sensitive out to 2350-nm. These teeth were sectioned after imaging and assessed with polarized light microscopy (PLM) and transverse microradiography (TMR) to confirm lesion presence in dentin. Eleven of the teeth had lesions confined to the outer half of enamel (E1), twenty-six teeth had lesions penetrating to the inner half of enamel (E2), and lesions in the remaining fourteen teeth penetrated into the dentin (D).

A second group of 25 teeth were used to assess the influence of stain on the lesion contrast. The lesion contrast was measured from 400 to 1600-nm in reflectance and from 400-nm to 1380-nm in occlusal transillumination measurements before and after stain removal. A special germanium (Ge)-enhanced silicon (Si) imaging array was used, which

was capable of operating from 400-nm to 1600-nm so that the same imager could be used for all the measurements. Wavelengths beyond 1380-nm were not used for occlusal transillumination because of increased water absorption. Stain was removed with an ultrasonic scaler and the teeth were not sectioned after removal.

3.3.2 Near-Infrared Reflectance Measurements 400-nm to 2350-nm (Group 1 n=55 Teeth)

Visible color images of the samples were acquired using a USB microscope, Model AM7915MZT from AnMO Electronics Corporation (New Taipei City, Taiwan) with extended depth of field and cross polarization. The digital microscope captures 5-megapixel (2952 × 1944) color images.

The second setup of Fig. 3.2 was used for reflectance measurements at 400-nm to 1000-nm and from 900-nm to 2350-nm using the light sources and NIR cameras described later. The tooth occlusal surface was illuminated by the light sources at a 30-degree angle to the surface normal of the tooth occlusal surface as shown in Fig. 3.2. Crossed polarizers were used to remove specular reflection (glare).

A DMK-3002-IR NIR sensitive CCD camera (Imaging Source, Charlotte, North Carolina) equipped with an Infinity Infinimite lens was used to acquire 400-nm to 1000-nm and 850-nm images. A 150-W fiber-optic illuminator FOI-1 (E Licht Company, Denver, Colorado) coupled to an adjustable aperture was used as a light source and an 850-nm filter with a 70-nm bandwidth was used for the 850-nm images.

A Xenics (Leuven, Belgium) Model Xeva-2.35-320 extended range InGaAs camera sensitive from 900-nm to 2350-nm (320×240 pixel) with a Navitar SWIR optimized f 1/4 35-mm lens (f/1.4) was used to acquire images from 1000-nm to 2350-nm. A stabilized Tungsten IR light source, Model SLS202, from Thorlabs (Newton, New Jersey) with a peak output at 1500-nm and collimating optics was used. Several bandpass [BP wavelength (bandwidth)] and longpass [LP wavelength] filters were used to select wavelength intervals in the NIR, including BP850(90), BP1150(78), BP1300(90), BP1460(85), BP1675(90), and LP1695.

All image analysis was carried out using Igor Pro software, Wavemetrics (Lake Oswego, Oregon). Intensity values (I) in arbitrary units with a bit density of 10 bits (0 to 1024) were recorded from each camera. An area of at least 500 pixels was chosen in the area of most severe staining and demineralization for the lesion intensity (I_L) and an equivalent area of sound enamel was chosen for the sound intensity (I_S). The darkest area in the color (visible light) image was used to demarcate the most severely stained area. The following formula was used to calculate the lesion contrast for reflection $(I_L - I_S)/I_L$, which varies from 0 to 1 for positive contrast, where 1 is the maximum achievable contrast and 0 is no contrast. In reflectance, demineralization increases I_L while absorption by stains decreases I_L . Since we are interested in detecting demineralization, large positive differences between I_L and I_S are desirable for caries detection. At shorter wavelengths, the high absorption by stains masks the demineralization and the contrast becomes negative, and in this case, the contrast is no longer bound between 0 and 1. Negative contrast is not meaningful and should not be compared to positive contrast values, i.e., the negative contrast can approach infinity. Repeated measures one-way analysis of

variance (ANOVA) followed by the Tukey–Kramer post-hoc multiple comparison test were used to compare the contrast measurements between wavelengths using the statistical software Prism from GraphPad (San Diego, California).

3.3.3 Quantitative Light Fluorescence

QLF images were acquired using a USB microscope with 5 blue light-emitting diodes (LEDs) and a 510-nm LP filter, Model AM4115TW-GFBW from BigC (Torrance, California). Fluorescence intensity values were measured for the same lesion and sound enamel areas for the 55 samples in Sec. 3.3.2. However, QLF utilizes fluorescence loss so the intensity of sound enamel is higher than stained and demineralized enamel and the following formula for contrast was used $(I_S - I_L)/I_S$, where I_L is the intensity of the fluorescence from lesion areas and I_S is the fluorescence from sound areas. A paired t-test (two-tailed) was used to compare the lesion contrast for fluorescence (QLF) and the highest lesion contrast measured with NIR reflectance.

3.3.4 Near-Infrared Reflectance Measurements (400-nm to 1600-nm) and Near-Infrared Transillumination (830-nm to 1380-nm) before and after Stain Removal (Group 2 n=25 Teeth)

A NoblePeak Vision Triwave Imager, Model EC701 (Wakefield, Massachusetts) was used, which employs a Ge-enhanced complementary metal–oxide–semiconductor focal plane array sensitive in the visible and NIR from 400-nm to 1600-nm with an array of 640 × 480 pixels and a 10- μ m pixel pitch. An Infinimite™ video lens (Infinity, Boulder, Colorado) was attached to the Triwave imager. Light from a 150-W fiber-optic illuminator

FOI-1 (E Licht Company, Denver, Colorado) coupled to an adjustable aperture and several BP and LP filters were used to provide different spectral distributions of NIR light. The following filters: BP830(70), BP1150(78), BP1300 (90), BP1380(90), and LP1500 (1500-nm to 1600-nm) were used for the reflectance and transillumination imaging configurations as shown in Fig. 3.2. Transillumination images of natural teeth with stains on the occlusal surfaces were acquired using the first setup as shown in Fig. 3.2 [51, 81]. For occlusal transillumination, NIR wavelengths were delivered by a low-profile fiber optic with dual-line lights, Model P39-987 (Edmund Scientific, Barrington, New Jersey) with each light line directed at the cementum–enamel junction (CEJ) beneath the crown on the buccal and lingual sides of each tooth. The fiber-optic line lights were set at a downward angle of ~20-degree and directed just above the CEJ. The angle and position were extremely important. If the light is directed too high on the tooth or at an upward angle, the light does not enter the dentin of the crown and the contrast of the lesion is greatly reduced, i.e., the light has to be directed under the lesion. For reflectance, the second setup in Fig. 3.2 was used with the Triwave imager and the 150-W FOI-1 fiber-optic illuminator.

A region of the most severely stained area of each tooth was imaged using both reflectance and transillumination before and after stain removal with a Varios 350 Lux ultrasonic scaler from NSK (Kanuma, Japan). The darkest area in the visible image was used to demarcate the most severely stained area. The lateral surface of the scaling tip was adapted to the tooth and applied in brief strokes at sites with extrinsic staining. The transillumination contrast formula used was $(I_S - I_L)/I_S$ and the reflectance contrast

formula used was $(I_L - I_S)/I_L$ for positive contrast. For positive contrast, the contrast varies from 0 to 1.

Repeated measures ANOVA followed by the Tukey–Kramer post-hoc multiple comparison test were used to compare the contrast measurements between groups for reflectance and transillumination before and after removal.

3.3.5 Polarized Light Microscopy and Transverse Microradiography

After all diagnostic images were captured, samples were serially sectioned into ~200- μ m-thick mesiodistal slices using a linear precision saw, Isomet 5000 (Buehler, Lake Bluff, Illinois). Thin sections were examined by PLM and TMR.

PLM was used to examine the thin sections using a Meiji Techno RZT microscope (Saitama, Japan) with an integrated digital camera, Canon EOS Digital Rebel XT (Tokyo, Japan). Sample sections 200- μ m thick were imbibed in deionized water and examined in the bright-field mode with crossed polarizers and a red I plate with 550-nm retardation.

PLM is reliable for assessing demineralization in enamel since sound enamel weakly scatters light and demineralization scrambles the polarization causing lesion areas to appear dark; however, it is more difficult to interpret in dentin due to the very high light scattering in sound dentin. Therefore, we used TMR to confirm lesion penetration into dentin for those samples where the demineralization appeared to reach the dentin. A custom-built digital microradiography system was used to measure the volume percent mineral content in the areas of demineralization on the tooth sections [106]. High-resolution microradiographs were taken using Cu K α radiation from a Philips 3100 x-ray

generator and a Photonics Science FDI x-ray digital imager, Microphotonics (Allentown, Pennsylvania). The x-ray digital imager consisted of a 1392×1040 pixel interline CCD directly bonded to a coherent microfiber-optic coupler that transfers the light from an optimized gadolinium oxysulfide scintillator to the CCD sensor. The pixel resolution was $2.1\text{-}\mu\text{m}$ and the images were acquired at 10 frames per second. A high-speed motion control system with Newport UTM150 and 850G stages and an ESP 300 controller coupled to a video microscopy and a laser targeting system was used for precise positioning of the samples in the field of view of the imaging system.

3.4 Results

Examples of reflectance images taken from one of the samples with both light stain and occlusal demineralization are shown in Fig. 3.3. The visible (color) light image in Fig. 3.3(a) shows white areas in the grooves indicative of demineralization and some darker discolored areas in the grooves due to stains. The small red and green boxes in Fig. 3.3(a) demarcate the areas on the tooth surface used to calculate I_L and I_S , respectively. The QLF image in Fig. 3.3(c) shows dark areas that correspond to lesion areas. NIR reflectance images are shown in the last four images of Fig. 3.3 and areas of demineralization all appear whiter than the surrounding sound enamel. The tooth was sectioned at the position of the two thin black lines shown in Fig. 3.3(a) and PLM and TMR images of that cut section are shown in Figs. 3.3(b) and 3.3(d), respectively. The darker areas in the PLM and TMR images indicate areas of demineralization, and there is extensive demineralization in the occlusal groove penetrating to the dentin.

A second tooth with extensive staining and minimal demineralization is shown in Fig. 3.4. In the visible (color) image [Fig. 3.4(a)], the tooth looks somewhat similar to the tooth in Fig. 3.3 with extensive staining in fissure areas; however, there are no whiter areas visible indicative of demineralization. The darkest most severely stained fissure area is in the position of the small red box located in between the two thin black lines in Fig. 3.4(a). The small red and green boxes in Fig. 3.4(a) demarcate the areas on the tooth surface used to calculate I_L and I_S , respectively. The darker fissures areas in Fig. 3.4(a) also appear dark in the QLF image [Fig. 3.4(c)] and in the shorter wavelength NIR reflectance image at 850-nm [Fig. 3.4(e)]. The longer wave-length NIR reflectance image at 1300-nm [Fig. 3.4(f)] shows only very minor whiter areas indicative of demineralization in a few of the fissures; however, there is no demineralization visible in the area of the red box shown in Fig. 3.4(a). Beyond 1675-nm [Figs. 3.4(g) and 3.4(h)], there is still no demineralization (whiter areas) visible in the marked fissure area (red box). Note that some of the white spots around the outside of the tooth in Figs. 3.4(g) and 4(h) are due to specular reflection and not demineralization. High extinction ratio polarizers operating at wave-lengths beyond 1700-nm have only become recently available, and the extinction ratio was lower for wavelengths beyond 1700-nm. Specular reflection changes with a slight tilt of the tooth while the reflectivity of demineralization remains stable so the specular reflection is easily differentiated from demineralization. In addition, the intensity of specular reflection is strongly affected by rotation of the polarizer compared to the actual areas of demineralization. The tooth was sectioned at the position of the two thin black lines, and the center of the fissure in the PLM micrograph of Fig. 3.4(b) corresponds to the position of the red box in Fig. 3.4(a). The PLM micrograph shows that there is a dark mass of

organic material (stain) filling the fissure; however, the fissure walls are completely intact and there is no demineralization visible on the walls. The TMR image of the same section [Fig. 3.4(d)] is of a higher magnification, matching the area of the white box in the PLM image of Fig. 3.4(b). The dark mass in the fissure is not visible in the TMR image suggesting it has a mineral density of zero and is likely organic matter, i.e., stain or noncalcified plaque. It is remarkable that it was possible to cut a section only 200- μm thick of the tooth without loss of the mass of organic matter in the fissure. In addition, the tooth while the reflectivity of demineralization remains stable so the specular reflection is easily differentiated from demineralization. In addition, the intensity of specular reflection is strongly affected by rotation of the polarizer compared to the actual areas of demineralization. The tooth was sectioned at the position of the two thin black lines, and the center of the fissure in the PLM micrograph of Fig. 3.4(b) corresponds to the position of the red box in Fig. 3.4(a). The PLM micrograph shows that there is a dark mass of organic material (stain) filling the fissure; however, the fissure walls are completely intact and there is no demineralization visible on the walls. The TMR image of the same section [Fig. 3.4(d)] is of a higher magnification, matching the area of the white box in the PLM image of Fig. 3.4(b). The dark mass in the fissure is not visible in the TMR image suggesting it has a mineral density of zero and is likely organic matter, i.e., stain or noncalcified plaque. It is remarkable that it was possible to cut a section only 200- μm thick of the tooth without loss of the mass of organic matter in the fissure. In addition, the TMR image also indicates that the walls of the fissure are intact and that there is no demineralization present.

The mean lesion contrast (reflectance) \pm standard deviation for all the 55 teeth of group 1 is plotted in Fig. 35 for visible, 850-nm, 1150-nm, 1300-nm, 1460-nm, 1675-nm, and 1695-nm to 2350-nm wavelengths. The mean contrast was highly negative, -1.85 ± 2.7 , for visible/NIR (400-nm to 1000-nm) and also negative for 850-nm. The contrast increased with increasing wavelength and was highest for 1695-nm to 2350nmnm, where it was 0.68 ± 0.21 . All the groups were significantly different from each other ($P < 0.01$). The lesion contrast for fluorescence (QLF) was 0.48 ± 0.18 , which was significantly lower than the contrast at 1695-nm to 2350-nm. The mean lesion contrast \pm sd for the early lesions (E1) of group 1 that are limited to the outer enamel ($n = 11$) is plotted in Fig. 3.6. The same trend with wavelength is observed although the contrast is lower for each wavelength. A similar plot of the more severe lesions of group 1 that have penetrated to dentin (D lesions, $n = 14$) also shows the same trend albeit with higher lesion contrast. NIR occlusal transillumination and reflectance images of tooth occlusal surfaces were acquired of a second group of 25 teeth before and after stain removal with an ultrasonic scaler. Filters centered at 830-nm, 1150-nm, 1300-nm, 1380-nm, and 1550-nm (1500-nm to 1600-nm) were used to segregate the NIR region for each corresponding image. Sample images of a tooth that has stained fissures with shallow demineralization present under the stain along with interproximal lesions are shown in Fig. 3.7 before and after stain removal. In transillumination, both the stain and demineralization appear dark. At 830-nm, most of the dark areas are removed after scaling; however, at 1380-nm, there is little change since the stain is not visible. In reflectance, the stain appears darker and the demineralization appears whiter. Note how the interproximal lesion appears dark in transillumination and white in reflectance. At 830-nm, the fissures appear very dark due

to the strong absorption by the stain. At 1380-nm and 1550-nm, the stain is not visible and the demineralization under the stain is clearly visible as whiter areas in the fissures. The contrast of the demineralization is highest at 1550-nm. After scaling, most of the dark areas at 830-nm are no longer visible and some of the underlying demineralization can now be seen. At 1550-nm after scaling some of the whiter areas have been removed, this suggests that the scaler also removed some of the demineralization and that the demineralization present was fairly shallow.

Plots of the mean lesion contrast \pm sd versus wavelength measured for the second group of 25 samples before and after stain removal are shown in Fig. 3.8 for NIR reflectance and NIR occlusal transillumination.

The greatest changes in contrast in the images for NIR occlusal transillumination occur at 830-nm and 1150-nm while there is little change at the longer wavelengths of 1300 and 1380-nm after removal of the stain. Even at 830-nm, after the aggressive use of an ultrasonic scaler to remove the stain, it was still visible in most of the samples. The magnitude of the change falls off significantly when the imaging wavelength is increased to 1150-nm. There was a significant difference ($P < 0.05$) in the change in lesion contrast before and after stain removal at 830-nm and 1150-nm. The change with lesion removal was smaller and was no longer significant at 1300-nm and 1380-nm. In contrast to reflectance, in NIR transillumination, stain and demineralization both reduce the intensity so that it is not possible to differentiate between them.

The NIR reflectance images appear similar to those observed in NIR transillumination where the stain is visible at 830-nm and 1150-nm before removal and most of it vanishes

after removal, although there is also some stain still visible at 830-nm after removal. Some whiter areas in the fissures due to demineralization become visible in reflectance at 1300-nm and 1380-nm before and after stain removal, and there are only small changes after removal. However, at 1550-nm, the demineralization is clearly visible before removal. The mean contrast decreased after stain removal indicating that the ultrasonic scaler actually removed some demineralized enamel in addition to removing the stain. For NIR reflectance, there was a significant difference in contrast before and after stain removal for 830-nm, 1150-nm, and 1550-nm. The contrast was negative for 83-nm and 1150nm before stain removal indicating the contrast at these wavelengths was dominated by stains. The mean lesion contrast remained negative even after lesion removal at 830-nm; however, the contrast flipped to positive at 1150-nm after removal. The contrast was positive at 1300-nm, 1380-nm, and 1550-nm, and it decreased with stain removal as opposed to increasing with 830-nm and 1150-nm.

3.5 Discussion

The occlusal surfaces of posterior teeth typically have stains in the pits and fissures of the occlusal surface that interfere with visual diagnosis and fluorescence-based caries detection systems. Manufacturers advise thoroughly cleaning the pits and fissures before taking measurements; however, a thorough removal of all stain from the pits and fissures is obviously not feasible. In this study, it was necessary to use an ultrasonic scaler to remove most of the stains. Such an invasive system is too destructive and aggressive for clinical use, and even after use there was still sufficient stain remaining to mask the demineralization at 830-nm.

The lesion contrast measurements presented in Fig. 3.5 indicate that the lesion contrast continues to increase beyond 1700-nm (1695-nm to 2350-nm), where there is decreasing light scattering in the sound enamel and there is increasing light absorption by water (Fig. 3.1). Current NIR imaging devices on the market for caries detection operate at 780-nm and 850-nm, where these studies show that there is significant interference from stains. In addition, the contrast between sound and demineralized tooth structure is markedly higher at longer NIR wavelengths than it is at 850-nm. The primary disadvantage of operating at longer NIR wavelengths is that Si-based imaging technologies are only efficient at wavelengths under 1000-nm. Alternative imaging technologies such as InGaAs and Ge-enhanced Si are still expensive. Less expensive scanned NIR LED and NIR diode light sources and galvanometer or MEMS-based scanning systems are also feasible. The limited use of these more innovative semiconductor technologies is a major reason for the high cost. However, with expanded use, those prices are expected to decrease. The cost has decreased significantly in the past 10 years and the performance has increased markedly. Using the newly available extended range InGaAs imaging array sensitive beyond 1700-nm, we have demonstrated that even higher lesion contrast is attainable at longer NIR wavelengths. Imaging at longer wavelengths beyond 1700-nm may also be advantageous for assessing lesion activity by looking at the lesion contrast during drying since the longer wavelengths are more sensitive to changes in water. Since many of the caries imaging devices use fluorescence, we compared our results with QLF. QLF is highly effective for increasing image contrast on tooth surfaces since there is no interference from specular reflectance. However, QLF uses visible light for excitation and the fluorescence is in the visible range so that stains interfere with both excitation and

fluorescence. Demineralization and absorption by stains increase the lesion contrast for QLF and it is not possible to differentiate between the two. Therefore, it is unreliable on tooth surfaces where stains occur. However, even with stains contributing to the positive lesion contrast in QLF, the contrast in NIR reflectance beyond 1700-nm was significantly higher. Stains are also a potential problem for the red or porphyrin-based caries detection systems that employ both blue light and red light for excitation and then image the fluorescence at longer red and NIR wavelengths since stains also interfere at 600-nm to 800-nm.

Using the second group of 25 teeth, it was demonstrated that at NIR wavelengths <1150-nm, the lesion contrast in the occlusal surfaces is masked by interference from stains. At 830-nm, the stain still dominated the lesion contrast in reflectance and the mean contrast was still negative even after extreme measures were taken to remove it. In transillumination at 830-nm, the lesion contrast dropped by almost a factor of 4 after removal. The contrast dropped slightly beyond 1300-nm in transillumination but that is likely due to loss of demineralization. Although we did not directly measure the depth of demineralization before and after removing the stains with the ultrasonic scaler, there is strong evidence that some of the demineralization was also removed in addition to the stains. The mean lesion contrast for reflectance increased markedly (became more positive) at 850-nm and 1150-nm when the stains were removed while that contrast decreased at longer wavelengths, 1300-nm and 1550-nm, where only demineralization contributes to lesion contrast. If there was significant reflectivity

from the stains or plaque on the surface, then we would expect a reduction in the reflectance at all the NIR wavelengths. In addition, we would expect to see an increase in the lesion contrast in transillumination at wavelengths >1300-nm after removal of the stain, not a decrease as was observed. Moreover, images before and after removal for deeper areas of demineralization at 1550-nm do not show as great a change in the lesion area as seen for the tooth shown in Fig. 3.7. Damage occurs only near the surface of the lesion where only shallow and superficial demineralization is removed, deeper lesion areas remain intact.

This study suggests that stains on teeth interfere significantly with the lesion contrast at wavelengths shorter than 1150-nm and imaging wavelengths ranging beyond 1300-nm are not significantly influenced by the presence of stain in the pits and fissures found on occlusal surfaces. Therefore, NIR imaging performed above 1150-nm can detect early demineralization below stained surfaces. In addition, these studies show that the contrast of demineralization increases significantly at wavelengths beyond 1700-nm. Therefore, based on these and previous studies, it appears that wavelengths near 1300-nm where light scattering and water absorption are both low are best for NIR transillumination while wavelengths beyond 1700-nm where light scattering is low and water absorption is high are best for NIR reflectance measurements.

3.6 Figures

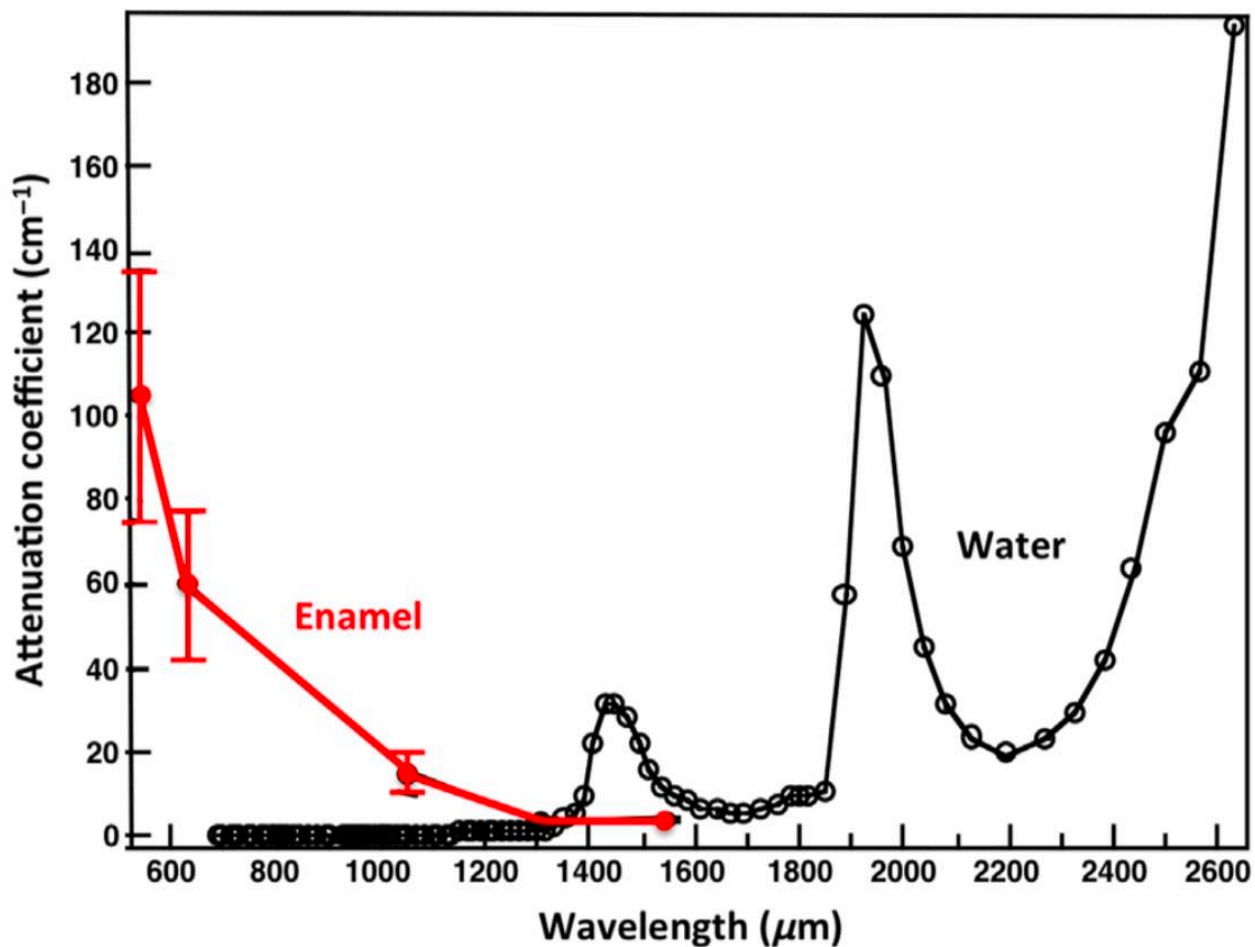


Figure 3.6.1. The attenuation coefficient for dental enamel (red) and the absorption coefficient of water (black) in the visible and NIR.

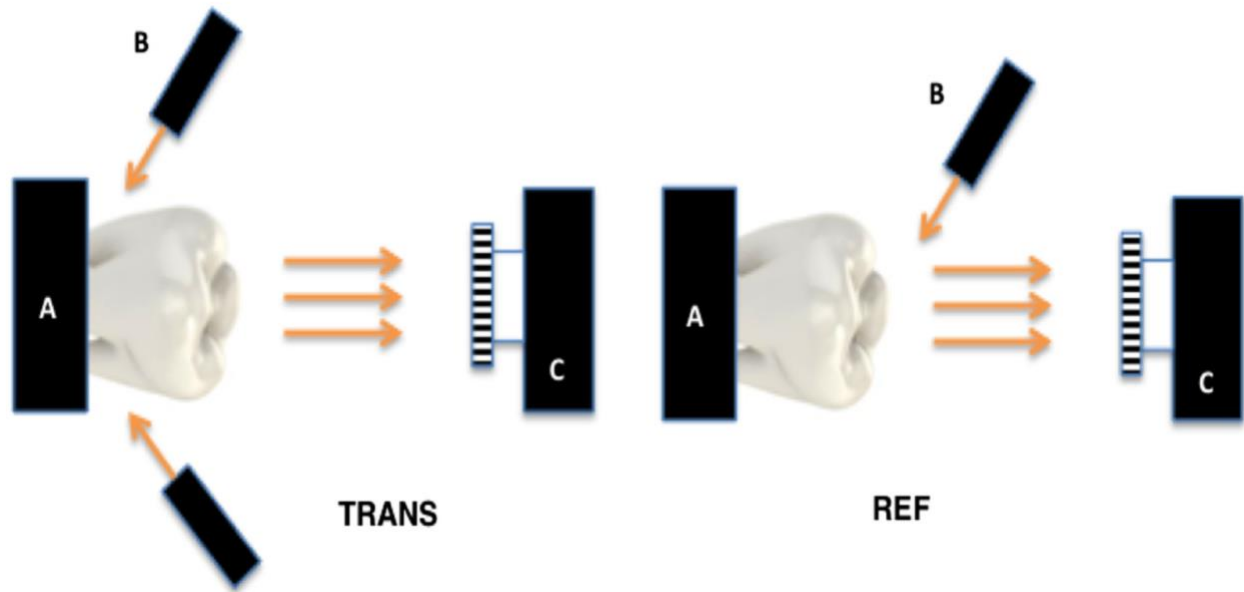


Figure 3.6.2. Imaging configurations for (TRANS) NIR occlusal transillumination and (REF) cross-polarized reflectance with (A) tooth, (B) light source, and (C) imaging camera.

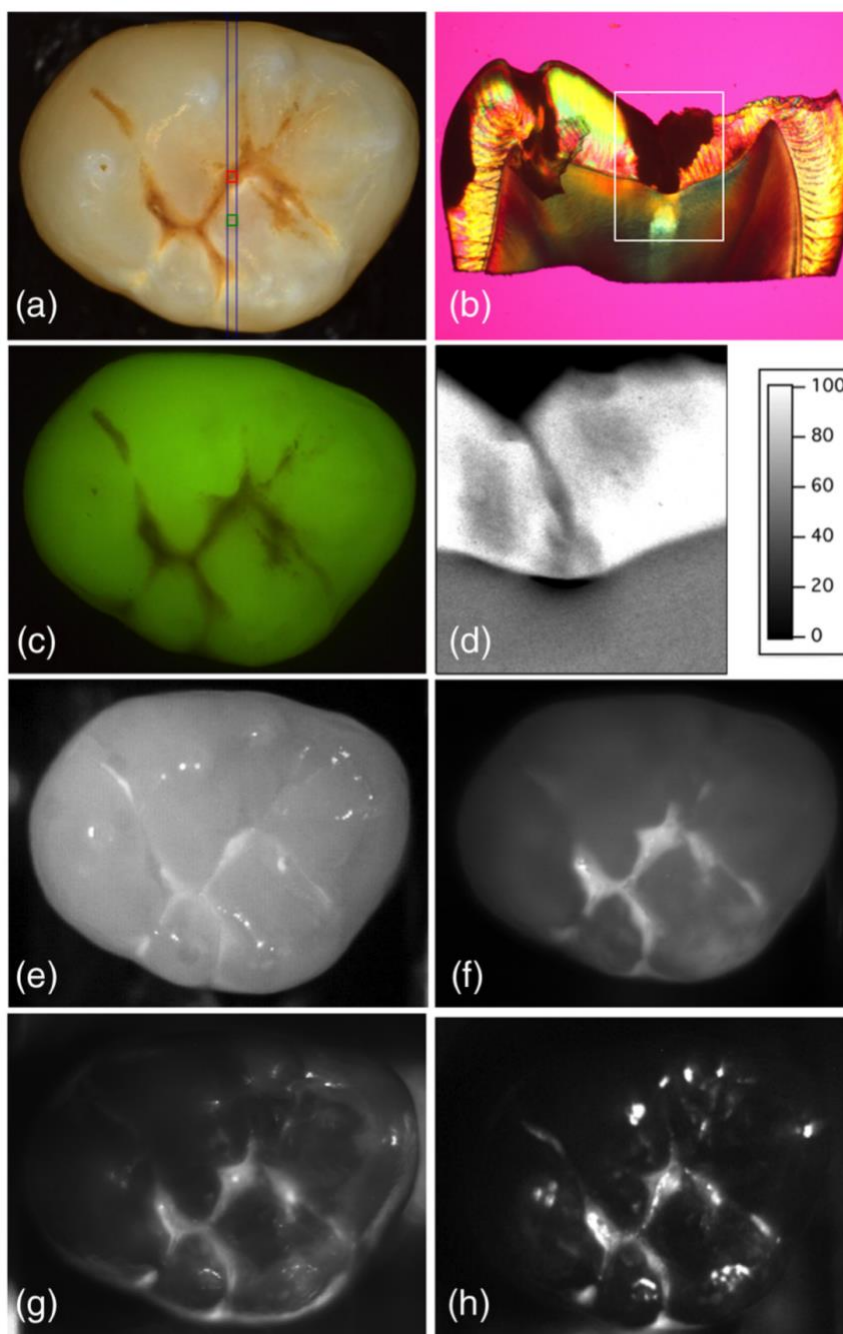


Figure 3.6.3. Images of a tooth from group 1 with demineralization in the fissure. (a) visible (color), (b) PLM image cut at the position of the two fine blue lines in (a), (c) QLF, TMR measurements of the % mineral compared to sound enamel for a region marked in the PLM image (d), NIR reflectance at (e) 850-nm, (f) 1300-nm, (g) 1675-nm, and (h) 1695-nm to 2350-nm. The upper red and lower green boxes mark the area chosen for lesion and sound for the contrast calculations, respectively.

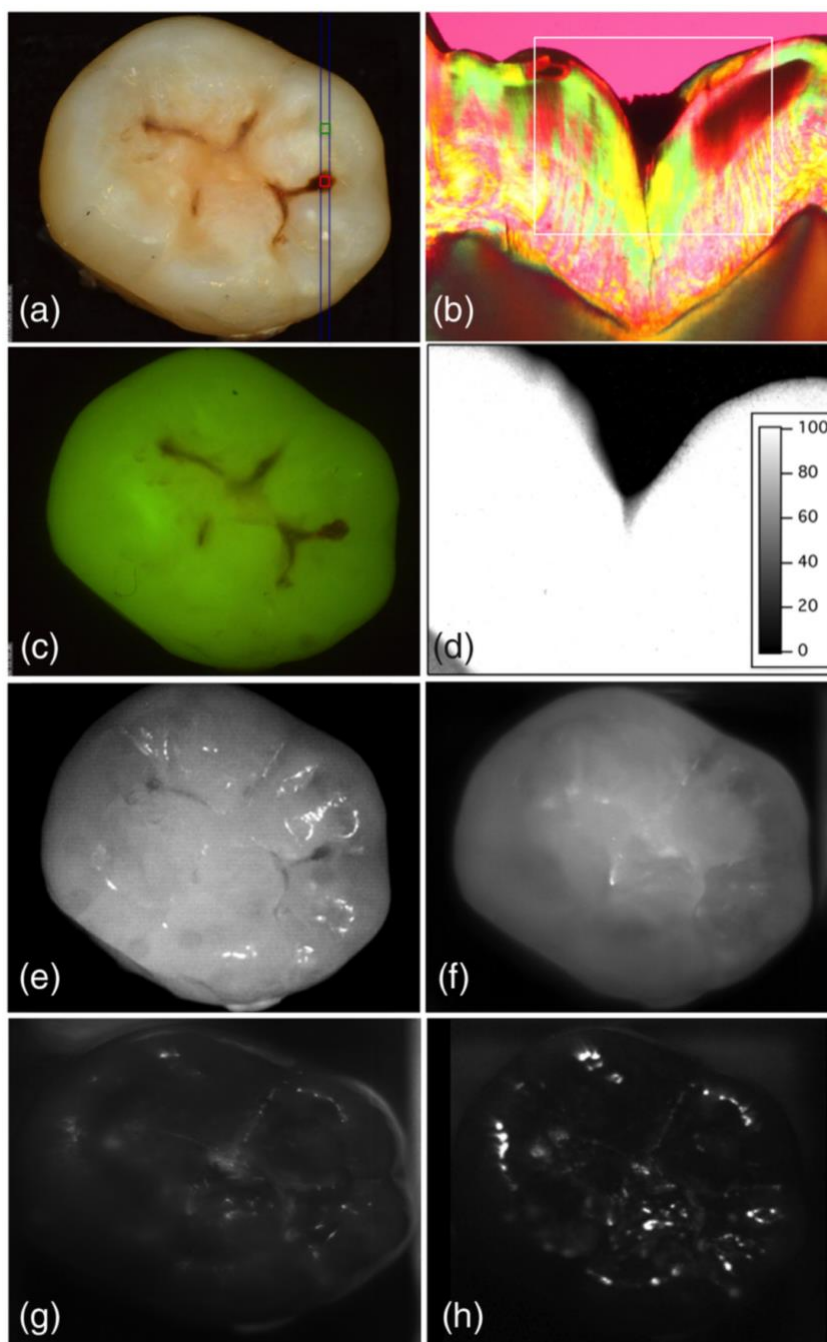


Figure 3.6.4. Images of another tooth from group 1 without demineralization in the fissure. (a) visible (color), (b) PLM image cut at the position of the two thin blue lines in (a), (c) QLF, TMR measurements of the % mineral compared to sound enamel for a region marked in the PLM image (d), NIR reflectance at (e) 850-nm, (f) 1300-nm, (g) 1675-nm, and (h) 1695-nm to 2350-nm. Only stain is visible suspended in the occlusal pit. The lower red and upper green boxes mark the area chosen for lesion and sound for the contrast calculations, respectively.

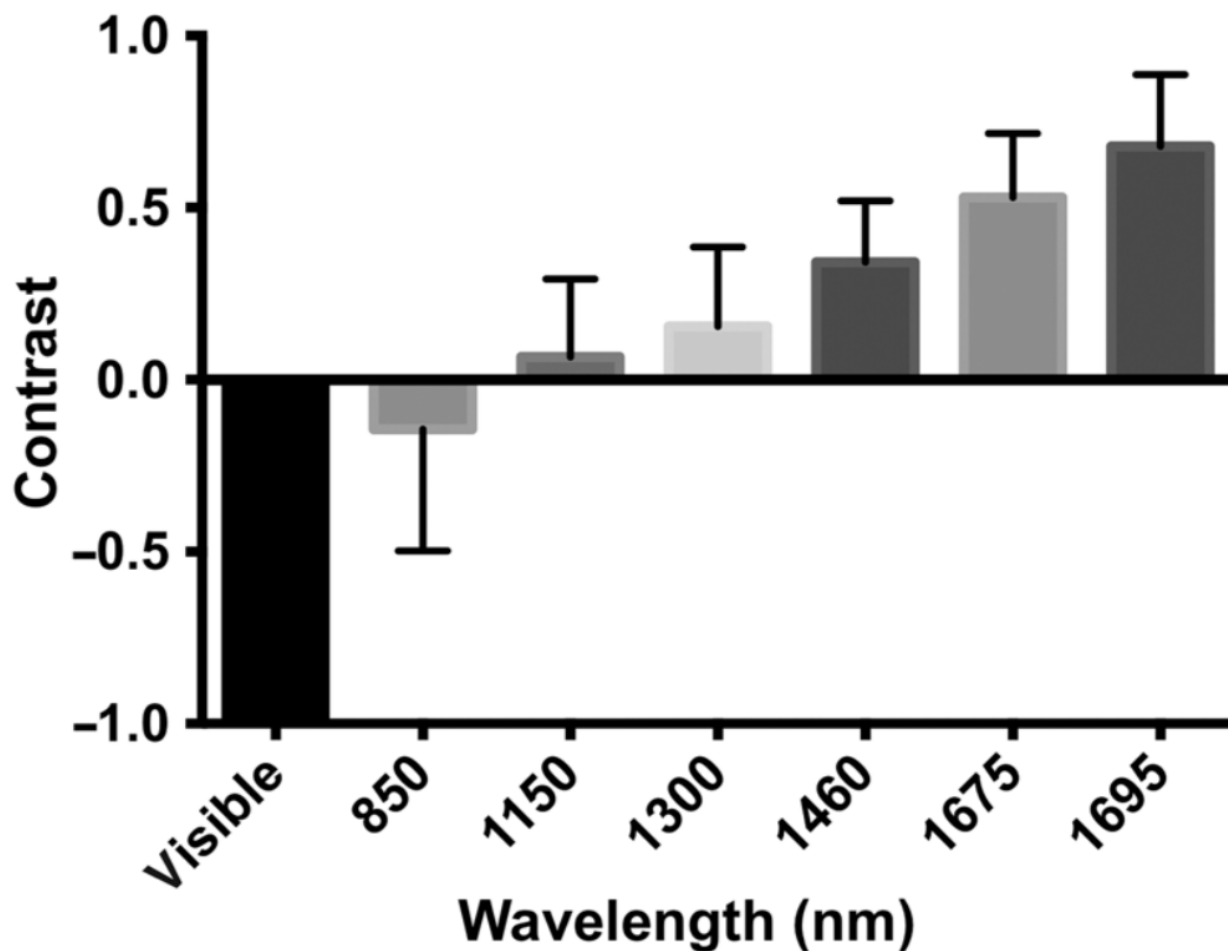


Figure 3.6.5. The mean lesion contrast \pm sd for the 55 teeth in group 1: 400-nm to 1000-nm, 850-nm, 1150-nm, 1300-nm, 1460-nm, 1675-nm and 1695-nm to 2350-nm wavelengths are shown. All the groups are significantly different ($P < 0.01$). The mean contrast in the visible is -1.85 ± 2.7 and extends beyond the graph.

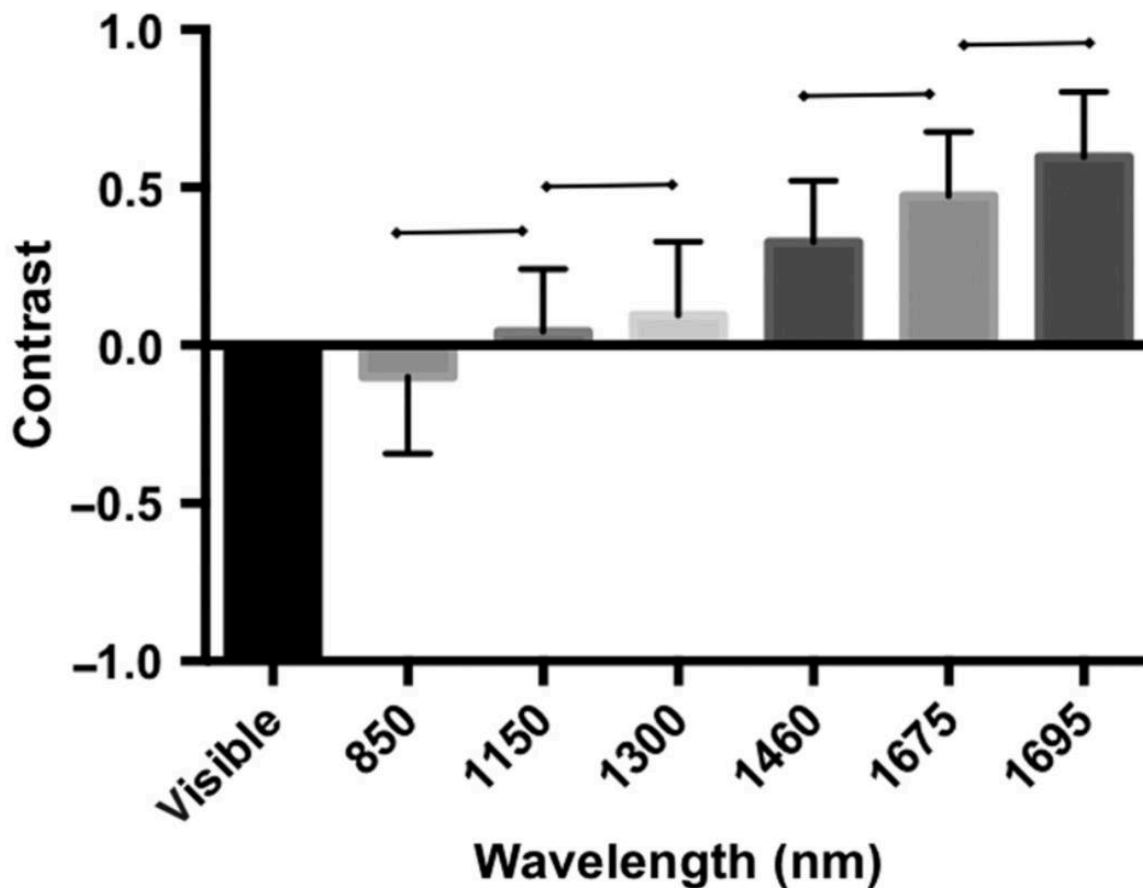


Figure 3.6.6. The mean lesion contrast \pm sd for the 11 teeth in group 1 that were limited in depth to the first half of enamel, E lesions: 400-nm to 1000-nm, 850-nm, 1150-nm, 1300-nm, 1460-nm, 1675-nm and 1695-nm to 2350-nm wavelengths are shown. Groups with a connecting line above are statistically similar ($P > 0.05$). The mean contrast in the visible is -1.4 ± 1.4 and extends beyond the graph.

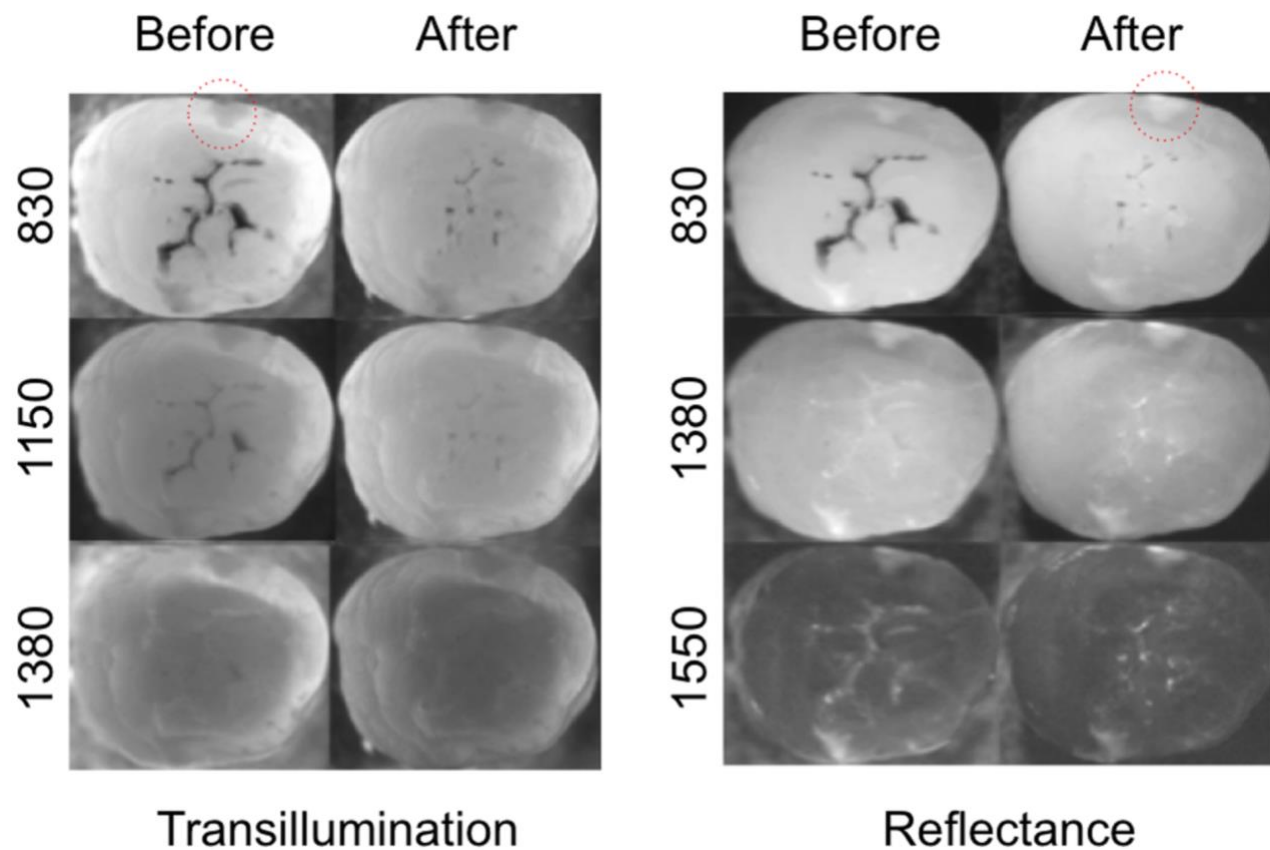


Figure 3.6.7. Sample NIR transillumination and NIR reflectance images from a tooth of the group 2 samples before and after stain removal with the cavitrone at different wavelengths. An interproximal lesion is also present on the tooth in the area of the red circle.

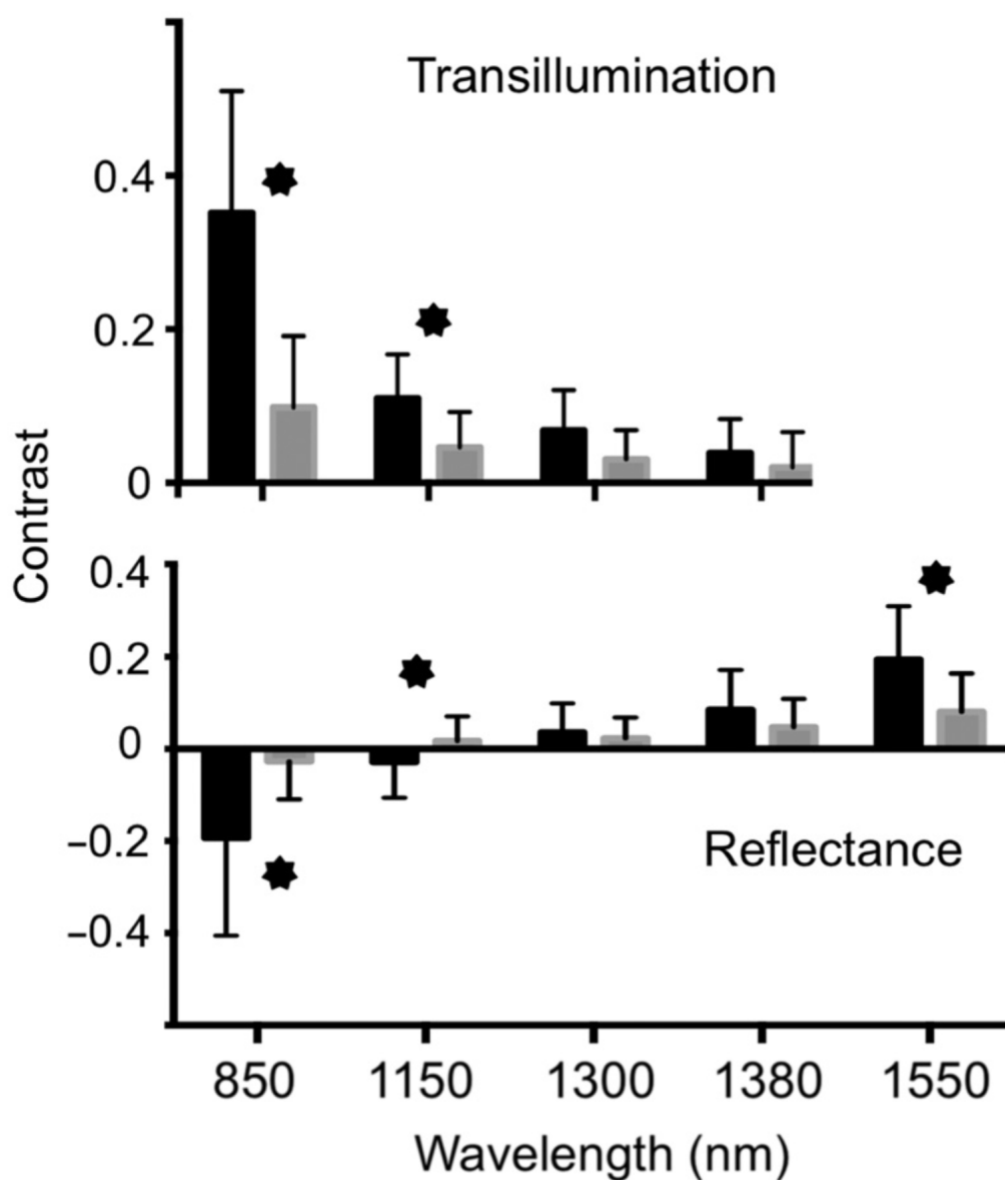


Figure 3.6.8. The mean lesion contrast \pm sd for NIR reflectance and transillumination of the 25 teeth in group 2 before and after stain removal with the cavivron. Wavelengths of 830-nm, 1150-nm, 1300-nm, 1380-nm, and 1550-nm are shown. Groups for which the contrast changed significantly ($P < 0.05$) after stain removal have an asterisk.

CHAPTER IV

Multispectral Near-Infrared Reflectance and Transillumination Imaging of Occlusal Carious Lesions: Variations in Lesion Contrast with Lesion Depth

4.1 Summary

In vivo and *in vitro* studies have demonstrated that near-infrared (NIR) light at $\lambda=1300$ - 1700 -nm can be used to acquire high contrast images of enamel demineralization without interference of stains. The objective of this study was to determine if a relationship exists between the NIR image contrast of occlusal lesions and the depth of the lesion. Extracted teeth with varying amounts of natural occlusal decay were measured using a multispectral-multimodal NIR imaging system which captures $\lambda=1300$ -nm occlusal transillumination, and $\lambda=1500$ - 1700 -nm cross-polarized reflectance images. Image analysis software was used to calculate the lesion contrast detected in both images from matched positions of each imaging modality. Samples were serially sectioned across the lesion with a precision saw, and polarized light microscopy was used to measure the respective lesion depths relative to the dentinoenamel junction. Lesion contrast measured from NIR cross-polarized reflectance images positively correlated ($p<0.05$) with increasing lesion depth and a statistically significant difference between inner enamel and dentin lesions was observed. The lateral width of pit and fissures lesions measured both in NIR cross-polarized reflectance and NIR transillumination positively correlated with lesion depth.

4.2. Introduction

The most recent epidemiological data gathered from the National Health and Nutritional Survey (NHANES) [29, 30] and Dental Practice-Based Research Network (DPBRN) [31-33] indicates that nearly one third of all patients have a questionable occlusal carious lesion (QOC) located on a posterior tooth. QOC's are given the name "questionable"

because presently, clinicians' lack instrumentation capable of measuring the depth of pit and fissure lesions and determining if the dental decay has reached the underlying dentin. Digital x-rays are not sensitive enough to these occlusal lesions, and visible diagnosis is confounded by stain trapped in the occlusal anatomy. A clinical study we performed in 2017 demonstrated that near infrared (NIR) reflectance images at $\lambda=1500-1700$ nm yielded significantly higher contrast of the demineralization in the occlusal grooves compared with visible reflectance imaging. Stains in the occlusal grooves reduced the lesion contrast in the visible range yielding negative values. Additionally, only half of 26 lesions diagnosed as carious lesions and requiring restoration showed the characteristic surface demineralization and increased reflectivity below the dentinoenamel (DEJ) in 3D OCT images indicative of penetration into the dentin [107]. These results indicated that near infrared imaging holds great potential for the assessment of occlusal lesion depth, due to the high transparency of enamel and stain to light at $\lambda=1300-1700$ -nm, which allows direct visualization and quantified measurements of enamel demineralization.

The development of NIR imaging has produced three distinct imaging modalities that have been tested *in vivo* and directly compared with digital x-rays on matched teeth [26-28, 45]. These three modalities namely, cross-polarized reflectance, interproximal transillumination and occlusal transillumination were built into hand held intraoral probes and acquire high resolution diagnostic images of teeth by capturing light ranging from $\lambda=300-1700$ -nm with an InGaAs camera [45]. Previous *in vitro* studies demonstrated that images from this spectral region provides the greatest contrast between sound and

demineralized enamel due to marked changes in the tissues optical properties that occur upon enamel demineralization[108].

The data collected from the clinical studies demonstrated that despite NIR imaging's superior performance in detecting early occlusal decay, NIR reflectance measurements alone are limited in utility for approximating occlusal lesion depth beyond >200- μm due to light attenuation from the lesion body [45, 109]. Additionally, both NIR reflectance and occlusal transillumination were valuable in combination for the identification of potential false positives when used for subjective diagnosis by a trained clinician. Prior *in vitro* studies attempted to combine NIR reflectance and transillumination measurements taken at $\lambda=1300\text{-nm}$ in order to estimate QOC depth [7, 77]. Since, multispectral NIR reflectance and transillumination experiments have demonstrated that the tooth appears darker at wavelengths coincident with increased water absorption, multispectral images can be used to produce increased contrast between different tooth structures such as sound enamel and dentin, dental decay and composite restorative materials[51, 110, 111]. Combining measurements from different NIR imaging wavelengths and comparing them with concurrent measurements acquired by complementary imaging modalities should provide improved assessment of lesion depth and severity.

The objective of this study was to quantify the relationship between lesion contrast and lesion depth using a new imaging system that combines multispectral near-IR reflectance and occlusal transillumination imaging modalities into a single device for the imaging of QOC's.

4.3. Materials and Methods

4.3.1 Sample Preparation

Posterior teeth (n=37) were selected with sound or demineralized occlusal grooves/surfaces for participation in this study. Teeth were collected from patients in the San Francisco Bay area with approval from the UCSF Committee on Human Research. The teeth were sterilized using gamma radiation and stored in 0.1% thymol solution to maintain tissue hydration and prevent bacterial growth. Samples were mounted in black orthodontic resin in order to facilitate repeatable imaging angle and orientation.

4.3.2 Visible Images

A Dino-Lite digital microscope, Model 5MP Edge AM7915MZT, AnMO Electronics Corp. (New Taipei City, Taiwan) equipped with a visible polarizer was used to acquire visible images of all samples. The digital microscope captures 5 mega-pixel (2,952 x 1,944) color images. Eight white LED lights contained in the camera illuminate the sample and a single polarization element is utilized to help reduce glare.

4.3.3 Combined NIR Occlusal Transillumination and Cross-Polarized Reflectance Imaging System

A high sensitivity, InGaAs, SWIR camera (SU640CSX) from Sensors Unlimited (Princeton, NJ), with a 3320x256-pixel focal plane array and 12.5- μm pixel pitch was used to capture NIR cross-polarized reflectance and occlusal transillumination images of posterior teeth *in vitro* [112, 113]. Sample images were illuminated with filtered light from

a two broadband tungsten halogen lamps (E Light) delivered through separate reflectance and transillumination fiber optic cable bundles. Reflectance illumination was achieved using a ring light from Volpi (Auburn, NY) equipped with a toroidal NIR linear polarizer custom made from a 3x3-inch polarizing sheet (Edmund Scientific, Barrington, NJ). Occlusal transillumination used a quadfurcated fiber optic bundle to deliver unpolarized light angled apically at the cemento-enamel junction from both sides (buccal/lingual) of the tooth. The near-IR camera lens system was equipped with an orthogonal linear polarizer from Thorlabs (Newtown, NJ) to produce cross-polarized reflectance images with greatly reduced specular reflection.

The outputs of both broadband light sources were filtered with optical filters housed in a two motorized filter wheels, FW102 from Thorlabs. The reflectance filter wheel contained long pass $\lambda=1500$ -nm filters from Spectragon (Parsippany, NJ) and the occlusal transillumination filter wheel contained long pass $\lambda=1200$ -nm from Thorlabs. Each filter wheel also contained an aluminum disk (3-mm thick) used to block the light source providing on/off functionality to the multimodal system. Detailed schematics covering the geometry of each modality and theory of the resulting image contrast can be found in previous publications [112, 113]. Image data (12-bit) was delivered over a camera link cable to a Real Time PXIe-1071 chassis with NI-8133 embedded controller and NI-1428 frame grabber from National Instruments (Austin TX). A host computer, iMac (Retina 5K, 27-inch, Late 2015) (Apple, Cupertino, CA) running bootcamp and Windows 10 is used to control the Real Time PXIe.

4.3.4 Sectioning and Polarized Light Microscopy (PLM)

Samples were serially sectioned in to ~200- μm thick slices using a linear precision saw, Isomet 5000 (Buehler, Lake Buff, IL). Thin sections containing the pit or fissure of interest were subjected to histological examination. Polarized light microscopy (PLM) was used for histological examination using a Meiji Techno RZT microscope (Saitama, Japan) with integrated digital camera, Canon EOS Digital Rebel XT (Tokyo, Japan). Sample sections ~200- μm thick were imbibed in deionized water and examined in the bright field mode with crossed-polarizers and a red I plate (500-nm retardation).

Lesions were examined and classified according to the lesion depths: (E1) less than halfway through the enamel thickness, (E2) more than halfway through the enamel thickness, and (D) penetrating the dentinoenamel junction. The actual lesion depth and the percent penetrance (lesion depth/enamel thickness) was measured using a standard reticle slide and image analysis package, IgorPro from Wavemetrics (Lake Oswego, OR).

4.3.5 Near-Infrared Image Analysis

The lesion contrast was calculated for a single carious region of interest (ROI) matched on registered reflectance and transillumination images. Image analysis package, IgorPro was utilized to extract image line profiles 10-pixels in width through the ROI. The maximum (reflectance) or minimum (transillumination) value from the image line profile was used to calculate the lesion contrast with the formulas: reflectance = $(I_L - I_S) / I_L$ and transillumination = $(I_S - I_L) / I_S$. These formulas normalize the percent contrast from 0-1. The lesion width was measured using the Spatial Measurement package in Igor Pro.

Measurements of the lesion were acquired in the direction perpendicular to the direction of the groove in order to determine the lateral spread of the lesion.

4.3.6 Statistical Analysis

InStat statistical software from GraphPad (San Diego, CA) was used for one-way analysis of variance (ANOVA) followed by Tukey-Kramer post-hoc multiple comparison test.

4.4. Results and Discussion

Natural extracted human posterior teeth (n=37) were imaged in cross-polarized reflectance from $\lambda=1500-1700$ -nm and the occlusal transillumination from $\lambda=1200-1700$ -nm *in vitro* using a multimodal-multispectral imaging apparatus equipped with an InGaAs camera. Samples were serially sectioned with a precision wet saw and analyzed for enamel lesion depth with polarized light microscopy (PLM). An independent examiner blinded to the NIR sample images utilized PLM data to stratify the lesions by depth into E1-outer half of enamel (n=7), E2-inner half of enamel (n=11), and D-penetrating into dentin (n=19) (Table 4.1). Sample lesion depths were measured using PLM images yielding group averages of E1=0.33±0.19-mm, E2=1.19±0.27-mm, and D=1.62±0.32-mm. To account for the limitation that PLM lesion depths are only reliable through the enamel a metric termed, “lesion penetrance” was calculated by dividing the measured lesion depth by the enamel depth at the analyzed location to scale the lesions from 1-100%. The stratified mean lesion penetrance values are shown in Table 4.1.

The lesion contrast measured from NIR images was calculated by relating the intensity of sound tooth structure (I_s) to the intensity of the suspected lesion (I_L) using the formulas: reflectance = $(I_L - I_s) / I_L$ and transillumination = $(I_s - I_L) / I_s$. I_s was calculated using two different methods for NIR reflectance. The traditional method (sound), uses the mean intensity from a region enamel on an unaffected surface that is hand selected by the operator using image processing software. An alternative method (total) utilizes all pixels from the tooth and is therefore easily automated. The total method was previously proven capable of calculating contrast values in real time and it uses an image processing algorithm to isolate the tooth occlusal surface from its surroundings, and calculate the mean intensity of all pixels contained within the sample [113]. The mean contrast in reflectance calculated using both methods is shown in Table 4.1. The performance of the total method is as successful as the traditional method for early enamel occlusal lesions but as the lesion depth and size increases, the contrast plateaus due to the fact that the fraction of pixels defining the lesion increase for the total mean value set. The total method demonstrated a statistically significant difference in the lesion contrast between E1 and D depth lesions. The sound method demonstrated a statistically significant difference in the lesion contrast between E2 and D depth lesions. Transillumination mean contrast values calculated using the 'sound' method are presented in Table 4.1. No differences in lesion contrast among the stratified samples were detected.

The size of the lesion detected in the NIR reflectance and transillumination images was measured as the pixel quantity in the dimension perpendicular to the direction of the occlusal groove or as a circular diameter in the affect occlusal pit. The lesion boundary

was defined as the pixel where the lesion contrast was less than 10% contrast. Both NIR reflectance and transillumination images demonstrated a statistically significant difference in the lesion width between E2 and D depth lesions (Table 4.1).

Tooth samples were then analyzed based on their measured lesion depths to determine the relationship in lesion contrast as a function of absolute lesion depth in the occlusal-apical (top-bottom) dimension. Figure 4.1 is a graph of the NIR reflectance contrast for both sound and total calculation methods compared to the measured lesion depths. Regression lines for each method are statistically significant ($p < .05$). The sound method typically yields a higher contrast value compared to the total method. The plot demonstrates that NIR reflectance from $\lambda = 1500\text{-}1700\text{-nm}$ is more likely to underestimate the lesion size, most likely due to water absorption within the lesion. Additionally, there is a relative jump in lesion contrast when the lesion is greater than 1-mm in depth.

Figure 4.2 shows the NIR transillumination contrast for sound, total and occlusal calculation methods compared to the measured lesion depths. The occlusal calculation method is analogous to the sound method but it samples a region within the occlusal table where the dentin underlies the sound enamel. The regression lines for each method were not statistically significant. The lack of significance is most likely due to the high contrast values measured from sound (lesion depths $< 0.25\text{-mm}$) samples which can be seen on the left side of Figure 4.2. Even though the groves and fissures of the occlusal anatomy are small in width they are dark relative to the surround sound tooth enamel.

The lateral width of the lesion correlated ($p < 0.05$) with the lesion depth for the NIR cross-polarized reflectance and transillumination images (Figure 4.3). This result is consistent with our findings in other OCT studies where we were able to measure the lateral spread of occlusal lesions when they reached the dentinoenamel junction [7, 26, 107]

In summary, the lesion contrast measured from NIR cross-polarized reflectance images positively correlated ($p < 0.05$) with increasing lesion depth and a statistically significant difference between inner enamel and dentin lesions was observed. The lateral width of pit and fissures lesions measured both in NIR cross-polarized reflectance and NIR transillumination positively correlated with lesion depth.

4.5 Tables and Figures

Table 4.5.1. Sample population statistics stratified by lesion depth into E1(<50% enamel), E1(>50% enamel), and D(dentin) depths (column 1-4). Lesion contrast values for NIR reflectance $\lambda=1500-1700\text{-nm}$ are presented for two calculation methods, “sound” and “total” (column 5-6). Lesion contrast values for NIR transillumination $\lambda=1200-1700\text{-nm}$ are shown for the “sound” method (column 7). The mean lesion width measured in pixels (column 8-9). Letters represent statistical grouping based on ANOVA.

Lesion Category	Sample Size	Mean Lesion Depth (mm)	Mean Lesion Penetrance	Mean Reflectance Contrast (total)	Mean Reflectance Contrast (sound)	Mean Transillumination Contrast (sound)	Mean Reflectance Lesion Width (pixels)	Mean Transillumination Lesion Width (pixels)
E1	7	0.33 ± 0.19	28.3% ± 13.6	10.6% ± 8.71 a	13.7% ± 11.4 a	31.2% ± 20.8 a	4.65 ± 5.31 a	1.6 ± 2.53 a
E2	11	1.19 ± 0.27	77.9% ± 9.72	24.7% ± 20.6 a,b	24.8% ± 23.7 a	26.2% ± 10.9 a	8.8 ± 6.43 a	7.10 ± 4.3 a
D	19	1.63 ± 0.32	100%	28.3% ± 15.4 b	43.5% ± 16.8 b	35.8% ± 13.3 a	22.4 ± 11.2 b	19.4 ± 10.6 b

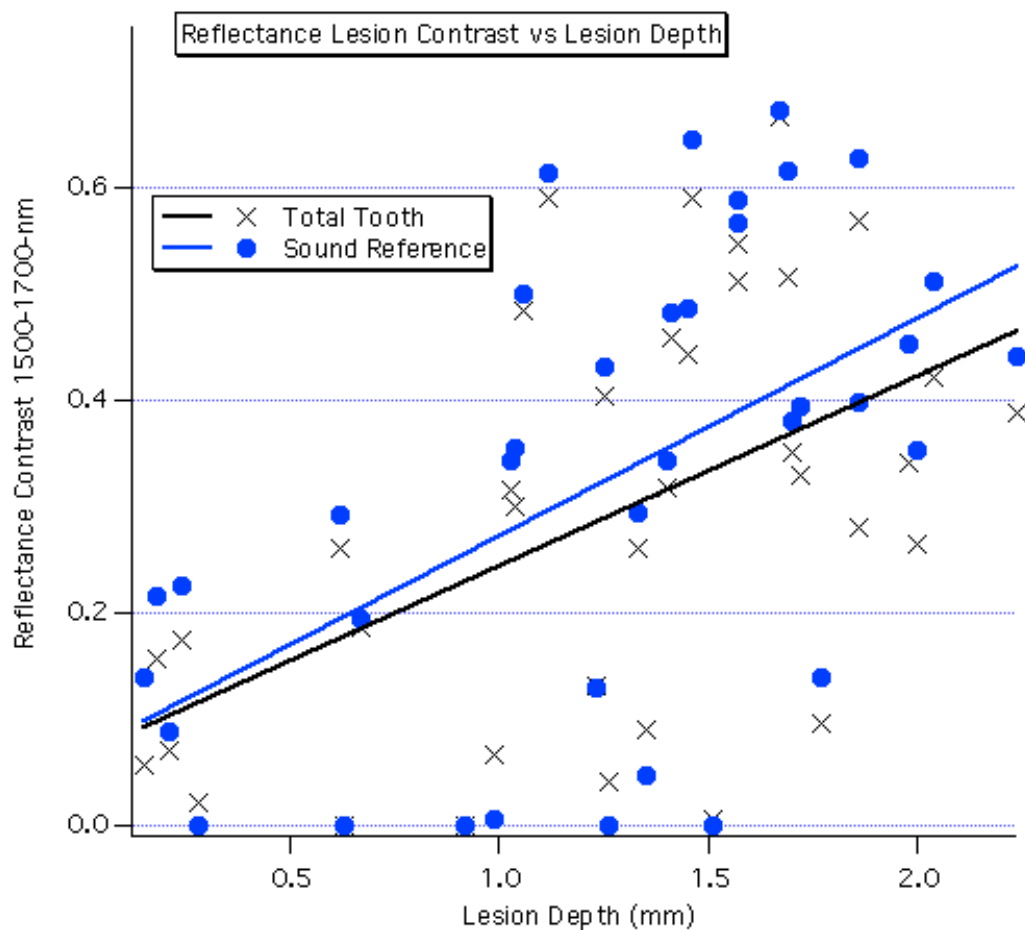


Figure 4.5.1. NIR reflectance contrast values vs. measured lesion depth from PLM histology. Blue circles and blue regression line represent contrast values from the traditional (sound) method. Black (X) and the black regression line represent contrast values from the automated (total) method. Both regressions are statistically significant ($p < 0.05$).

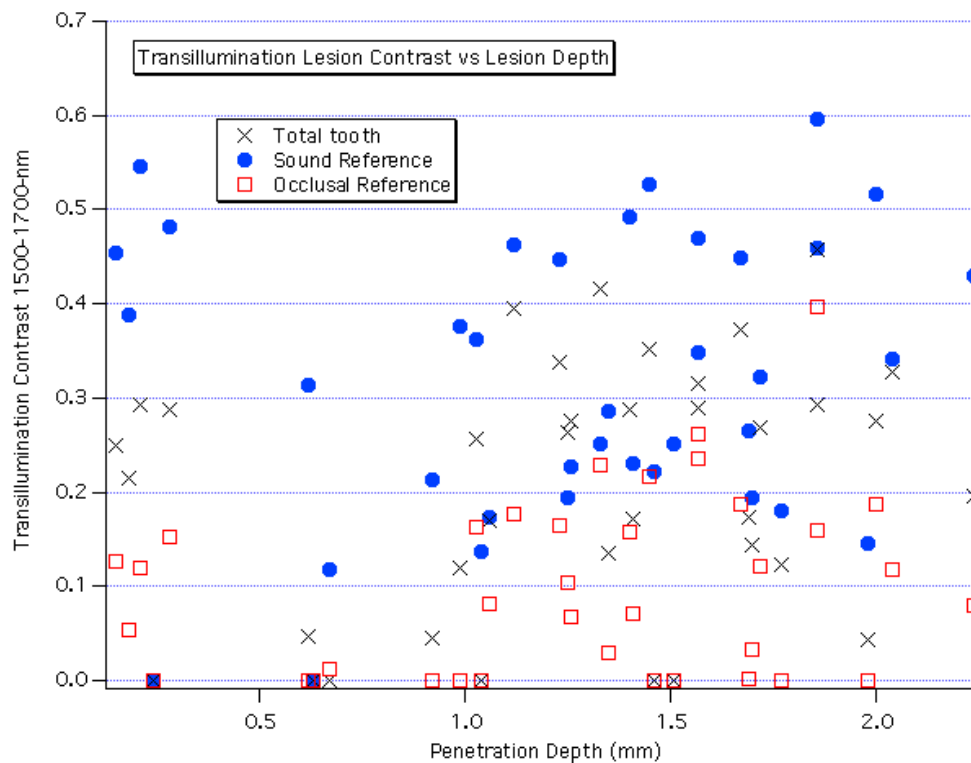


Figure 4.5.2. NIR transillumination contrast vs. measured lesion depth acquired from PLM histology. Blue circles represent contrast values from the traditional (sound) method. Black (X) symbols represent contrast values from the automated (total) method. Red boxes represent values from the occlusal method. Individual regression calculations showed no statistical significance ($p > 0.05$).

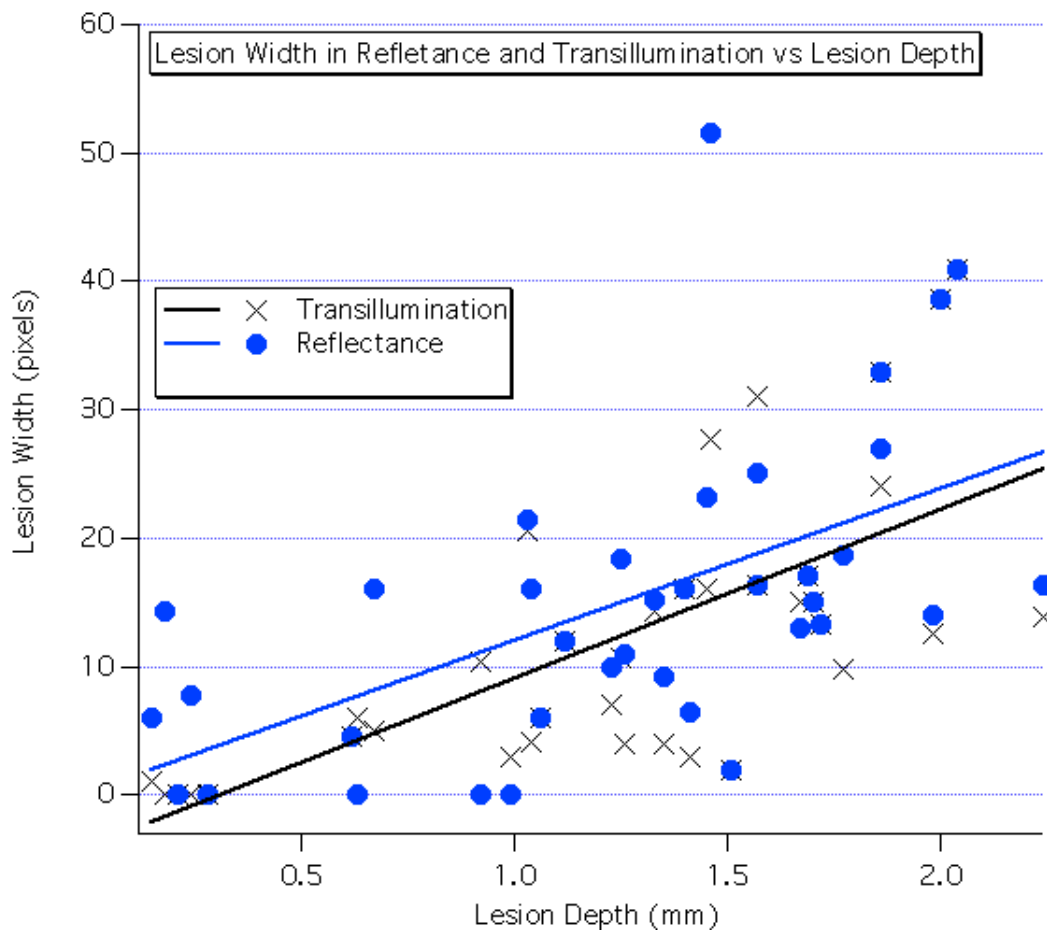


Figure 4.5.3. NIR reflectance and transillumination lesion widths vs. measured lesion depth from PLM histology. Blue circles represent reflectance measurements. Black (X) symbols represent transillumination measurements. Both regressions are statistically significant ($p < 0.05$).

CHAPTER V

A System for Simultaneous Near-Infrared Reflectance and Transillumination Imaging of

Occlusal Carious Lesions

5.1 Summary

Clinicians need technologies to improve the diagnosis of questionable occlusal carious lesions (QOC's) and determine if decay has penetrated to the underlying dentin. Assessing lesion depth from near-infrared (NIR) images holds great potential due to the high transparency of enamel and stain to NIR light at $\lambda=1300\text{--}1700\text{-nm}$, which allows direct visualization and quantified measurements of enamel demineralization. Unfortunately, NIR reflectance measurements alone are limited in utility for approximating occlusal lesion depth $>200\text{-}\mu\text{m}$ due to light attenuation from the lesion body. Previous studies sought to combine NIR reflectance and transillumination measurements taken at $\lambda=1300\text{-nm}$ in order to estimate QOC depth and severity. The objective of this study was to quantify the change in lesion contrast and size measured from multispectral NIR reflectance and transillumination images of natural occlusal carious lesions with increasing lesion depth and severity in order to determine the optimal multimodal wavelength combinations for estimating QOC depth. Extracted teeth with varying amounts of natural occlusal decay were measured using a multispectral-multimodal NIR imaging system at prominent wavelengths within the $\lambda=1300\text{--}1700\text{-nm}$ spectral region. Image analysis software was used to calculate lesion contrast and area values between sound and carious enamel regions.

5.2 Introduction

The development of near-IR imaging technologies for the detection of dental carious lesions has resulted in the fabrication and clinical testing of three distinct imaging modalities [26-28, 46]. These three modalities namely, reflectance, interproximal

transillumination and occlusal transillumination are built into hand held intraoral probes and acquire high resolution diagnostic images of teeth by capturing light ranging from 1300–1700-nm with an InGaAs camera. Images from this spectral region provide the greatest contrast between sound and carious enamel due to marked changes in the tissues optical properties that occur upon enamel demineralization and because this change is so large, early stages of caries progression are easily detected with near-IR light [43].

Clinicians need new technologies that not only can identify early stages of dental caries to facilitate preventative treatment, but also measure lesion depth and determine if the dental decay has reached the underlying dentin to justify restoration. This is most important for lesions located on the tooth occlusal (top) surface, so called questionable occlusal carious lesions (QOC's), where conventional diagnostic methods are very poor. Reports from the National Health and Nutritional Survey (NHANES) [29, 30] and Dental Practice-Based Research Network (DPBRN) [31-33] show nearly one third of all patients have a QOC located on a posterior tooth. Using near-IR images to assess lesion depth holds great potential due to the high transparency of enamel and stain to light at $\lambda=1300\text{--}1700\text{-nm}$, which allows direct visualization and quantified measurements of enamel demineralization. Unfortunately, NIR reflectance measurements alone are limited in utility for approximating occlusal lesion depth beyond $>200\text{-}\mu\text{m}$ due to light attenuation from the lesion body [40, 45, 109]. Previous studies sought to combine NIR reflectance and transillumination measurements taken at $\lambda=1300\text{-nm}$ alone in order to estimate QOC depth and severity and these data showed a correlation between the lesions contrast with depth and lesion area with depth [7, 77].

Recently, multispectral NIR reflectance and transillumination experiments have demonstrated that the tooth appears darker at wavelengths coincident with increased water absorption and multispectral images can be used to produce increased contrast between different tooth structures such as sound enamel and dentin, dental decay and composite restorative materials [51, 110, 114]. Combining measurements from different NIR imaging wavelengths and comparing them with concurrent measurements acquired by complementary imaging modalities should provide improved assessment of lesion depth and severity.

The objective of this study was to design and fabricate a new imaging system that combines multispectral near-IR reflectance and occlusal transillumination imaging modalities into a single device specifically for the detection of QOC's.

5.3 Materials and Methods

5.3.1 Sample Preparation

Posterior teeth were selected with sound or demineralized occlusal grooves/surfaces for participation in this study. Teeth were collected from patients in the San Francisco Bay area with approval from the UCSF Committee on Human Research. The teeth were sterilized using gamma radiation and stored in 0.1% thymol solution to maintain tissue hydration and prevent bacterial growth.

5.3.2 NIR Occlusal Transillumination and NIR Cross-Polarized Reflectance

A high sensitivity, InGaAs, SWIR camera (SU640CSX) from Sensors Unlimited (Princeton, NJ), with a 640×512-pixel focal plane array and 12.5- μm pixel pitch was used

to capture NIR cross-polarized reflectance and occlusal transillumination images of posterior teeth *in vitro*. Sample images were illuminated with filtered light from two broadband tungsten halogen lamps, Model FOI-1 from E Light Company (Denver, CO) delivered through separate reflectance and transillumination fiber optic cable bundles (Fig. 5.1). Reflectance illumination was achieved using a ring light from Volpi (Auburn, NY) equipped with a toroidal NIR linear polarizer custom made from a 3×3-inch polarizing sheet from Edmund Scientific (Barrington, NJ). Occlusal transillumination used a quadfurcated fiber optic bundle to deliver unpolarized light angled apically at the cementoenamel junction from both sides (buccal/lingual) of the tooth. The near-IR camera lens system was equipped with an orthogonal linear polarizer from Thorlabs (Newton, NJ) to produce cross-polarized reflectance images with greatly reduced specular reflection.

The outputs of both broadband light sources were filtered with optical filters housed in a two motorized filter wheels, FW102 from Thorlabs. The reflectance filter wheel contained a short pass 830-nm, band pass 1300-nm and 1460-nm, and long pass 1500-nm filters from Spectragon (Parsippany, NJ). The occlusal transillumination filter wheel contained long pass 1200-nm and 1500-nm filters from Thorlabs. Each filter wheel also contained an aluminum disk used to block the light source providing on/off functionality to the multimodal system. Detailed schematics covering the geometry of each modality and theory of the resulting image contrast can be found in previous publications. A single axis Newport (Irvine, CA) 850G actuator driven by a Newport ESP300 motion controller was utilized to focus each image in the acquisition sequence by moving the camera position. 12-bit image data was delivered over a camera link cable to a Real Time PXIe-1071 chassis with NI-8133 embedded controller and NI-1428 frame grabber from National

Instruments (Austin TX). A host computer, Mac Mini 2014 from Apple (Cupertino, CA) running bootcamp and Windows 7 is used to control the Real Time PXIe, both filter wheels and ESP300 motion controller.

5.4 Results and Discussion

An *in vitro* multispectral multimodal NIR imaging system was fabricated using the components illustrated in Fig. 5.1. The imaging system is controlled by a computer network consisting of a host PC and LabView Real Time computer equipped with a camera link frame grabber. Figure 5.2 is a diagram of the custom LabView host/real time program that synchronizes image acquisition through the real time computer with the changing of imaging wavelength and modalities by the host computer.

The imaging sequence begins with a continuous acquisition of NIR cross polarized reflectance images using an 830-nm short pass filter. This spectral region has the greatest scattering coefficient in sound enamel of all other wavelengths detectable by this InGaAs camera and was chosen because of the uniformity of the tooth appearance. The increased scattering at 830-nm results in light reflections localized closer to the surface of the tooth making focusing easier than at other NIR wavelengths. The host computer is used to drive a single- axis linear stage moving the camera into a focused position. After focusing on the sample, the image acquisition sequence commences with the push of a button synchronizing the timing between the real time and host computers. The host computer facilitates the switching of NIR filters and imaging modalities in the following order: NIR cross-polarized reflectance at $\lambda=1500\text{--}1700\text{-nm}$, $\lambda=1460\text{-nm}$, $\lambda=1300\text{-nm}$ followed by NIR occlusal transillumination at $\lambda=1500\text{--}1700\text{-nm}$ and $\lambda=1200\text{--}1700\text{-nm}$.

Live raw and processed images are streamed from the real time computer to the host using a gigabit crossover Ethernet cable and the images are saved onto an external hard drive connected to the real time computer. For each individual image the real time program sets the camera operational settings, acquires the image frames, performs image processing on the raw data, saves the raw and processed measurements, and then communicates to the host computer that imaging was successful using a network published shared variable. Upon receiving communication from the real time computer, the host responds by changing the filter wheels to the next multispectral imaging modality and positions the camera so the next image is in focus.

A major advantage of this multispectral imaging design is that the multispectral-multimodal images are already registered facilitating faster image processing and multispectral pixel by pixel comparison among images. This program relies upon this auto-registration to segregate the tooth surface from its surroundings based on the tooth location measured from the 830-nm image. Due to the high scattering and uniformity of tooth appearance in this spectral region, the image pixel values consistently demonstrate a bimodal distribution in which the tooth is brighter than its surroundings. Figure 5.3 contains a series of images at multiple stages during the image processing scheme used in this program. First, the raw 830-nm reflectance image (Fig 5.3-A) is converted into a binary image (Fig. 5.3-B) by applying a statistical threshold equal to the pixel mean plus 0.33 times the pixel standard deviation. The binary image is then eroded a number of times with a 5×5 hexagonal matrix to remove small bright objects which are not part of the tooth structure followed by a morphological operation to reject border objects without 8-pixel connectivity. To restore the tooth image, the binary undergoes a series of dilations

with a 5×5 hexagonal matrix then closed with a 31×31 -pixel structuring element. The image is then processed with a Convex Hull procedure which functions to outline the tooth region by finding the smallest convex set that contains all the points in the processed binary images (Fig. 5.3-D). The middle left image in figure 3 outlines the pixel region selected by the image processing algorithm on the original image. The final processed binary image is then multiplied with the raw image to remove the background objects from view (Fig. 5.3-E). The resulting image is then normalized which results in a higher contrast tooth image (Fig. 5.3-F). With the following multispectral-multimodal images in the sequence preregistered with this initial 830-nm image, the tooth pixel locations are the same and therefore the morphological image from Fig. 5.3-D can be multiplied by the next raw image in the sequence and normalized very quickly. Figure 4 shows histograms of the pixel values from the raw (top) and processed/normalized (bottom) images found in Fig. 5.3. Cleaning the image by removing the background and redistributing the pixel values of the bit range will facilitate the use of statistics to aid in the identification of demineralized tooth regions.

This work resulted in an imaging system through which a reliable pixel to pixel comparison of multispectral images is achievable by automatic image registration and focusing. The next phase of this study is to use the multispectral-multimodal images and histological data from tooth occlusal surfaces to build a multiple regression model for predicting lesion depth. This system is also capable of performing angular resolved measurements, which will be investigated for inclusion in the regression model.

5.5 Figures

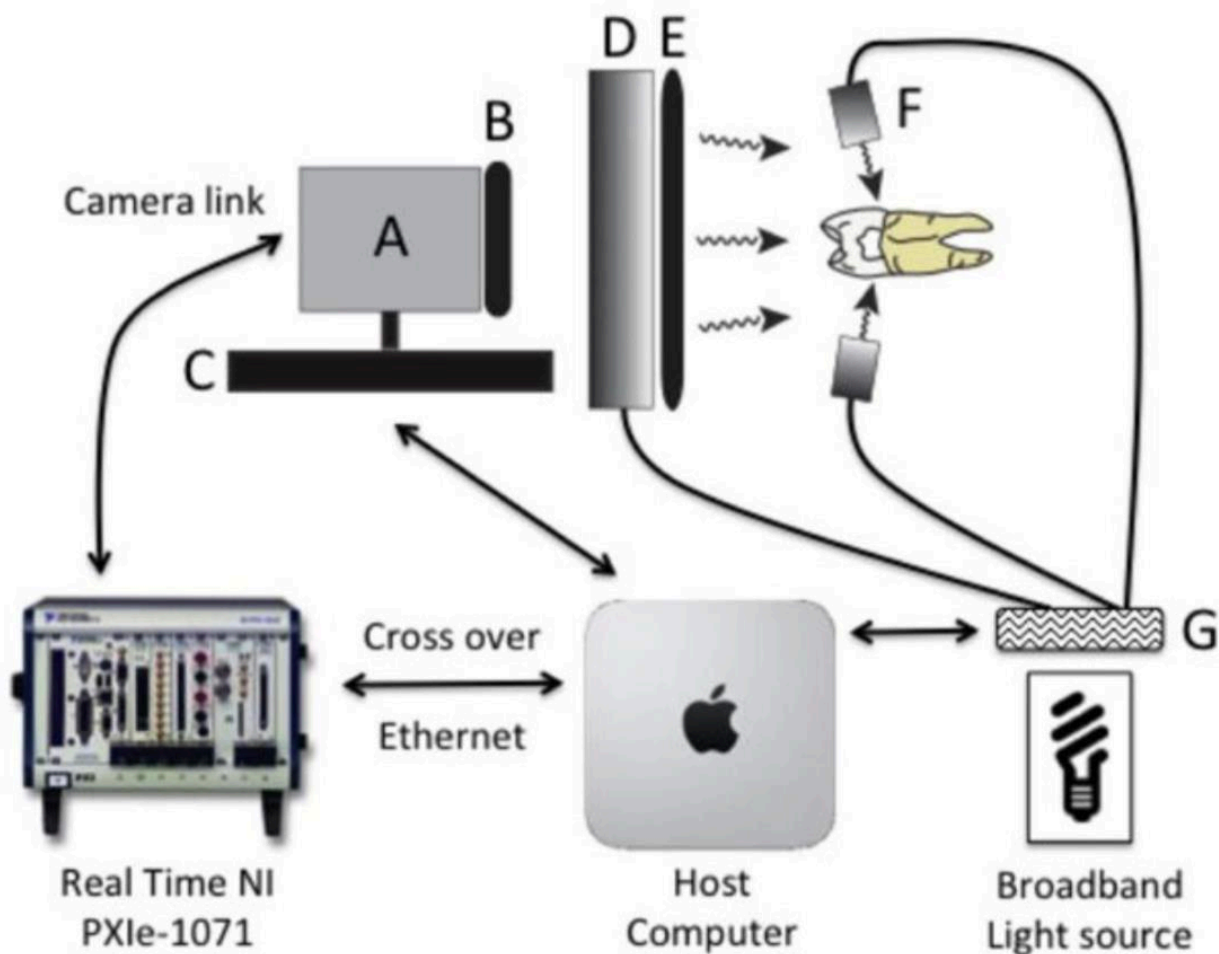


Figure 5.5.1. Imaging schematic for multispectral-multimodal NIR reflectance and occlusal transillumination system. Solid black lines represent fiber optic bundles. Black arrows represent data communication and control. (A) SU640CSX InGaAs NIR camera. (B) NIR linear polarizer. (C) Single axis focusing stage (850G Actuator). (D) Reflectance ring light. (E) Toroidal linear polarizer. (F) Unpolarized occlusal transillumination lights (2 of 4 illustrated). (G) Filter wheel (1 of 2 illustrated).

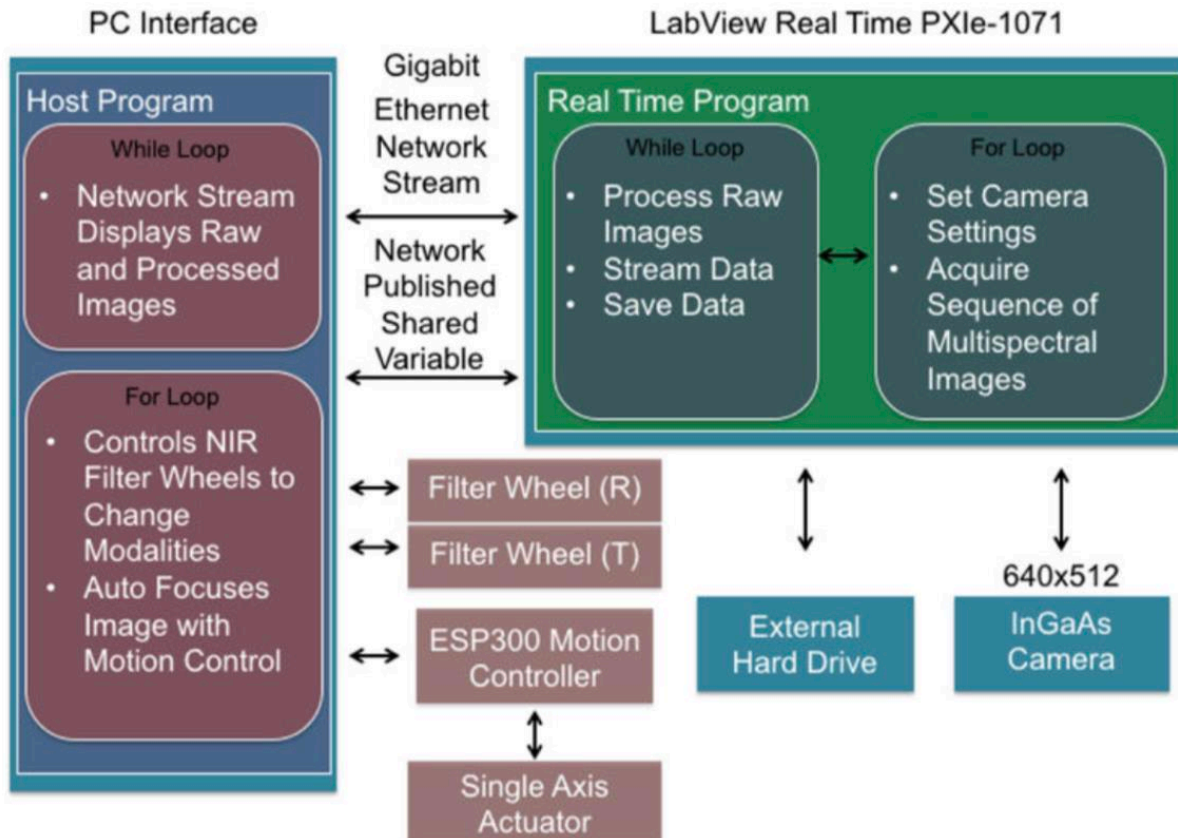


Figure 5.5.2. Computer network schematic for multispectral-multimodal NIR reflectance and occlusal transillumination system. Black arrows represent data communication and external device control. Image acquisition is controlled by the real time PXIe-1071 (green) computer which is responsible for changing the cameras operational settings for each different modality and wavelength in order to optimize image contrast. The image sequence begins with a continuous reflectance acquisition and then acquires a set number of frames/images for the following multispectral modalities. Images are live streamed and viewed on the host computer over a gigabit Ethernet network stream. The real time computer communicates which image modality to acquire to the host using a network published variable.

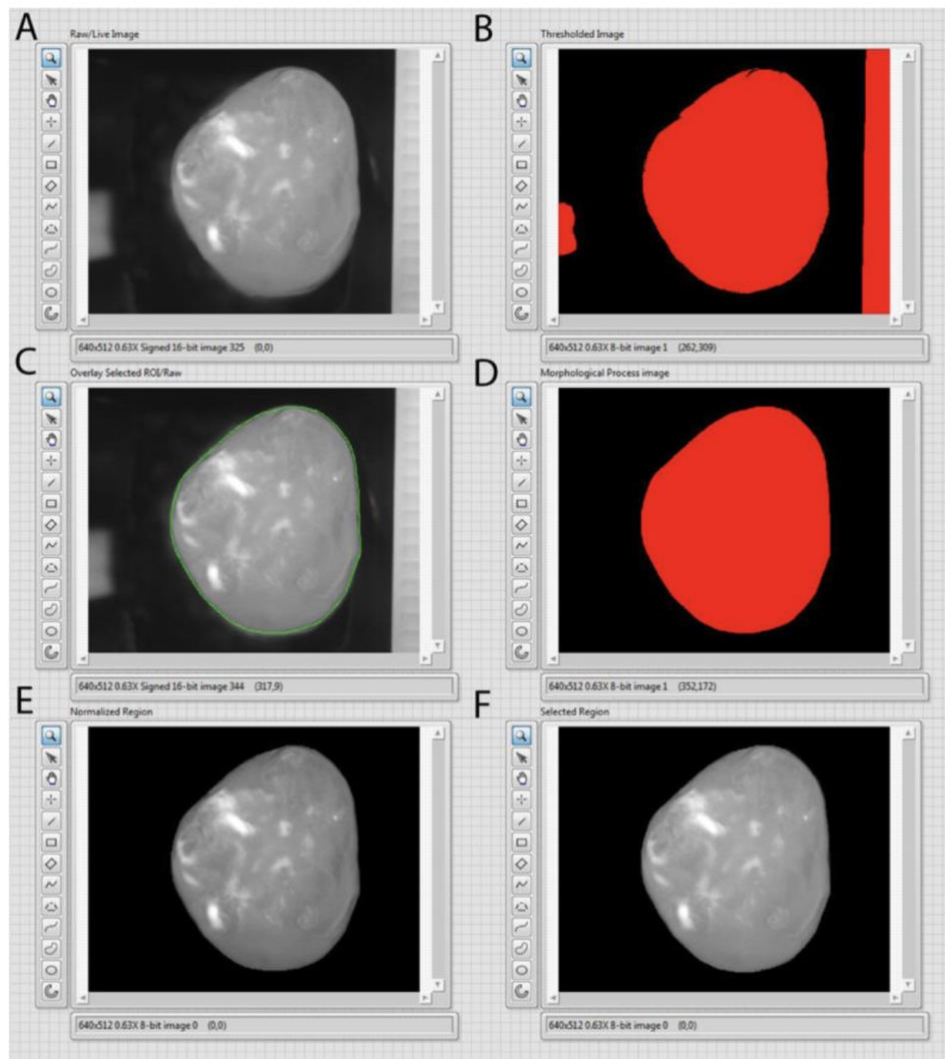


Figure 5.5.3. Cross polarized reflectance image at 830-nm and processing steps for tooth pixel extraction, (A) Raw 830-nm cross polarized reflectance image with object placed to the right of the tooth to demonstrate robustness of isolation, (B) Binary image after statistical thresholding, (C) Overlay of selected pixel region with raw image after morphological processing, (D) Binary image post morphological operations, (E) Normalized tooth image of selected pixels, and (F) Raw tooth image of selected pixels.

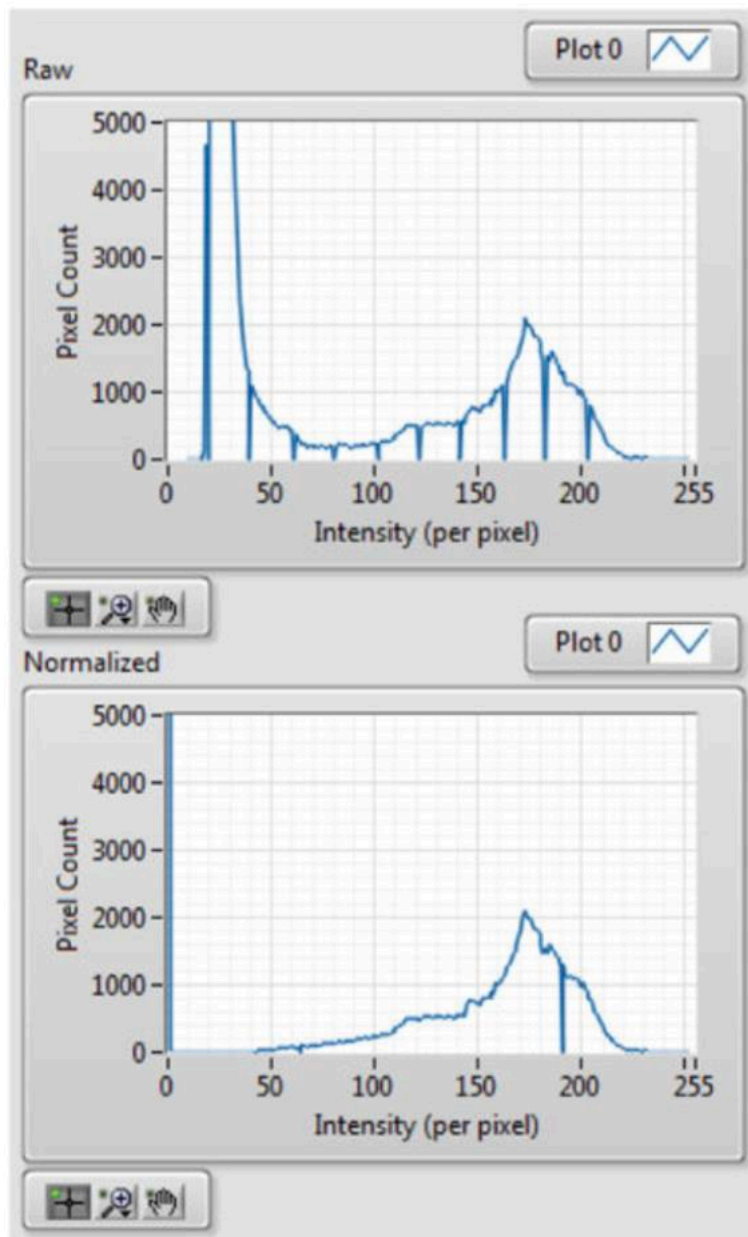


Figure 5.5.4. Histogram of pixel values from the raw (top) and processed/normalized image (bottom).

CHAPTER VI

Assessment of Cavitation in Artificial Approximal Dental Lesions with Near-IR Imaging

6.1 Summary

Bitewing radiography is still considered state-of-the-art diagnostic technology for assessing cavitation within approximal carious dental lesions, even though radiographs cannot resolve cavitated surfaces but instead are used to measure lesion depth in order to predict cavitation. Clinicians need new technologies capable of determining whether approximal carious lesions have become cavitated because not all lesions progress to cavitation. Assessing lesion cavitation from near-infrared (NIR) imaging methods holds great potential due to the high transparency of enamel in the NIR region from $\lambda=1300\text{--}1700\text{-nm}$, which allows direct visualization and quantified measurements of enamel demineralization. The objective of this study was to measure the change in lesion appearance between non-cavitated and cavitated lesions in artificially generated lesions using NIR imaging modalities (two-dimensional) at $\lambda =1300\text{-nm}$ and $\lambda=1450\text{-nm}$ and cross-polarization optical coherence tomography (CP-OCT) (three-dimensional) $\lambda =1300\text{-nm}$. Extracted human posterior teeth with sound proximal surfaces were chosen for this study and imaged before and after artificial lesions were made. A high speed dental hand piece was used to create artificial cavitated proximal lesions in sound samples and imaged. The cavitated artificial lesions were then filled with hydroxyapatite powder to simulate non-cavitated proximal lesions.

6.2 Introduction

Radiography is the main diagnostic tool for the detection and diagnosis of proximal caries (dental decay in between teeth). Cavitation is accepted as a definitive endpoint for which restoration is necessary, however cavitation cannot be determined radiographically and

most proximal surfaces are not clinically accessible for visual inspection [103, 115-117]. Studies suggest that cavitation is likely for most radiolucency's that extend into the dentin [88, 118-120]. However, with the widespread use of fluoride, lesions have changed markedly with cavitation occurring much later and many lesions are arrested due to remineralization [116]. Radiography cannot distinguish between an active and an arrested lesion with only one measurement point [116]. It is well known that radiographs underestimate the depth of lesion penetration and the probability of cavitation depends on several factors including tooth type and the nature of the contact [9, 103, 115, 117]. Moreover, the radiographic depiction of proximal lesions is greatly influenced by the lesion shape and is often inaccurate, e.g. shallow wide lesions may appear deep while deep narrow lesions may appear shallow. Enamel manifests its highest transparency near 1300-nm where the scattering coefficient of enamel is 20–30 times lower than it is at visible wavelengths [41, 42]. Due to the high transparency of enamel, novel imaging configurations are feasible in which the tooth can be imaged from the occlusal surface after shining light at and below the gum line, which we call occlusal transillumination [28, 46, 71, 75, 121]. Upon demineralization the scattering coefficient of enamel increases by 1–2 orders of magnitude at 1300-nm to yield high contrast between sound and demineralized enamel for caries detection [43]. Therefore, this wavelength range is ideally suited for the transillumination of approximal dental caries lesions. Carious lesions appear dark in transillumination images due to increased scattering and absorption by the lesion that reduces optical transmission. Approximal lesions can also be imaged in reflectance from the occlusal surface at NIR wavelengths due to the high transparency of enamel. Such lesions appear dull white compared to the transparent sound enamel. Based on that

knowledge, we demonstrated the high potential of the NIR for imaging caries on both proximal and occlusal surfaces [28, 71, 75, 121, 122] and that novel imaging configurations such as occlusal transillumination and cross-polarization reflectance imaging can be used to image lesions on both occlusal and proximal surfaces. NIR images can be acquired from multiple perspectives to gain a more accurate depiction of the lesion. Imaging devices that can more effectively show the severity of lesions on proximal surfaces and detect cavitation should have a significant impact on the diagnosis of proximal caries.

We have carried out four prior clinical studies involving NIR transillumination imaging and one recent study involving NIR reflectance. In 2011, we carried out a clinical study of teeth with non-cavitated occlusal caries lesions that were not visible on radiographs. Teeth with suspect lesions were examined using near-IR occlusal transillumination at 1300-nm and polarization optical coherence tomography prior to restoration. In a near-IR imaging clinical study completed last year, we employed three NIR imaging probes to screen for lesions on premolars scheduled for extraction, and we demonstrated that NIR image methods can achieve higher diagnostic performance than radiographs for the detection of lesions on both proximal and occlusal surfaces.

In previous studies we have demonstrated that OCT can be used to determine if occlusal lesions have penetrated to the underlying dentin by detecting the lateral spread across the DEJ. Even though the optical penetration of NIR light can easily exceed 7-mm through sound enamel to image lesions on proximal surfaces with high contrast, the large increase in light scattering due to demineralization typically limits optical penetration in highly

scattering lesions (also dentin and bone) to 1–2-mm, thus cutting off the OCT signal before it reaches the dentinal-enamel junction (DEJ). However, most occlusal lesions rapidly spread laterally under the enamel upon contacting the more soluble softer dentin and those lesion areas under sound enamel can be readily detected with OCT. Since approximal lesions are typically located under sound enamel the same principle applies. In a recent clinical study, we acquired both NIR transillumination and reflectance images and OCT images of an in vivo approximal clinical lesion.

In this pilot study, we explore the use of NIR imaging methods including NIR reflectance, NIR transillumination and optical coherence tomography for detecting lesion cavitation on simulated approximal lesions.

6.3 Materials and Methods

6.3.1 Sample Preparation

Posterior teeth with sound interproximal surfaces were selected for participation in this study. Teeth were collected from patients in the San Francisco Bay area with approval from the UCSF Committee on Human Research. The teeth were sterilized using gamma radiation and stored in 0.1% thymol solution to maintain tissue hydration and prevent bacterial growth. Samples were imaged with NIR technologies before artificial cavitated and noncavitated interproximal lesions were made. Images were acquired at sound, cavitated, and noncavitated stages. A high-speed dental hand piece and #34D diamond burr was used to drill an artificial cavitated lesion into the interproximal surface of the samples at the mesial or distal contacts. Cavitated interproximal lesions were subsequently filled with powdered hydroxyapatite and sealed with cyanoacrylate

adhesive Loctite (Rocky Hill, CT) to create noncavitated artificial lesions. The grain boundaries of the hydroxyapatite powder highly scatter light in a similar fashion to the porosities in caries lesions.

6.3.2 NIR Occlusal Transillumination and NIR Cross-Polarized Reflectance

A high sensitivity, InGaAs, SWIR camera (SU640CSX) from Sensors Unlimited (Princeton, NJ), with a 640×512-pixel focal plane array and 12.5- μm pixel pitch was used to capture NIR cross-polarized reflectance and occlusal transillumination images of posterior teeth in vitro. Sample images were illuminated with filtered light from two broadband tungsten halogen lamps, E Light company (Denver, CO) delivered through independent reflectance and transillumination fiber optic cable bundles (Fig. 6.1). Reflectance illumination was achieved using a ring light from Volpi (Auburn, NY) equipped with a toroidal NIR linear polarizer custom made from a 3×3-inch polarizing sheet, Edmund Scientific (Barrington, NJ). Occlusal transillumination used a quadfurcated fiber optic bundle to deliver unpolarized light angled apically at the cemento-enamel junction from both sides (buccal/lingual) of the tooth to illuminate interproximal regions. The near-IR camera lens system was equipped with two orthogonal linear polarizers from Thorlabs (Newtown, NJ) to produce cross-polarized reflectance images with greatly reduced specular reflection.

The outputs of both broadband light sources were filtered with optical filters housed in two motorized filter wheels, FW102 from Thorlabs. The reflectance filter wheel contained 1300-nm and 1460-nm band pass, and 1500-nm long pass filters from Spectragon (Parsippany, NJ). The occlusal transillumination filter wheel contained 1200-nm and

1500-nm long pass filters from Thorlabs. Each filter wheel also contained an aluminum disk used to block the light source providing on/off functionality to the multimodal system. Detailed schematics covering the geometry of each modality and theory of the resulting image contrast can be found in previous publications. A single axis Newport 850G actuator driven by a Newport ESP300 motion controller was utilized to focus each image in the acquisition sequence by moving the camera position. Images (12-bit) were delivered over a camera link cable to a Real Time PXIe-1071 chassis with NI-8133 embedded controller and NI-1428 frame grabber (National Instruments, Austin TX). A host computer, iMac 27-inch, Late 2015 (Apple, Cupertino, CA) running bootcamp and Windows 10 was used to control the Real Time PXIe, both filter wheels and ESP300 motion controller.

6.3.3 NIR Image Analysis

NIR images were analyzed using the image analysis package provided by IgorPRO software from Wavemetrics, (Lake Oswego, OR). Image line profiles 20 pixels in width were extracted from the sample across the distal/mesial margin in the buccal lingual direction for NIR reflectance and transillumination images. The line profiles were used to calculate lesion contrast based on the formulas, $(I_L - I_S)/I_L$ for reflectance and $(I_S - I_L)/I_S$ for transillumination due to their different lesion appearance. A representative value was chosen from the line profile of the lesion and sound regions. The reported contrast values can range from 0 to 1 where a 0 value represents no contrast, a 1 value represents maximum contrast, and negative values represents inverse contrast. The reported lesion contrast ranges from 0 to 1 when the lesion intensity is greater than the measured sound intensity. A negative contrast can occur when the measured sound intensity exceeds the

lesion intensity and the reported values do not have a confined range. Contrast values were compared with near-IR measurements using repeated measures one-way analysis of variance (ANOVA) followed by Tukey–Kramer post- hoc multiple comparison tests using InStat statistical software (GraphPad, San Diego, CA).

6.3.4 Cross-polarization Optical Coherence Tomography

A cross-polarization OCT system purchased from Santec (Komaki, Aichi, Japan) was used to acquire 3D tomographic images of sound, cavitated, and noncavitated lesion stages on the samples. This system acquires only the cross-polarization image (CP-OCT), not both the cross and co-polarization images (PS-OCT). The device, Model IVS-300-CP, utilizes a swept laser source; Santec Model HSL- 200–30 operating with a 33-kHz a-scan sweep rate. The interferometer is integrated into the handpiece which also contains the microelectromechanical (MEMS) scanning mirror and the imaging optics. This CP-OCT system can acquire complete tomographic images of a volume 6×6×7-mm in size in ~3 -seconds. This system operates at a wavelength of 1321-nm with a bandwidth of 111-nm with a measured axial resolution in air of 11.4-mm (3 dB). The lateral resolution is 80-mm ($1/e^2$) with a transverse imaging window of 6×6-mm and a measured imaging depth of 7-mm in air. The polarization extinction ratio was measured to be 32-dB.

6.3.5 CP-OCT Image Analysis

CP-OCT scans were analyzed using software that we developed using LabView (National Instruments, Austin, TX). Tomographic images of the sample were reconstructed from the cross-polarization image. Background subtraction was carried out by subtracting the mean reflectivity of 5,000 data points measured in air from the top 100 pixels (~0.8-mm) of the 50 unprocessed a-scans (~1.0-mm) outside the sample area. The images were convolved with a Gaussian filter (3×3 filter, sigma = 4) to reduce speckle noise. The 5×5 rotating kernel transformation (RKT) technique was applied in x–z and y–z spaces to emphasize thin edges while further suppressing speckle noise. B-scans were extracted from the center of the lesion, cavity or sound region or image comparison. C-scans were also used to orient the view to the location of the lesion and the extracted cross-sectional images.

6.4 Results and Discussion

This study found distinct measurable differences in the appearance among sound, noncavitated approximal lesions, and cavitated approximal lesions using an artificial cavitation model imaged with near-IR (NIR) cross-polarized reflectance, transillumination and cross-polarized optical coherence tomography (CP-OCT). NIR cross-polarized reflectance and occlusal transillumination imaging modalities were capable of imaging different dental lesion states at multiple wavelengths throughout the NIR spectral region (Table 6.1) [123]. The measured lesion contrast from line profiles extracted from regions across the lesion structure demonstrated statistically higher values for noncavitated lesions than lesions post cavitation with high significance at all tested NIR wavelengths. Figure 6.2 is an array of multispectral NIR images acquired in this study from a

representative sample. The noncavitated lesion is visible in high contrast for all imaging wavelengths and modalities. At this stage the lesion is observed in highest contrast in reflectance at 1460-nm and at 1500-nm, and previous studies have demonstrated that these regions yield similar contrast values (for this reason they are grouped into one category in Table 6.1). Surprisingly, and possibly due to the “severity” of the artificial lesion, the occlusal transillumination at wavelengths coincident with increased water absorption, $\lambda=1500\text{--}1700\text{-nm}$, performed remarkably well yielding clear images of the approximal lesions.

In the cavitated state, the contrast measured in the respective cavitated areas was either not detectable, or increased, i.e. the area appeared brighter than the surrounding sound tissue due to the vacancy in the cavity ($n=2$). This behavior explains the negative contrast values reported in Table 6.1. The cavitated lesions were still evident in the reflectance images coincident with high water absorption, but the contrast was greatly reduced relative to the noncavitated state (23.5 difference in mean contrast). Reflectance images at $\lambda=1300$ demonstrated improved potential compared to $\lambda=1500\text{--}1700$ in recognizing lesion cavitation. At this stage the lesion areas were barely detectable in the cavitated images (Fig. 6.2K) and the loss of signal in the NIR reflectance image at $\lambda=1300$ may be a reliable indicator of active cavitation.

The results from the NIR reflectance and transillumination images in this study of artificial cavities suggest that there are distinct and detectable changes in lesion contrast that could indicate the cavitation state of active lesions. This approach would require monitoring the lesion contrast of active lesions over time using multispectral multimodal

probes as the method relies on detecting changes in the lesion appearance, i.e. a significant loss in contrast and possible negative contrast in transillumination.

Figure 6.3 shows 3D CP-OCT images acquired from the sample shown in Fig. 6.2. The left column of Fig. 6.3 shows the occlusal surface of the tooth (c-scan) in the sound, noncavitated lesion, and cavitated lesion states. In Figs. 6.3 D & G the lesion is highlighted in red and the occlusal surface is shown in blue. The middle and right columns show b-scan cross sections extracted from the mesiodistal (vertical) and faciolingual (horizontal) yellow lines in the respective c-scan image. In the CP-OCT b-scans, the presence of a noncavitated lesion and cavitated lesion is clearly seen. Figure 6.3E manifests high scattering at the surface of the lesion with increased signal intensity extending into the body of the decay in both axes. In the cavitated images (Fig. 6.3H & I) there is a detectable signal at the surface of the cavity due to the interface. The signal is less intense and there is no signal from the underlying void till the bottom of the cavity is detected which is indicated by the bottom arrow in Fig. 6.3 H.

6.5 Tables and Figures

Table 6.5.1 The mean lesion contrast measure for image line profiles extracted from NIR reflectance and transillumination images at different lesion stages.

Means and Difference of Means in NIR image contrast before and after Cavitation		Noncavitated Lesion Mean (SD)	Cavitated Lesion Mean (SD)	Difference of Means
Cross -polarized Reflectance Wavelength	1300-nm n =8	37.3 (8.5)	7.2 * (4.2)	30.1
	1460–1700-nm n =10	62.8 (15.4)	39.3 * (10.9)	23.5
Transillumination Wavelength	1200–1700-nm n =4	30.1 (21.4)	0 * (0)	30.1
	1500–1700-nm n =6	39.6 (22.4)	-12.3 * (19.9)	51.9

* The decrease in lesion contrast upon cavitation of the artificial lesions was statistically significant ($P < 0.05$) for each modality.

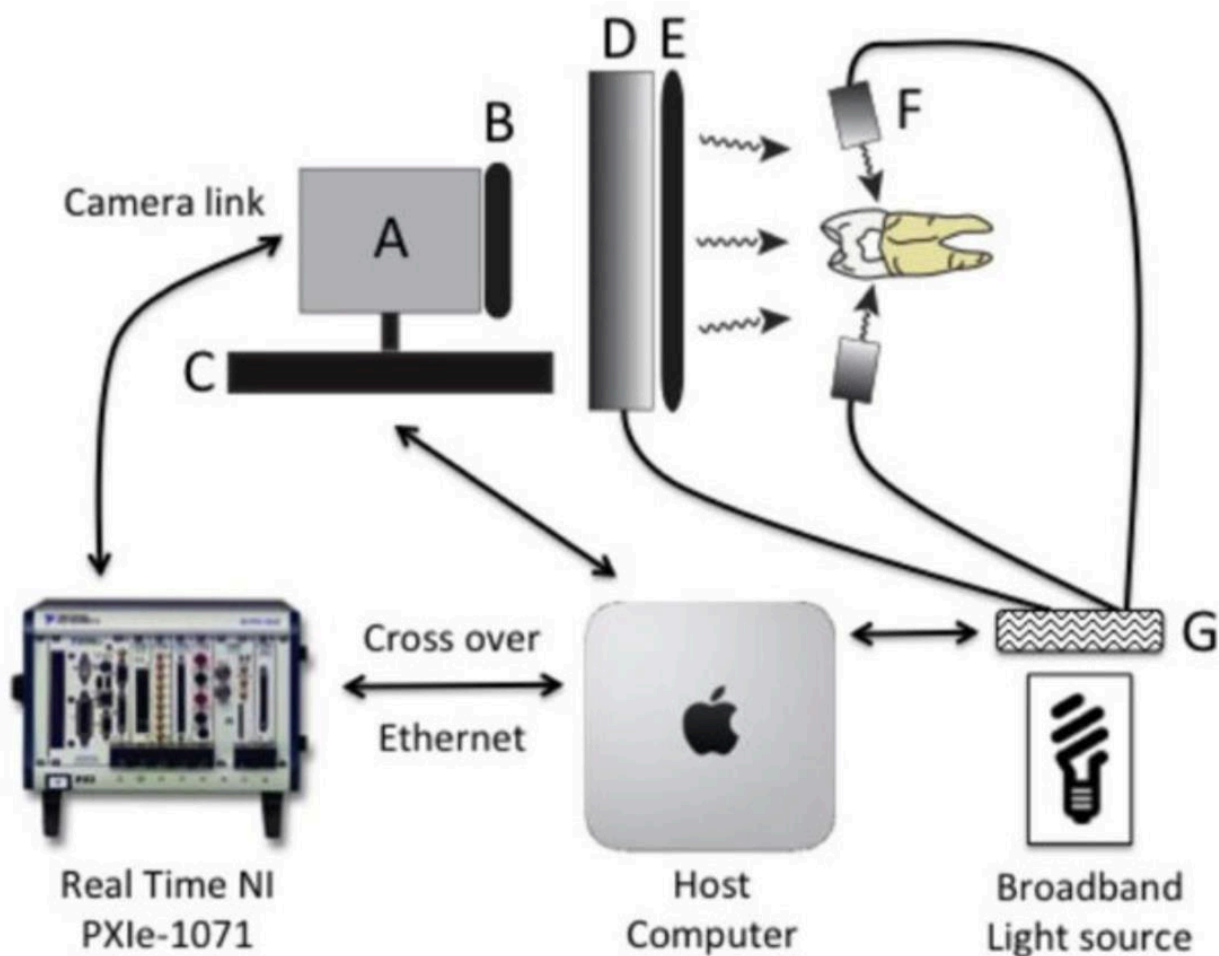


Figure 6.5.1. Imaging schematic for multispectral-multimodal NIR reflectance and occlusal transillumination system. Solid black lines represent fiber optic bundles. Black arrows represent data communication and control. (A) SU640CSX InGaAs NIR camera. (B) NIR linear polarizer. (C) Single axis focusing stage (850G Actuator). (D) Reflectance ring light. (E) Toroidal linear polarizer. (F) Unpolarized occlusal transillumination lights (2 of 4 illustrated). (G) Filter wheel (1 of 2 illustrated).

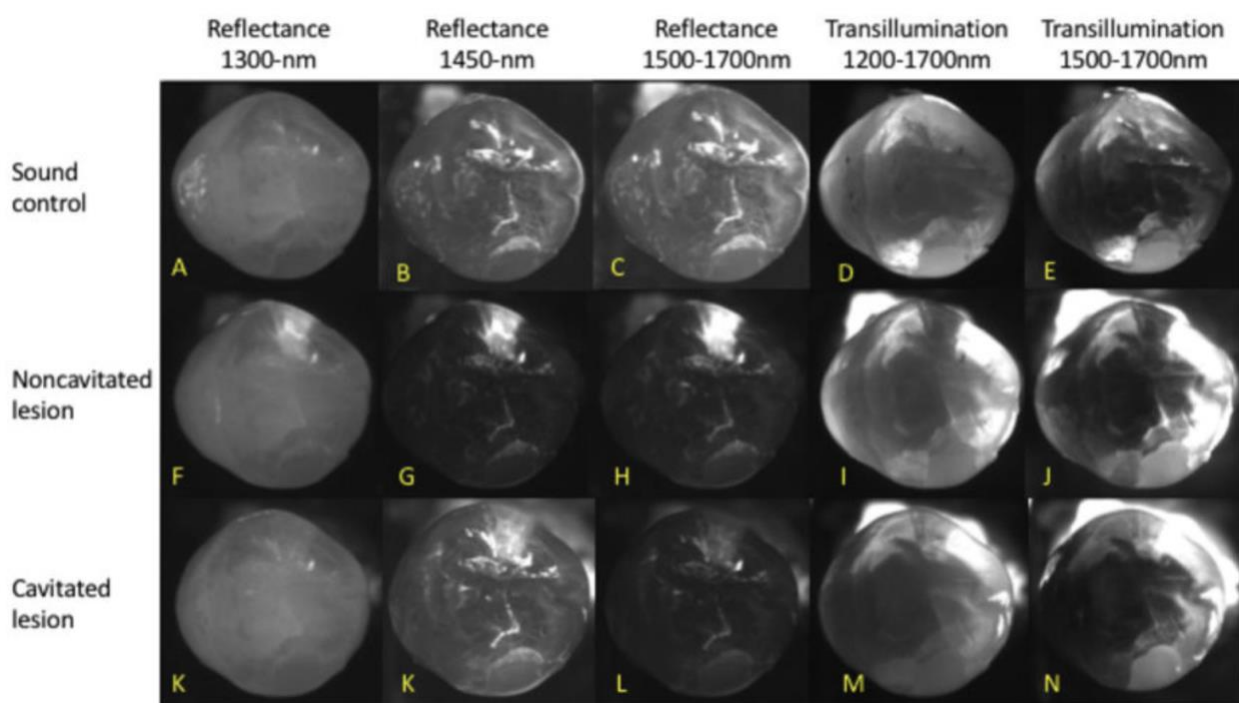


Figure 6.5.2. Multispectral NIR cross-polarized reflectance and occlusal transillumination images of sound, noncavitated lesion and cavitated lesions.

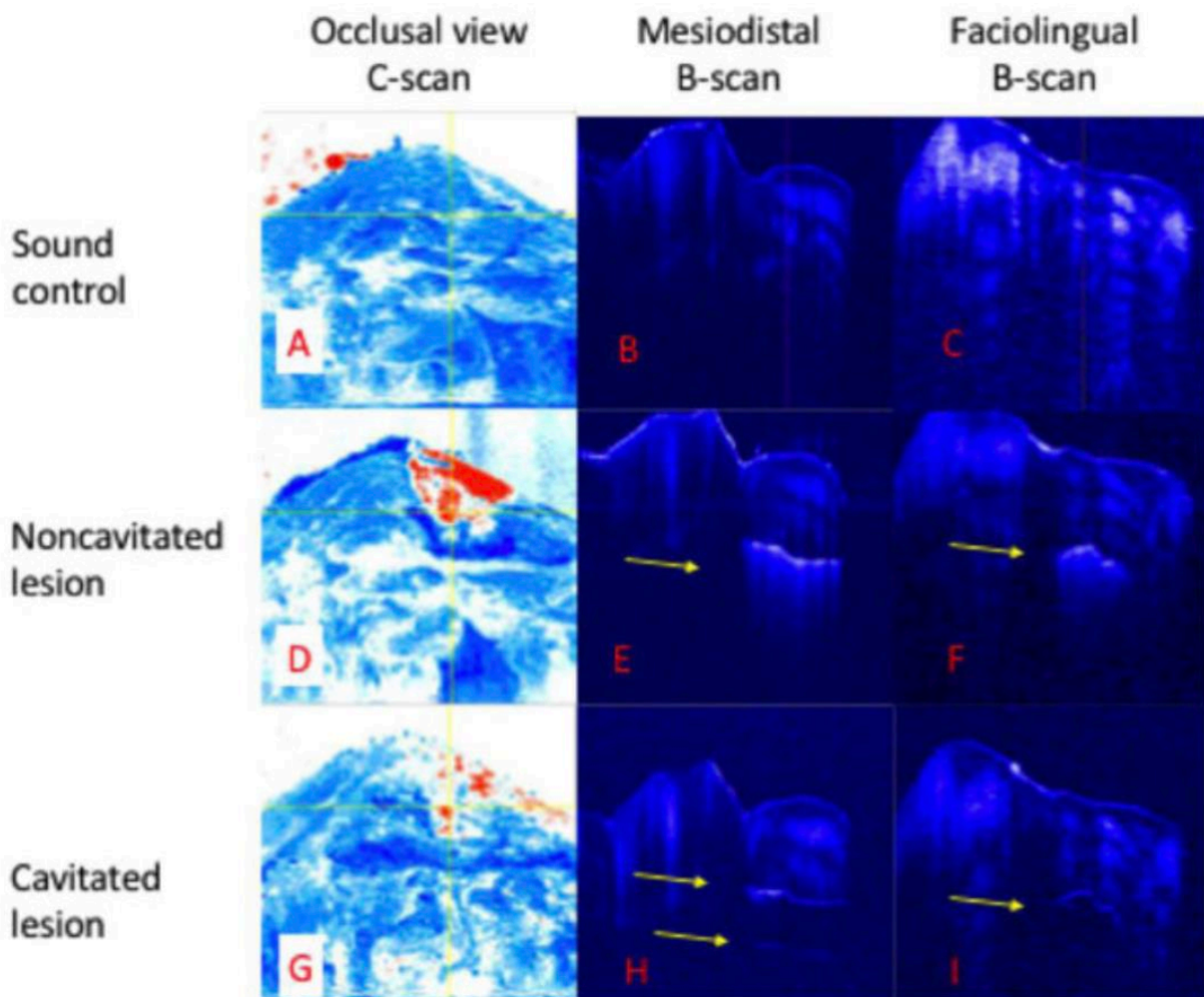


Figure 6.5.3 CP-OCT Images of sound, noncavitated, and cavitated lesion states of the sample in Fig. 2. Panels A,D & E are c-scan OCT images of the occlusal surface and should be compared with the reflectance images in Fig.2. The lesion is shown in red. Vertical yellow line corresponds to mesiodistal b-scan (B,E & H). Horizontal yellow line correspond with faciolingual b-scan (C,F & I).

CHAPTER VII

Near-Infrared Imaging of Demineralization Under Sealants

7.1 Summary

Previous studies have shown that near-infrared (NIR) reflectance and transillumination imaging can be used to acquire high contrast images of early caries lesions and composite restorative materials. The aim of the study was to determine the optimum NIR wavelengths for imaging demineralized areas under dental sealants. Fifteen natural human premolars and molars with occlusal lesions were used in this *in vitro* study. Images before and after application of sealants were acquired using NIR reflectance and NIR transillumination at wavelengths of 1300-nm, 1460-nm, and 1500-nm to 1700-nm. Images were also acquired using polarization sensitive optical coherence tomography (OCT) for comparison. The highest contrast for NIR reflectance was at 1460-nm and 1500-nm to 1700-nm. These NIR wavelengths are coincident with higher water absorption. The clear Delton sealant investigated was not visible in either copolarization or cross-polarization OCT images. The wavelength region between 1500-nm and 1700-nm yielded the highest contrast of lesions under sealants for NIR reflectance measurements.

7.2 Introduction

Near-infrared (NIR) reflectance, NIR transillumination, and optical coherence tomography (OCT) are new imaging techniques that are capable of imaging caries lesions with high contrast in the wavelength region from 1300-nm to 1700-nm [26, 28, 51, 71, 74, 123, 124]. We have found that 1300-nm yields the highest contrast for transillumination while wavelengths with higher water absorption, 1450-nm and 1500-nm to 1700-nm, yield the highest contrast for NIR reflectance. Higher lesion contrast is important for improved diagnostic performance and earlier detection of caries lesions. Several studies have

demonstrated the utility of OCT for measuring defects in composite restorations and sealants, the marginal adaptation of sealants, and the presence of secondary or residual caries [125-131]. Dentists spend more time replacing existing restorations than placing new ones. Composite restorations are color-matched to the teeth and are often difficult to discriminate from sound tooth structure in the visible range. Recent studies have shown that NIR reflectance and transillumination can be used to enhance the contrast of composite restorations compared with visual detection [40, 132]. The contrast of the composite is enhanced since it contains less water than enamel and dentin. The purpose of this paper was to determine the influence of a clear sealant on the contrast of small natural caries lesions in the pits and the fissures of tooth occlusal surfaces measured using NIR reflectance and transillumination. Polarization sensitive optical coherence tomography (PS-OCT) was employed to confirm the severity of the occlusal lesions before application of the sealant and to evaluate the severity of demineralization. Several studies both *in vitro* and *in vivo* have shown that PS-OCT can be used to quantify the severity of early demineralization on tooth occlusal surfaces [59, 63, 133]. The cross-polarization OCT (CP-OCT) image is advantageous for removing the strong surface reflection and the contrast for the lesion area is higher, *i.e.*, the ratio of the reflectivity of the demineralized area/sound area is higher in the cross-polarization image versus the copolarization image. The reflectivity in the CP-OCT image can be integrated over the lesion depth to provide a measure of the lesion severity. Detailed comparison with microradiography measurements, the gold standard for demineralization, has established that the integrated reflectivity (ΔR) correlates with the integrated mineral loss [59, 63, 133].

It is recommended that preventive resin sealants be placed on the occlusal surfaces of posterior teeth on patients with deep fissures or a history of caries. Resin sealants prevent decay by acting as a physical barrier to acidogenic bacteria. However, the sealants are not always successful in preventing the development of lesions. Sealants are typically sold with opaque or clear shades. The opaque shades contain an optical opacifier, titanium dioxide, which strongly attenuates NIR light. The opaque sealant is preferred by many clinicians since it is more visible on the tooth. Jones *et al.* [126] demonstrated that the decay under sealants can be quantified with PS-OCT, and there have been other subsequent studies showing the utility of OCT for imaging caries lesions under sealants [125, 129].

In the previous study of Jones *et al.* [126], it was discovered that the composites/sealants did not scramble (depolarize) the incident polarized light nor were they birefringent. Therefore, it appeared most advantageous to analyze the lesion severity under sealants using cross-polarization images. This was a significant advantage of using the CP-OCT image in addition to the reduction of strong reflections at the air/tooth and the air/sealant interfaces. The copolarization images can also be used to detect the lesions under the sealant, but there are distinct disadvantages. However, there have been studies utilizing conventional OCT systems to image sealants [125]. Holtzman *et al.* [129] used a conventional OCT system to detect sealants placed over natural lesions. In this study, we also placed sealants over existing natural lesions.

The NIR reflectance measurements yield high contrast for both artificial and natural caries lesions without interference from stains and color variations since none of the known

chromophores absorb light in the NIR beyond 1300-nm. More recent NIR imaging studies suggest that the NIR wavelengths coincident with increased water absorption are well suited for the detection of early demineralization on tooth surfaces. We hypothesize that the higher water absorption in the underlying dentin and enamel reduces the reflectivity in sound areas and this, in turn, results in higher contrast between sound and demineralized enamel. Hyperspectral reflectance measurements by Zakian *et al.* show that the tooth appears darker with increasing wavelength [51]. Recent studies by Chung *et al.* [40] and Fried *et al.* [52] on natural and simulated occlusal lesions indicated that other NIR wavelengths coincident with higher water absorption provide significantly higher contrast than at 1300-nm or at visible wavelengths.

7.3 Materials and Methods

7.3.1 Sample Preparation

Fifteen human teeth with suspected lesions on the occlusal surface were collected with the approval of the Committee of Human Research and sterilized with gamma radiation. Teeth were visually examined and those that scored ICDAS 1 or 2 were selected. Teeth were mounted in black orthodontic acrylic blocks. Samples were stored in a moist environment of 0.1% thymol to maintain tissue hydration and prevent bacterial growth. The outlines of 5×5-mm windows ~50-µm deep were cut on the occlusal surface of each tooth using a CO₂ laser (Impact 2500, GSI Lumonics, Rugby, United Kingdom) around the suspected lesion area. The channels cut by the laser serve as reference points for imaging and serial sectioning and are sufficiently narrow that they do not interfere with calculations of the image contrast.

A clear sealant (without an optical opacifier), DELTON® FS+ pit and fissure sealant (Dentsply, York, Pennsylvania) was applied to the suspected fissure area according to the manufacturer's instructions. NIR and PS-OCT images of the occlusal surface were acquired before and after the sealant was applied. A diamond suspension (3000 mesh, 6- μm) from CrystaLite Inc. (Lewis Center, Ohio) was sprayed onto the tooth surface to show the surface of the sealant for PS-OCT imaging in order to determine the sealant thickness.

7.3.2 Composite Attenuation Measurements

Delton clear sealant was cast into rods using clear straws and light cured for the recommended duration. Discs were cut using an IsoMet 2000 wet saw from Buehler (Lakebluff, Illinois) to produce samples 1.0, 1.5, 2.0, 2.5, and 3.0-mm in thickness ($n=3$ for each thickness). Sample disks were serially polished on both sides with 12, 9, 5, 3, and 0.3- μm Buehler fiber- met aluminum oxide polishing discs and measured with a digital caliper 500 series from Mitutoyo (Aurora, Illinois). Light from an Ocean Optics (Dunedin, Florida) fiber-coupled tungsten-halogen lamp, Model HL-2000-FHSA, with a filter wheel with bandpass filters, FB series [full-width half-maximum (FWHM) 12-nm] from Thorlabs (Newton, New Jersey) centered at 50-nm intervals from 1300-nm to 1650-nm was used to illuminate specific areas of the sample with a spot size of $\sim 100\text{-}\mu\text{m}$. The spot size was confirmed through knife-edge beam profiling techniques. Phase sensitive detection was employed using a lock-in amplifier (Model SR 850) and an optical chopper from Stanford Research Systems (Stanford, California). A large-area Ge photoreceiver Model 2033 from New Focus (Santa Clara, California) equipped with a variable aperture was used for

detection. This procedure ensured that the position of the incident collimated light beam was fixed while cycling through the filters. Three measurements of collimated transmission were recorded at various sections within each sample and averaged. The collimated signal (I) at the detector was compared with the initial intensity of the beam (I_0). Using this ratio and the thickness of the samples (d), the attenuation coefficient (μ_t) was calculated using Beer–Lambert plots:

$$\mu_t = -\ln(I/I_0)/d$$

The aperture in the front of the detector was sufficiently small to ensure that light scattered at small angles did not contribute significantly to the collimated transmission.

7.3.3 Visible-Light Depth Composition Tooth Images

Images of the tooth occlusal surfaces were examined using a digital microscopy system, the VHX-1000 from Keyence (Elmwood, New Jersey) with the VH-Z25 lens with a magnification from 25 to 175 \times . Images were acquired by scanning the image plane of the microscope and reconstructing a depth composition image with all points at optimum focus displayed in a two-dimensional image. Figure 7.1 shows depth composition images of a tooth before and after placement of the transparent sealant. The sealant does change the appearance of the occlusal surface, increasing the contrast of the edges of the pits and the fissures. The sealant itself is not visible and one cannot estimate the sealant thickness and coverage by visual examination alone.

7.3.4 Near-IR Cross-Polarization Reflectance Images

In order to acquire reflected light images, NIR light was directed toward the occlusal surface through a broadband-fused silica beam splitter (1200 to 1600-nm) Model BSW12 (Thorlabs, Newton, New Jersey), and the reflected light from the tooth was transmitted by the beam splitter to the imaging camera (Fig. 7.2). Crossed polarizers were placed after the light source and before the detector and used to remove specular reflection (glare) that interferes with measurements of the lesion contrast.

The NIR reflectance images were captured using a 320 × 240 element InGaAs area camera Model SU320-KTSX from Sensors Unlimited (Princeton, New Jersey) with a 25- μm pixel pitch. Reflectance measurements were taken for three spectral bands using two bandpass filters and a longpass filter. The bandpass filters were Model #'s BP1300-90 and BP1460-85 from Spectrogon (Parsippany, New Jersey). The 1500-nm-long-pass filter Model # the FEL 1500 from Thorlabs (Newton, New Jersey), which resulted in a spectral range of 1500-nm to 1700-nm due to the sensitivity of the InGaAs camera.

7.3.5 Near-IR Transillumination Images

A 150-W fiber-optic illuminator, Model FOI-1 from the E Licht Company (Denver, Colorado) with a low-profile fiber optic with dual-line lights, Model P39-987 (Edmund Scientific, Barrington, New Jersey), was used with each light line directed at the cement-to-enamel junction beneath the crown on the buccal and lingual sides of each tooth (Fig. 7.2). Light leaving the occlusal surface was directed by a right-angle prism to the SU320 InGaAs camera equipped with a Navitar (Rochester, New York) SWIR-35 lens, a 75-mm

plano-convex lens LA1608-C Thorlabs (Newton, New Jersey), and a 90-nm wide bandpass filter centered at 1300-nm, BP1300-90 Spectrogon, (Parsippany, New Jersey).

7.3.6 Polarization Sensitive-Optical Coherence Tomography

An all-fiber-based optical coherence domain reflectometry system (time-domain) with polarization maintaining optical fiber, high-speed piezoelectric fiber-stretchers, and two balanced InGaAs receivers that was designed and fabricated by Optiphase, Inc., Van Nuys, California, was used. This two-channel system was integrated with a broadband superluminescent diode Denselight (Jessup, Maryland) and a high-speed XY-scanning system (ESP 300 controller and 850G-HS stages, National Instruments, Austin, Texas) for *in vitro* time-domain OCT. The system had a lateral resolution of $\sim 20 \mu\text{m}$ and an axial resolution of $10\text{-}\mu\text{m}$ in air. The PS-OCT system is completely controlled using Labview software (National Instruments, Austin, Texas). The system is described in detail in Refs. [134] and [70]. Acquired scans are compiled into b-scan files. Image processing was carried out using Igor Pro data analysis software (Wavemetrics Inc., Lake Oswego, Oregon).

The CP-OCT scans were assessed to evaluate the integrated reflectivity (ΔR) over the depth of demineralization in units of $(\text{dB} \times \mu\text{m})$. A program written in Labview as described in Ref [67] was used to automatically calculate the lesion depth using an edge detection approach and then integrate the reflectivity over that depth.

7.3.7 Image Analysis and Statistics

Line profiles were extracted across the same position in the lesions within the 5×5-mm boxes for each spectral band, and the image contrast was calculated using the equation $(I_L - I_S)/I_L$; where I_S is the mean intensity of the sound enamel outside the window area, and I_L is the mean intensity of the lesion inside the window for reflectance. Transillumination $(I_S - I_L)/I_S$ has the reverse contrast, *i.e.*, the intensity in lesion areas is lower than the sound enamel. The image contrast varies from 0 to 1 with 1 being maximum contrast and 0 no contrast. All image analysis was carried out using Igor Pro software (Wavemetrics, Lake Oswego, Oregon). Repeated measures of one-way analysis of variance followed by the Tukey–Kramer posthoc multiple comparison test was used to compare groups for each type of lesion employing Prism software (GraphPad, San Diego, California) before and after application of the sealant.

7.4 Results

7.4.1 Attenuation Measurements

The optical attenuation coefficients as a function of wavelength are plotted in Fig. 7.3 from 1300-nm to 1650-nm. The coefficients lie between 5-cm^{-1} and 10-cm^{-1} and are consistent with the varying absorption of water with the lowest attenuation at 1300-nm and the highest attenuation at 1450-cm^{-1} matching the water absorption band.

7.4.2 PS-OCT Measurements

S-OCT b-scans of both polarization states of the occlusal surface of one of the teeth before and after application of the sealant are shown in Fig. 7.4. The laser marks 5-mm apart are visible on the left and right sides of the sample near each cusp and they appear as small depressions along with very strong surface reflection; they also strongly attenuate light and there is a loss of signal intensity under them. They are marked by the stars in the copolarization image in Fig. 7.4(a). A small shallow lesion is located at the base of the central fissure and the dentinal-enamel junction (DEJ) is clearly visible in the initial b-scans for both polarizations [Fig. 7.4(a)]. The lesion is located in the center of the white circle. After application of the sealant, the underlying DEJ is no longer visible [Fig. 7.4(b)] in either polarization. It is also very difficult to resolve the surface of the sealant in both polarization images [Fig. 7.4(b)]. In addition, the reflectivity from the lesion at the base of the fissure is greatly reduced in the copolarization image, whereas, it is not reduced in the cross-polarization image.

A 6- μm grit diamond powder suspension was sprayed onto the tooth surface, which rendered the surface of the sealant visible without greatly reducing the OCT imaging depth [Fig. 7.4(c)]. This facilitated measurement of the sealant thickness. The ΔR values were calculated from images without the diamond powder.

The ΔR values were measured and calculated for the lesions before and after application of the sealant. The mean (s.d.) of ΔR for all the samples for the copolarization and cross-polarization (\perp) images, pre and post-sealant, is plotted in Fig. 7.5. Bars of the same color

are statistically similar ($P > 0.05$). Only the copolarization image manifested a significant reduction ($P < 0.05$) in ΔR after application of the sealant.

7.4.3 NIR Reflectance

Figure 7.6 shows NIR reflectance images of a tooth before and after sealant placement for three wavelength regions 1300-nm, 1450-nm, and 1500-nm to 1700-nm. There is shallow demineralization in the central fissure, which appears whiter than the surrounding enamel, and it shows up with the highest contrast in Figs. 7.6(c) and 7.6(e). The fissure is located in the center of the 5×5-mm reference box cut into the tooth. In Fig. 7.6(a) (1300-nm), it appears that either cracks or the premolar anatomy interfered with light transmission in the tooth causing segmentation of the light; one section of the tooth appears much brighter than the rest of the tooth. After application of the sealant, the reflected light is more uniform [Fig. 7.6(b)]. It is possible that the sealant filled in the cracks allowing better transmission of light through the tooth.

It is very difficult to resolve the increased light reflectivity from the lesion in the fissure in Fig. 7.6(a), and it is not at all visible after application of the sealant [Fig. 7.6(b)]. The narrow zone of demineralization in the fissure appears with high contrast in Figs. 7.6(c) and 7.6(e) (1450-nm and 1500-nm to 1700-nm), and the surrounding sound enamel appears very dark. After application of the sealant, the demineralization appears less continuous in the fissure and has lower contrast [Figs. 7.6(d) and 7.6(f)].

The mean (s.d.) of the lesion contrast in reflectance is plotted in Fig. 7.7 for the three NIR spectral regions before and after application of the sealant. The lesion contrast was

significantly higher ($P < 0.05$) at 1460-nm, and 1500-nm to 1700-nm, versus 1300-nm before application of the sealant. Application of the sealant significantly reduced ($P < 0.05$) the lesion contrast at 1460-nm and 1500-nm to 1700-nm. The lowest mean contrast was at 1300-nm (0.08), and it dropped by 37% after adding the sealant. The highest contrast was at 1500-nm to 1700-nm (0.26) and it decreased by 49% after adding the sealant. The greatest change in contrast occurred at 1460-nm where the initial contrast (0.19) dropped by 80%. After application of the sealant, the mean lesion contrast at 1500-nm to 1700-nm was significantly higher than that for both 1300-nm and 1460-nm ($P > 0.05$).

7.4.4 NIR Transillumination

Figure 7.8 shows NIR transillumination images at 1300-nm of a tooth before and after placement of the sealant. Note that the contrast is inverted for transillumination and the lesion appears darker instead of whiter than the surrounding sound tissues. The previous studies have shown that 1300-nm performs best for transillumination of the occlusal surfaces. The other wavelengths, 1450-nm, and 1500-nm to 1700-nm, failed to yield high contrast due to the high water absorption of the sealant and the underlying dentin. Moreover, NIR transillumination yields poor contrast for shallow lesions on tooth surfaces [50].

7.5 Discussion

The primary objective of this study was to determine the influence of clear sealants on the contrast of lesions in tooth occlusal surfaces in NIR reflectance and transillumination

images. The PS-OCT images were acquired to confirm that the lesions were present. We did not anticipate the low visibility of the sealant in both the copolarization and the cross-polarization OCT (CP-OCT) images. In our previous study, using another clear sealant, Aeliteflo (Bisco, Schaumburg, Illinois), we found that the sealant was clearly visible in the copolarization image but was not visible in the cross-polarization image [126]. This indicated that the sealant neither scrambled the polarization (due to increased scattering) nor rotated the polarization axis (birefringence). The size and the shape of filler particles are expected to influence both the magnitude of attenuation and the interaction with polarized light [126, 131]. The Aeliteflo sealant was visible in the copolarization image because the scattering was sufficiently high. Therefore, light scattering by the Delton sealant is likely lower than the Aeliteflo clear sealant used in the previous study. The lower light scattering is certainly advantageous for monitoring demineralization under sealants using OCT.

The low visibility of the sealant surface is even more surprising because if a drop of water is placed in the fissure, the surface of the water droplet can be clearly resolved in the OCT images. The sealant has a higher refractive index, ~ 1.5 versus 1.3, than water which is expected to increase the magnitude of the surface reflection. It is likely that the cured and the solidified surfaces of the sealant are irregular and not as flat and perfectly perpendicular to the incident beam as the surface of a liquid.

Even though the clear sealant was not visible in the PS-OCT images, it did reduce the contrast in both NIR reflectance and NIR transillumination images. Attenuation was

greater in the sealant for wavelengths with higher water absorption, namely 1450-nm and from 1500-nm to 1700-nm, due to the small but significant water content.

The polymerized bisphenol A-glycidyl methacrylate (Bis-GMA) resin of the sealant contains 1% water by weight, which can increase to 4% due to absorption of water if stored in water for an extended period [135]. Enamel and dentin are 4% and 10% water by weight, respectively. In the NIR, the scattering coefficient of dentin is more than 10 times higher than enamel [42, 136]. Much of the light diffusely reflected from the tooth surfaces is due to light that is backscattered from the highly scattering dentin under the transparent enamel. At wavelengths coincident with higher water absorption, *e.g.*, 1450-nm, the tooth appears very dark because much of that light is absorbed by the water in the enamel and the dentin [40, 51]. Upon demineralization, the scattering coefficient of enamel increases by one to two orders of magnitude [43], so that the light incident in the lesion areas does not penetrate deeply. The areas appear very bright in reflectance, and the loss of reflectivity due to water absorption is small since the photons are backscattered before they can penetrate deep into the enamel. This loss of penetration in demineralized enamel can be seen in OCT images. Normally, the DEJ can be resolved through the transparent sound enamel, but the visibility is lost in areas where there is demineralization near the surface [26, 63]. Hence, the contrast between the sound and the demineralized enamel in reflectance is greatly enhanced at wavelengths coincident with higher water absorption, with the contrast highest at 1460-nm but almost as high at 1500-nm to 1700-nm. Water present in the layer of the transparent sealant reduces the reflectivity from the lesion and reduces the contrast. At 1460-nm, attenuation in the thin layer of sealant due to water is sufficient to markedly reduce the lesion contrast. At 1500-nm to 1700-nm there

is also a reduction in lesion contrast, but it is less severe due to the lower absorption coefficient of water.

Transillumination is not feasible at 1460-nm or 1500-nm to 1700-nm since the photons must transverse several millimeters through enamel and dentin, and the high water absorption produces greater attenuation than the scattering by the lesion. Areas of the occlusal surface with underlying dentin appear very dark due to the higher water absorption in the dentin and even severe lesions cannot be resolved [40]. The influence of water absorption in the sealant on the lesion contrast in transillumination is minimal since the distance traversed in the sealant is small compared to that in the enamel and the dentin.

In conclusion, this study shows that clear sealants do attenuate NIR light, significantly reducing the contrast of demineralization in the pits and the fissures of the occlusal surfaces. The wavelength range of 1500-nm to 1700-nm is best suited for monitoring demineralization under sealants using NIR reflectance measurements since the lesion contrast is higher than other wavelengths both before and after application of the sealant.

7.6 Figures

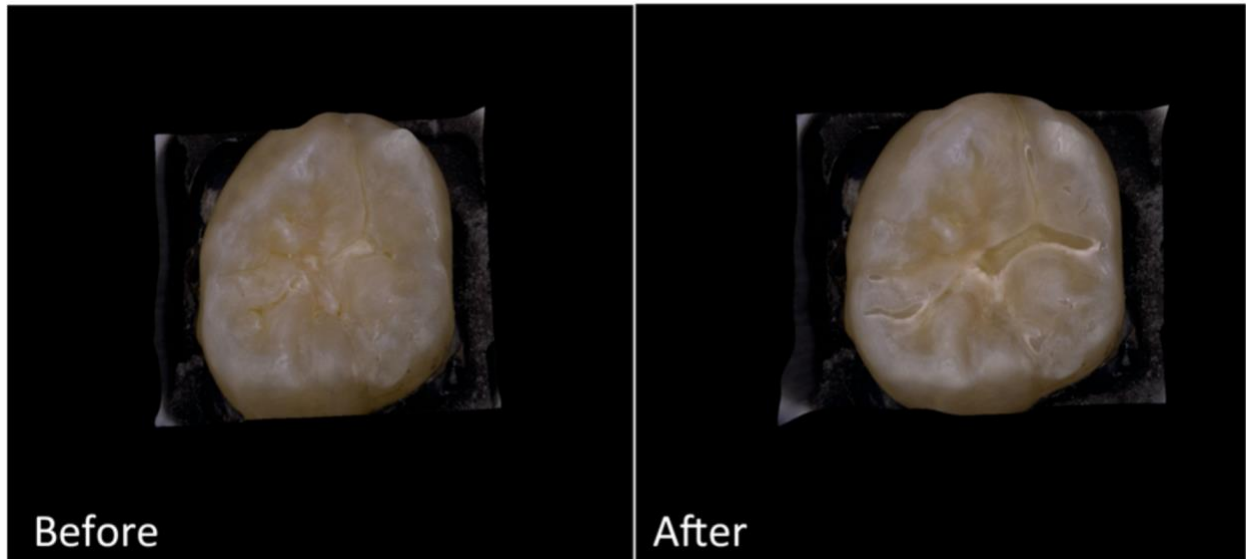


Figure 7.6.1. Digital microscopy images of one of the samples before and after application on transparent sealant. These are depth composition images with all surfaces in focus.

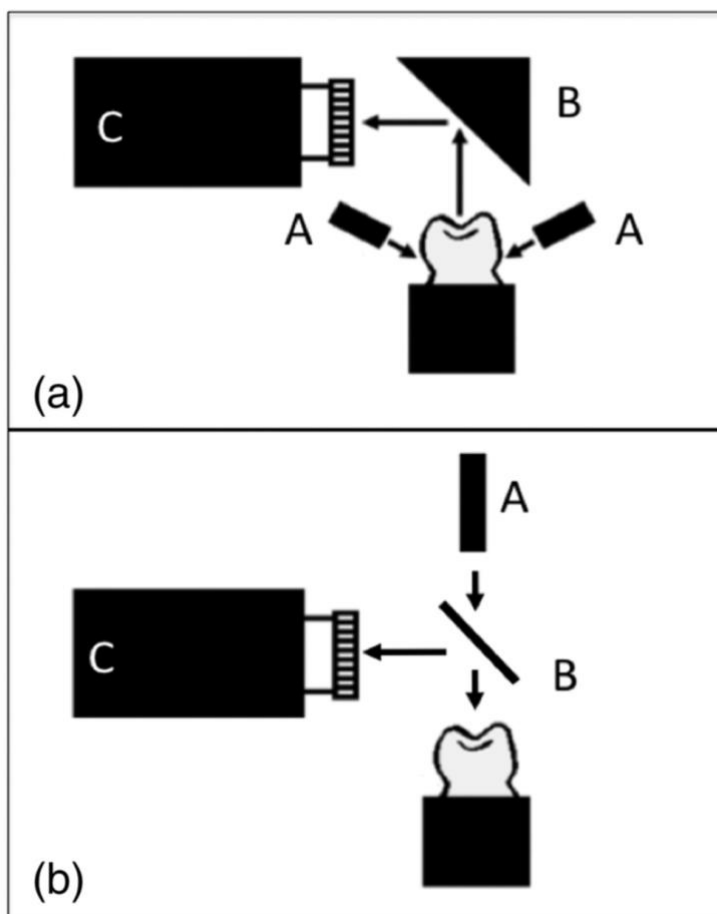


Figure 7.6.2. (a) Occlusal transillumination setup with A. line lights, B. prism, and C. InGaAs camera with 1300-nm filter. (b) Reflectance setup with A. polarized light source, B. beam splitter, and C. InGaAs camera with filters and polarizer.

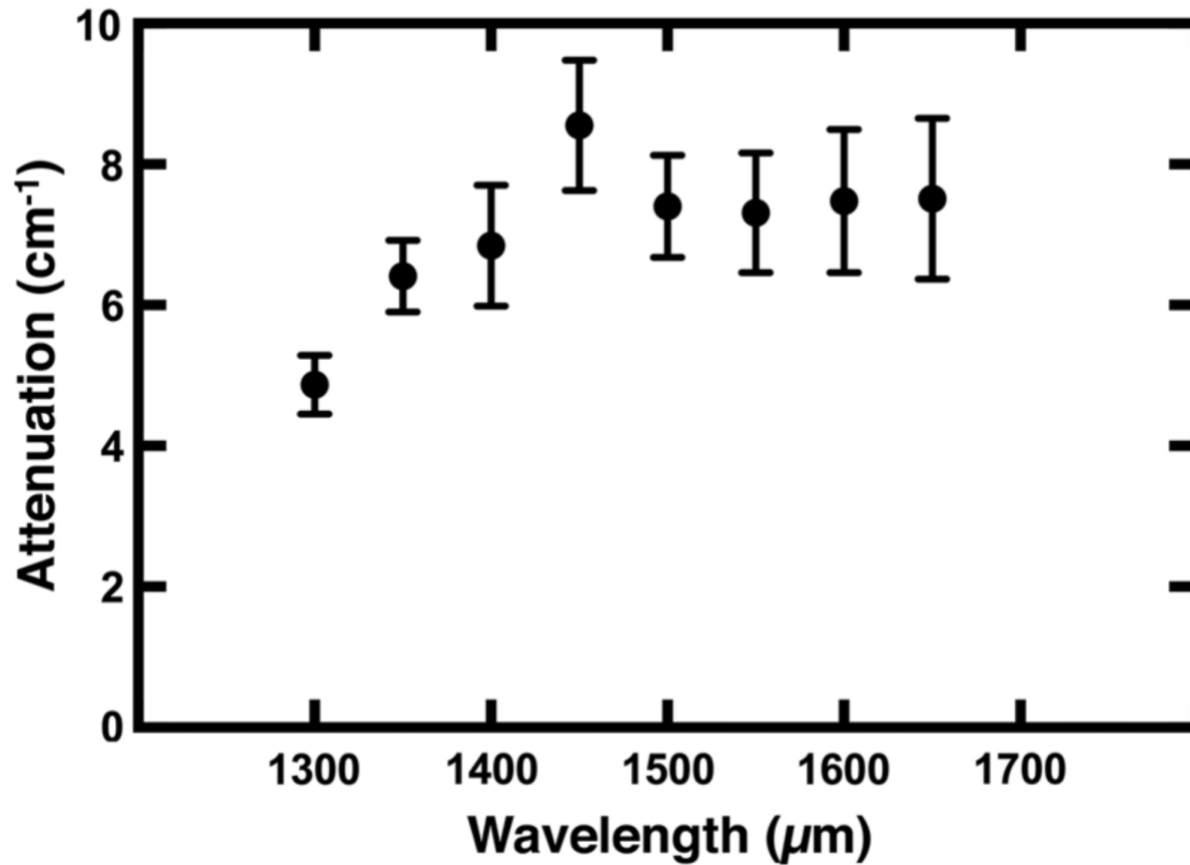


Figure 7.6.3. Plot of attenuation coefficient of Delton clear sealant versus wavelength.

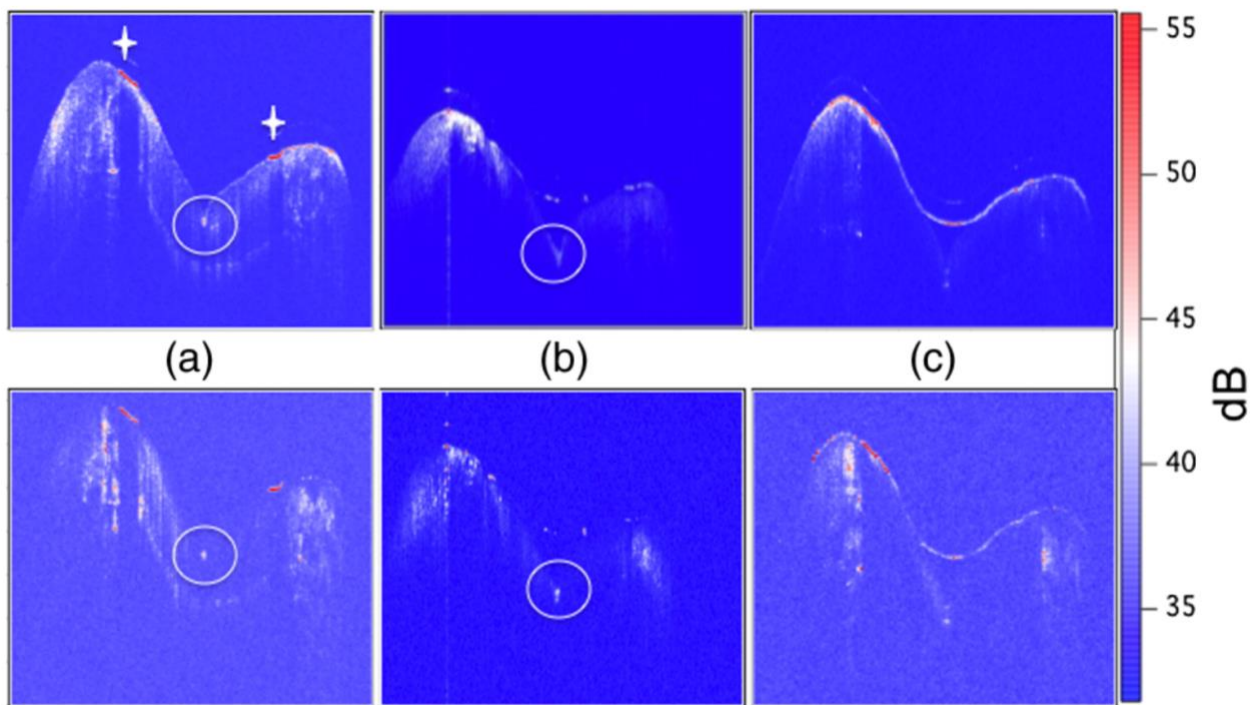


Figure 7.6.4. Polarization sensitive optical coherence tomography (PS-OCT) scans of occlusal fissure before application of the sealant (a) after application of the sealant (b) and with the diamond suspension added (c) to view the sealant surface. The upper images are copolarization images, whereas the lower images are the cross-polarization (\perp) images. In (A) the stars mark the position of the laser incisions and the white circle marks the position of the lesion in the fissure. The images are red-white blue false color with the intensity in decibels.

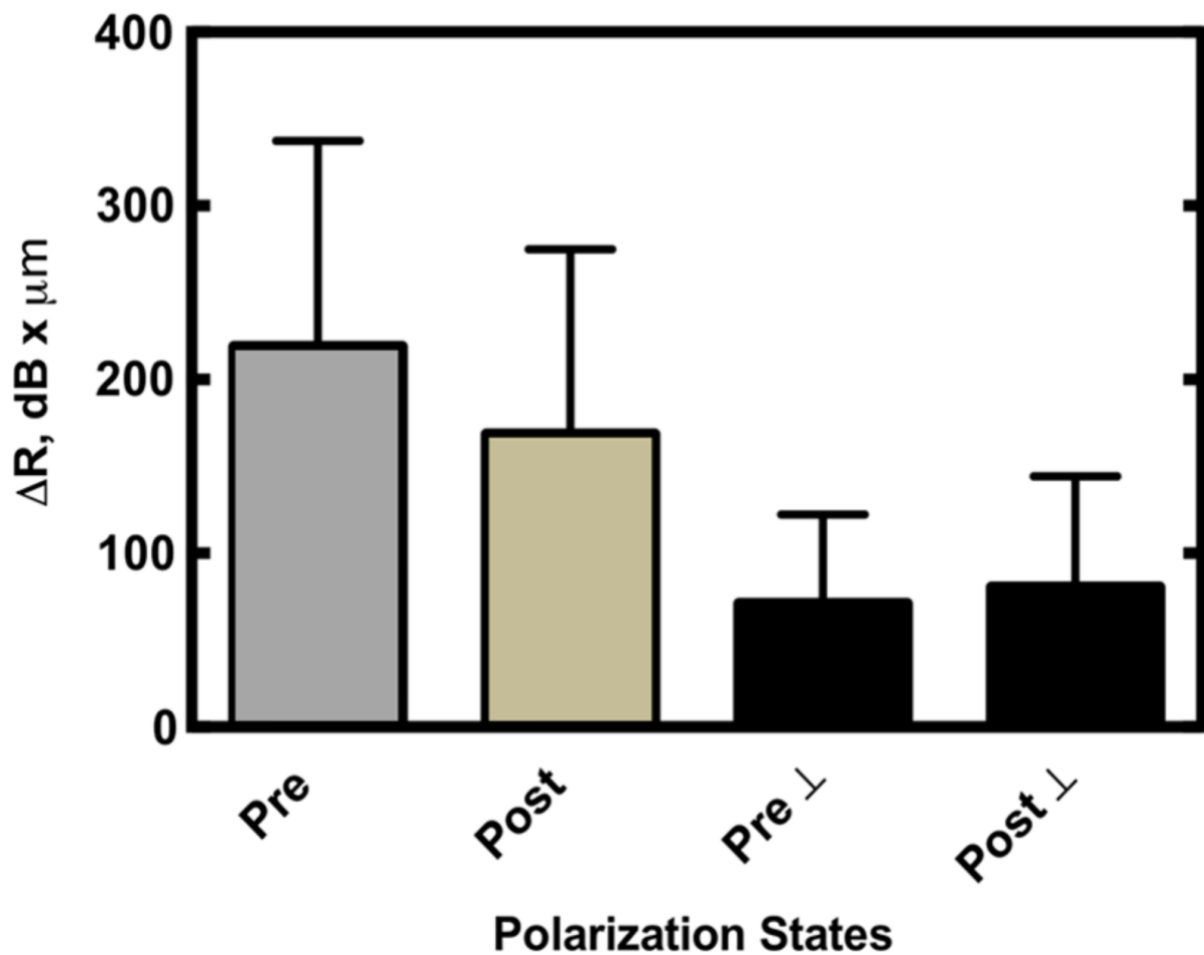


Figure 7.6.5. The mean (sd) of the integrated reflectivity with lesion depth, ΔR (dB \times μm) calculated from the PS-OCT images before and after application of the sealant. Bars of the same color are statistically similar $P > 0.05$.

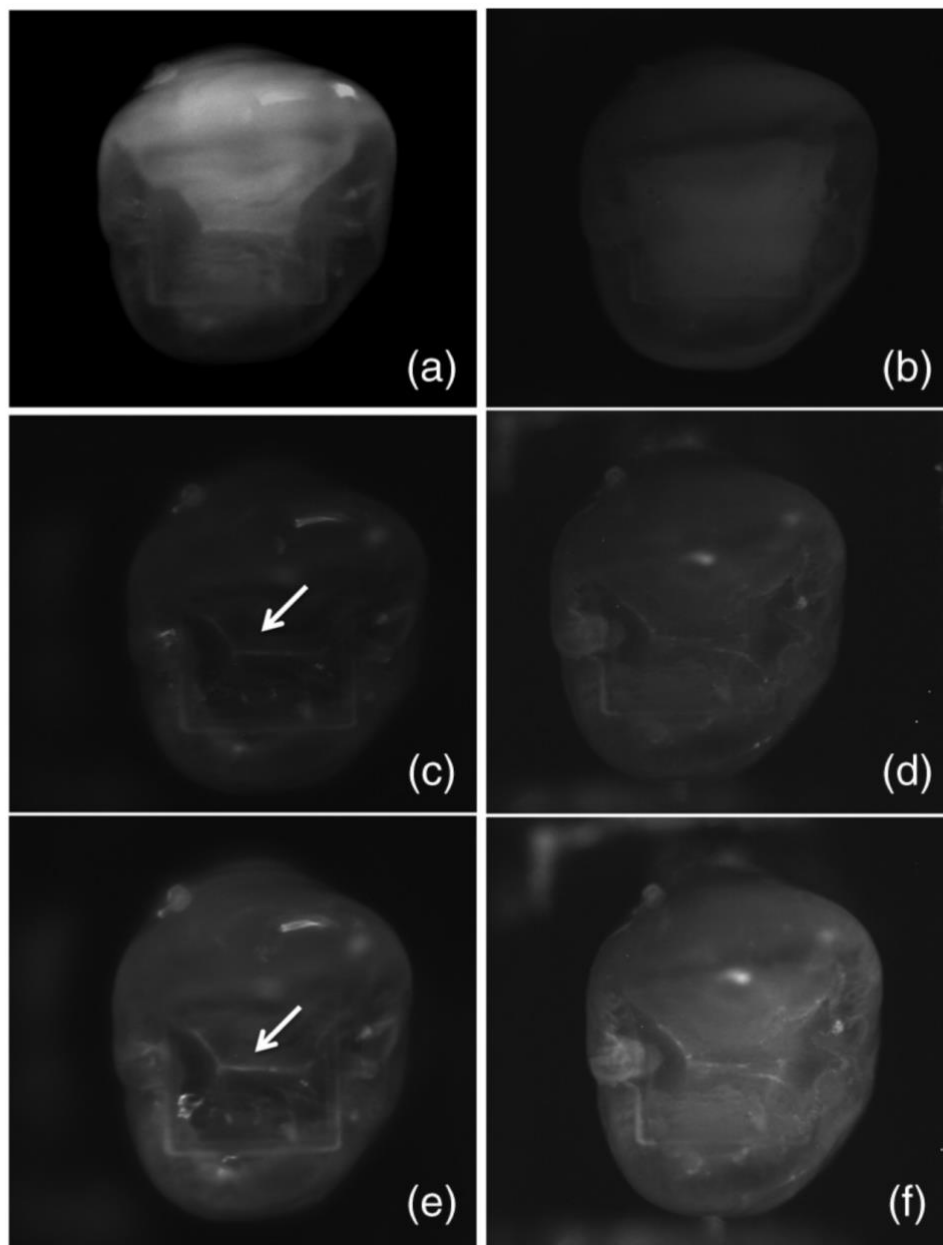


Figure 7.6 6. Near-IR reflectance images before application of the sealant at 1300-nm, 1450-nm, and 1500-nm to 1700-nm (a, c, e) and after the application of the sealant at 1300-nm, 1450-nm, and 1500-nm to 1700-nm (b, d, f). The demineralization in the fissure is located at the position indicated by the with arrows in (c) and (e).

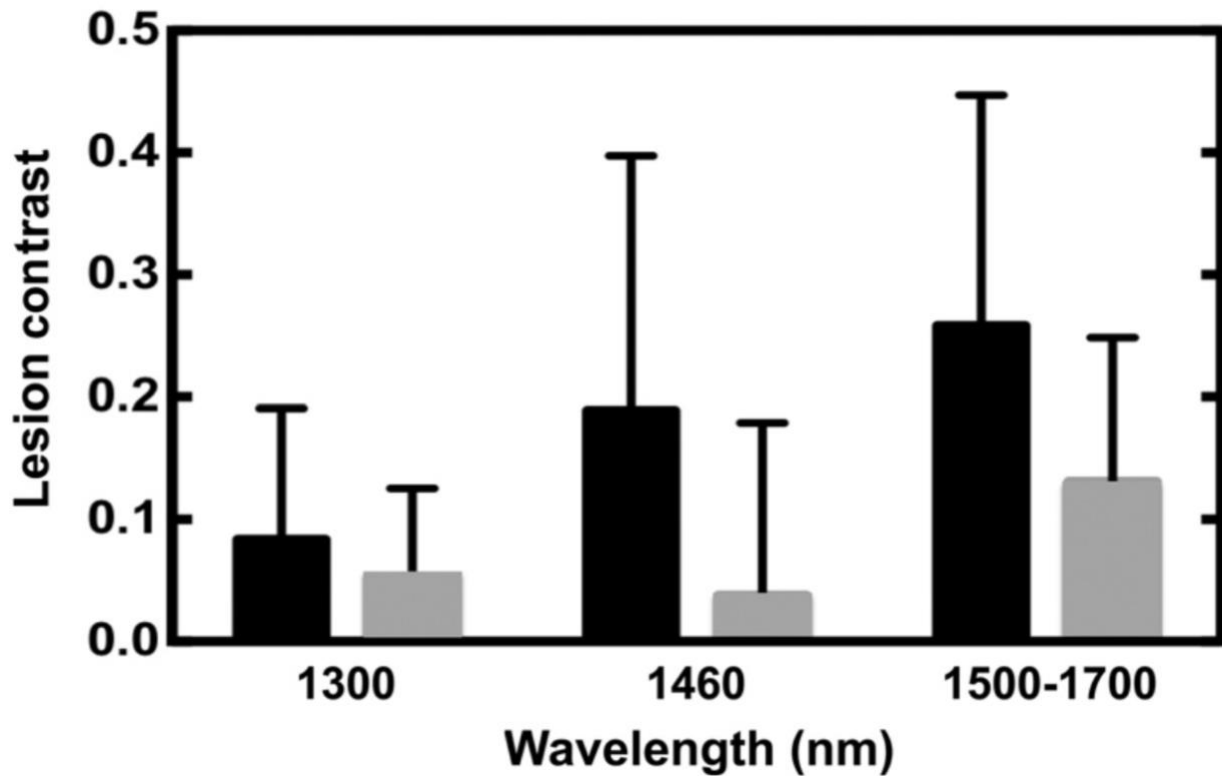


Figure 7.6.7. The mean (sd) of the lesion contrast calculated from the near-IR reflectance images before and after application of the sealant at each wavelength range investigated. The dark bars (left) are before application of the sealant and the light bars (right) are after application of the sealant.

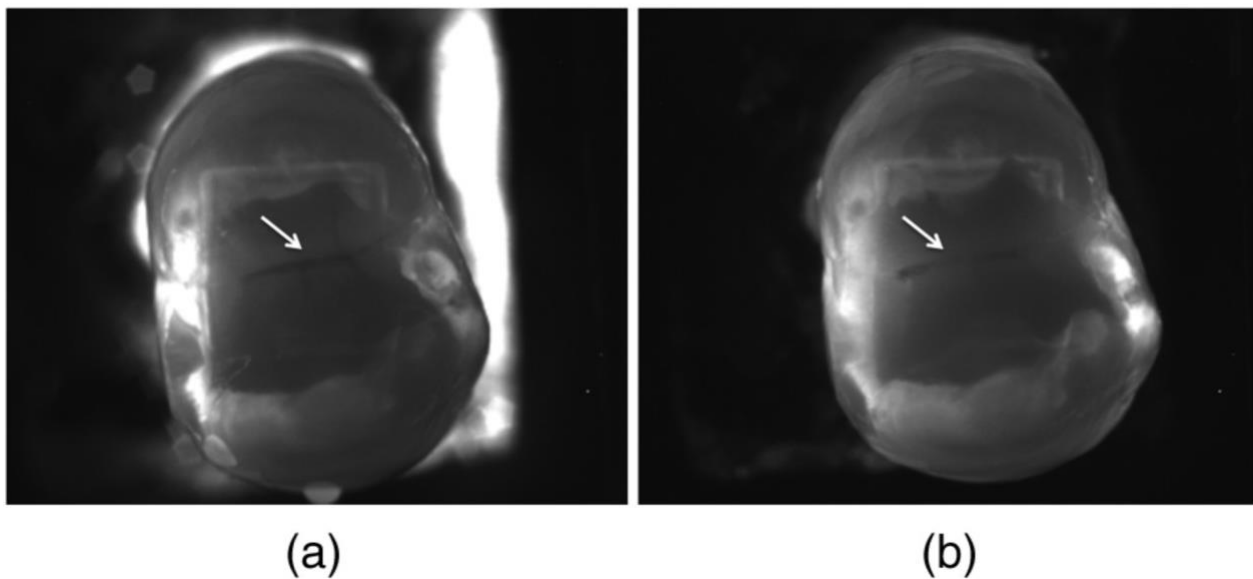


Figure 7.6.8. Near-IR transillumination images acquired at 1300-nm before (a) and after (b) application of the sealant. The demineralization in the fissure is located at the position indicated by the white arrows.

CHAPTER VIII

Near-infrared Imaging of Secondary Caries Lesions around Composite Restorations at Wavelengths from 1300-1700-nm

8.1 Summary

Current clinical methods for diagnosing secondary caries are unreliable for identifying the early stages of decay around restorative materials. The objective of this study was to assess the integrity of restoration margins in natural teeth using near-infrared (NIR) reflectance and transillumination images at wavelengths between 1300–1700-nm and to determine the optimal NIR wavelengths for discriminating composite materials from dental hard tissues. Twelve composite margins (n=12) consisting of class I, II & V restorations were chosen from ten extracted teeth. The samples were imaged *in vitro* using NIR transillumination and reflectance, polarization sensitive optical coherence tomography (PS-OCT) and a high-magnification digital microscope. Samples were serially sectioned into 200- μ m slices for histological analysis using polarized light microscopy (PLM) and transverse microradiography (TMR). Two independent examiners evaluated the presence of demineralization at the sample margin using visible detection with 10 \times magnification and NIR images presented digitally. Composite restorations were placed in sixteen sound teeth (n=16) and imaged at multiple NIR wavelengths ranging from λ =1300–1700-nm using NIR transillumination. The image contrast was calculated between the composite and sound tooth structure. Intensity changes in NIR images at wavelengths ranging from 1300–1700-nm correlate with increased mineral loss measured using TMR. NIR reflectance and transillumination at wavelengths coincident with increased water absorption yielded significantly higher ($P<0.001$) contrast between sound enamel and adjacent demineralized enamel. In addition, NIR reflectance exhibited significantly higher ($P<0.01$) contrast between sound enamel and adjacent composite

restorations than visible reflectance. This study shows that NIR imaging is well suited for the rapid screening of secondary caries lesions.

8.2 Introduction

Secondary (recurrent) caries is the major etiologic factor in the failure of dental restorations, and dentists spend more time replacing restorations than placing new ones [137, 138]. Conventional clinical methods for evaluating demineralization surrounding restorations rely upon visible inspection for discoloration and gaps/microleakage, and tactile sensation with an explorer or periodontal probe. It is clear from clinical data that neither discoloration nor ditching (for gap distances $<500\text{-}\mu\text{m}$, which are considerable) is a consistent indicator of the integrity of the enamel or dentin, and a considerable number of restorations are unnecessarily replaced using such criteria [9, 138-142]. Inspection via tactile examination also presents the risk of accelerating decay by damaging the protective lesion surface zone. New imaging methods that can discriminate between sound enamel, demineralized enamel and composites with higher diagnostic performance for secondary caries lesions are needed.

To address this need, optical techniques including digital radiographs (X-rays), quantitative laser fluorescence (QLF, collagen fluorescence), and red laser fluorescence (LF, porphyrin fluorescence) have been investigated as alternative, nondestructive approaches for diagnosing recurrent decay, albeit that each modality has significant limitations.

Digital radiographs lack the sensitivity to detect changes present during the early stages of lesion progression. Generating radiographic images requires ionizing x-rays and a direct viewing angle of the interproximal regions to produce a diagnostic image [143]. When imaging restored teeth, amalgam and composite restorations are radiopaque and may mask the presence of caries either partially or completely which contributes to the difficulty of diagnosis, and therefore are poorly suited for detecting secondary caries [144-148].

Quantitative light fluorescence (QLF) uses UV or blue light ranging from 370–470-nm in wavelength to excite the proteins in enamel and dentin, and identifies lesions by measuring the loss of fluorescence at wavelengths >500-nm (green light) [149-151]. Measuring lesion severity based on a loss of signal with visible light is problematic due to the high absorption from stain that attenuates light and results in false positives using this method. Secondary caries detection using QLF has been comparable in accuracy to visual diagnosis [148, 152, 153].

Laser fluorescence (LF) uses ~655-nm light to excite fluorescence of bacteria-produced porphyrins and measures light emission at wavelengths >680-nm (near-infrared) [101, 154]. In LF, the presence of a fluorescent signal is used to locate infected areas as a function of bacteria concentration and studies suggest that LF out performs visible and QLF methods for the detection of recurrent decay [148, 152, 153, 155-157]. Unfortunately, LF is prone to false positives due to poor correlation between porphyrin concentration and lesion severity and requires cleaning of tooth surfaces for effective use. Furthermore, the excitation wavelengths used in LF has been shown to cause fluorescence in many

dental restorative materials, including some sealants. For LF devices such as the DIAGNOdent, this requires the user to continually calibrate the device against a ceramic standard, and against sound enamel for each individual tooth [148].

Near-infrared (NIR) imaging, has the potential for improved performance over current methods used to detect recurrent decay by illuminating and capturing images of tooth structures formed by deeply penetrating, non-ionizing light ranging from 700–1700-nm in wavelength. Compared to visible light, light scattering in sound enamel at $\lambda=1300$ -nm is $\sim 20\times$ – $30\times$ less making sound enamel virtually transparent [42]. When sound enamel becomes demineralized by caries, pores within the lesion grow to a similar size of the wavelength of light and act as Mie scatters increasing the scattering coefficient 2–3 orders of magnitude [43]. Differences in light scattering between sound and demineralized enamel can be detected by imaging light transmitted through or reflected back from the tooth [46]. Imaging with longer wavelength ($\lambda \geq 1300$ -nm) NIR light also avoids the absorption bands of organic molecules responsible for pigmentation allowing direct imaging of decay beneath stained surfaces such as the occlusal grooves [123]. Additionally, composite restorative materials have unique spectral signatures in the NIR resulting from combination absorption bands that can be exploited for differentiating tooth structure and other type of composites. The most prominent dental resin absorption bands lie at 1171-nm, 1400-nm, 1440-nm, 1620-nm and 1700-nm and result from overtones and combinations of the fundamental mid-IR vibrational bands from C-H, N-H, and O-H groups found in both resin and water [135, 158, 159] .

Recent studies have investigated the use of polarization sensitive optical coherence tomography (PS-OCT), at ~1300-nm, for the detection of demineralization beneath sealants and composites in addition to primary lesions [128, 129, 131, 160]. These studies demonstrated the ability of PS-OCT to produce three-dimensional data sets that accurately indicate demineralized tissue surrounding restorations. Furthermore, PS-OCT can be used to calculate the integrated reflectivity with depth of the tissue, ΔR , a physical quantity that directly correlates with ΔZ , the integrated mineral loss with depth, and the gold standard for lesion severity. Although PS-OCT is a powerful imaging technique, the vast amounts of data produced from each scan and inherent difficulty of presenting and comprehending three-dimensional data sets make it poorly suited as a caries-screening tool. Another challenge is that the scanning area is relatively small compared to the size of the tooth such that you cannot 'see' the entire tooth anatomy, and increasing the scanning area increases the size of the data set and computational burden.

NIR two-dimensional imaging modalities have demonstrated high image contrast for early surface demineralization using NIR reflectance at $\lambda=1460$ -nm and NIR transillumination at $\lambda=1300$ -nm [28, 45, 50, 71, 161]. Many composite restorative materials are translucent to NIR light and allow demineralization to be imaged directly through the restorations [162, 163]. Additionally, the overall visualization of the restoration boundaries can be enhanced when viewed at different NIR wavelengths [132]. A technique with these abilities should be ideally suited for the detection of recurrent caries in both planes; the surface enamel and the enamel of the cavity wall as defined by [139]. These caries affected planes are classified as either *outer lesions*, primary lesions that develop from the surface adjacent to the restoration, or *wall lesions*, decay along the enamel of the cavity as a result of

microleakage or ditching. With the advantage of real-time video acquisition and presentation with simple interpretation, NIR imaging is poised to be a viable rapid screening tool for secondary caries and restoration monitoring.

Currently, the major factor limiting the use of NIR techniques in dentistry is the cost of the NIR sensitive camera sensors. With increased interest in NIR imaging for dental and other medical applications, these costs are projected to decrease.

The objective of this study was to calculate the lesion contrast in NIR reflectance and NIR transillumination images of natural recurrent decay and compare that contrast with changes in tissue mineral density to determine the optimal wavelengths for imaging secondary caries. NIR images were acquired of extracted teeth with composite restorations and preexisting natural secondary caries lesions with an InGaAs camera. These images were compared with PS-OCT 2D (\perp) integrated reflectivity C-scan projections, PS-OCT (\perp) B-scans, and visible images. Polarized light and transverse microradiography images were obtained from thin sections produced by serial sectioning with a diamond saw. Normalized NIR cross-polarized reflectance and NIR transillumination image line profiles were overlaid with TMR percent mineral line profiles across the region of interest for each sample. In addition, multispectral NIR transillumination images were acquired of newly placed 3M Z250 composite restorations in extracted sound teeth to identify the NIR wavelengths that provide the highest contrast of composites relative to sound enamel.

8.3 Materials and Methods

8.3.1 Sample Preparation

Twenty-eight teeth were collected from patients in the San Francisco Bay area without patient identifiers (exempt from approval by UCSF Committee on Human Research). The teeth were sterilized using gamma radiation and stored in a 0.1% thymol solution to maintain tissue hydration and prevent bacterial growth. Twelve composite margin segments (n=12) were selected from teeth with existing composite restorations for NIR imaging. Sixteen sound posterior extracted teeth (n=16) were then drilled on one side using a high-speed dental burr and filled with Z250 composite (3M, Minneapolis, MN).

A CO₂ laser (Impact 2500, GSI Lumonics Rugby, UK) was used to produce small incisions on extracted teeth forming the outline of a 4×4-mm square around the region of interest (ROI) and served as fiducial marks for PS-OCT scans. The laser was modified to produce a Gaussian output beam (single spatial mode) and pulse duration of between 10–15-μs at a wavelength of 9.3-μm. A planoconvex ZnSe lens with 90-mm focal length was used to focus the laser beam to a spot size of around ~200-μm and fluence of 20 J/cm². Individual laser spots were scanned using a pair of XY actuators (Newport 850G) at 50-μm increments with an automated water spray directed to the surface of the tooth to prevent peripheral thermal damage.

After all images were acquired, the samples were serially sectioned into ~200-μm thick slices using a linear precision saw, Isomet 5000 (Buehler, Lake Buff, IL) perpendicular to the restoration margin. Thin sections were subjected to histological examination with polarized light microscopy and transverse microradiography.

8.3.2 High Resolution Digital Microscopy

Images were taken of the region of interest on each tooth surface using a digital microscopy/3D surface profilometry system, the VHX-1000 from Keyence (Elmwood, NJ) outfitted with the VH-Z25 lens (magnification from 25–175×). Depth composition images (DCDM) were generated by translating the image plane of the objective along the vertical axis capturing a series of images containing all points of the tooth surface in optimum focus, followed by construction of an optimized 2D image using only in focus image regions from the series.

The lesion contrast measurements from visible light images were calculated by averaging the pixel values taken from a ROI approximately 25 × 25-pixels from areas of sound enamel, demineralized enamel and the composite regions. The contrast of the decay relative to both the adjacent sound enamel and restorations were calculated using the formula $(I_L - I_{S/C})/I_L$, where I_L represents the lesion intensity and $I_{S/C}$ represents either the intensity from the sound or composite regions. The image contrast varies from 0 to 1 with 1 being very high contrast and 0 having no contrast.

8.3.3 NIR Transillumination and NIR Cross-Polarized Reflectance

A high sensitivity, InGaAs, camera (SU320-KTSX-1.7RT/RS170) from Sensors Unlimited (Princeton, NJ), with a 320 × 256 pixel focal plane array and 25- μ m pixel pitch was used to capture NIR cross-polarized (CP) reflectance, cross-polarized interproximal transillumination and occlusal transillumination images. CP-reflectance images were acquired using polarized light from a tungsten halogen lamp (E Light) and capturing the

reflected signal through an orthogonal linear polarizer, long pass 1500–1700-nm optical filter and lens system. CP-interproximal transillumination images were acquired by focusing (40-mm NIR AC ThorLabs, Newton, New Jersey) polarized light from a tungsten halogen lamp laterally onto the sample and collecting the transmitted signal through an orthogonal linear polarizer, band pass 1300-nm optical filter (Spectragon, FWHM=80-nm) and lens system. Occlusal transillumination images utilized light from a tungsten halogen source and bifurcated fiber optic bundle equipped with two linear arrays to impart light angled apically at the cemento-enamel junction from both sides of the tooth and collect transmitted signal through a band pass 1300-nm optical filter and lens system. Detailed schematics covering the geometry of each modality and theory of the resulting image contrast can be found in previous publications [28]. NIR images were analyzed using the image analysis package provided by IgorPRO software (Wavemetrics, Lake Oswego, OR). Image line profiles five pixels in width were extracted from the sample ROI across the same sample plane for NIR reflectance and transillumination images. The line profiles were normalized from 0 to 1, where 1 represents the maximum contrast value and 0 the minimum across the ROI.

The lesion contrast measurements from NIR reflectance images were calculated by averaging the pixel values taken from a ROI approximately 25×25 -pixels from areas of sound enamel, demineralized enamel and the composite regions. The contrast of the decay relative to both the adjacent sound enamel and restorations were calculated using the formula $(I_L - I_{S/C})/I_L$, where I_L represents the lesion intensity and $I_{S/C}$ represents either the intensity from the sound or composite regions. NIR transillumination images appear in the opposite contrast as reflectance images and are calculated using the

equation $(I_S/C - I_L)/I_S/C$, where I_L represents the lesion intensity and I_S/C represents either the intensity from the sound or composite regions. The image contrast varies from 0 to 1 with 1 being very high contrast and 0 having no contrast.

Sound-restored composite samples were imaged in transillumination at three principal wavelength bands in the NIR using band-pass (BP) filters BP-1300-90, BP-1460-85 from Spectrogon (Parsippany, NJ) and BP1550-40 from Thorlabs. A ROI, approximately 25×25 pixels was extracted from an occlusal surface area of sound enamel and a region within the composite and averaged to calculate the mean intensity from the respective regions I_S and I_C . Image contrast was calculated using the equation $(I_C - I_S)/I_C$. The image contrast varies from 0 to 1 with 1 being very high contrast and 0 having no contrast. The contrast was calculated for each wavelength. For teeth with composites that extended into the dentin, the same analysis was performed to calculate the image contrast between the sound dentin and composite restoration. A one-way analysis of variance (ANOVA) followed by the Tukey-Kramer post hoc multiple comparison test was used to compare groups for each wavelength employing Prism software (GraphPad, San Diego, CA).

8.3.4 Measure of Image Reliability

Four clinicians (2 per method) examined tooth samples using visible light or NIR images while blind to the other modality, and provided yes or no responses to the question, *does demineralized tissue exist at the restoration margin?* Visible inspection permitted the use of $10\times$ magnification, LED lights and dental instruments to examine the extracted tooth surface. Clinicians chosen for visible inspection were trained dental educators. NIR inspection consisted of viewing 2D still images of samples obtained via transillumination

or reflectance geometries on a digital display. Clinicians chosen for NIR inspection had limited experience interpreting NIR images due to the novelty of the technology.

8.3.5 Polarization Sensitive Optical Coherence Tomography

An all-fiber-based optical coherence domain reflectometry (OCDR) system was used with polarization maintaining (PM) optical fibers, high-speed piezoelectric fiber-stretchers and two balanced InGaAs receivers that was designed and fabricated by Optiphase, Inc., Van Nuys, CA. The two-channel system was integrated with a broadband superluminescent diode (SLD) Denselight (Jessup, MD) and a high-speed XY-scanning system (ESP 300 controller and 850G-HS stages, Newport, Irvine, CA) for *in vitro* optical coherence tomography. The high power (15-mW) polarized SLD source, emitted near-IR light at a center wavelength of 1317-nm with a spectral bandwidth full-width at half-maximum (FWHM) of 84-nm. The beam was focused onto the sample surface using a 20-mm focal length AR-coated planoconvex lens. This configuration provided lateral and axial resolutions of approximately 20- μm and 10- μm in air with a signal to noise ratio of greater than 40–50-dB. When imaging enamel tissues with refractive index $n \approx 1.63$, spatial resolution is increased relative to air due to the tissues greater refractive index. The PS-OCT system is completely controlled using Labview software (National Instruments, Austin, TX).

8.3.6 CP-OCT Integrated Reflectivity Collapsed C-scan 2D Projections

Raw OCT data was analyzed using a program written in Labview. Co-polarization and cross-polarization (CP-OCT) OCT images were acquired for each sample, however only the cross-polarization images were processed and analyzed. For speckle noise reduction, signals not exceeding four standard deviations from the mean background noise floor were reduced to the mean background value and a Gaussian blur smoothing algorithm was applied using a 5×5 pixel convolution kernel. In the edge-detection approach, the enamel edge and the lower lesion boundary were determined by applying an edge locator. The program first locates the maximum of each a-scan and differentiates the a-scan maximum as either demineralized or sound using the signal-to-noise ratio as a threshold. The lesion depth is calculated by locating the upper and lower lesion boundaries, calculated by determining the first pixel that does not satisfy the threshold of e^{-2} of the maximum value. The distance per pixel conversion factor was obtained experimentally by system calibration. A linear relationship was established between the OCT lesion depth and the histological depths measured using polarized light microscopy (PLM). Based on this relationship, a linear correction was applied to the lesion depth calculated from OCT (Corrected Pixel Depth = $(1.55 \times \text{Measured OCT pixel depth}) - 37.6$).

Each A-scan of the CP-OCT images was reduced to single values representing the mean reflectivity per pixel integrated over the calculated lesion depth. The mean reflectivity per pixel was calculated by dividing the sum of each A-scan in linear intensity units (IU) by the number of pixels in each A-scan. The integrated reflectivity (ΔR) was calculated by

integrating the reflectivity in IU units over lesion depth calculated as described above. Two dimensional maps, referred to as collapsed C-scans were produced with each pixel representing the integrated reflectivity over the lesion depth at each pixel [67].

8.3.7 Polarized Light Microscopy (PLM)

Polarized light microscopy (PLM) was used for histological examination using a Meiji Techno RZT microscope (Saitama, Japan) with an integrated digital camera, Canon EOS Digital Rebel XT (Tokyo, Japan). Sample sections 200- μm thick are imbibed in deionized water and examined in the brightfield mode with crossed polarizers and a red I plate with 550-nm retardation.

8.3.8 Digital Transverse Microradiography (TMR)

A custom-built digital TMR system was used to measure mineral loss in the lesion areas. A high-speed motion control system with UTM150 and 850G stages and an ESP300 controller Newport (Irvine, CA) coupled to a video microscopy and laser targeting system was used for precise positioning of the tooth samples in the field of view of the imaging system. The volume percent mineral for each sample thin section was determined by comparison with a calibration curve of X-ray intensity vs. sample thickness created using sound enamel sections of 86.3 ± 1.9 vol.% mineral varying from 50 to 300- μm in thickness using IgorPRO image analysis software. The calibration curve was validated via comparison with cross-sectional microhardness measurements, $r^2 = 0.99$. Image line profiles 100–150 pixels in width were extracted from the sample ROI representing the percent mineral at each pixel.

8.4 Results

8.4.1 NIR images of Suspected Secondary Caries

Near-infrared images of composite restoration margins (n=12) revealed the presence of natural recurrent decay as high contrast optical signals from both wall and outer-type lesions. Polarization sensitive optical coherence tomography (PS-OCT) nondestructively validated the signals obtained in the NIR images through integrated reflectivity (ΔR) collapsed C-scans and profiled the lesions variation with depth from the surface with b-scans. Polarized light microscope (PLM) images of 200- μm cross-sections provided histological evidence of the presence of decay and were utilized to classify the lesion type. Transverse microradiography (TMR) images of the same cross-sections were used as the “gold standard” in determining the presence of recurrent decay and reported the percent mineral of the sample per pixel.

Figure 8.1 displays the data obtained from a sample with a class I composite restoration presenting a wall and outer dentinal lesion. The restoration margin of this sample was determined to be sound by both examiners via visual examination. All examiners assessed the NIR transillumination image as positive for secondary caries and the NIR reflectance image as negative. PS-OCT and the histology of thin sections over the sample ROI confirmed the presence of demineralization along the wall of the restoration penetrating the outer enamel and dentin. The PS-OCT B-scan displayed in panel H of Fig. 8.1 shows decay running along the angle of the occlusal restoration that expands considerably at the point where the lesion meets the dentinoenamel junction. This demineralization profile is corroborated exactly by the TMR image shown in panel E. The

black line in panel G represents the TMR percent mineral line profile and indicates that the lesion is demineralized to a minimum of approximately 25–30% at the margin. NIR reflectance (blue) and NIR transillumination (red) line profiles extracted from panels B & C respectively, are overlaid with TMR in panel G. Despite being assessed by the examiners as sound, the NIR reflectance image shows an increase in signal coincident with increased demineralization presenting high contrast (0.74) relative to the adjacent enamel and moderate contrast (0.27) contrast value versus the neighboring composite. The NIR transillumination image exhibits a loss in signal from the lesion area with high contrast (0.68) compared to the bordering enamel and moderate contrast (0.18) relative to the composite.

The sample presented in Fig. 8.2 has another class I composite restoration with a wall and an outer enamel lesion. Similar in location to the lesion depicted in Fig. 1, the margin of the sample in Fig. 8.2, has demineralization present which was identified by all examiners for visual, NIR reflectance and NIR transillumination. There is a broad lesion that runs across a significant part of the margin while extending into the adjacent enamel. The TMR images shown in panel E and percent mineral line profile (black) in panel G indicate that the mineral content of the lesion profile varies from ~70% mineral in the outer lesion to less than ~30% at the restoration margin. NIR transillumination (panel B), reflectance (panel C) and PS-OCT (panels F & H) each show increased contrast due to demineralization consistent with the PLM and TMR histology. Line profiles extracted from the NIR reflectance (blue) and NIR transillumination (red) are overlaid with the TMR mineral profile in panel G. The NIR reflectance signal exhibits a maximum intensity at the restoration margin presenting the decay with high contrast compared to enamel (0.47)

and moderate contrast (0.35) relative to the composite. The NIR transillumination image exhibits high attenuation across the body of the outer lesion providing high contrast (0.63) versus enamel and poor contrast (0.012) compared to the composite. The PS-OCT B-scan in panel H of Fig. 8.2 manifests increased scattering at the margin from the wall portion of the lesion, and the adjacent enamel resulting from the outer lesion.

8.4.2 Secondary Caries lesion contrast measurements

For a secondary caries lesion to be easily detected using optical imaging technologies the carious lesion needs to demonstrate high contrast relative to both the adjacent sound enamel and the composite restorative material. To determine if NIR technologies provide significantly higher contrast images of secondary caries compared to visible light, the mean lesion contrast relative to both the adjacent sound enamel and composite restoration was calculated from visible, NIR reflectance and NIR transillumination images of sample restoration margins (Table 8.1). Compared to the sound enamel, visible images averaged almost no contrast (-0.052) because of their either bright (white spot) or dark (stained) appearance. NIR transillumination demonstrated moderate contrast (0.45) and significantly outperformed visual, and NIR reflectance demonstrated greatest contrast (0.72) and was significantly different from both visible and NIR transillumination. Compared to the composite material, NIR reflectance contrast (0.31) was significantly greater than visible (-0.13) and NIR transillumination (0.13) contrast measurements. Table 8.1 also shows the range of contrast values calculated for each modality relative to sound enamel and the composite material. For the NIR reflectance measurements

relative to the composite, the contrast ranges from -0.71 to 0.73 due to the variety of restorative materials used in natural teeth and their different NIR optical properties.

8.4.3 Examiner diagnosis of NIR images compared to visual inspection

Histology indicated the presence of secondary caries on all of the teeth selected (12/12). For visual examination the two examiners indicated secondary caries on only 13 out of the 24 assessments (2 per tooth), while for NIR transillumination (19/24) and (11/24) for NIR reflectance. For combined NIR transillumination and reflectance there was at least one positive prediction on 11/12 samples while for visible there was at least one positive prediction for only 8/12 of the teeth.

8.4.4 Multispectral NIR images of composite restorations in sound teeth

Multispectral NIR occlusal transillumination images centered at 1300-nm, 1460-nm and 1550-nm enhanced the visibility of Z250 composite restorations placed in sound posterior teeth. Figure 8.3 shows sample NIR images at each wavelength as well as a visible reflectance image with the sample air dried and viewed under 25 \times magnification (Fig. 8.3 A). Confidently determining the restorations boundaries with visible inspection remains difficult despite the aforementioned aids. When observed under NIR transillumination (Fig. 8.3 B,C,D), the restoration boundaries are clearly defined and appear lighter compared to the darker adjacent enamel. Based on the mean contrast values measured from $n=16$ samples, the Z250 composite manifested the highest contrast for transillumination with 1460-nm (0.55 ± 0.16 Fig. C) and 1550-nm (0.59 ± 0.14 Fig. D) light and exhibited significantly lower contrast at 1310-nm (0.10 ± 0.12 Fig. B). This is likely due to the reduced water content of the composite material compared to enamel.

8.5 Discussion

The accurate diagnosis of secondary caries requires the detection of demineralization adjacent to and along the restoration, accompanied with an assessment of the lesion activity [18, 164, 165]. This study demonstrates that two-dimensional near-infrared images can show recurrent decay from either wall or outer secondary caries lesions. The agreement between PS-OCT collapsed ΔR C-scans and 2D NIR images (panels C and F in Figs. 8.1 & 8.2) are striking in terms of contrast and spatial features. The similarities in 2D NIR imaging and collapsed C-scan OCT data sets suggest that NIR images are suitable for the rapid screening of anterior and posterior teeth. Furthermore, the transparency of enamel and composite to light in the wavelength range between 1300–1700-nm allows evaluation of areas masked by the many commercially available restorative materials demonstrated previously [162].

The advantage of using NIR light at wavelengths greater than 1300-nm, which are not absorbed by the organic molecules responsible for exogenous stains, cannot be overstated. Imaging teeth without the interference of stain will allow a direct assessment of the actual demineralization present in the lesion and prevent false-positive diagnosis based on lesion contrast owing to absorption from stain. This is an important advantage over visual and fluorescence based methods that require clean surfaces and are confounded by stains.

The ability to distinguish between composite, sound enamel and demineralized enamel is necessary for both the detection of recurrent decay and the replacement of restorations with minimal loss of sound tissue structure. The panel of visible and NIR transillumination

images in Fig. 8.3, demonstrate that tooth-color-matched restorations manifest very high contrast with sound tooth structure at NIR wavelengths coincident with high water absorption. NIR light is attenuated to a lesser degree in composite due to the lower water content of composite compared to enamel and dentin.

Ease of interpretation is an important advantage of NIR images for use in detecting dental decay. The natural affinity for such images is supported by the examiner agreement in which this study found NIR images are evaluated more consistently than visual inspection by removing color interpretation and making the comprehension grayscale. This was achieved by clinicians whom have minimal training with this new technology and did not have the ability to view the sample in real time from any angle, which is advantageous for diagnosis and is standard protocol when imaging *in-vivo*.

The main functional limitation when imaging primary caries and secondary caries with NIR imaging technologies is that they rely on light scattering to distinguish between sound and demineralized tooth structure. The complex tooth topography, cracks in dental enamel, and restorative materials with unknown NIR optical properties can all contribute to either masking or generating optical signals that appear as enamel demineralization and can cause false-positive and false-negative diagnoses. Using two-dimensional NIR imaging does well to overcome these limitations by providing high-definition images of the whole tooth surface that enables the clinician to identify if the tooth has any factors that can confound diagnosis.

8.6 Conclusion

Near-infrared imaging modalities are ideally suited for the detection of demineralization adjacent to and beneath restorative materials due to the high transparency of enamel and dental composites to NIR light. Specifically, NIR reflectance and transillumination imaging are viable methods for the rapid screening of restored tooth surfaces that are capable of detecting early stages of caries lesions.

8.7 Tables and Figures

Table 8.7.1. Mean Lesion Contrast Relative to Adjacent Sound Enamel and Composite Restoration.

	Mean Contrast	±SD	Min.	Max	Statistical group*
<i>Sound Enamel</i>					
Visible	-0.052	± 0.25	-0.47	0.26	a
NIR reflectance ($\lambda=1500-1700$ -nm)	0.72	± 0.13	0.49	0.87	b
NIR transillumination ($\lambda=1300$ -nm)	0.45	± 0.25	0.12	0.75	c
<i>Composite Material</i>					
Visible	-0.13	± 0.27	-0.56	0.20	a
NIR reflectance ($\lambda=1500-1700$ -nm)	0.31	± 0.40	-0.71	0.73	b
NIR transillumination ($\lambda=1300$ -nm)	0.13	± 0.16	-0.12	0.44	a,b

* Groups with same letter are statistically similar $P > 0.05$.

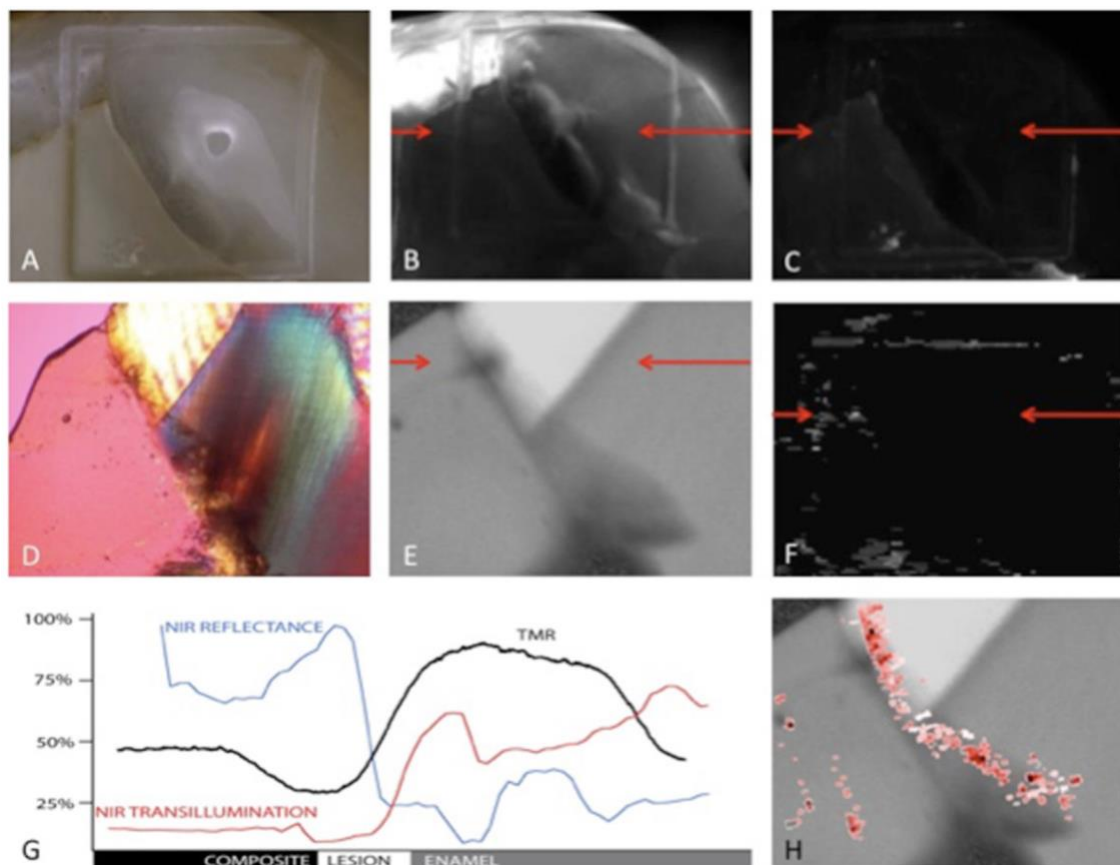


Figure 8.7.1. (A) High magnification digital image (25x magnification) (B) NIR transillumination image (0.68 contrast vs. enamel & 0.18 contrast vs. composite) (C) NIR cross-polarized reflectance image (0.74 contrast vs. enamel & 0.27 contrast vs. composite) (D) Polarized light microscope image (40x magnification) of 200- μ m cross section (E) Transverse microradiography of 200- μ m cross section (F) PS-OCT 2D projection of the integrated reflectivity (G) Line profiles (NIR trans-Red, NIR ref-Blue, TMR-Black) normalized from 1–0 (percent mineral for TMR, normalized image NIR pixel values) NIR Line profiles, TMR and PLM cross-section, and PS-OCT B-scan locations are indicated by red arrows. (H) PS-OCT B-scan (red) overlaid with TMR image (gray scale).

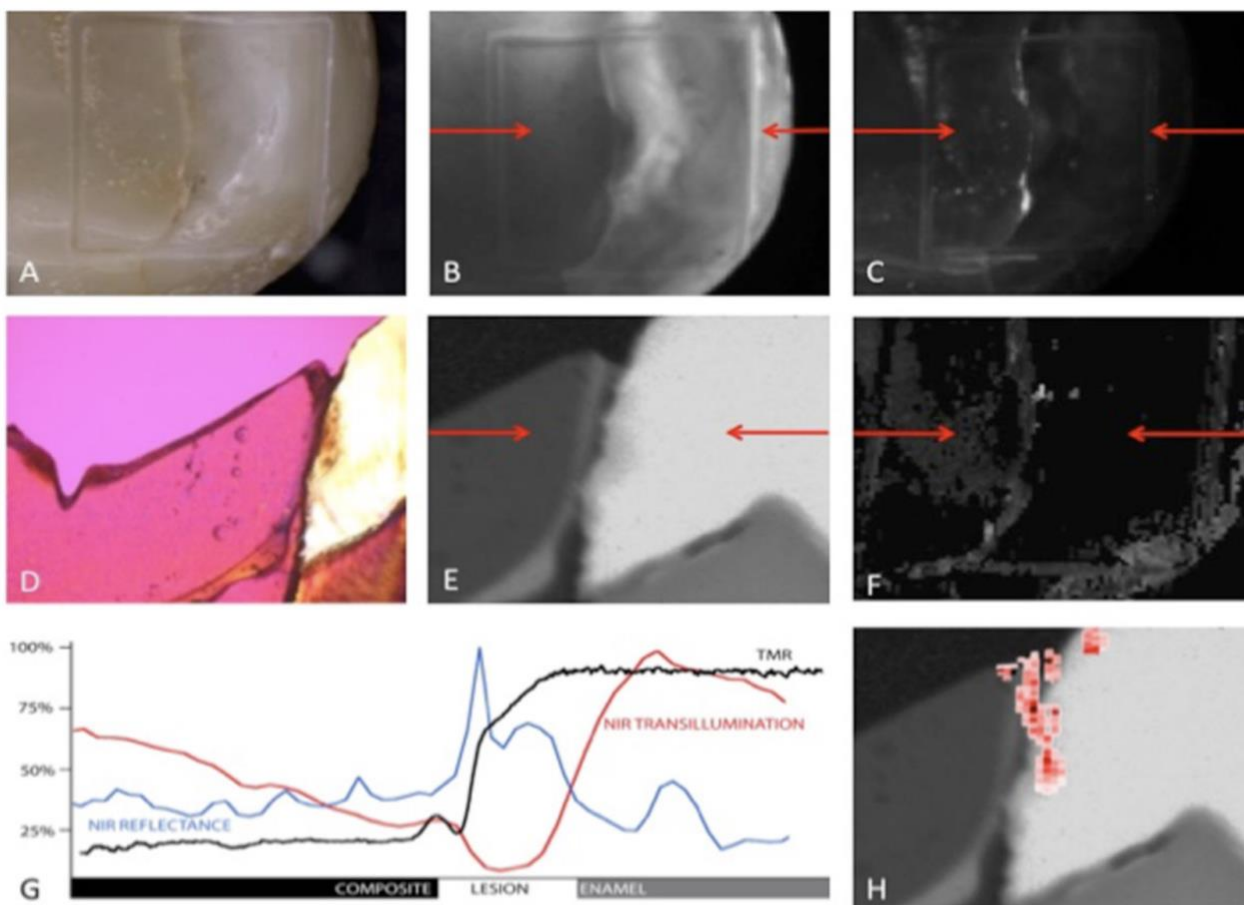


Figure 8.7.2 (A) High magnification digital image (25× magnification) (B) NIR transillumination image (0.63 contrast vs. enamel & 0.012 contrast vs. composite) (C) NIR cross-polarized reflectance image (0.47 contrast vs. enamel & 0.35 contrast vs. composite) (D) Polarized light microscope image (40× magnification) of 200- μ m cross-section. (E) Transverse microradiography of 200- μ m cross-section (F) 2D projection of the integrated reflectivity (G) Line profiles (NIR trans-Red, NIR ref-Blue, TMR-Black) normalized from 1–0 (percent mineral for TMR, normalized image NIR pixel values). NIR Line profiles, TMR and PLM cross-section, and PS-OCT B-scan locations are indicated by red arrows. (H) PS-OCT B-scan (red) overlaid with TMR image (grayscale).

CHAPTER IX

Near-IR Transillumination and Reflectance Imaging at 1300-nm and 1500-1700-nm for

In Vivo Caries Detection

9.1 Summary

Several studies suggest that near-IR imaging methods at wavelengths longer than 1300-nm have great potential for caries detection. In this study, the diagnostic performance of both near-IR transillumination and near-IR reflectance was assessed on teeth scheduled for extraction due to orthodontic treatment (n = 109 teeth on 40 test subjects). Three intra-oral near-IR imaging probes were fabricated for the acquisition of in vivo images using a high definition InGaAs camera and near-IR broadband light sources. Two transillumination probes provided occlusal and approximal images using 1,300nm light which manifests the highest transparency in enamel. A third reflectance probe utilized cross-polarization and operated at wavelengths greater than 1500nm where water absorption is higher which reduces the reflectivity of sound tissues, significantly increasing lesion contrast. Teeth were collected after extraction and sectioned and examined with polarized light microscopy and microradiography which served as the gold standard. In addition, radiographs were taken of the teeth and the diagnostic performance of near-IR imaging was compared with radiography. Near-IR imaging was significantly more sensitive ($P < 0.05$) than radiography for the detection of lesions on both occlusal and proximal surfaces. Near-IR imaging methods are ideally suited for screening all tooth surfaces for carious lesions.

9.2 Introduction

Dental enamel manifests its highest transparency near 1,300-nm where the scattering coefficient of enamel is 20–30 times lower than it is at visible wavelengths [41, 42]. Due to the high transparency, novel imaging configurations are feasible in which the tooth can

be imaged from the occlusal surface after shining light at and below the gum line, which we call occlusal transillumination [28, 123]. Upon demineralization the scattering coefficient of enamel increases by 1–2 orders of magnitude at 1300-nm to yield high contrast between sound and demineralized enamel for caries detection [43]. Therefore, this wavelength range is ideally suited for the transillumination of approximal dental caries lesions (dental decay in between teeth). Previous studies carried out by our group over the past 12 years have demonstrated that approximal lesions can be imaged by occlusal transillumination of the proximal contact points between teeth and by directing near-IR light below the crown while imaging the occlusal surface [28, 74, 76]. The latter approach is capable of imaging occlusal lesions as well with high contrast [7, 28, 71, 121, 123]. Optical transillumination was used extensively before the discovery of X-rays for detection of dental carious lesions. Over the past two decades there has been continued interest in this method, especially with the availability of high intensity fiber optic based illumination systems for the detection of approximal lesions [84-88, 166]. A digital fiber optic transillumination system, called DiFoti from Electro-optics Sciences (Irvington, NY) that utilizes visible light for the detection of caries lesions was introduced several years ago [89]. Carious lesions appear dark upon fiber optic transillumination (FOTI) due to increased scattering and absorption by the lesion reducing optical transmission. Several studies have been carried out using visible light transillumination either as an adjunct to bite-wing radiography or as a competing method for the detection of approximal carious lesions [89, 167-169]. However, FOTI and DIFOTI operate in the visible range where strong light scattering prevents imaging through the entire tooth [41, 42]. More recently, another system has been introduced called the Diagnocam from Kavo (Biberach,

Germany) that uses an occlusal transillumination probe with 780-nm light [81, 82]. We previously investigated using transillumination imaging at 830-nm which has the advantage of utilizing a low-cost silicon CCD sensor optimized for the near-IR. The 830-nm system was capable of higher performance than visible systems, but the contrast was significantly lower than 1310-nm and simulated lesions could not be imaged through the full enamel thickness [76]. Other groups have confirmed the high potential of the near-IR for imaging dental decay [51, 170].

There are other important advantages of imaging dental decay in the near-IR. Stains that are common on tooth occlusal surfaces do not interfere at near-IR wavelengths since none of the known chromophores absorb light in the near-IR beyond 1300-nm [51, 123]. More recently, Almaz et al. demonstrated that it was necessary to use near-IR wavelengths greater than 1150-nm to avoid significant interference from stains when measuring lesion contrast in reflectance and transillumination modalities [171]. Therefore, stains can be easily differentiated from actual demineralization in the near-IR range, which is not possible at visible wavelengths. Chung et al. [40] indicated that absorption due to stains contributed more to the lesion contrast than increased scattering due to demineralization at visible wavelengths [64]. Since it is impractical to remove stains from the deep grooves and fissures on tooth occlusal surfaces, lack of interference from stains at longer near-IR wavelengths is a significant advantage.

Additionally, reflectance imaging at wavelengths greater than 1300-nm have yielded extremely high contrast of early demineralization [27, 40, 45, 50-52]. More recent near-IR imaging studies suggest that near-IR wavelengths coincident with high water

absorption namely, 1450-nm or 1,500–1700-nm, yield the highest contrast of demineralization on tooth surfaces. We hypothesize that higher water absorption at these wavelengths reduces the reflectivity in the underlying sound enamel and dentin resulting in even higher contrast between sound and demineralized enamel than observed at 1300-nm. Hyperspectral reflectance measurements by Zakian et al. [51] show that the tooth appears darker at wavelengths coincident with higher absorption by water.

Two prior clinical studies involving near-IR transillumination imaging have been published [26, 28]. In 2009, we demonstrated that approximal lesions that appeared on radiographs could be detected with near-IR imaging with similar sensitivity [28]. This was the first step in demonstrating the clinical potential of near-IR imaging for approximal caries detection. Even though the sensitivity of radiographs is not very high [172-176], most studies indicate the specificity of radiographs is above 90%, which makes it a suitable standard for comparison with the first test of this new imaging technology. In addition to demonstrating that the sensitivity of near-IR transillumination was as high as radiography, we found that multiple imaging geometries could be employed to aid in diagnosis, and that the occlusal imaging geometry in which light is applied near the gumline is extremely valuable for detecting approximal lesions [28]. In a second study completed in 2011, teeth with non-cavitated occlusal caries lesions that were not radiopositive were examined in test subjects using near-IR occlusal transillumination at 1300-nm prior to restoration [26]. That study demonstrated that occlusal caries lesions can be imaged with high contrast in vivo and that near-IR occlusal transillumination is an excellent screening tool for occlusal lesions. The next logical step is to carry out in vivo studies in which the near-IR is used as a screening tool to detect lesions and assess the diagnostic performance of our custom

fabricated near-IR system. In addition, the clinical potential of near-IR reflectance imaging has not been investigated.

In this study, we assessed the diagnostic performance of both near-IR transillumination and near-IR reflectance probes that we fabricated in our laboratory for both occlusal and approximal lesions. Premolar teeth scheduled for extraction due to orthodontic considerations were imaged and after extraction the teeth were collected and sectioned and examined with polarized light microscopy and transverse microradiography which served as the gold standard. In addition, extra-oral radiographs were taken of teeth and the diagnostic performance of near-IR imaging was compared with radiography.

9.3. Materials and Methods

9.3.1 Visible Images

A Dino-Lite digital microscope, Model AM7013MZT, AnMO Electronics Corp. (New Taipei City, Taiwan) equipped with a dental mirror was used to acquire visual images, both wet and dry, of the patients' teeth prior to near-IR imaging. The digital microscope captures 5-megapixel ($2,592 \times 1,944$) color still images and video. Eight white LED lights contained in the camera illuminate the teeth and the device features a single polarizing element that helps reduce glare. Visual images are taken for reference and compared with near-IR techniques at the beginning of each imaging session.

9.3.2 Near-IR Imaging System

The individual probes are designed to work interchangeably by attaching to a set of universal components connecting the probes to the near-IR camera through relay optics.

Two near-IR achromatic lenses, $f = 60\text{-mm}$ AC254-060-C and $f = 150\text{-mm}$ AC254-150-C (Thorlabs, Newton, NJ) were used to project the captured light onto a high sensitivity InGaAs focal plane array camera, Model GA1280J (Sensors Unlimited, Princeton, NK) with a 1280×1024 -pixel format and $15\text{-}\mu\text{m}$ pixel pitch. A 360° rotation element allows simple rearrangement of the imaging probe to access the upper and lower teeth. The assembly is physically supported via an aluminum post attached to an elastic band wrapped around the forearm of the clinician. A power supply and output cable attaches to the backside of the camera and connects the instrumentation with computers and optical fibers through a mesh bundle. Near-IR video was acquired at a rate of 30 frames per second and the imaging time ranged from 1 to 2 minutes per probe.

9.3.3 Near-IR Approximal Transillumination

Near-IR approximal transillumination produces diagnostic images similar in appearance to that of conventional bitewing X-rays from both the facial and lingual viewpoints. Figure 9.1A is a schematic drawing of the imaging probe that couples with the common optical components of the system described in Near-IR Imaging System section. Light centered at 1310-nm is generated using a super-luminescent laser diode (SLD), Model SLD72 (COVEGA Corporation, Jessup, MD) with 50nm bandwidth. Fiber optic cables are used to deliver the light into a Teflon diffusing element. Light emitted from the diffusing element propagates through the tooth, that is located between the diffusing element and a right-angled mirror and is reflected down the imaging tube through the relay optics and onto the focal plane array of the camera. Each tooth is imaged from the facial side and then the probe is rotated 180° and the tooth is imaged from the lingual position. The approximal

transillumination probe delivered a 6–10-mW cone of light onto the lingual and buccal surfaces with a circular area of 1.5-cm in diameter.

9.3.4 Near-IR Occlusal Transillumination

Near-IR occlusal transillumination produces diagnostic images unique to near-IR imaging systems and is capable of detecting both occlusal and approximal lesions. Figure 9.1B shows a diagram of the probe. Light centered at 1310-nm is generated using a SLD, SLD72 with a 50-nm bandwidth. Fiber optic cables are used to deliver the light into two diffusing elements made of Teflon. The diffusing elements are positioned using copper tubes that direct the light below the cementum-enamel junction (CEJ) into the gingival tissue from both the lingual and facial sides at a shallow angle. Light that enters the tooth diffuses throughout its interior and out the occlusal tooth surface. A right-angled mirror reflects the emitted light down the imaging tube through the relay optics and onto the focal plane array of the camera. The probe is designed to rotate 180° for the imaging of both upper and lower teeth. The occlusal transillumination probe delivered a 6–10-mW cone of light onto the lingual and buccal surfaces with a circular area 3-mm in diameter.

9.3.5 Cross-polarized Near-IR Reflectance

Initially, a near-IR reflectance probe without cross-polarization elements was used to acquire in vivo images. For this probe, light from an SLD operating at 1600-nm was used to deliver NIR light into a fiber optic with a Teflon diffusing element. Light passes through the hollow width of the imaging probe and interacts with the surface of the tooth where it is reflected or scattered back towards the relay right-angled mirror. Specular reflections

from the tooth surfaces make identification of demineralized areas difficult. To overcome this phenomenon, cross-polarization techniques are used to reduce the amount of reflected light reaching the detector.

A schematic drawing of the cross-polarized reflectance probe is shown in Figure 9.1C. Light from a tungsten-halogen lamp, Model HL-2000 (Ocean Optics, Dunedin, Florida) and a long pass 1,500nm filter, Model FEL1500 (Thorlabs) was used. The tungsten-halogen source replaced the SLD source used by the previous model in order to reduce speckle noise from interference of the coherent light. Wavelengths longer than 1,500nm were delivered to the probe through a glass fiber optic waveguide (Dolan-Jenner, Boxborough, MA). The light emitted from the waveguide is incident on a polarizing beam splitter cube, Model PBS054 (Thorlabs) where a single linear polarization state is reflected down through the hollow width of the probe and onto the sample surface. The light interacts with the tooth and is reflected or scattered back to a right-angled mirror and directed down the imaging tube to the focal plane array. A second linear polarizer, Model MPIRE-100-C (Thorlabs) inserted into the rotating element and oriented orthogonally to the polarization state of the first is used to eliminate specular reflected light from reaching the detector. The reflectance probe delivered a 6–10 mW cone of light over a circular area 1.5-cm in diameter.

9.3.6 Patient Recruitment

After obtaining IRB approval and written informed consent, 40 participants were recruited from the patient population of the University of California, San Francisco School of

Dentistry. Subjects aged 12–60 with 2–4 premolars (universal numbering system 4/5, 12/13, 20/21, and 28/29) scheduled for extraction were recruited. A total of 109 teeth were imaged in the study. None of the collected premolars were excluded from the study.

9.3.7 Visible and Near-IR Clinical Imaging Protocol

Each premolar tooth was imaged in vivo with the visible and near-IR imaging systems while viewing a live video feed of the captured images on a computer monitor. Imaging was employed in the following order: (i) Conventional photos of the teeth were taken (both wet and air dried) using a digital camera; (ii) Cross-polarized near-IR reflectance images were acquired for the detection of surface demineralization in the pits and fissures and other external (surface) signs of decay; (iii) Occlusal near-IR transillumination was used to detect approximal lesions and deeper (more severe) occlusal lesions; (iv) Approximal near-IR transillumination images were captured for the detection of lesions on proximal surfaces. During near-IR reflectance imaging an air spray was employed to dry the tooth surface (increasing lesion contrast) and prevent water/saliva accumulation on the occlusal surface. The air spray is also used to remove air bubbles during near-IR transillumination imaging. The video output from the InGaAs array was recorded and displayed simultaneously for all three near-IR probes through the coupled computer system.

9.3.8 Extra-oral Digital Radiographs

After the extracted premolars ($n = 109$) were collected from the clinic, samples were sterilized using gamma radiation and stored in 0.1% thymol solution to maintain tissue

hydration and prevent bacterial growth. Then, samples were mounted in black orthodontic acrylic blocks (Great Lakes Orthodontics, Tonawanda, NY) and imaged with digital radiographs using a CareStream 2200 System (Kodak, Rochester, NY) operating at 60 kV.

9.3.9 Clinical Evaluation of Digital Radiographs and Near-IR Images

One clinician examined only the diagnostic radiographs while another clinician examined only the near-IR digital videos for each of the near-IR probes while blinded to the other modalities. Each clinician was a practicing dentist with an active private practice and more than 20 years of experience. The clinician chosen to evaluate digital radiographs was a trained dental educator. The clinician who performed near-IR inspection had prior experience with near-IR transillumination and had participated in our previous near-IR transillumination study [28].

During video recording the probes were rotated to acquire images at various angles. This was particularly important for near-IR reflectance imaging to avoid the interference of specular reflection from the tooth. Specular reflection is only visible at normal incidence and vanishes at other angles while lesions remain visible at all angles. Based on the diagnostic video, evaluators diagnosed the presence and depth (S, E1, E2, D1, D2) of approximal and occlusal lesions: S—sound (no lesion present); E1—lesion present with depth restricted to the outer half of enamel; E2—lesion present with depth greater than half the enamel thickness but not yet penetrating into the dentin; D1—lesion present and penetrating into the inner half of dentin; D2—lesion present and penetrating into second

half of dentin. Differential diagnosis was requested to ensure that the clinicians would not overlook the earliest signs of decay in each modality. The comparison of the NIR and X-ray did not account for the differential diagnosis of lesion depth.

9.3.10 Sectioning, Polarized Light Microscopy (PLM), and Transverse Microradiography (TMR)

After all diagnostic images were captured, samples were serially sectioned into ~200 μm thick mesio-distal slices using a linear precision saw, Isomet 5000 (Buehler, Lake Buff, IL). Thin sections were subjected to histological examination by polarized light microscopy and transverse microradiography.

Polarized light microscopy (PLM) was used for histological examination using a Meiji Techno RZT microscope (Saitama, Japan) with an integrated digital camera, Canon EOS Digital Rebel XT (Tokyo, Japan). Sample sections 200 μm thick were imbibed in deionized water and examined in the bright field mode with crossed-polarizers and a red I plate (550-nm retardation).

A custom-built digital TMR system was used to measure mineral loss in the lesion areas. A high-speed motion control system with UTM150 and 850G stages and an ESP300 controller Newport (Irvine, CA) coupled to a video microscopy and laser targeting system was used for precise positioning of the tooth samples in the field of view of the imaging system. The volume percent mineral for each thin section was determined by comparison with a calibration curve of X-ray intensity versus sample thickness created using sound enamel sections of 86.3 ± 1.9 vol.% mineral varying from 50 to 300 μm in thickness using

IgorPRO image analysis software. The calibration curve was validated via comparison with cross-sectional microhardness measurements, $r^2 = 0.99$. Image line profiles 100–150 pixels in width were extracted from the sample ROI representing the percent mineral at each pixel.

TMR images for occlusal and proximal surfaces of each sample were ranked based on lesion depth using the following ordinal ratings (S, E1, E2, D1, D2) as defined in Evaluation of Digital Radiographs and Near-IR Images section.

9.3.11 Statistical Analysis

The depths of carious lesions located on the occlusal and proximal surfaces measured from histological TMR analysis were analyzed using the χ^2 statistic calculated using InStat software (GraphPad, San Diego, CA). The diagnostic performance of each modality was measured by comparing the clinical evaluations of digital X-rays and NIR images to the gold standard TMR measurements using contingency tables. The sensitivity and specificity statistics, as well as the paired comparison McNemar's test, were calculated using InStat software (GraphPad).

9.4 RESULTS

9.4.1 Approximal Lesions in Near-IR Images *In Vivo*

Near-IR imaging was successfully performed on 40 patients in vivo with three NIR imaging modalities using custom built optical probes and an InGaAs camera. Figure 9.2 shows still images captured from a representative approximal lesion acquired using visible light (A), each near-IR modality (B–D), a histological polarized light image (E), and

an extra-oral digital radiograph (F). Individual images are extracted frames from real time video captured by the InGaAs camera that was observed by the clinician during the imaging sessions and lesion assessment. The location of the lesion is demarcated by the dashed yellow outline (B– D,F) and the location of the histological cross section (E) is demarcated by the red dashed line in (A). Figure 9.2B is a near-IR reflectance image acquired at $\lambda = 1,500\text{--}1,700\text{nm}$ and should be directly compared with visible reflectance (Fig. 9.2A). When imaging using near-IR reflectance, carious lesions appear bright (white) compared to darker (black) sound enamel, analogous to a white spot lesion. It is clear that there is a marked increase in the contrast of the lesion when imaged using near-IR wavelengths compared to visible light. Figure 9.2C and D are images acquired from occlusal and approximal near-IR transillumination modalities at $\lambda=1,310\text{nm}$ in which the lesion contrast is flipped relative to the interpretation of near-IR reflectance images. In transillumination sound enamel appears bright (white) and the demineralized tissue appears dark (black). Near-IR occlusal transillumination provides a diagnostic image of the light penetrating upwards to the occlusal surface which can be attenuated by demineralized enamel regions. In doing so the technique samples the transverse dimensions of the carious lesions which is unique to this modality. Figure 9.2D is a near-IR approximal transillumination image that should be directly compared with the digital extraoral radiograph shown in Figure 9.2F in which the lesion appears dark compared to the surrounding sound tissue.

9.4.2 Occlusal Lesions in Near-IR Images *In Vivo*

Figure 9.3 shows a representative sample with occlusal demineralization in the occlusal pits and fissures (A–C) and another sample with staining in the pits and fissures but

without decay (D–F). Figure 9.3A is a visible image of a sample that demonstrates no signs of early demineralization in the pits and fissures even without the presence of stain to mask these early optical changes (clean pits and fissures). Figure 9.3B is the near-IR cross-polarized reflectance image of the sample which easily identifies decay in the distal pit in high contrast as indicated by the yellow outline. Figure 9.3C is a PLM image of a histological cross section taken across the pit which reveals the lesion depth to be approaching the dentinoenamel junction. Figure 9.3D is a visible image of another sample that has stain in the distal pit. Despite the strong absorbance from stain in the visible image, the near-IR cross-polarized reflectance image (Fig. 9.3E) does not demonstrate any lesion contrast from the distal pit. The histological data from the PLM image (Fig. 9.3F) confirms that there is no lesion developing in the distal pit of this sample

9.4.3 Histological Analysis of Lesion Location and Depth

Transverse microradiography (TMR) performed on 200 μm thick mesiodistal premolar cross sections determined that 105 of 109 (96.3% prevalence) had at least early demineralization (lesion depth $\geq\text{E1}$) on either a proximal or occlusal tooth surface. Carious lesions were more prevalent on the occlusal surface (89/109, 81.7% prevalence) than the mesial or distal proximal surfaces (30/109, 27.5% prevalence) in this premolar population. Thirteen of the 105 (12.4%) carious premolars had coexisting occlusal and proximal lesions. Occlusal and approximal lesions exhibited similar variation in lesion depth determined by a Chi Squared test yielding $\chi^2 = 2.430$ and $P = 0.3$. No severe D2 lesions were found.

9.4.4 Comparison of Digital Radiographs and Near-IR Imaging

Two clinicians evaluated the extraoral digital radiographs and the near-IR video data acquired during the patient imaging sessions. They carried out the evaluations blinded to the other imaging modalities. The reported diagnoses were stratified by lesion location for each modality and were analyzed for sensitivity and specificity followed by repeated measures McNemar's statistic to test for significance in observed differences between techniques against the histological gold standard, TMR. For carious lesions located on the occlusal tooth surface digital radiographs were only able to identify a single lesion (1/109) and demonstrated a sensitivity of 0.01 (95%CI -0.00 to 0.07) and specificity of 1.00 (95%CI - 0.83 to 1.00), (Table 9.1). The near-IR imaging system demonstrated substantial improvement in the sensitivity to occlusal lesions compared to radiographs yielding a calculated value of 0.49 (95%CI -0.38 to 0.59), and associated specificity of 0.70 (95%CI -0.46 to 1.88). The 95% confidence intervals and McNemar's test show that the near-IR system was more sensitive ($P = 0.0001$) and as specific ($P = 0.077$) as digital radiographs when detecting occlusal decay. For carious lesions located on proximal tooth surfaces digital radiographs demonstrated a sensitivity of 0.23 (95%CI -0.10 to 0.42) and specificity of 0.96 (95%CI - 0.89 to 0.99). The near-IR imaging system demonstrated marked improvement in the sensitivity to detected approximal lesions compared to radiographs yielding a calculated value of 0.53 (95%CI -0.34 to 0.72) and associated specificity of 0.86 (95%CI -0.76 to 0.93). The 95% confidence intervals and McNemar's test show that the near-IR system was more sensitive ($P = 0.013$) and as specific ($P = 0.09$) as digital radiographs when detecting occlusal decay.

9.4.5 Comparison of Diagnostic Performance of Individual Near-IR Imaging Probes

The near-IR imaging system employed in this study consisted of three different imaging probes that deliver light into the tooth with different geometries. The sensitivity and specificity of each individual probe for occlusal and proximal surfaces are shown in Table 9.2. For lesions found on the occlusal surface the near-IR cross-polarized reflectance probe was by far the most sensitive modality measuring 0.48 (95%CI -0.38 to 0.59) with a specificity of 0.70 (95%CI -0.46 to 0.88). For lesions found on the proximal surface each near-IR modality demonstrated similar sensitivity and specificity levels.

9.5. Discussion

In this paper, we present the results from the first clinical study assessing the diagnostic performance of near-IR imaging for screening for dental caries. Teeth were imaged without prior knowledge of lesion presence, whereas in all previous clinical studies, lesions were either previously identified by visual examination or radiography before near-IR imaging.

We anticipated that 10–20% of the premolar teeth would have demineralization in the occlusal grooves and that a sample size of 80–160 teeth would be sufficient, based on our previous study that utilized only teeth with radio-positive lesions on proximal surfaces [28]. Histology indicated that 89 of the 109 teeth had demineralization on the occlusal surfaces and 30 out of the 109 teeth had lesions on the proximal surfaces. The great majority of these lesions were small and confined to the enamel and only 28% penetrated to dentin. It is important to stress that these are small lesions that are much more difficult

to detect and image, in comparison to lesions imaged in the recent clinical studies involving the Diagnocam at 780-nm where 96% of the lesions were dentinal lesions [81, 82].

The sensitivity of the combined near-IR imaging probes was significantly higher than radiographs for both occlusal and proximal lesions. It was anticipated that near-IR methods would be more sensitive than radiographs since the radiographic sensitivity for occlusal lesions is extremely poor; however, the sensitivity was also much higher for approximal lesions than radiography, 0.53 versus 0.23. In addition, the sensitivity of each near-IR probe was either individually equal to or higher than radiography.

In reflectance, demineralization appears whiter due to increased light scattering by the pores of the lesion and in the near-IR all the lesions appear white because stains do not interfere [51, 123]. In transillumination, the lesions appear darker due to light scattering which blocks light from penetrating through the tooth. Water absorption causes sound and demineralized areas to appear darker both in reflection and transillumination. In reflectance, at wavelengths with higher water absorption (1,600nm and 1,500–1,700nm) absorption by water of the deeply penetrating near-IR causes sound areas of the tooth to appear darker enhancing the contrast.

The greatest surprise of the study was the remarkable performance of near-IR reflectance imaging considering the high absorption of H₂O at the wavelengths employed. It had the highest diagnostic performance of any of the near-IR probes for both occlusal and approximal lesions. Based on our prior studies on extracted teeth, we had anticipated that near-IR reflectance would be extremely sensitive to early demineralization in the pits and

fissures of the occlusal surfaces. However, we did not anticipate that near-IR reflectance measurements would pick up approximal lesions located well below the surface, as shown in Figure 9.2. This is exciting since near-IR reflectance is the easiest method to employ clinically and is potentially the fastest for clinical screening. It only involves shining light on tooth surfaces and does not require careful positioning of the light sources at the contact point in between teeth for approximal transillumination or at the gums for occlusal transillumination. We were initially concerned about the performance of this probe in the clinical environment due to the high absorption of water and the presence of water on tooth surfaces. Air drying for a few seconds was sufficient to maximize the contrast of the lesions and we had more trouble with strong specular reflections from the tooth surface than absorption by water.

Dentists have based their detection of carious lesions on bite-wing radiographs for more than a century and even though such radiographs may not accurately show the depth, activity or cavitation of these lesions, the standard of care has evolved based on such images. Near-IR imaging is a new imaging technology, and it is important to point out that preliminary use of this device by clinicians is needed to develop/evolve methods to effectively interpret the near-IR images in order to assess the depth and severity of the decay and identify potential false positives before this technology can reach its full potential. Only one evaluator was used for each diagnostic technology and that may have had some impact on the statistical outcome. One must also be concerned about over-detection leading to over-treatment by a technology that may be more sensitive than existing methods.

However, since these near-IR devices do not employ ionizing radiation, there are no restrictions on image acquisition and this method is ideal for monitoring lesions over time. In addition, images collected from the multiple probes and imaging geometries can be integrated to produce a more comprehensive picture of the lesion's location. Marked differences of the appearance of stains, composites, and developmental defects such as fluorosis in the near-IR can be exploited to differentiate them from sound enamel and carious lesions.

Near-IR imaging has been shown to be significantly more sensitive ($P < 0.05$) than radiography for the detection of lesions on both occlusal and proximal tooth surfaces in vivo. Near-IR imaging methods are ideally suited for screening all tooth surfaces for carious lesions.

9.6 Tables and Figures

Table 9.6.1. Sensitivity and specificity calculations for digital radiographs and the NIR imaging system stratified by lesion location compared to the gold standard TMR histology.

Diagnostic variable	Diagnostic performance			
	Occlusal		Proximal	
	X-ray	NIR	X-ray	NIR
Sensitivity	0.01	0.49 [*]	0.23	0.53 [*]
(95%CI)	(0.00–0.07)	(0.38–0.59)	(0.10–0.42)	(0.34–0.72)
Specificity	1.00	0.70	0.96	0.86
(95%CI)	(0.83–1.00)	(0.46–0.88)	(0.89–0.99)	(0.76–0.93)

McNemar's test and 95% confidence intervals were used to determine the significance of the results.

* Indicates statistical significance between digital radiographs and the NIR imaging system.

Table 9.6.2. Sensitivity and specificity calculations for each NIR imaging probe stratified by lesion location compared to the gold standard TMR histology.

Individual NIR probe diagnostic performance						
	Occlusal			Proximal		
Diagnostic variable	R	O	P	R	O	P
Sensitivity	0.48	0.08	–	0.27	0.23	0.23
(95%CI)	(0.38–0.59)	(0.03–0.16)		(0.12–0.46)	(0.1–0.42)	(0.10–0.42)
Specificity	0.70	0.95	–	0.92	0.91	0.96
(95%CI)	(0.46–0.88)	(0.75–1.00)		(0.84–0.97)	(0.83–0.96)	(0.89–0.99)

R, reflectance; O, occlusal transillumination; P, approximal transillumination.

95% confidence intervals were used to determine the significance of the results.

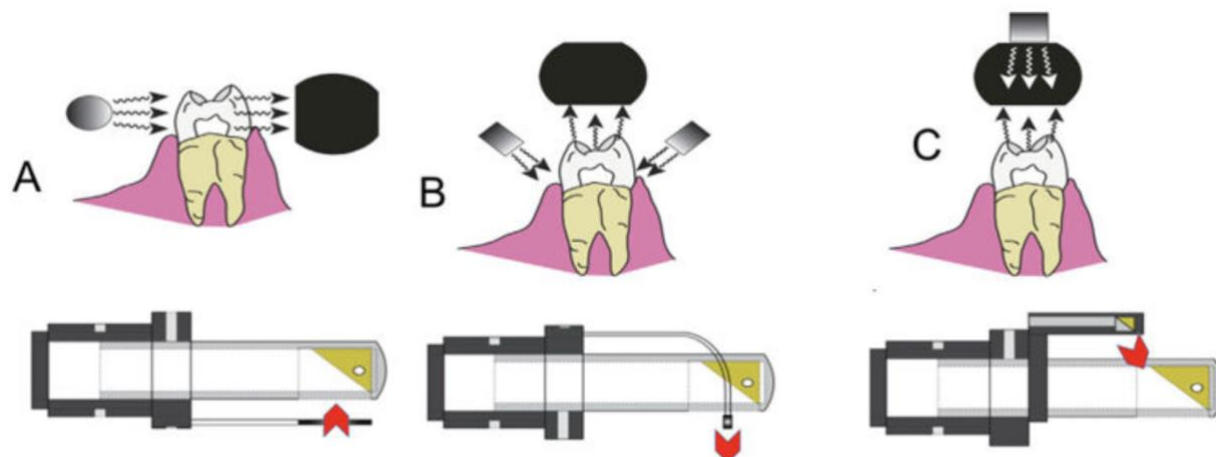


Figure 9.6.1 Imaging configurations and diagrams for the three near-IR imaging probes used in the study. (A) Near-IR approximal transillumination at 1310-nm, (B) near-IR occlusal transillumination at 1310-nm and (C) cross-polarized near-IR reflectance at 1,500-1,700-nm. On the upper diagram the arrows pointing towards the tooth show the position of illumination while the arrows pointing away from the tooth show the reflected or transmitted light incident on the camera. On the lower diagrams the camera is attached to the left side of each probe, the red arrows show the direction of the light emanating from each probe, and the reflecting prisms are shown in yellow.

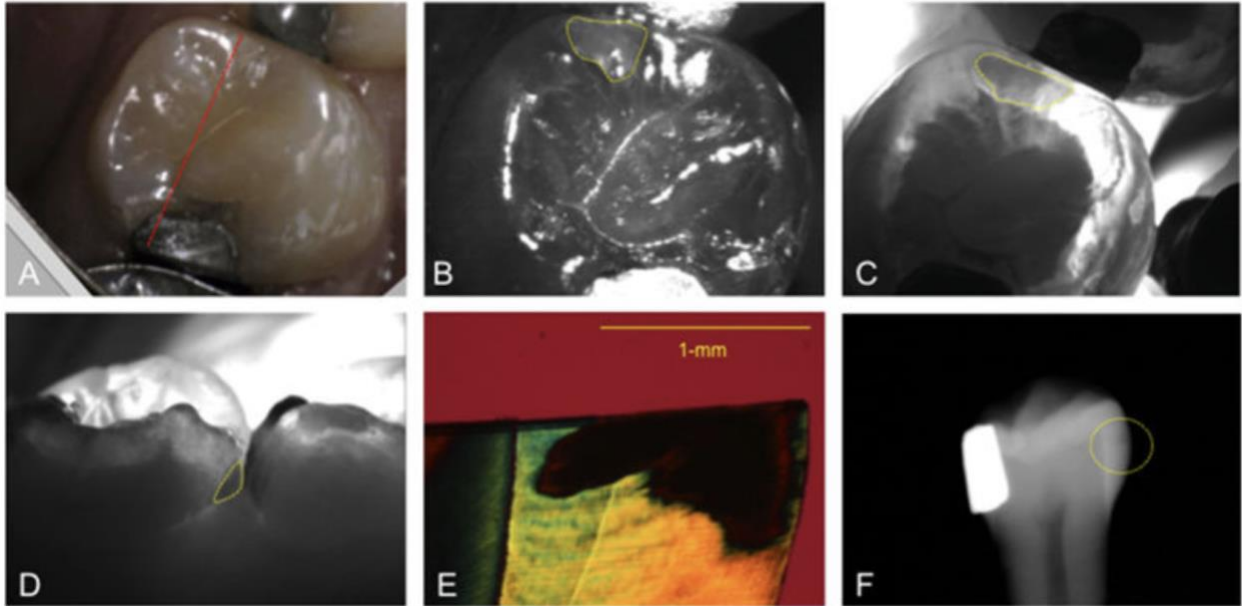


Figure 9.6.2 Images of an approximal lesion located 2-3mm below the occlusal surface. Visible light (A), near-IR reflectance (B), near-IR occlusal transillumination (C), near-IR approximal transillumination (D), histological polarized light image (E), and extra-oral digital radiograph (F). Dashed yellow margin outlines the lesion areas. The dashed red line in (A) indicates the location of the histological sample slice in (E).

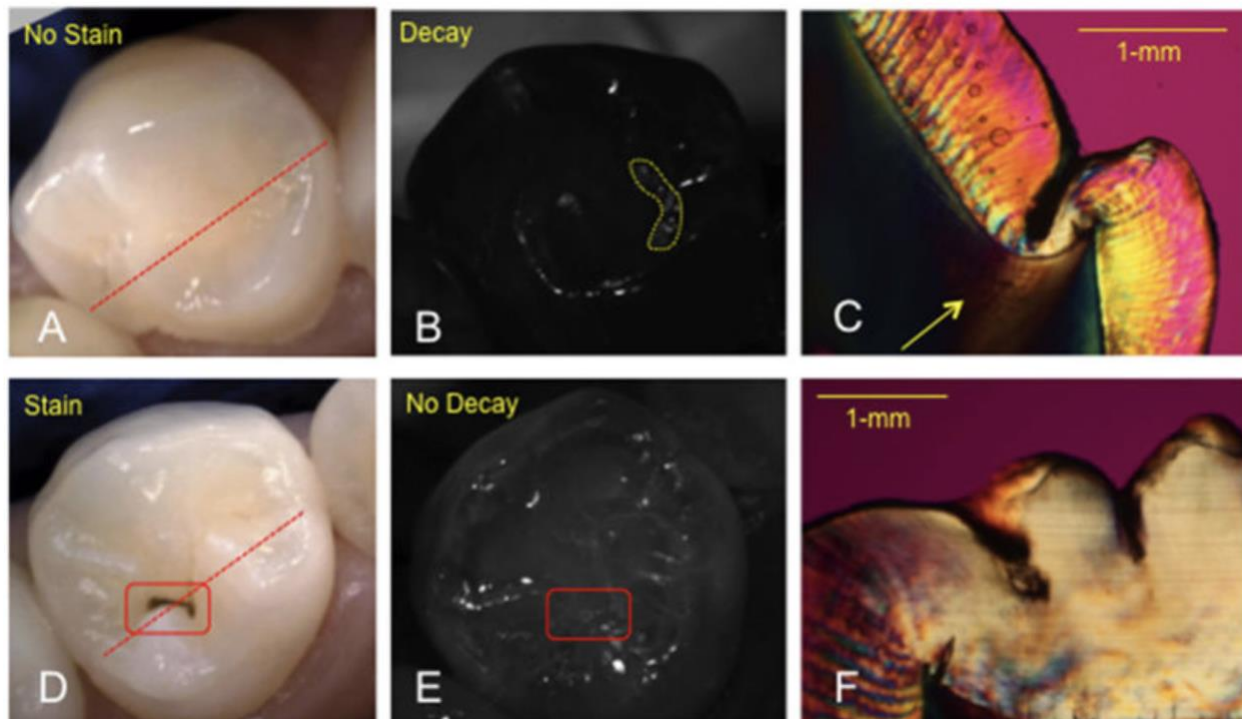


Figure 9.3 Images of an unstained fissure with demineralization (A-C). Visible light (A), near-IR reflectance (B), and histological polarized light image (C). Images of a stained fissure without demineralization (D-F). Visible light (D), near-IR reflectance (E), and histological polarized light image (F). The yellow dashed margin in (B) indicated lesion areas and the red dashed box in (D and E) shows the position of the stained fissure. The dashed red lines in (A and D) indicated the location of histological sample slices in (C and F). The yellow arrow in (C) points to the dentin affected by the lesion in the fissure.

CHAPTER X

Near-IR and CP-OCT Imaging of Suspected Occlusal Caries Lesions

10.1 Summary

Radiographic methods have poor sensitivity for occlusal lesions and by the time the lesions are radiolucent they have typically progressed deep into the dentin. New more sensitive imaging methods are needed to detect occlusal lesions. In this study, cross-polarization optical coherence tomography (CP-OCT) and near-IR imaging were used to image questionable occlusal lesions (QOC's) that were not visible on radiographs but had been scheduled for restoration on 30 test subjects. Near-IR reflectance and transillumination probes incorporating a high definition InGaAs camera and near-IR broadband light sources were used to acquire images of the lesions before restoration. The reflectance probe utilized cross-polarization and operated at wavelengths from 1500–1700-nm where there is an increase in water absorption for higher contrast. The transillumination probe was operated at 1300-nm where the transparency of enamel is highest. Tomographic images ($6\times 6\times 7\text{-mm}^3$) of the lesions were acquired using a high-speed swept-source CP-OCT system operating at 1300-nm before and after removal of the suspected lesion. Near-IR reflectance imaging at 1500–1700-nm yielded significantly higher contrast ($p<0.05$) of the demineralization in the occlusal grooves compared with visible reflectance imaging. Stains in the occlusal grooves greatly reduced the lesion contrast in the visible range yielding negative values. Only half of the 26 lesions analyzed showed the characteristic surface demineralization and increased reflectivity below the dentinal-enamel junction (DEJ) in 3D OCT images indicative of penetration of the lesion into the dentin. This study demonstrates that near-IR imaging methods have great potential for improving the early diagnosis of occlusal lesions.

10.2 Introduction

Occlusal caries lesions are routinely detected in the United States using visual/tactile (explorer) methods coupled with radiography. Radiographic methods have poor sensitivity for detecting occlusal lesions, and by the time the lesions are radiolucent they have typically progressed deep into the dentin at which point it is too late for non-surgical intervention to be effective [9]. Some of these “hidden” lesions may show up in radiographs but most do not [177, 178]. Such hidden lesions are more common today with the widespread use of fluoride and new more sensitive methods are needed to detect these lesions. Fluorescence based methods that detect the fluorescence of porphyrin molecules found in bacteria have been developed for detecting hidden lesions, however they suffer from a high rate of false positives and neither the depth or exact position of the lesions is indicated [102, 179]. Recent studies utilizing the Practice Based Research Network (<http://www.nationaldentalpbrn.org>) [31-33] funded by the National Institutes of Health, indicated that 1/3 of all patients have a questionable occlusal caries lesion (QOC). QOC's can be defined as an occlusal surface without cavitation or radiographic radiolucencies, but caries is suspected due to shadows, roughness, surface opacities or staining. After monitoring QOC's for 20 months in the PBRN study, 90% did not require surgical intervention or restoration. Furthermore, the identification of occlusal lesions penetrating to the dentin is poor with an accuracy of ~50% [35, 36].

Enamel manifests its highest transparency near 1300-nm where the scattering coefficient of enamel is 20–30 times lower than it is at visible wavelengths [41, 42]. Due to the high transparency of enamel, novel imaging configurations are feasible in which the tooth can

be imaged from the occlusal surface after shining light at and below the gum line, which we call occlusal transillumination [7, 28, 71, 121, 123]. Upon demineralization the scattering coefficient of enamel increases by 1–2 orders of magnitude at 1300-nm to yield high contrast between sound and demineralized enamel for caries detection [43]. Therefore, this wavelength range is ideally suited for the transillumination of occlusal caries lesions. Carious lesions appear dark in transillumination images due to the combination of increased scattering and absorption by the lesion that reduces optical transmission. Recently, a commercial near-IR transillumination system has been introduced called the Diagnocam from Kavo (Biberach, Germany) that uses an occlusal transillumination probe with 780-nm light[81, 82]. We previously investigated using transillumination imaging at 830-nm which has the advantage of utilizing a low-cost silicon CCD sensor optimized for the near-IR. The 830-nm system was capable of higher performance than visible systems, but the contrast was significantly lower than 1310-nm and simulated lesions could not be imaged through the full enamel thickness[76]. Other groups have confirmed the high potential of the near-IR for imaging dental decay[51, 170].

There are other important advantages of imaging dental decay in the near-IR. Stains that are common on tooth occlusal surfaces do not interfere at near-IR wavelengths since none of the known chromophores absorb light in the near-IR beyond 1300-nm [51, 123]. More recently, Almaz et al. demonstrated that it was necessary to use near-IR wavelengths greater than 1150-nm to avoid significant interference from stains when measuring lesion contrast in reflectance and transillumination modalities[171]. Therefore stains can be easily differentiated from actual demineralization in the near-IR range, which is not possible at visible wavelengths. Chung et al. [40] indicated that the absorption

due to stains contributed more to the lesion contrast than actual demineralization at visible wavelengths [64]. Since it is impractical to remove stains from the deep grooves and fissures on tooth occlusal surfaces, lack of interference from stains at longer near-IR wavelengths is a significant advantage.

Additionally, reflectance imaging at wavelengths greater than 1300-nm have yielded extremely high contrast of early demineralization [27, 40, 45, 50-52]. More recent near-IR imaging studies suggest that longer near-IR wavelengths coincident with high water absorption namely, 1450-nm or 1500–1700-nm, yield the highest contrast of demineralization on tooth surfaces [45, 52]. We hypothesize that higher water absorption at these wavelengths reduces the reflectivity in the sound enamel and the underlying dentin resulting in even higher contrast between sound and demineralized enamel than that observed at 1300-nm. Hyperspectral reflectance measurements by Zakian et al. [51] show that the sound regions of the tooth appear darker at wavelengths coincident with higher absorption by water.

Near-IR imaging reflectance and transillumination imaging methods are ideally suited for caries screening, i.e., detecting that lesions are present on tooth surfaces. Optical coherence tomography (OCT) is a noninvasive technique for creating cross-sectional images of internal biological structure [180]. Several groups have used OCT and PS-OCT to image dental caries on both smooth surfaces and occlusal surfaces[59, 181-183]. OCT is poorly suited for rapid caries screening since it takes too long to acquire images of all tooth surfaces, however it is extremely valuable for acquiring 3D images of suspect lesions to assess the depth of lesion penetration to aid in diagnosis. We have

demonstrated that polarization sensitivity is necessary for accurate depth-resolved measurements of the severity of demineralization both *in vitro* and *in vivo*[59, 184, 185]. Quantitative depth resolved measurements are useful for clinical studies and for monitoring the state of early lesions and our studies indicate that polarization sensitivity provides considerable advantages for the measurement of early demineralization on tooth surfaces [59, 184, 185]. We postulate that OCT is ideally suited for monitoring and improving the diagnosis of QOC's. Even though the optical penetration of near-IR light can easily exceed 7-mm through sound enamel to image lesions on proximal surfaces with high contrast [76], the large increase in light scattering due to demineralization [43] typically limits optical penetration in highly scattering lesions (also dentin and bone) to 1–2-mm, thus cutting off the OCT signal before it reaches the dentinal-enamel junction (DEJ). However, most occlusal lesions rapidly spread laterally under the enamel upon contacting the more soluble softer dentin, with the largest lateral spread usually at the DEJ and that lateral spread can be detected under the sound enamel with OCT.

We have carried out three prior clinical studies involving near-IR transillumination imaging [26, 28, 78] and one recent study involving near-IR reflectance [78]. In our most recent near-IR imaging clinical study [78], we employed three near-IR imaging probes to screen for lesions on premolars scheduled for extraction, and we demonstrated that near-IR image methods can achieve higher diagnostic performance than radiographs for the detection of lesions on both proximal and occlusal surfaces. In 2011, we carried out a clinical study of teeth with non-cavitated occlusal caries lesions that were not visible on radiographs. Teeth with suspect lesions were examined using near-IR occlusal transillumination at 1300-nm and polarization optical coherence tomography prior to

restoration. In that study, we used a relatively slow time-domain OCT system (150-Hz scan rate) to acquire individual b-scan images across the occlusal lesions. That study demonstrated that near-IR transillumination at 1300-nm can be used to image occlusal caries lesions with high contrast in vivo and that OCT can be used to detect lesion penetration into dentin. That study also indicated that it is necessary to acquire entire tomographic OCT scans to resolve the lateral spread of the lesions in all directions as opposed to single b-scans. This requires a high-speed OCT system and in this study we employ a swept-source CP-OCT system operating at a scan rate of 33- kHz to acquire entire 3D images of the lesions.

We also use near-IR occlusal transillumination and reflectance probes to acquire high-resolution images of suspected occlusal lesions using a high-definition (1024 × 1280 element) InGaAs camera and measured the lesion contrast with both imaging modes. In addition, to avoiding the interference of stains at wavelengths beyond 1200-nm, which is likely the principal reason for the misdiagnosis of QOC's, we postulate that the acquisition of both near-IR reflectance and transillumination images will help avoid false positives due to specular reflection or anatomical features. Moreover, since superficial (shallow) demineralization in the pits and fissures of the occlusal surfaces may not be visible in transillumination images while being visible with high contrast in reflectance images, the differential appearance will be useful for assessing lesion severity. Namely, demineralization that is visible only in near-IR reflectance images is likely localized to the outer enamel and surgical intervention is not needed.

10.3 Material and Methods

10.3.1 Patient Recruitment

After obtaining IRB approval and written informed consent, 30 participants were recruited from the predoctoral clinics of the University of California, San Francisco, School of Dentistry. Adult subjects aged 18 to 60 with a questionable occlusal lesion (QOC) that was not apparent on a radiograph and had been scheduled for restoration were recruited. A total of 30 teeth were imaged in the study. Four samples were excluded after imaging with one due to frank cavitation, two due to preexisting sealants on the occlusal surface, and the images were unreadable for one lesion.

10.3.2 Visible Images

A Dino-Lite digital USB microscope, Model AM7013MZT, AnMO Electronics Corp. (New Taipei City, Taiwan) equipped with a dental mirror was used to acquire visual digital images, both wet and dry, of the patients' teeth prior to near-IR imaging. The digital microscope captures 5 mega-pixel (2592 × 1944) color still images and video. Eight white LED lights contained in the camera illuminate the teeth and the device features polarization optics to eliminate specular reflection and reduce glare. Visual images were taken for reference and comparison with near-IR techniques at the beginning of each imaging session.

10.3.3 Near-IR imaging probes with InGaAs FPA

Two near-IR imaging probes were utilized to capture cross-polarized reflectance and occlusal transillumination videos of samples prior to restoration. The cross-polarized reflectance probe used a broadband light from a tungsten-halogen lamp, Model HL-2000 (Ocean Optics, Dunedin, FL) filtered using a long pass 1500-nm filter, Model FEL1500 (ThorLabs, Newton, NJ) and delivered to the probe through a glass fiber optic waveguide (Dolan-Jenner, Boxborough, MA) to yield light detectable in the range from 1500–1700-nm. The light emitted from the waveguide is incident on a polarizing beam splitter cube, Model PBS054 (Thorlabs) where a single linear polarization state is reflected down through the hollow width of the probe and onto the sample surface. The light interacts with the tooth and is reflected or scattered back to a right-angled mirror and directed down the imaging tube to the focal plane array. A second adjustable linear polarizer, Model MPIRE-100-C (Thorlabs) was inserted into a rotating element and oriented orthogonally to the polarization state of the first to eliminate specular reflected light from reaching the detector. The reflectance probe delivered a 6–10-mW cone of light over a circular area 1.5-cm in diameter.

The near-IR occlusal transillumination probe employed light centered at 1310-nm generated using a superluminescent diode with a 50-nm bandwidth. Fiber optic cables were used to deliver the light into two diffusing elements made of Teflon. The diffusing elements are positioned using copper tubes that direct the light below the cementum-enamel junction (CEJ) into the gingival tissue from both the lingual and facial sides at a

shallow angle. Light that enters the tooth diffuses throughout its interior and out the occlusal tooth surface. A right-angled mirror reflects the emitted light down the imaging tube through the relay optics and onto the focal plane array of the camera. The probe is designed to rotate 180-degrees for the imaging of both upper and lower teeth. The occlusal transillumination probe delivered a 6–10-mW cone of light onto the lingual and buccal surfaces with a circular area 3-mm in diameter.

Each individual probe is attached to common optical components consisting of two iris diaphragms, $f=60$ -mm AC254-060-C and $f=150$ -mm AC254-150-C (Thorlabs) near-IR achromatic lenses, coupled to a high sensitivity InGaAs focal plane array (FPA), Model GA1280J (Sensors Unlimited, Princeton, NJ) with a 1280×1024 pixel format and $15\text{-}\mu\text{m}$ pixel pitch. A 360-degree rotation element allows simple rearrangement of the imaging probe to access both the maxillary (upper) and mandibular (lower) teeth. The assembly is physically supported via an aluminum post attached to an elastic band wrapped around the forearm of the clinician. A power supply and output cable attaches to the backside of the camera and connects the instrumentation with computers and programming through a mesh bundle. Diagrams of each probe can be found in reference [78]. Probes were sterilized in an autoclave before each imaging session.

10.3.4 Visible and near-IR clinical imaging protocol

Each tooth was imaged *in vivo* with the visible and near-IR imaging systems (OCT and near-IR probes) while viewing a live video feed of the captured images on a computer monitor before the tooth was restored. After the preparation was cut into the occlusal surface, visible and OCT images were acquired of the sample. Imaging was employed in

the following order: (1) Conventional photos of the teeth were taken (both wet and air dried) using a digital camera. (2) Cross- polarized near-IR reflectance images were acquired for the detection of surface demineralization in the pits and fissures and other external (surface) signs of decay. (3) Two OCT scans were performed on the occlusal surface of each tooth before and after the tooth was prepared for a restoration. During near-IR reflectance and OCT imaging an air spray was employed to dry the tooth surface and increase lesion contrast. The air spray was also used to remove air bubbles during near-IR transillumination imaging and to prevent moisture build up on the OCT sensor window. Imaging was carried out in a separate clinical research room outside the predoctoral clinics from where the test subjects were recruited and the clinicians carrying out the initial diagnosis, treatment plan and cavity preparations had no access to the imaging data.

10.3.5 Image Analysis

Visible images were analyzed using the image analysis package, IgorPro (Wavemetrics, Lake Oswego, OR). Both the suspected lesion area and sound tissue intensities were measured using a freehand Region of Interest (ROI) tool in order to calculate the mean intensities from each region. Visible-light reflectance lesion contrast was calculated using the equation $(I_L - I_S)/I_L$, where I_L is the intensity of the lesion area and I_S is the intensity of the surrounding sound area. Increased scattering from demineralized tissue produces a greater intensity signal and I_L should be higher than I_S . The reported contrast values can range from 0 to 1 where a 0 value represents no contrast, a 1 value represents maximum contrast, and negative values represents inverse contrast. The reported lesion

contrast ranges from 0 to 1 when the lesion intensity is greater than the measured sound intensity. A negative contrast can occur when the measured sound intensity exceeds the lesion intensity and the reported values do not have a confined range. Contrast values were compared with near-IR measurements using repeated measures one-way analysis of variance (ANOVA) followed by Tukey-Kramer post-hoc multiple comparison tests using InStat statistical software (GraphPad, San Diego, CA).

Near-IR cross-polarized reflectance and occlusal transillumination videos were analyzed using software developed using LabView (National Instruments, Austin, TX). Near-IR videos were screened frame by frame and the single best lesion image was selected for analysis. A circular ROI was used to capture the whole occlusal tooth surface (excluding edges) and the mean of this ROI was used as the threshold for sound tissue. Sample images were then converted into contrast maps by replacing each pixel value with a new contrast value calculated using the equation $(I_L - I_S)/I_L$ for reflectance and $(I_S - I_L)/I_S$ for transillumination due to their different lesion appearance. Using the contrast maps, areas of similar contrast from the regions identified by the clinicians were selected as the lesion areas and the mean contrast of those selected lesion areas was calculated.

10.3.6 Cross-Polarization (CP-OCT) System

A cross-polarization OCT system purchased from Santec (Komaki, Aichi, Japan) was used to acquire 3D tomographic images in vivo. This system acquires only the cross-polarization image (CP-OCT), not both the cross and co-polarization images (PS-OCT). The device, Model IVS-300-CP, utilizes a swept laser source; Santec Model HSL-200-30 operating with a 33 kHz a-scan sweep rate. The interferometer is integrated into the

handpiece which also contains the microelectromechanical (MEMS) scanning mirror and the imaging optics. This CP-OCT system is capable of acquiring complete tomographic images of a volume 6×6×7-mm in size in ~3 seconds. The body of the handpiece is 7×18-cm with an imaging tip that is 4-cm long and 1.5-cm across. This system operates at a wavelength of 1,321-nm with a bandwidth of 111-nm with a measured axial resolution in air of 11.4- μm (3-dB). The lateral resolution is 80- μm ($1/e^2$) with a transverse imaging window of 6 × 6-mm and a measured imaging depth of 7-mm in air. The polarization extinction ratio was measured to be 32-dB.

We previously developed a small sleeve made out of Delrin that fits over the window and prevents tooth structure from coming in direct contact with the window of the scanner. Cellophane film is used as an infection control barrier on the handpiece which we found only minimally interferes with the images. The sleeve was placed in direct contact with the tooth surface and it prevents damage to the window covering the OCT scanner. The Delrin sleeve was sterilized by autoclave prior to each procedure.

During clinical procedures the images were acquired by positioning the scanner against the tooth occlusal surface while acquiring real-time *en face* images of the tooth surface.

10.3.7 Analysis of CP-OCT Images

CP-OCT scans were analyzed using software that we developed using LabView (National Instruments, Austin, TX). Tomographic images of the sample were reconstructed from the cross-polarization image. Background subtraction was carried out by subtracting the mean reflectivity of 5000 data points measured in air from the top 100 pixels (~0.8-mm)

of the 50 unprocessed a-scans (~1.0-mm) outside the sample area. The images were convolved with a Gaussian filter (3×3 filter, sigma=4) to reduce speckle noise. The 5×5 rotating kernel transformation (RKT) technique was applied in x–z and y–z spaces to emphasize thin edges while further suppressing speckle noise. Selected a-scans were chosen from acquired b-scans which contained subsurface reflections 2 to 3-mm below the surface adjacent to the fissures with occlusal lesions characteristic of increased reflectivity at the DEJ. The reflectance at the lesion surface in the center of the fissure was very strong and the OCT signal is quickly attenuated. However, lesions that penetrate to the DEJ typically spread laterally in the less acid resistant dentin so adjacent areas of the lesion are located under sound enamel and show up in OCT images as strong reflections well below the tooth surface, usually at the position of the DEJ. These b-scans typically have two areas of increased reflectivity corresponding to the tooth surface or lesion surface (top arrow in Fig.10.1B) and the position of the DEJ or the subsurface lesion (lower arrow in Fig. 10.1.B). The lesion depth or distance separating the peaks at the tooth surface and lesion position of the dentin or DEJ was measured. For tooth samples prepared for restoration, the depth or distance separating the peaks at the tooth surface and internal floor of the preparation was measured. Aviso 3D software (FEI, Hillsboro, OR) was used to manipulate the 3D CP-OCT images to generate 3D volumetric renderings and movies.

10.4 Results

Figure 10.1 shows a lesion for which CP-OCT clearly showed that the lesion in the fissure had penetrated beyond the DEJ and spread laterally under the adjacent enamel. In the

visible light reflectance image, Fig. 10.1A, only the dark stain in the fissure is visible. A CP-OCT b-scan image is shown in Fig. 10.1B. Increased light scattering due to demineralization is shown in white. The thin dotted white line shows the position of the tooth surface and the red dotted line shows the position of the dentinal enamel junction (DEJ). The top red arrow indicates a strong reflective signal near the tooth surface in the fissure and the scattering is strong enough to cause complete loss of signal beneath the lesion. This combination of signals is the telltale signature that a lesion is present. There is a corresponding strong signal to the right of the fissure at the position of the DEJ (upward pointing arrow). This indicates the lesion has spread to the right of the lesion beneath the DEJ. Figure 10.1C is a 3D volumetric rendering of the entire 6 × 6-mm CP-OCT image and areas of high subsurface reflectivity are indicated in white. From the volumetric rendering of Fig. 10.1C it can be seen that the lesion has penetrated to the DEJ, at the position of the red arrows, and there are large areas of lateral spread into dentin at both ends of the fissure. This is more clearly evident in the attached 3D movie (Movie1.mpg). The near-IR reflectance image shows areas of demineralization and the stains are not visible. Areas of demineralization appear whiter and with high contrast. A CP-OCT b-scan across the cavity preparation is shown in Fig. 10.1E acquired at the position of the green dotted line in the visible reflectance image of Fig. 10.1F showing the tooth after the preparation. The depth was ~ 2.2-mm and the preparation was fairly large extending well beyond the fissure.

In Fig. 10.2 another tooth with a stained fissure is shown which appears to have a lesion of similar severity to that of Fig. 10.1 viewed in visible light. The CP-OCT b-scan image in Fig. 10.2B shows a very shallow V-shaped lesion in the center of the fissure (red arrow)

which causes only a slight increase in reflectivity and does not completely attenuate the signal below it. No deeper signal is apparent near the DEJ on either side of the fissure. Figure 10.2C shows a volumetric rendering of the CP-OCT 3D image showing the fissure area (yellow dots) and no subsurface demineralization is visible in areas peripheral to the fissure. The near-IR image in Fig. 10.2D shows a narrow band of demineralization confined to the center of the fissure and the contrast is weaker than in Fig. 1 suggesting that the surface demineralization is less severe. The cavity preparation is shown in Figs. 10.2 E & F and it is similar in depth (1.9-mm) and breadth to that of Fig. 10.1 (2.2-mm).

The tooth shown in Fig. 10.3 manifests a shadow that is clearly visible peripheral to the fissure. The shadow is demarcated by the yellow dots in Fig. 10.3A while the lesion is surrounded by the red dots. There was no lateral spread of the lesion in the demarcated shadow area (yellow dots) evident in the surface rendering of the CP-OCT 3D image, Fig. 10.3B, or in the reflectance and transillumination near-IR images, Figs. 10.3C & D. Since stain is not visible in the near-IR this suggests that the shadow or tooth discoloration is caused by stained or "affected" dentin and not demineralized dentin. The cavity preparation penetrates to the dentin, Fig. 10.3E, but the size of the preparation shown in Fig. 10.3F appears smaller than the area of the stain in Fig. 10.3A.

Figure 10.4 shows a tooth with a large interproximal lesion that is visible in the near-IR images, Figs. 10.4B and 10.4C, with high contrast but was not apparent at visible wavelengths, Fig. 10.4A. This tooth was included in the study because it was also diagnosed with occlusal decay in the central groove. Stain is present in the groove, Fig. 10.4A, but no demineralization is visible in the groove at near-IR wavelengths, Figs. B &

C, or with CP-OCT. Figures 10.4E–G show 3D renderings of the CP-OCT scan along with an extracted b-scan image showing the rise in reflectivity caused by the subsurface interproximal lesion. This example also demonstrates how OCT images taken from the occlusal surface can be used for the diagnosis of lesions on tooth proximal surfaces. Thirty teeth were imaged and four were rejected, two had sealants, one had frank cavitation and the images were unreadable for a 4th tooth. A fifth tooth was diagnosed with an occlusal lesion and an interproximal lesion. Although the large interproximal lesion was clearly evident in the near-IR and OCT images there was no demineralization present in the occlusal fissure and it was also rejected from the statistical analysis. Twenty-five teeth were analyzed and the contrast between the sound and demineralized areas of the lesion were measured using cross-polarized visible light reflectance, cross-polarized near-IR reflectance at 1500–1700-nm, and near-IR occlusal transillumination at 1300-nm. In addition, the CP-OCT images taken before and after lesion removal were analyzed to determine whether there was lateral spread of the lesion beneath the DEJ and the maximum depth of penetration of the lesion and the depth of the cavity preparation were recorded. The mean lesion contrast values and the mean lesion and preparation depths are tabulated in Table 10.1. Out of the twenty-six teeth analyzed, CP-OCT analysis indicated that 13/26 of the lesions had penetrated to the dentin and that there was lateral spread under the enamel. Near-IR and CP-OCT images showed that demineralization was present on twelve more teeth but there was no evidence of lateral spread of these lesions in dentin and on one tooth the near-IR and CP-OCT images showed that no demineralization was present on the occlusal surface (Fig. 10.4).

10.5 Discussion

In this study, we utilized CP-OCT and near-IR imaging at 1300 and 1500–1700-nm to image occlusal lesions that were not visible on radiographs but had been scheduled for restoration based on visual and tactile examination. Such lesions are commonly referred to as questionable occlusal caries (QOCs) due to the poor diagnostic performance of visual and tactile methods. Clinicians are forced to rely on these methods due to the extremely low sensitivity of radiographs for early occlusal lesions. The lesion contrast measured using near-IR reflectance at 1500–1700-nm was markedly higher than for visible light reflectance. The contrast approached 0.5 which is remarkably high. Demineralization increases light scattering and increases the amount of light reflected (backscattered) from the tooth surface at both visible and near-IR wavelengths, therefore demineralization should yield high positive contrast. If stains are not present, "white spot lesions" of high contrast are visible on tooth surfaces. The mean lesion contrast was negative in this study for visible wavelengths, indicating that the demineralization was completely masked by stain. This suggests that diagnosis is unreliable for the pits and fissures of occlusal surfaces in the visible range and that longer near-IR wavelengths are much better suited for assessing lesion presence. Demineralized surfaces are typically more porous increasing the retention of stains so more often than not stained surfaces are also demineralized. However, as demonstrated in this study, surfaces can be stained without any demineralization, particularly the pits and fissures, and that stain masks the degree of demineralization present.

3D CP-OCT images showed lateral spread for 13 out of the 26 lesions analyzed in this study. This is consistent with the findings of the PBRN [35, 36]. Since none of the lesions were visible on the radiographs, at a minimum this potentially represents an improvement of sensitivity of over 50%. Unfortunately, there is no gold standard for confirming lesion penetration. The depth and size of the cavity preparation is the only data available since the teeth were not extracted. One would anticipate that the lesions for which the spread into dentin was confirmed with OCT would have significantly higher cavity preparation depths than those smaller lesions for which the spread was not evident. However, as can be seen in Table I, the depths of the preparations were not significantly different, moreover even though no demineralization was visible in either the near-IR images or the CP-OCT image for the stained fissure for the tooth shown in Fig. 10.4, a sizable preparation was still cut along the entire length of the occlusal groove, measuring ~ 2.4-mm. Therefore, it is clear that the

depth of the preparation is not a reliable confirmation that the lesion actually penetrated to the dentin. In fact, these results suggest that many of the clinicians based their diagnosis of the occlusal caries lesions on stain in the grooves, which is clearly unreliable. Moreover, accurate visual and tactile diagnosis is highly dependent on the training and experience of the clinician. In our prior similar study utilizing a much slower time-domain PS-OCT system that only acquired individual b-scans a higher percentage of the QOC's (~87%) manifested a spread into the dentin. In that study a clinician with more than 30 years of experience diagnosed all the lesions prior to the study while in this study the lesions were diagnosed in the predoctoral clinic with several different faculty mentors. It is also difficult to identify if sealants or restorations are present using visual and tactile

examination and near-IR imaging methods were able to identify that sealants were present for 2/30 lesions.

Clinicians spend more time replacing failed composite restorations than placing new ones and they are difficult to identify when properly color matched. Composite restorations are much easier to visualize at near-IR wavelengths that are more highly by water due to large differences in water absorption [40, 132] between dental hard tissues and composites. We have demonstrated that near-IR imaging is also well suited for the detection of secondary caries lesions around composite restorations and under sealants on occlusal surfaces[110, 161].

This study further demonstrates the utility of CP-OCT for the diagnosis of QOC's and this is the first clinical study utilizing a fast swept-source system capable of acquiring entire $6 \times 6 \times 7$ -mm 3D images to determine the lesion spread in all directions. This was also the first clinical study to compare the image contrast of occlusal lesions in the visible and near-IR in vivo. The very high lesion contrast attained for near-IR reflectance at 1500–1700-nm is very promising. The acceptance of visible and fluorescence based caries imaging systems has been limited by the high number of false positives due to stains, particularly on tooth occlusal surfaces, and the ability to acquire images of lesions free of interference of stain is likely to have a greater impact on caries detection. In addition, near-IR imaging methods free of interference of stains can yield quantitative measures of lesion severity that are less subjective and less dependent on the training and experience.

10.6 Tables and Figures

Table 10.6.1. Mean lesion contrast values (SD) and the depth of the cavity preparation (n=25) along with the depth of lesion penetration for the n-13 samples that penetrated beyond the DEJ. I_L is the lesion intensity and I_s is the intensity of the surrounding area.

Imaging Method (n=25)	Mean Lesion Contrast (SD)
Reflectance (400–700-nm) (I_L-I_s)	-37.9 (14.6)
Reflectance (1500–1700-nm) (I_L-I_s)	46.7 (7.1) *
Occlusal Transillumination (1300-nm)	25.9 (7.7)
CP-OCT (Lesion Penetration) n=13	2.4 mm (0.7)
CP-OCT (Preparation Depth) n=25	3.2 mm (0.5)
CP-OCT (Preparation Depth) n=13 (lateral spread evident)	2.5 mm (0.9)
CP-OCT (Preparation Depth) n=12 (no lateral spread evident)	2.3 mm (0.6)

*

The lesion contrast was significantly higher for near-IR reflectance at 1500–1700-nm ($P<0.05$).

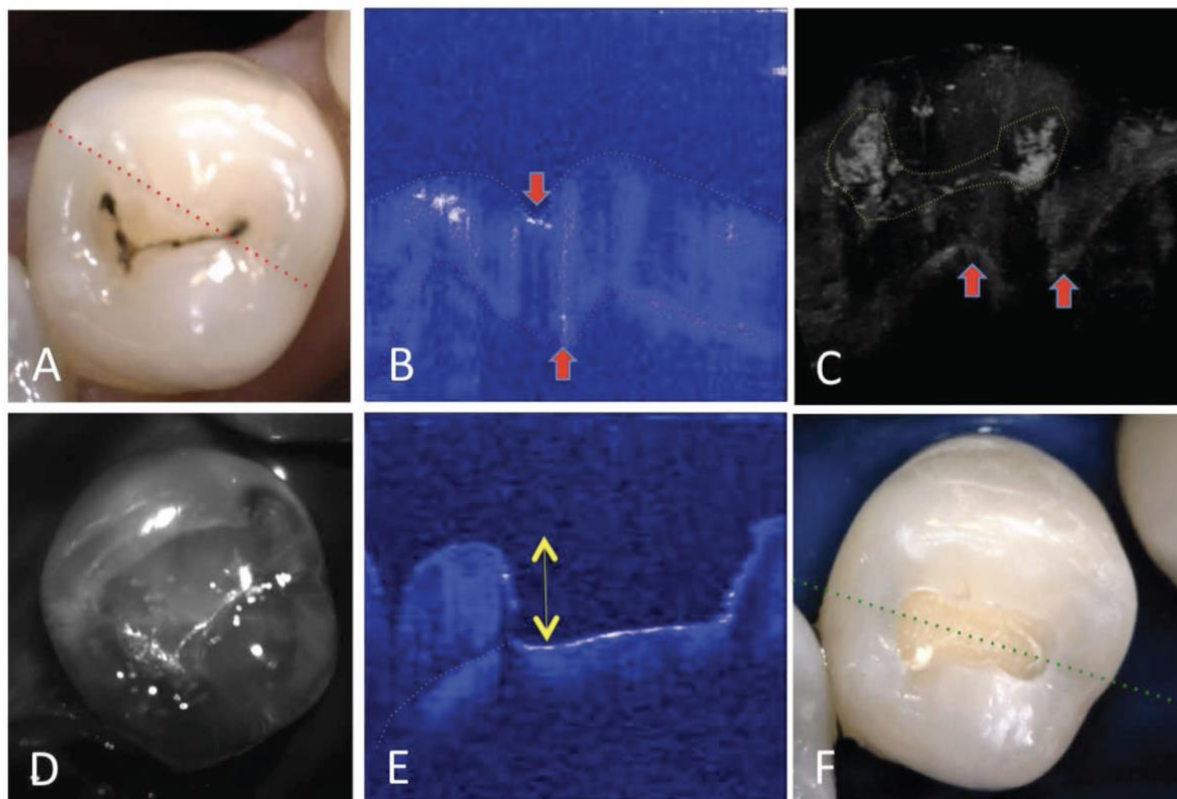


Figure 10.6.1. Example of an occlusal lesion in which the penetration of the lesion beyond the DEJ is apparent in the CP-OCT image. (A) Visible light reflectance image of the tooth, (B) CP- OCT b-scan image extracted at the position of the red dotted line in (A). The downward pointing red arrow indicates demineralization at the surface of the fissure which blocks penetration of light below it while the upward pointing arrow shows the increased reflectance at the position of the DEJ indicating that the lesion has spread laterally in the dentin. The yellow and red dotted lines indicate the position of the tooth surface and the DEJ. (C) A 3D volumetric rendering of the entire $6 \times 6 \times 7$ -mm CP-OCT image shows the lesion at the tooth surface indicated by the high reflectivity in white surrounded by yellow dots. Below the surface between the position of the two red arrows there is a complete loss of reflectivity just below the lesion and increased reflectivity at the DEJ at the position of each red arrow. (D) A near-IR reflectance image of the tooth. (E) CP-OCT b-scan across the cavity preparation at the position of the green dotted line in the visible reflectance image of (F). The cavity depth indicated by the yellow arrow is 2.16-mm. (note attached video file of Fig. 1C - 3D CP-OCT image - movie1.mpg)

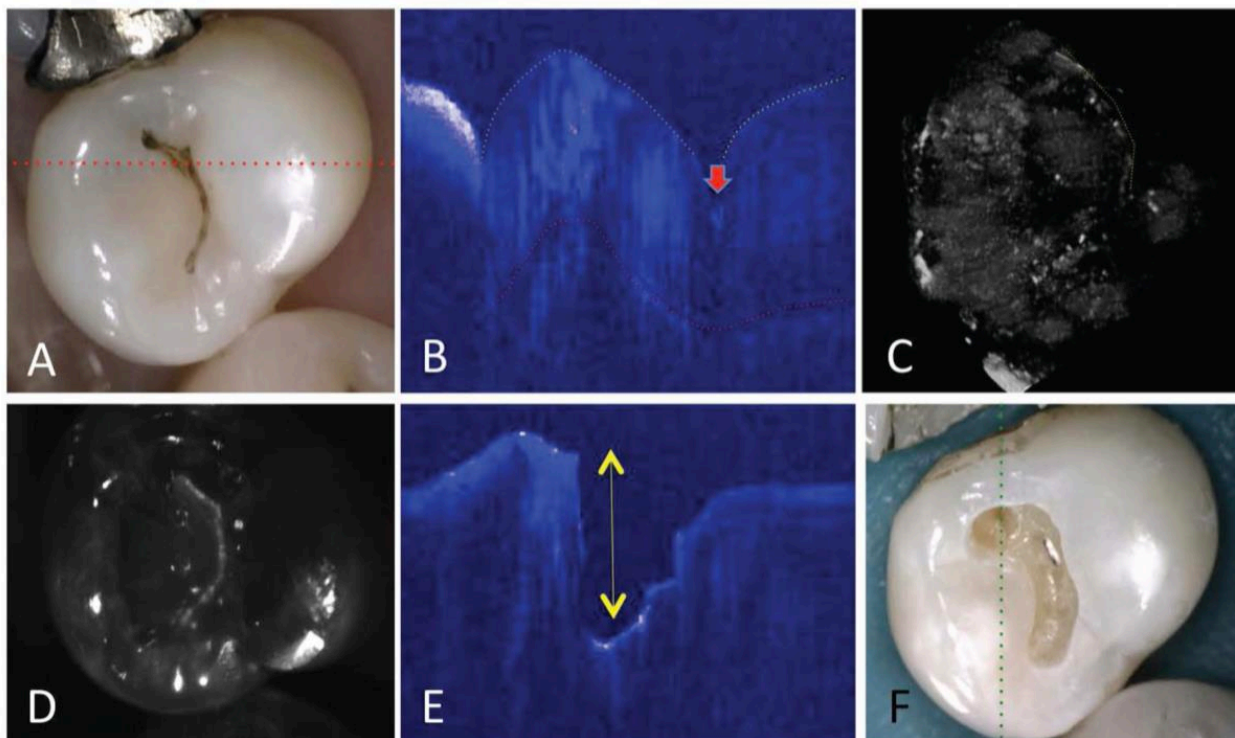


Figure 10.6.2 Example of an occlusal lesion in which the penetration depth of the lesion beyond the DEJ was not apparent in the CP-OCT image. (A) Visible light reflectance image of the tooth, (B) CP-OCT b-scan image extracted at the position of the red dotted line in (A). The red arrow indicates the position of the small v-shaped lesion in the fissure. (C) The 3D volumetric rendering of the CP-OCT image shows some increased reflectivity in the fissure at the position indicated by the yellow dotted line. No rise in the subsurface reflectivity is evident. (D) Near-IR reflectance image of the tooth. (E) CP-OCT b-scan across the cavity preparation at the position of the green dotted line in the visible reflectance image of (F). The cavity depth indicated by the yellow arrow is 1.93-mm.

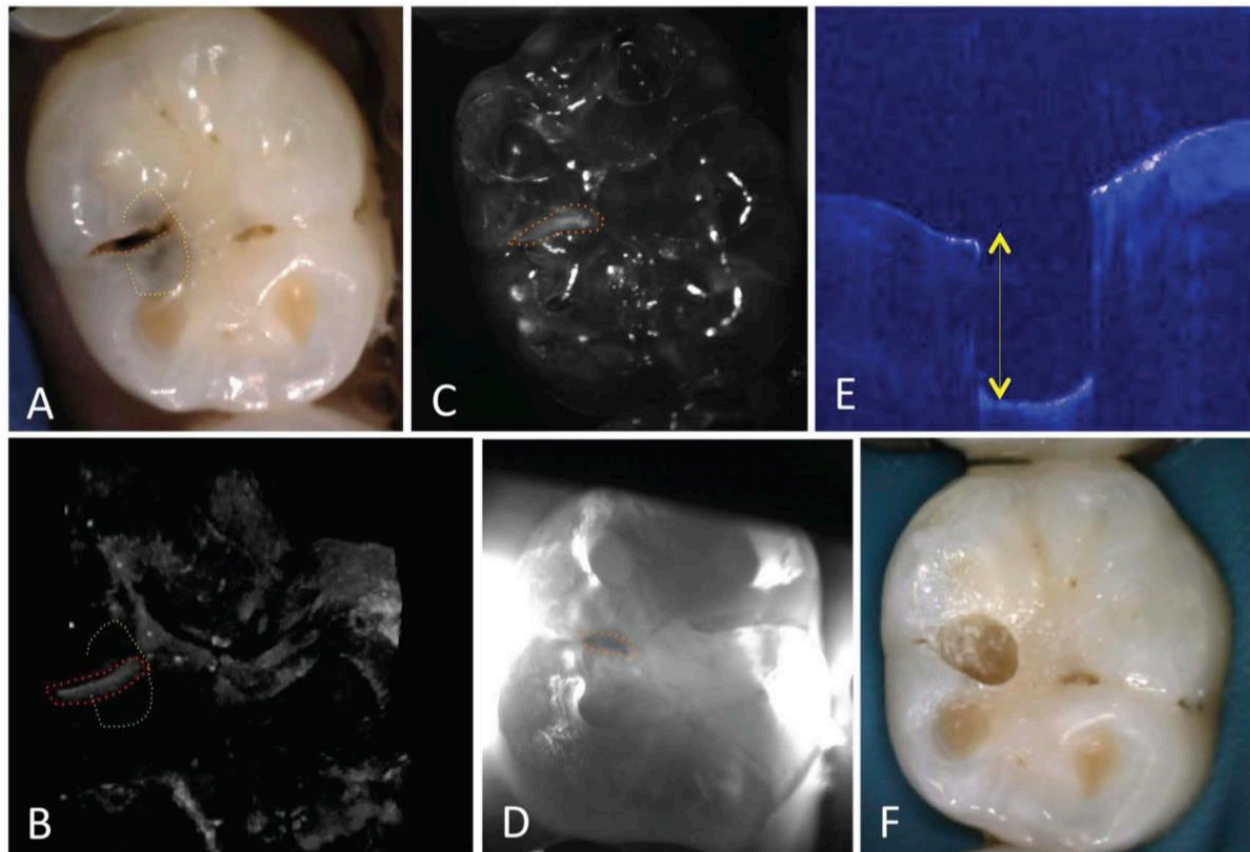


Figure 10.6.3 An occlusal lesion that manifested a distinct shadow peripheral to the stained fissure. (A) Visible light reflectance image of the tooth, (B) The 3D volumetric rendering of the CP-OCT image shows some increased reflectivity in the fissure at the position surrounded by the red dots. There is no rise in the subsurface reflectivity in the area of the shadow demarcated by the yellow dots. (C) Near-IR reflectance image and (D) near-IR occlusal transillumination image (E) CP-OCT b-scan across the cavity preparation at the position of the green dotted line in the visible reflectance image of (F) the cavity depth indicated by the yellow arrow is 2.59-mm.

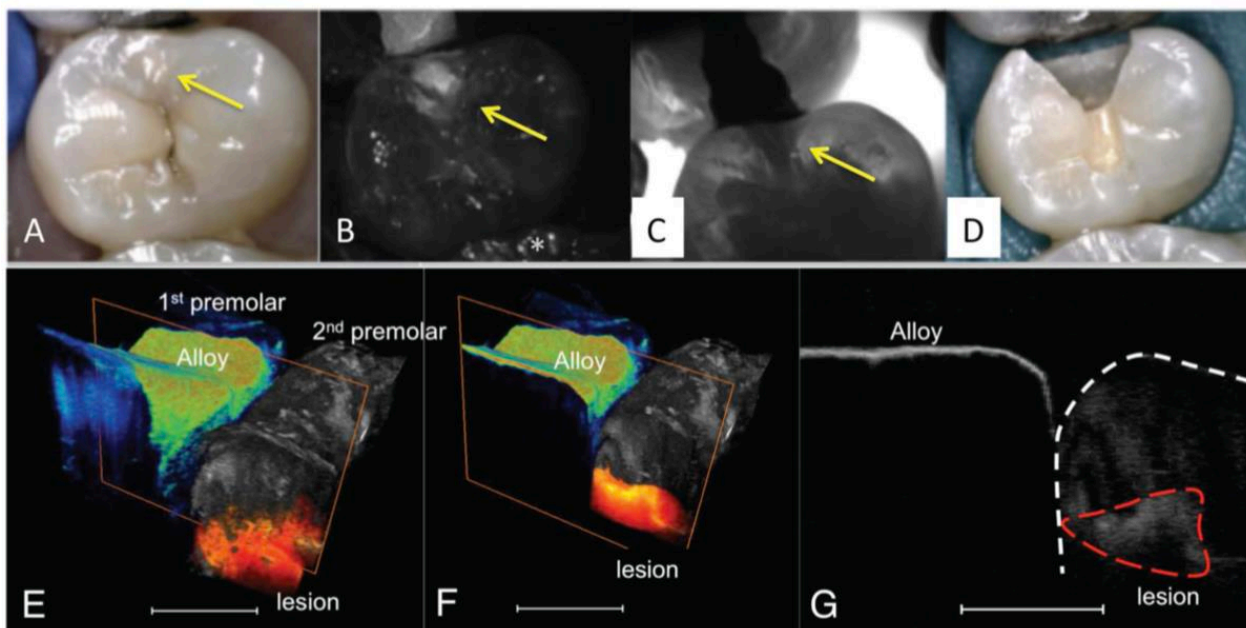


Figure 10.6.4 Images of a tooth with a suspected occlusal lesion in the central fissure (stained fissure) and an interproximal lesion indicated at the position of the yellow arrow in the visible light reflectance image (A) of the tooth are shown. Near-IR reflectance (B) and near-IR occlusal transillumination images (C) Visible image of the preparation (D) are shown. A rendered CP-OCT 3D image (E) shows the amalgam (alloy) filling on the adjoining 1st premolar in green and the lesion in red. The length of the bar is images (E-G) is 300- μm . In (F) the same 3D CP-OCT image is shown with the image truncated at the position of the extracted b-scan show in (F) to better show the lesion. In the extracted b-scan (G) the surface of the 2nd premolar and the subsurface lesion are shown by the white and red dashed lines, respectively.

CHAPTER XI

Conclusions

11.1 Perspective

The clinical practice of dentistry is undergoing a technological shift as digital devices become more affordable and a new generation of clinicians with advanced computer skills enter the field. Optical impressions, three-dimensional printing, and dynamic navigation guidance systems each have grown in use over the last decade as newly trained doctors have seen the capabilities of new instrumentation and utilized them in their practices. With the introduction to the iTero Element 5D on March 24, 2020, near-infrared technologies are also now in the hands of modern clinicians and can aid in diagnosis of dental decay. This device, and other commercially available devices use 850-nm light for diagnostic reflectance imaging of the internal structure of teeth and monitoring of dental decay. While this is a great advance for the dental community and patients, the results of this dissertation demonstrate that there are superior imaging wavelengths within the near-IR spectral region.

11.2 Conclusions

The major conclusion from this research is that reflectance imaging with wavelengths coincident with increased water absorption in the near infrared results in the highest contrast for early dental decay. Water absorption peaks at 1460-nm and 1900-nm can be exploited to generate very high contrast due to the quenching of back scattered signal from the underlying dentin in the tooth leaving just the highly scattering lesions visible. Reflectance SWIR methods perform the best for detecting occlusal and interproximal decay, but the overall diagnostic performance is improved by combining reflectance with transillumination images.

Transillumination imaging with wavelengths that have minimal attenuation, low scattering and absorption, result in the most transparent images of the internal tooth structure and allow both transverse transillumination and occlusal transillumination.

Combining reflectance and transillumination images results in increased identification of dental decay a less false positives. Combining both reflectance and transillumination into a single probe that acquires both images nearly simultaneously in vivo has been achieved and is in clinical testing in an ongoing caries detection study.

REFERENCES

1. Kaste, L.M., et al., *Coronal caries in the primary and permanent dentition of children and adolescents 1-17 years of age: United States, 1988-1991*. J Dent Res, 1996. **75**: p. 631-641.
2. Winn, D.M., et al., *Coronal and root caries in the dentition of adults in the United States, 1988-1991*. J Dent Res, 1996. **75**: p. 642-651.
3. Chauncey, H.H., R.L. Glass, and J.E. Alman, *Dental caries, principal cause of tooth extraction in a sample of US male adults*. Caries Res, 1989. **23**: p. 200-205.
4. Selwitz, R.H., A.I. Ismail, and N.B. Pitts, *Dental caries*. Lancet, 2007. **369**(9555): p. 51-9.
5. Bowen, W.H., *Dental caries - not just holes in teeth! A perspective*. Mol Oral Microbiol, 2016. **31**(3): p. 228-33.
6. Hale, G.M. and M.R. Querry, *Optical constants of water in the 200-nm to 200- μ m wavelength region*. Appl. Optics, 1973. **12**: p. 555-563.
7. Lee, C., et al., *Nondestructive assessment of the severity of occlusal caries lesions with near-infrared imaging at 1310 nm*. Journal of Biomedical Optics, 2010. **15**(4): p. 047011.
8. Kidd, E.A.M. and S. Joyston-Bechal, *Essentials of Dental Caries*. 3rd ed. 2005: Oxford University Press.
9. Fejerskov, O. and E. Kidd, eds. *Dental Caries: The Disease and its Clinical Management*. 2003, Blackwell: Oxford.
10. Kidd, E.A.M. and S. Joyston-Bechal, *Dental Caries: The*

Disease and its Clinical Management. 3rd ed. 1997: Oxford University Press.

11. O'Mullane, D.M., et al., *Fluoride and Oral Health*. Community Dent Health, 2016. **33**(2): p. 69-99.
12. Memarpour, M., et al., *Comparison of Oral Health Education and Fluoride Varnish to Prevent Early Childhood Caries: A Randomized Clinical Trial*. Caries Res, 2016. **50**(5): p. 433-442.
13. Whelton, H.P., et al., *Fluoride Revolution and Dental Caries: Evolution of Policies for Global Use*. J Dent Res, 2019. **98**(8): p. 837-846.
14. Carey, C.M., *Focus on fluorides: update on the use of fluoride for the prevention of dental caries*. J Evid Based Dent Pract, 2014. **14 Suppl**: p. 95-102.
15. NIH, *Diagnosis and Management of Dental Caries throughout Life*. 2001, NIH Consensus Statement. p. 1-24.
16. Hume, W.R. *Need for change in dental caries diagnosis*. in *Early Detection of dental caries*. 1996. Indianapolis: Indiana University.
17. ten Cate, J.M. and J.P. van Amerongen. *Caries Diagnosis: Conventional Methods*. in *Early Detection of dental caries*. 1996. Indianapolis: Indiana University.
18. Featherstone, J.D.B. *Clinical Implications: New Strategies for Caries Prevention*. in *Early Detection of dental caries*. 1996. Indianapolis: Indiana University.
19. Dhingra, S., et al., *Sugar Clock: A Primordial Approach to Prevent Dental Caries*. Int J Clin Pediatr Dent, 2020. **13**(2): p. 174-175.
20. Islam, B., S.N. Khan, and A.U. Khan, *Dental caries: from infection to prevention*. Med Sci Monit, 2007. **13**(11): p. RA196-203.

21. Featherstone, J.D.B., *Prevention and reversal of dental caries:role of low level fluoride*. Community Dent Oral Epidemiol, 1999. **27**: p. 31-40.
22. Tubiana, M., et al., *The debate on the use of linear no threshold for assessing the effects of low doses*. J Radiol Prot, 2006. **26**(3): p. 317-24.
23. Tubiana, M., et al., *The linear no-threshold relationship is inconsistent with radiation biologic and experimental data*. Radiology, 2009. **251**(1): p. 13-22.
24. Mullenders, L., et al., *Assessing cancer risks of low-dose radiation*. Nat Rev Cancer, 2009. **9**(8): p. 596-604.
25. Hong, J.Y., et al., *Association of Exposure to Diagnostic Low-Dose Ionizing Radiation With Risk of Cancer Among Youths in South Korea*. JAMA Netw Open, 2019. **2**(9): p. e1910584.
26. Staninec, M., et al., *Nondestructive Clinical Assessment of Occlusal Caries Lesions using Near-IR Imaging Methods*. Lasers in Surgery and Medicine, 2011. **43**(10): p. 951-959
27. Fried, D., et al. *In vivo Near-IR Imaging of Occlusal Lesions at 1310-nm*. in *Lasers in Dentistry XVII*. 2011. SPIE.
28. Staninec, M., et al., *In vivo near-IR imaging of approximal dental decay at 1,310 nm*. Lasers in Surgery and Medicine, 2010. **42**(4): p. 292-8.
29. Dye, B.A., et al., *Trends in oral health status, United States, 1988-1994 and 1999-2004*. Vital Health Stat 11. 2007;(248):1-92., 2007. **248**: p. 1-92.
30. Dye, B.A., et al., *Dental Caries and Tooth Loss in Adults in the United States, 2011–2012*, in *NCHS Data Brief, #197*, N.C.f.H. Statistics, Editor. 2015.

31. Makhija, S.K., et al., *The prevalence of questionable occlusal caries: findings from the Dental Practice-Based Research Network*. J Am Dent Assoc, 2012. **143**(12): p. 1343-50.
32. Makhija, S.K., et al., *Characteristics, detection methods and treatment of questionable occlusal carious lesions: findings from the national dental practice-based research network*. Caries Res, 2014. **48**(3): p. 200-7.
33. Makhija, S.K., et al., *Twenty-month follow-up of occlusal caries lesions deemed questionable at baseline: findings from the National Dental Practice-Based Research Network*. J Am Dent Assoc, 2014. **145**(11): p. 1112-8.
34. Hamilton, J.C., et al., *Early treatment of incipient carious lesions: a two-year clinical evaluation*. J Am Dent Assoc, 2002. **133**(12): p. 1643-51.
35. Bader, J.D. and D.A. Shugars, *The evidence supporting alternative management strategies for early occlusal caries and suspected occlusal dentinal caries*. J Evid Based Dent Pract, 2006. **6**(1): p. 91-100.
36. Bader, J.D., D.A. Shugars, and A.J. Bonito, *A systematic review of the performance of methods for identifying carious lesions*. Journal of Public Health Dentistry, 2002. **62**(4): p. 201-213.
37. Kleter, G.A., *Discoloration of dental carious lesions (a review)*. Arch. Oral. Bio. , 1998. **43**: p. 629-632.
38. Sarna, T. and R.C. Sealy, *Photoinduced oxygen consumption in melanin systems. Action spectra and quantum yields for eumelanin and synthetic melanin*. Photochem. Photobiol. , 1984. **39**: p. 69-74.

39. Simon, J.C., et al. *Multispectral near-infrared reflectance and transillumination imaging of occlusal carious lesions: variations in lesion contrast with lesion depth.* in *Lasers in Dentistry XXIV.* 2018.
40. Chung, S., et al., *Multispectral near-IR reflectance and transillumination imaging of teeth* Biomed Opt Express, 2011. **2**(10): p. 2804-2814.
41. Fried, D., et al., *Nature of light scattering in dental enamel and dentin at visible and near-infrared wavelengths.* Applied optics, 1995. **34**(7): p. 1278-85.
42. Jones, R.S. and D. Fried. *Attenuation of 1310-nm and 1550-nm Laser Light through Sound Dental Enamel.* in *Lasers in Dentistry VIII.* 2002. San Jose: Proc SPIE.
43. Darling, C.L., G.D. Huynh, and D. Fried, *Light Scattering Properties of Natural and Artificially Demineralized Dental Enamel at 1310-nm.* J. Biomed. Optics, 2006. **11**(3): p. 034023
44. Lee, D., D. Fried, and C. Darling. *Near-IR multi-modal imaging of natural occlusal lesions.* in *Lasers in Dentistry XV.* 2009. San Jose: SPIE.
45. Simon, J.C., et al., *Multispectral near-IR reflectance imaging of simulated early occlusal lesions: variation of lesion contrast with lesion depth and severity.* Lasers Surg Med, 2014. **46**(3): p. 203-15.
46. Simon, J.C., et al. *Transillumination and reflectance probes for near-IR imaging of dental caries.* in *Lasers in Dentistry XX.* 2014. Proc SPIE
47. Ngaotheppitak, P., et al., *PS-OCT of Occlusal and Interproximal Caries Lesions viewed from Occlusal Surfaces.* Lasers in Dentistry XII, 2006. **6137**(L): p. 1-9.

48. Sharma, U., E.W. Chang, and S.H. Yun, *Long-wavelength optical coherence tomography at 1.7 microm for enhanced imaging depth*. Opt Express, 2008. **16**(24): p. 19712-23.
49. Ishida, S. and N. Nishizawa, *Quantitative comparison of contrast and imaging depth of ultrahigh-resolution optical coherence tomography images in 800-1700 nm wavelength region*. Biomed Opt Express, 2012. **3**(2): p. 282-94.
50. Wu, J. and D. Fried, *High contrast near-infrared polarized reflectance images of demineralization on tooth buccal and occlusal surfaces at $\lambda = 1310\text{-nm}$* . Lasers in Surgery and Medicine, 2009. **41**(3): p. 208-13.
51. Zakian, C., I. Pretty, and R. Ellwood, *Near-infrared hyperspectral imaging of teeth for dental caries detection*. Journal of Biomedical Optics, 2009. **14**(6): p. 064047-7.
52. Fried, W.A., et al., *High Contrast Reflectance Imaging of Simulated Lesions on Tooth Occlusal Surfaces at Near-IR Wavelengths*. Lasers Surg Med, 2013. **45**(8): p. 533-541.
53. ten Bosch, J.J., *General aspects of optical methods in dentistry*. Adv. Dent. Res., 1987. **1**(1): p. 5-7.
54. ten Bosch, J.J., H.C. van der Mei, and P.C.F. Borsboom, *Optical monitor of in vitro caries*. Caries Res., 1984. **18**: p. 540-547.
55. Zhang, L., L.Y. Nelson, and E.J. Seibel, *Spectrally enhanced imaging of occlusal surfaces and artificial shallow enamel erosions with a scanning fiber endoscope*. Journal of Biomedical Optics, 2012. **17**(7): p. 076019.

56. Spitzer, D. and J.J. ten Bosch, *The absorption and scattering of light in bovine and human dental enamel*. Calcif. Tiss. Res., 1975. **17**: p. 129-137.
57. Zijp, J.R., J.J. ten Bosch, and R.A. Groenhuis, *HeNe laser light scattering by human dental enamel*. J Dent Res, 1995. **74**: p. 1891-1898.
58. Amaechi, B.T., et al., *Use of Optical Coherence Tomography for Assessment of Dental caries*. J Oral Rehab, 2001. **28**(12): p. 1092-1093.
59. Fried, D., et al. *Imaging Caries Lesions and lesion progression with Polarization Optical Coherence Tomography*. in *Lasers in Dentistry VIII*. 2002. San Jose: SPIE.
60. Sowa, M.G., et al., *A comparison of methods using optical coherence tomography to detect demineralized regions in teeth*. Journal of biophotonics, 2011. **4**(11-12): p. 814-23.
61. Jones, R.S., et al., *Imaging artificial caries on the occlusal surfaces with polarization-sensitive optical coherence tomography*. Caries research, 2006. **40**(2): p. 81-89.
62. Manesh, S.K., C.L. Darling, and D. Fried, *Polarization-sensitive optical coherence tomography for the nondestructive assessment of the remineralization of dentin*. Journal of Biomedical Optics, 2009. **14**(4): p. 044002.
63. Ngaotheppitak, P., C.L. Darling, and D. Fried, *Measurement of the severity of natural smooth surface (interproximal) caries lesions with polarization sensitive optical coherence tomography*. Lasers in Surgery and Medicine, 2005. **37**(1): p. 78-88.

64. Chong, S.L., C.L. Darling, and D. Fried, *Nondestructive measurement of the inhibition of demineralization on smooth surfaces using polarization-sensitive optical coherence tomography*. *Lasers Surg Med*, 2007. **39**(5): p. 422-7.
65. Le, M.H., C.L. Darling, and D. Fried, *Automated analysis of lesion depth and integrated reflectivity in PS-OCT scans of tooth demineralization*. *Lasers Surg Med*, 2010. **42**(1): p. 62-8.
66. Kang, H., et al., *Nondestructive Assessment of Early Tooth Demineralization Using Cross-Polarization Optical Coherence Tomography*. *Selected Topics in Quantum Electronics, IEEE Journal of*, 2010. **16**(4): p. 870-876.
67. Chan, K.H., et al., *Use of 2D images of depth and integrated reflectivity to represent the severity of demineralization in cross-polarization optical coherence tomography*. *J Biophotonics*, 2015. **8**(1-2): p. 36-45
68. Benson, P.E., A. Ali Shah, and D. Robert Willmot, *Polarized versus nonpolarized digital images for the measurement of demineralization surrounding orthodontic brackets*. *Angle Orthod*, 2008. **78**(2): p. 288-93.
69. Everett, M.J., et al. *Non-invasive diagnosis of early caries with polarization sensitive optical coherence tomography (PS-OCT)*. in *Lasers in Dentistry V*. 1999. San Jose: SPIE.
70. Fried, D., et al., *Early detection of dental caries and lesion progression with polarization sensitive optical coherence tomography*. *J. Biomed. Optics*, 2002. **7**(4): p. 618-627.
71. Fried, D., et al., *Early Caries Imaging and Monitoring with Near-IR Light*. *Dental Clinics of North America - Incipient and Hidden Caries*, 2005. **49**(4): p. 771-794.

72. Zhang, L., L.Y. Nelson, and E.J. Seibel, *Red-shifted fluorescence of sound dental hard tissue*. Journal of Biomedical Optics, 2011. **16**(7): p. 071411.
73. Congalton, R.G. and K. Green, *Assessing the Accuracy of Remotely Sensed Data: Principles and Practices*. 2009: CRC Press.
74. Jones, R., et al., *Near-infrared transillumination at 1310-nm for the imaging of early dental decay*. Optics Express, 2003. **11**(18): p. 2259-65.
75. Bühler, C.M., P. Ngaotheppitak, and D. Fried. *Imaging of occlusal dental caries (decay) with near-IR light at 1310-nm*. in *Lasers in Dentistry XI*. 2005. San, Jose, CA: SPIE.
76. Jones, G., R.S. Jones, and D. Fried. *Transillumination of interproximal caries lesions with 830-nm light*. in *Lasers in Dentistry X*. 2004. San Jose: SPIE.
77. Lee, C., C.L. Darling, and D. Fried. *In vitro near-infrared imaging of occlusal dental caries using a germanium enhanced CMOS camera*. in *Lasers in Dentistry XVI*. 2010. Proc. SPIE
78. Simon, J.C., et al., *Near-IR Transillumination and Reflectance Imaging at 1300-nm and 1500-1700-nm for in vivo Caries Detection*. Lasers Surg Med, 2016. **48**(6): p. 828-836.
79. Salsone, S., et al., *Histological validation of near-infrared reflectance multispectral imaging technique for caries detection and quantification*. J Biomed Opt, 2012. **17**(7): p. 076009.
80. Usenik, P., et al., *Automated Classification and Visualization of Healthy and Diseased Hard Dental Tissues by Near-Infrared Hyperspectral Imaging*. Appl Spect, 2014. **66**(9): p. 1067-1074.

81. Kuhnisch, J., et al., *In vivo validation of near-infrared light transillumination for interproximal dentin caries detection*. Clin Oral Investig, 2015. **20**(4): p. 821-829.
82. Sochtig, F., R. Hickel, and J. Kuhnisch, *Caries detection and diagnostics with near-infrared light transillumination: clinical experiences*. Quintessence Int, 2014. **45**(6): p. 531-8.
83. Jablonski-Momeni, A., B. Jablonski, and N. Lippe, *Clinical performance of the near-infrared imaging system VistaCam iX Proxi for detection of approximal enamel lesions*. BDJ Open, 2017. **3**: p. 17012.
84. Barenie, J., G. Leske, and L.W. Ripa, *The use of fiber optic transillumination for the detection of proximal caries*. Oral Surg, 1973. **36**: p. 891-897.
85. Pine, C.M. *Fiber-Optic Transillumination (FOTI) in Caries Diagnosis*. in *Early Detection of dental caries*. 1996. Indianapolis: Indiana University.
86. Holt, R.D. and M.R. Azevedo, *Fiber Optic transillumination and radiographs in diagnosis of approximal caries in primary teeth*. Community Dent Health, 1989. **6**: p. 239-247.
87. Mitropoulis, C.M., *The use of fiber optic transillumination in the diagnosis of posterior approximal caries in clinical trials*. Caries Res, 1985. **19**: p. 379-384.
88. Hintze, H., et al., *Reliability of visual examination, fibre-optic transillumination, and bite-wing radiography, and reproducibility of direct visual examination following tooth separation for the identification of cavitated carious lesions in contacting approximal surfaces*. Caries Res, 1998. **32**(3): p. 204-9.

89. Schneiderman, A., et al., *Assessment of Dental caries with Digital Imaging Fiber-Optic Transillumination (DIFOTI):In vitro Study*. Caries Res., 1997. **31**: p. 103-110.
90. Benson, P.E., N. Pender, and S.M. Higham, *Quantifying enamel demineralization from teeth with orthodontic brackets--a comparison of two methods. Part 2: validity*. Eur J Orthod, 2003. **25**(2): p. 159-65.
91. de Josselin de Jong, E., A.F. Hall, and A.H.I.M. van der Linden. *QLF:A Monte Carlo simulation model*. in *Proceedings of the 1st Annual Indiana Conference, Early Detection of Dental Caries I*. 1996. Indianapolis, IN.
92. Stookey, G.K., *Quantitative Light Fluorescence: A Technology for Early Monitoring of the Caries Process*. Dental Clinics of North America - Incipient and Hidden Caries, ed. D.W. Boston. Vol. 49. 2005, Philadelphia: W. B Saunders Company. 753-770.
93. Tranaeus, S., et al., *Application of quantitative light-induced fluorescence to monitor incipient lesions in caries-active children. A comparative study of remineralisation by fluoride varnish and professional cleaning*. Eur J Oral Sci, 2001. **109**(2): p. 71-5.
94. Tranaeus, S., et al., *In vivo repeatability and reproducibility of the quantitative light-induced fluorescence method*. Caries Res, 2002. **36**(1): p. 3-9.
95. Alfano, R.R., et al., *Human teeth with and without caries studied by laser scattering, fluorescence and absorption spectroscopy*. IEEE J Quant Electr, 1984. **20**: p. 1512-1515.

96. Angmar-Masson, B.A., S. Al-Khateeb, and S. Tranaeus. *Intraoral use of quantitative light-induced fluorescence detection method*. in *Early Detection of dental caries*. 1996. Indianapolis: Indiana University.
97. Lussi, A., R. Hibst, and R. Paulus, *DIAGNOdent: an optical method for caries detection*. J Dent Res, 2004. **83 Spec No C**: p. C80-3.
98. Lussi, A., et al., *Performance and Reproducibility of a Laser Fluorescence System for Detection of Occlusal Caries in vitro*. Caries Res., 1999. **33**: p. 261-266.
99. Shi, X.Q., S. Tranaeus, and B. Angmar-Mansson, *Comparison of QLF and DIAGNOdent for quantification of smooth surface caries*. Caries Res, 2001. **35**(1): p. 21-6.
100. Stookey, G.K., *Optical methods--quantitative light fluorescence*. J Dent Res, 2004. **83 Spec No C**: p. C84-8.
101. ten Bosch, J.J. *Summary of Research of Quantitative Light Fluorescence*. in *Early detection of Dental caries II*. 1999. Indianapolis, IN: Indiana University.
102. Shi, X.Q., U. Welander, and B. Angmar-Mansson, *Occlusal caries detection with Kavo DIAGNOdent and Radiography: An in vitro comparison*. Caries Res, 2000. **34**: p. 151-158.
103. Ferreira Zandona, A.G., et al., *An in vitro comparison between laser fluorescence and visual examination for detection of demineralization in occlusal pits and fissures*. Caries Res, 1998. **32**(3): p. 210-8.
104. Watts, A. and M. Addy, *Tooth discolouration and staining: a review of the literature*. Br Dent J, 2001. **190**(6): p. 309-16.

105. Fu, D., et al., *Two-color, two-photon, and excited-state absorption microscopy*. J Biomed Opt, 2007. **12**(5): p. 054004.
106. Darling, C.L., et al., *An automated digital microradiography system for assessing tooth demineralization*. Lasers in Dentistry VX, 2009. **7162**: p. 1-7.
107. Simon, J.C., et al., *Near-IR and CP-OCT imaging of suspected occlusal caries lesions*. Lasers Surg Med, 2017. **49**(3): p. 215-224.
108. Darling, C.L., G.D. Huynh, and D. Fried, *Light scattering properties of natural and artificially demineralized dental enamel at 1310 nm*. Journal of Biomedical Optics, 2006. **11**(3): p. 34023.
109. Chung, S., et al. *Near infrared imaging of teeth at wavelengths between 1200 and 1600 nm*. in *Lasers in Dentistry XVII*. 2011. SPIE.
110. Tom, H., et al., *Near-infrared imaging of demineralization under sealants*. J Biomed Opt, 2014. **19**(7): p. 77003.
111. Simon, J.C., et al., *near-infrared imaging of natural secondary caries*. Proc SPIE Int Soc Opt Eng, 2015. **9306**.
112. Simon, J.C., C.L. Darling, and D. Fried. *A system for simultaneous near-infrared reflectance and transillumination imaging of occlusal carious lesions*. in *Lasers in Dentistry XXI*. 2016. Proc. SPIE
113. Simon, J.C., C.L. Darling, and D. Fried. *Assessment of cavitation in artificial approximal dental lesions with near-IR imaging*. in *Lasers in Dentistry XXIII*. 2017.

114. Simon, J.C., et al. *Near-infrared imaging of natural secondary caries*. in *Lasers in Dentistry XXI* 2015. Proc SPIE
115. Pitts, N.B. and P.A. Rimmer, *An in vivo comparison of radiographic and directly assessed clinical caries status of posterior approximal surfaces in primary and permanent teeth*. *Caries Res*, 1992. **26**: p. 146-152.
116. Wenzel, A., *Bitewing and digital bitewing radiography for detection of caries lesions*. *J Dent Res*, 2004. **83 Spec No C**: p. C72-5.
117. Wenzel, A., *Radiographic display of carious lesions and cavitation in approximal surfaces: Advantages and drawbacks of conventional and advanced modalities*. *Acta Odontol Scand*, 2014. **72**(4): p. 251-64.
118. Eli, I., et al., *Interpretation of bitewing radiographs. Part 1. Evaluation of the presence of approximal lesions*. *J Dent*, 1996. **24**(6): p. 379-83.
119. Weiss, E.I., et al., *Interpretation of bitewing radiographs. Part 2. Evaluation of the size of approximal lesions and need for treatment*. *J Dent*, 1996. **24**(6): p. 385-8.
120. Mejare, I. and B. Malmgren, *Clinical and radiographic appearance of proximal carious lesions at the time of operative treatment in young permanent teeth*. *Scand J Dent Res*, 1986. **94**(1): p. 19-26.
121. Hirasuna, K., D. Fried, and C.L. Darling, *Near-IR imaging of developmental defects in dental enamel*. *J. Biomed. Opt.*, 2008. **13**(4): p. 044011:1-7.
122. Jones, R.S., et al., *Near-IR Transillumination at 1310-nm for the Imaging of Early Dental Caries*. *Optics Express*, 2003. **11**(18): p. 2259-2265.
123. Buhler, C., P. Ngaotheppitak, and D. Fried, *Imaging of occlusal dental caries (decay) with near-IR light at 1310-nm*. *Optics Express*, 2005. **13**(2): p. 573-82.

124. Fried, D., et al. *Near-IR imaging of interproximal lesions from occlusal surfaces and the influence of stains and plaque*. 2006. SPIE.
125. Otis, L.L., et al., *Identification of Occlusal Sealants using Optical Coherence Tomography*. J. Clin. Dent., 2000. **14**(1): p. 7-10.
126. Jones, R.S., M. Staninec, and D. Fried, *Imaging artificial caries under composite sealants and restorations*. Journal of Biomedical Optics, 2004. **9**(6): p. 1297-304.
127. de Melo, L.S., et al., *Evaluation of enamel dental restoration interface by optical coherence tomography*. J Biomed Opt, 2005. **10**(6): p. 064027.
128. Stahl, J., H. Kang, and D. Fried. *Imaging simulated secondary caries lesions with cross polarization OCT*. in *Lasers in Dentistry XVI*. 2010. Proc. SPIE
129. Holtzman, J.S., et al., *Ability of optical coherence tomography to detect caries beneath commonly used dental sealants*. Lasers in Surgery and Medicine, 2010. **42**(8): p. 752-9.
130. Makishi, P., et al., *Non-destructive 3D imaging of composite restorations using optical coherence tomography: marginal adaptation of self-etch adhesives*. Journal of Dentistry, 2011. **39**(4): p. 316-25.
131. Lammeier, C., et al., *Influence of dental resin material composition on cross-polarization-optical coherence tomography imaging*. J Biomed Opt, 2012. **17**(10): p. 106002.
132. Logan, C.M., et al. *Multispectral near-infrared imaging of composite restorations in extracted teeth*. in *Lasers in Dentistry XX*. 2014. Proc. of SPIE

133. Louie, T., et al., *Clinical assessment of early tooth demineralization using polarization sensitive optical coherence tomography*. *Lasers in Surg. Med.*, 2010. **42**: p. 738-745.
134. Bush, J., P. Davis, and M.A. Marcus. *All-Fiber Optic Coherence Domain Interferometric Techniques*. in *Fiber Optic Sensor Technology II*. 2000. Proc SPIE.
135. Venz, S. and B. Dickens, *NIR-spectroscopic investigation of water sorption characteristics of dental resins and composites*. *Journal of Biomedical Materials Research*, Vol. 25, 1231-1248 (1991), 1991. **25**: p. 1231-1248.
136. Chan, A.C., et al., *Attenuation of near-IR light through dentin at wavelengths from 1300-1650-nm*. *Lasers in Dentistry XX*, 2014. **8929**: p. M1-5.
137. Demarco, F.F., et al., *Longevity of posterior composite restorations: not only a matter of materials*. *Dent Mater*, 2012. **28**(1): p. 87-101.
138. Mjor, I.A., *Clinical diagnosis of recurrent caries*. *J Am Dent Assoc*, 2005. **136**(10): p. 1426-33.
139. Kidd, E., *Diagnosis of secondary caries*. *J Dent Education*, 2001. **65**(10): p. 997-1000.
140. Kidd, E.A. and D. Beighton, *Prediction of secondary caries around tooth-colored restorations: a clinical and microbiological study*. *J Dent Res*, 1996. **75**(12): p. 1942-6.
141. Kidd, E.A.M., *Secondary caries*. *International Dental Journal*, 1992. **42**: p. 127-138.

142. Nassar, H.M. and C. Gonzalez-Cabezas, *Effect of gap geometry on secondary caries wall lesion development*. Caries Res, 2011. **45**(4): p. 346-52.
143. Moreira, P.L., et al., *Diagnosis of secondary caries in esthetic restorations: influence of the incidence vertical angle of the X-ray beam*. Braz Dent J, 2011. **22**(2): p. 129-33.
144. Rudolph, M.P., et al., *Validity of radiographs for diagnosis of secondary caries in teeth with class II amalgam restorations in vitro*. Caries Res, 1997. **31**(1): p. 24-9.
145. Rudolph, M.P., et al., *Validity of bite-wings for diagnosis of secondary caries in teeth with occlusal amalgam restorations in vitro*. Caries Res, 1993. **27**(4): p. 312-6.
146. Rudolph, M.P., J.P. van Amerongen, and J.M. ten Cate, *Radiopacities in dentine under amalgam restorations*. Caries Res, 1994. **28**(4): p. 240-5.
147. Neuhaus, K.W., et al., *Detection of proximal secondary caries at cervical class II-amalgam restoration margins in vitro*. J Dent, 2012. **40**(6): p. 493-9.
148. Braga, M.M., et al., *Validity and reliability of methods for the detection of secondary caries around amalgam restorations in primary teeth*. Braz Oral Res, 2010. **24**(1): p. 102-7.
149. Alammari, M.R., et al., *Quantitative light-induced fluorescence (QLF): a tool for early occlusal dental caries detection and supporting decision making in vivo*. J Dent, 2013. **41**(2): p. 127-32.
150. Ando, M., G.K. Stookey, and D.T. Zero, *Ability of quantitative light-induced fluorescence (QLF) to assess the activity of white spot lesions during dehydration*. Am J Dent, 2006. **19**(1): p. 15-8.

151. Pretty, I., et al., *Detection of in vitro demineralization adjacent to restorations using quantitative light induced fluorescence (QLF)*. Dental Materials 2003. **19**: p. 368-374.
152. Ando, M., et al., *Evaluation of Several Techniques for the Detection of Secondary Caries Adjacent to Amalgam Restorations*. Caries Res, 2004. **38**: p. 350-356.
153. Gonzalez-Cabezas, C., et al., *Early detection of secondary caries using quantitative, light-induced fluorescence*. Oper Dent, 2003. **28**(4): p. 415-22.
154. Konig, K., H. Schneckenburger, and R. Hibst, *Time-gated in vivo autofluorescence imaging of dental caries*. Cell Mol Biol (Noisy-le-grand), 1999. **45**(2): p. 233-9.
155. Boston, D.W., *Initial in vitro evaluation of DIAGNOdent for detecting secondary carious lesions associated with resin composite restorations*. Quintessence Int, 2003. **34**(2): p. 109-16.
156. Lussi, A., et al., *Clinical performance of a laser fluorescence device for detection of occlusal caries lesions*. Eur J Oral Sci, 2001. **109**(1): p. 14-9.
157. Hitij, T. and A. Fidler, *Effect of dental material fluorescence on DIAGNOdent readings*. Acta Odontol Scand, 2008. **66**(1): p. 13-7.
158. Li, X. and T.A. King, *Microstructure and Optical Properties of PMMA/Gel Silica Glass Composites*. Journal of Sol-Gel Science and Technology, 4, 75-82 (1995), 1995. **4**: p. 75-82.
159. Stansbury, J.W. and S.H. Dickens, *Determination of double bond conversion in dental resins by near infrared spectroscopy*. Dental Materials, 2001. **17**: p. 71-79.

160. Lenton, P., et al., *Imaging in vivo secondary caries and ex vivo dental biofilms using cross-polarization optical coherence tomography*. Dent Mater, 2012. **28**(7): p. 792-800.
161. Simon, J.C., et al., *Near-infrared imaging of secondary caries lesions around composite restorations at wavelengths from 1300-1700-nm*. Dent Mater, 2016. **32**(4): p. 587-95.
162. Tom, H., et al., *Near-IR imaging of demineralization under sealants*. Proc SPIE Int Soc Opt Eng, 2014. **8929**: p. 89290S.
163. Diaz-Arnold, A.M., M.A. Arnold, and V.D. Williams, *Measurement of water sorption by resin composite adhesives with near-infrared spectroscopy*. J Dent Res, 1992. **71**(3): p. 438-42.
164. Mjor, I.A. and F. Toffenetti, *Secondary caries: a literature review with case reports*. Quintessence Int, 2000. **31**(3): p. 165-79.
165. Kidd, E.A., S. Joyston-Bechal, and D. Beighton, *Microbiological validation of assessments of caries activity during cavity preparation*. Caries Res, 1993. **27**(5): p. 402-8.
166. Peltola, J. and J. Wolf, *Fiber optics transillumination in caries diagnosis*. Proc Finn Dent Soc, 1981. **77**: p. 240-244.
167. Bin-Shuwaish, M., et al., *The correlation of DIFOTI to clinical and radiographic images in Class II carious lesions*. J Am Dent Assoc, 2008. **139**(10): p. 1374-81.
168. Yang, J. and V. Dutra, *Utility of radiology, laser fluorescence, and transillumination*. Dent Clin North Am, 2005. **49**(4): p. 739-52, vi.

169. Keem, S. and M. Elbaum, *Wavelet representations for monitoring changes in teeth imaged with digital imaging fiber-optic transillumination*. IEEE Trans Med Imaging, 1997. **16**(5): p. 653-63.
170. Karlsson, L., et al., *Near-infrared transillumination of teeth: measurement of a system performance*. Journal of Biomedical Optics, 2010. **15**(3): p. 036001-8.
171. Almaz, E.C., et al. *Influence of stains on lesion contrast in the pits and fissures of tooth occlusal surfaces from 800-1600-nm*. in *Lasers in Dentistry XXII*. 2016. Proc. SPIE
172. Peers, A., et al., *Validity and reproducibility of clinical examination, fibre-optic transillumination, and bite-wing radiology for the diagnosis of small approximal carious lesions*. Caries Res., 1993. **27**: p. 307-311.
173. Pine, C.M. and J.J. ten Bosch, *Dynamics of and diagnostic methods for detecting small carious lesions*. Caries Res, 1996. **30**(6): p. 381-8.
174. Purdell-Lewis, D.J. and T. Pot, *A comparison of radiographic and fibre-optic diagnoses of approximal caries lesions*. J Dent, 1974. **2**(4): p. 143-8.
175. Vaarkamp, J., et al., *The real performance of bitewing radiography and fiber-optic transillumination in approximal caries diagnosis*. J Dent Res, 2000. **79**(10): p. 1747-51.
176. Stephen, K.W., et al., *Comparison of fibre optic transillumination with clinical and radiographic caries diagnosis*. Community Dent Oral Epidemiol, 1987. **15**(2): p. 90-4.
177. Boston, D.W., *Incipient and hidden caries*. Dental clinics of North America, 2005. **49**(4): p. xi-xii.

178. Ricketts, D., et al., *Hidden caries: what is it? Does it exist? Does it matter?* International dental journal, 1997. **47**(5): p. 259-65.
179. Lussi, A., et al., *Performance and reproducibility of a laser fluorescence system for detection of occlusal caries in vitro.* Caries Res, 1999. **33**(4): p. 261-6.
180. Bouma, B.E. and G.J. Tearney, *Handbook of Optical Coherence Tomography.* 2002/08/21 ed. 2002, New York, NY: Marcel Dekker.
181. Colston, B., et al., *Imaging of hard and soft tissue structure in the oral cavity by optical coherence tomography.* Applied Optics, 1998. **37**(19): p. 3582-3585.
182. Feldchtein, F.I., et al., *In vivo OCT imaging of hard and soft tissue of the oral cavity.* Optics Express, 1998. **3**(3): p. 239-251.
183. Baumgartner, A., et al., *Polarization-sensitive optical optical coherence tomography of dental structures.* Caries Res., 2000. **34**: p. 59-69.
184. Jones, R.S. and D. Fried. *The Effect of High Index Liquids on PS-OCT Imaging of Dental Caries.* in *Lasers in Dentistry XI.* 2005. San, Jose, CA: SPIE.
185. Ngaotheppitak, P., C.L. Darling, and D. Fried, *Polarization Optical Coherence Tomography for the Measuring the Severity of Caries Lesions.* Lasers Surg Med, 2005. **37**(1): p. 78-88.

Publishing Agreement

It is the policy of the University to encourage open access and broad distribution of all theses, dissertations, and manuscripts. The Graduate Division will facilitate the distribution of UCSF theses, dissertations, and manuscripts to the UCSF Library for open access and distribution. UCSF will make such theses, dissertations, and manuscripts accessible to the public and will take reasonable steps to preserve these works in perpetuity.

I hereby grant the non-exclusive, perpetual right to The Regents of the University of California to reproduce, publicly display, distribute, preserve, and publish copies of my thesis, dissertation, or manuscript in any form or media, now existing or later derived, including access online for teaching, research, and public service purposes.

DocuSigned by:

Jacob Simon

B44C3A8C704344E...

Author Signature

6/1/2021

Date